The Application of High Precision Timing in the High Resolution Fly's Eye Cosmic Ray Detector

A Thesis Submitted to the
Department of Physics and Mathematical Physics
at the
University of Adelaide
for the degree of
Doctor of Philosophy

by

Christopher Richard Wilkinson B.Sc (Hons.)

May 1998

Contents

Abstract

This thesis represents work performed by the author on the development of the High Resolution Fly's Eye (HiRes) detector for the study of extremely high energy ($> 10^{18}$eV) cosmic rays. Chapter 1 begins with an review of this field. This chapter details the development of the field, the physics questions we seek to answer, and our current understanding based on experimental and theoretical results. It provides the basis for understanding why detectors such as HiRes are being constructed.

This review leads into chapter 2, which discusses the development of cosmic ray induced extensive air showers (EAS) and the techniques used to study them. Particular emphasis is placed upon the air fluorescence technique utilised by HiRes. The two site HiRes prototype detector is then discussed in detail in chapter 3. This covers the different components that form the detector, together with details of the calibration performed to extract useful information from the data.

Chapter 4 discusses the installation and subsequent testing of GPS based clock systems for the two sites that make up the HiRes prototype detector. The entire timing system was checked, and some previously hidden bugs fixed. This chapter concludes with work performed on the time to digital converter calibration for the second HiRes site.

The high relative timing accuracy provided by the GPS clocks allowed the use of timing information in programs to reconstruct the arrival directions of cosmic rays. Chapter 5 covers the development of a program to use geometrical and timing information to reconstruct EAS viewed by both HiRes sites. This chapter concludes with an evaluation of the likely reconstruction accuracy of the new HiRes (stage 1) detector.

A well reconstructed EAS trajectory is the first step in the determination of more interesting parameters such as primary particle energy. Chapter 6 covers the collation and analysis of EAS viewed by the both sites of the prototype detector. This includes an evaluation of effects such as the atmosphere, and an estimation of the performance of the new (stage 1) HiRes detector based on results with the prototype detector.

Finally the conclusions from this thesis are summarised and suggestions made for further follow up work.

Statement of Originality

This thesis contains no material which has been accepted for the award of any other degree or diploma in any university or other tertiary institution and, to the best of my knowledge and belief, contains no material previously published or written by another person, except where due reference has been made in the text.

I give consent to this copy of my thesis, when deposited in the University Library, being available for loan and photocopying.

Christopher Wilkinson

Acknowledgements

Many people have been instrumental in helping me complete this work. First and foremost I would like to thank my wife, Bridget, for her love, support and understanding which has made the last few years so enjoyable (and made the bad bits bearable).

I would also like to thank my supervisors Bruce Dawson and Roger Clay, together with my unofficial supervisors, David Bird and Lawrence Wiencke, for their guidance, help, friendship and advice that has made this work possible. Projects such as HiRes are heavily dependent upon good technical support and thus I would like to thank our technicians/engineers, Neville Wild, Jeremy Smith and Stan Thomas for their explanations and advice throughout this work.

Thanks also to Matthew Kidd (and Nathan and Molly), for showing me around SLC and for writing such good code. I would also like to thank the entire HiRes collaboration for running the detector and helping to keep the project on track. I would also like to thank the astrophysics group (both past and present members) at the University of Adelaide. In particular I should mention Ken Simpson, since I helped rope him into this project thus condemning him to hours of both my and Troy's presence in the computing room. Special thanks must also go to Troy Porter, for his friendship and company these last few years.

I would also like to thank the usual Tuesday night crowd – Bridget, Michael, Mykal, and Sèana *et al.* – for providing both friendship and welcome relief from my thesis. Finally thanks go out to both my family, Mum, Dad, Susan, Philip, Peter and Allison; and my inlaws, Rick, Anita, David, Justine and Michael. Thank you for excellent support and encouragement throughout this ordeal – I do feel lucky to have such a supportive family network, it has meant a lot to me.

Finally thank you to anyone I've missed and to anyone who has helped me along the way. This work has been supported through the receipt of a University of Adelaide scholarship and travel grant.

Chapter 1

Cosmic Rays

Cosmic rays are highly energetic particles arriving from space. They cover a huge range of energies – from below 10^9eV (1 GeV) up to, and possibly beyond 10^{20}eV (100EeV). This large energy range requires the use of many different techniques to probe the entire range, and the different subranges provide information on different astronomical phenomena. This thesis will primarily be concerned with the extremely high energy range – particles with energies above 10^{17}eV which place them in the joule range (1 Joule = 6×10^{18}eV). Significant questions exist about where these particles originate, and the processes or environments that produced these particles with macroscopic amounts of energy.

An abbreviated history of cosmic ray physics will first be presented. This will set the scene for a discussion of the current physics questions we seek to answer, and how the observational evidence we currently possess has been interpreted.

1.1 A History of Cosmic Rays

The discovery of cosmic rays has its origins in the discovery of natural radioactivity by Becquerel in 1896[24]. One of his key discoveries (for cosmic rays) was the fact that the radiation from uranium could discharge electrosopes. An electroscope contains two pieces of gold-leaf (or similar material) which may be charged by an external source, which causes the two leaves to repel each other. When the electroscope is irradiated, the rate at which the leaves come together provides a measure of the amount

of ionisation from a source.

By 1901, research into natural radioactivity had discovered three particles capable of causing ionisation of air and discharging electroscopes. The three particles were characterised according to their penetrating power: α particles were stopped in about 0.05m of air, β particles traveled longer distances, and γ-rays were very penetrating requiring several cm of lead to drop their intensity by a factor of 10. The discovery that a charged electroscope kept away from natural sources of radioactivity would still discharge was a major mystery. In 1910, Wulf climbed to the top of the Eiffel Tower and showed that the ionisation was not due to γ-rays from the earth[174]. However the breakthrough was made by Hess who made a series of balloon flights during 1912[98] and 1913[99]. In 1914 Kolhörster ascended to 9km and confirmed Hess' findings[117]. They measured the amount of ionisation as a function of height and found that above a height of 1.5km, the average ionisation increased with respect to the sea-level value. The conclusion was unambiguous – the source of the highly penetrating radiation was extra-terrestrial. In 1926, after a series of measurements in California, Millikan proposed that these 'cosmic rays' were γ rays of a much higher penetrating power than was observed in sources of natural radioactivity[149].

Whilst the name may have stuck, the association of the radiation with gamma-rays did not. In 1927 Clay made a series of measurements of the intensity as a function of geomagnetic latitude, as he traveled from Java to the Netherlands[55]. He found the intensity increased as he increased his (geomagnetic) latitude from the equator. His results were confirmed by Compton in 1932 in the southern hemisphere[58]. This behaviour fitted the theory developed by Störmer for *charged particles* entering the geomagnetic field of the earth[164]. Further evidence for cosmic rays being particles came from experiments done by Bothe and Kolhörster in 1929 who used the newly developed Geiger-Müller detectors in coincidence to show that the radiation was probably particles with energies of around 10^9eV[41]. In the same year Skobelsyn produced the first pictures of cosmic ray tracks using cloud chambers and noted the existence of multiple tracks in some pictures[157]. Improved cloud chambers were developed leading to the discovery of the positron by Anderson in 1932[14]. This was confirmed in 1933 by Blackett and Occhianlini who used Geiger counters to act as a coincidence

trigger for a cloud chamber[39]. Rossi used three Geiger-Müller detectors in triangular arrangement such that they could only be triggered by the passage of multiple particles. He also found that by placing lead above his detectors he could increase his coincidence rate – maximising it at with about 1.5cm of lead[153]. Around the same time Johnson and Street[107], Rossi[154] and Clay[56] all detected an east-west asymmetry in the cosmic ray intensity about the vertical. This is best explained by the cosmic rays being particles and whose trajectories are affected by the earth's magnetic field. The positively charged particles will be deflected to the west whilst negatively charged particles will be to the east. The east-west asymmetry could be explained if the primary cosmic ray beam was predominantly positively charged. Thus by the early 1930's the evidence was clear – cosmic *rays* were in fact almost entirely *positively charged particles*[106].

The use of cloud chambers to detect cosmic rays led to a number of important discoveries for particle physics. The positron was detected[14] soon after it was proposed by Dirac[70]. Muons were then found in 1936[136] and were initially thought to be the pions predicted by Yukawa[178] around the same time. However these were not found until the development of emulsion chambers in 1947[138]. Following World War II the use of cosmic rays to discover elementary particles boomed. In 1947 Rochester and Anderson detected the decay of two previously unknown neutral particles via 'V' events[148]. In the next few years Kaons ($\kappa^{\pm}$, κ^{0}) and Lambdas (Λ) were found when cloud chambers were taken to high altitudes. These new particles were classed as heavy mesons and hyperons and possessed strange and puzzling properties that could not initially be explained. The use of bubble chambers led to the discovery of the Ξ^{-} hyperon in 1952[15] and the Σ hyperon in 1953[40]. By this time, particle physics had developed to the stage where particles could be accelerated on demand, with known energy and directions. This proved a significant advantage and thus after 20 years as the primary window into sub-atomic phenomena, particle physicists set aside cosmic rays for accelerators[78][152][128].

However particle physics was not the only area of research on cosmic rays. The discovery that particles came in showers led to the birth of current cosmic ray research. In 1938, Auger, Maze and Robley[18] made a pioneering series of measurements to

measure the coincidence rates as they separated their detectors. They made the remarkable discovery that cosmic ray showers had lateral extents out to at least 300m, recording an average of 1.5 showers per hour. From this they inferred they were seeing the secondary particles due to cascading effects caused by the interaction of a highly energetic primary particle high in the atmosphere. Their measurements indicated that these extensive air-showers (EAS) were caused by particles with energies of $\sim 10^{16}$eV [18][106][152].

Following the discovery of EAS caused by such high energy particles, there was significant interest in the primary particle's composition, the energy spectrum, the maximum energy and if any anisotropy or astronomical sources could be found. Early research into EAS indicated that the primary particles were predominantly protons and heavy nuclei. These particles interact with the atmosphere initiating a chain of nuclear interactions that form the core of the shower. Neutral pions are created in the interactions which decay to produce further electromagnetic cascades and charged pions produce penetrating muons. As the shower develops, scattering by the atmosphere causes shower particles to spread out laterally. The density is highest at the centre and the lateral extent is determined by the initial particle's energy. This lateral spread of the showers compensated for the reduced flux rates allowing detection. Advances in hardware made large scale detector arrays feasible in the 1950's, and arrays were constructed by many research groups throughout the world (many of the groups are still working in the area of cosmic ray research).

Important work was performed by Bassi, Clark and Rossi at MIT who used three liquid scintillators in several configurations to develop techniques to measure shower size and direction[22]. Scintillator detectors produce a detectable light pulse when a particle passed through them, and they were able to show that whilst the lateral extent of the shower was large, it was only of the order of a metre thick. By recording the arrival times at different parts of the array as this shower front passed they could determine the arrival direction of the shower. Given that all the particles quickly passed through a given detector, shower density measurements were possible. By combining information from separate detectors, the lateral distribution of particles and the total number of particles in the shower can be obtained, and this information

can be used to estimate the primary particle's energy[22]. Following demonstration of the EAS reconstruction technique, it was employed on an array at Agassiz from 1954-7 to try and detect any anisotropy in the arrival directions of cosmic rays. The array consisted of 15 plastic scintillators (each $0.9m^2$) within a circle with a diameter of 460m ($0.2km^2$) and was successful in detecting EAS generated by particles with primary particles in the range from 10^{15}eV to 10^{18}eV. The integral energy spectrum was measured as $J(>E) = 26(E/10^{15})^{-2.17}\ m^{-2}\ yr^{-1}\ sr^{-1}$ over their detection range – ie. for every 10 fold increase in energy, the flux above that energy drops by a factor of $10^{2.17} \approx 150$. No detectable cut-off was observed as they were limited by the low flux at high energies. Analysis of the 652 largest events yielded no detectable anisotropy, leaving the question of possible sources or acceleration mechanisms open[53][54][152].

The success of the detector array at Agassiz, and the isotropy observed paved the way for the first detector for extremely high energy cosmic rays ($> 10^{17}$eV) at Volcano Ranch, New Mexico, in 1959[124]. It was built primarily to gain information on the highest energy cosmic rays, as it was realised that for a 10^{18}eV proton the Larmor radius in the galaxy's magnetic field would be greater than the thickness of the galaxy. Thus detection of a significant number of extremely high energy particles might show anisotropy and possibly point to extragalactic sources. The detector consisted of 19 stations, arranged in two hexagonal grids, initially covering an area of $2km^2$ (1959-60 run) before expanding to an area of $8km^2$. Each station was a $3.3m^2$ scintillator detector which made measurements of particle density, and the time each detector was triggered enabled determination of the EAS direction within 5°. The threshold was estimated at $\approx 10^{17}$eV and the detector was run for 13000 hours between 1960-2. The integral energy spectrum over the range 10^{17}eV to 3×10^{19}eV was estimated using the simple relationship $E = 2 \times 10^9 N$ (where N is the estimated number of particles in the shower at ground level). Linsley claimed an average value for the integral exponent $\gamma = -d(\log J)/d(\log E)$ as being in the range 1.7 to 2.0, less than the 2.2 found using the Agassiz detector at lower energies. It was proposed that this change in the spectral slope was due to a cross over between galactic and extra-galactic cosmic rays[125].

In February 1962 the Volcano Ranch array was triggered by a particle with an estimated energy of 10^{20}eV[126]. Such a high energy particle was significant because its

trajectory was unlikely to be affected by the magnetic field of the galaxy. The full importance of such a discovery was not realised until 1966 when Griesen[93] and Zatsepin and Kuzmin[179] independently realised that cosmic rays above about 4×10^{19}eV would interact with the 3K cosmic microwave background given a sufficiently large path length. This implied that such high energy cosmic rays (like the 10^{20}eV event) had to come from sources within a few hundred megaparsecs rather than cosmological distances.

The results from Volcano Ranch, and the prospect of detectable anisotropy helped to drive the push for more experiments to detect extremely high energy cosmic rays.

The Sydney University Giant Airshower Recorder (SUGAR) consisted of 47 detectors comprising a collecting area of $\approx 70km^2$ and ran from 1968-79[43]. It has been the only southern hemisphere experiment in EHE cosmic rays, and was located in the Pilliga State Forest in New South Wales, Australia (149°43′E, 30°32′S). Each detector station comprised two $6m^2$ liquid scintillators separated by 50m which were buried to a depth of 1.7m to make measurements of the EAS muon density. Energy was estimated from the total muon number and the angular resolution for most showers was $6° \times \sec\theta$.

The University of Leeds operated the Haverah Park detector (longitude 1°38.2′W, latitude 53°58.2′N, and mean sea level (MSL) altitude of 200m) from 1968-87[121]. Haverah Park used 32 water Cerenkov tanks to provide a collecting area of $\approx 12km^2$. These tanks were 1.2m deep with sizes varying from $1m^2$ to $34m^2$ and detected Cerenkov light as the EAS particles passed through. This gave a particle density measurement and energy was estimated based on the density 600m from the core $E = \beta\rho(600)^{\alpha}$. This method is known as the $\rho(600)$ method (or sometimes S(600)) and $\beta \approx 10^{17}$ and $\alpha \approx 1.0$[102][103]. $\rho(600)$ was measured to an accuracy of better than 30%. The angular resolution was dependent upon the zenith angle θ of the EAS. The error in the zenith angle was estimated as $\sigma_\theta = 2.5° \times \sec\theta$ for $0 < \theta < 90°$, and the error in the azimuth angle ϕ as $\sigma_\phi = 2.5° \times cosec\,\theta$ for zenith angles $15° < \theta < 90°$.

The Yakutsk array located in Siberia (129.4°E, 61.7°N, 100mMSL) began as a $1km^2$ array in 1969. It was expanded to $18km^2$ in 1973 to enable detection of the highest energy showers. In 1990 ten outlying stations were shutdown reducing the array size

to $10km^2$[10]. The array utilises plastic scintillators, underground muon detectors and atmospheric Cerenkov light detectors to determine primary particle energy and composition (esentially a variant on the $\rho(600)$ method, see[9]). Meaurements of $\rho(600)$ have a resolution of 25% at 10^{17}eV which decreases to $\sim$ 20% for energies above 10^{18}eV[10]. Angular resolution is $\approx 2^\circ$ for zenith angles $< 60^\circ$ at an energy of 10^{19}eV (see Table 3 of [10] for resolution as a function of energy and zenith angle).

The Akeno Giant Air-Shower Array (AGASA) grew from the Akeno Air Shower Experiment (138°30′E, 35°30′N, 900mMSL) in 1990. The $100km^2$ array consists of 111 $2.2m^2$ plastic scintillators and 27 muon detectors ($2.8m^2$, $10m^2$ and $25m^2$) arranged in 4 branches which operated independently until they were unified in December 1995[177][95][97]. Energy is determined by the $\rho(600)$ method with the accuracy of $\rho(600)$ is $\sim 30\%$. Muon information is used in composition studies. Angular resolution is 1.6° for energies above 4×10^{18}eV. Figure 1.1 illustrates the intensity of cosmic rays (as a function of energy) measured by the Akeno Air Shower Experiment and AGASA. It illustrates the sharp decrease in intensity with energy which is why Akeno was increased from $1km^2$ to $20km^2$ to $100km^2$ to probe higher energy ranges[177].

The Fly's Eye detector was the first successful experiment to utilise the air fluorescence technique for detection of extremely high energy cosmic rays (an unsuccessful attempt had been made by Greisen and Bunner in 1966[44])[21]. It ran from 1981-93 with a collecting aperture of $\approx 1000km^2sr$ at the highest energies, although unlike the ground arrays previously mentioned, it could only be operated during clear moonless nights which restricts the duty cycle to ≈10%. The technique measures the amount of fluorescence light from the EAS as it develops in the atmosphere and provides an almost model independent estimation of energy, as well as allowing good composition measurements. Energy resolution was $\approx 30\%$ for showers viewed by a single site, and $\approx 20\%$ for showers viewed by both sites. The angular resolution varies from event to event due to the EAS-detector geometry and ranges from 10° down to 1°[46]. In 1991, the Fly's Eye detected a particle with an energy of 3.2×10^{20}eV – the highest energy event seen by any detector to the present time[33]. The High Resolution Fly's Eye is now being constructed at the site of the original Fly's Eye, and this thesis will deal with data from the two site prototype.

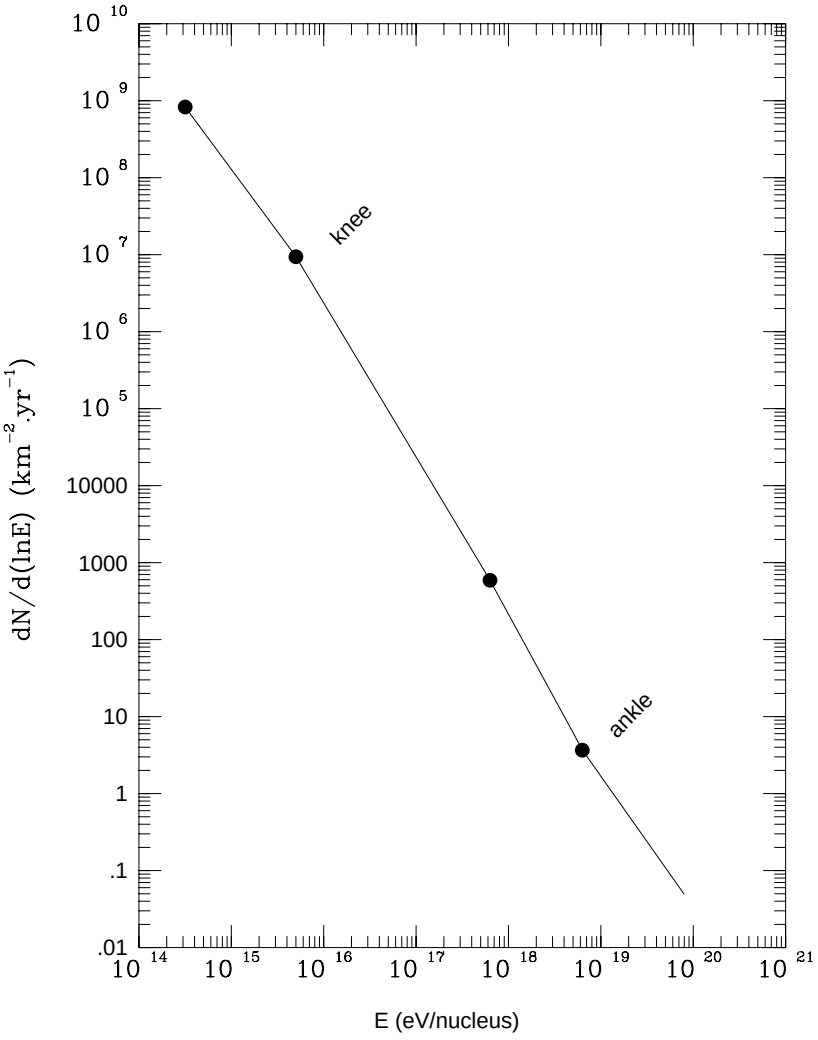

Figure 1.1: The intensity of cosmic rays as measured by the Akeno Air shower experiment and AGASA (zenith angles from 0 to 45°).[177].

1.2 Physics of Extremely High Energy Cosmic Rays

The purpose of studying Extremely High Energy (EHE) cosmic rays is to understand nature at its most energetic. EHE cosmic rays have macroscopic amounts of energy – the highest energy particle observed possessed 51 Joules. The underlying aim of the field is to understand the processes in nature that may generate particles with such huge energies.

To understand how these particles are created, we first need to know what they are, and where they are coming from. Observationally, we seek to answer these 'what' and

'where' questions so that appropriate theoretical models can be derived to explain the question of 'how'. By making measurements of the cosmic ray energy spectrum, the mass composition as a function of energy and the anisotropy in arrival directions, we can compare observations with different competing theories. In addition to generating EHE particles, theories must take into account the propagation of the particles to the Earth. Production theories must take into account the intervening medium, as this can directly affect the observed spectrum, composition and anisotropy.

At present no theory adequately explains the production of extremely high energy cosmic rays[104][52][140]. The most basic problem is the need for the size of the accelerating region to be at least twice the size of the gyro-radius of the particle in the magnetic field of the region. In a uniform magnetic a charged particle will spiral around the field lines with a constant radius known as the Larmor or gyro radius. The gyro-radius for a a cosmic ray nucleus of charge Z and in a magnetic field $B_{\mu G}$, in units of micro Gauss, with an energy E_{18} in units of 10^{18}eV, is:

$$R_{kpc} \approx \frac{E_{18}}{(Z\ B_{\mu G})} \tag{1.1}$$

This confinement requirement can be stated in terms of the maximum energy E_{18} that a particle of charge Z may be accelerated to in a region of size L_{kpc} (units of kiloparsecs) with a magnetic field of $B_{\mu G}$ as:

$$E_{18} = \frac{\beta\ Z\ L_{kpc}\ B_{\mu G}}{2} \tag{1.2}$$

The factor β (≤ 1) is the fraction of the maximum energy that can be obtained within the region and is related to the details of the acceleration mechanisms at the particular site (in simple shock acceleration $\beta = v_s/c$ where v_s is the velocity of the shock)[104][17][60]. At the highest energies synchrotron losses may prevent particles from reaching the maximum possible energy given in equation 1.2 – for a perpendicular shock moving at 0.1c, a proton is limited to $E_p^{\max} = 4 \times 10^{22} B_{\mu G}^{-1/2}$eV[140]. The sources capable of accelerating particles up to 10^{20}eV are illustrated in Figure 1.2 from Hillas[104]. This diagram clearly indicates that few sources are viable, and that most require efficient acceleration mechanisms (large β) to generate EHE particles.

Whilst several acceleration schemes may be viable, no detailed scheme satisfactorily explains the acceleration mechanism. Hopefully the situation should improve when

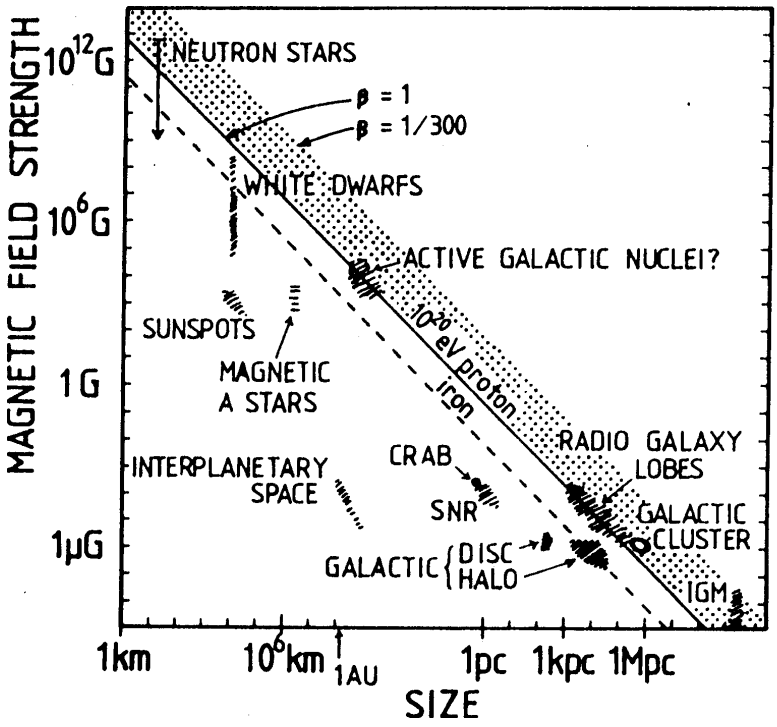

Figure 1.2: Size and magnetic field strengths of possible acceleration sites for EHE cosmic rays[104]. Objects below the solid line cannot accelerate protons to 10^{20}eV and those below the dashed line are unable to accelerate iron to 10^{20}eV. The edge of the shaded region represents a value of $\beta = 1/300$ which is probably typical for protons being accelerated by diffuse shock acceleration. Note the few possible acceleration sites and the large values of β needed to accelerate particles.

more data is obtained. More data should allow us to rule some schemes out, and allow us to concentrate theoretical efforts on the remaining schemes. As no current scheme exists, the way is also open for the discovery of new physics to explain the acceleration of such extremely high energy particles.

Prior to considering source theories it is worth examining the effects of intervening media between a source and the earth. An important effect is that due to the presence of magnetic fields, which cause charged particles to spiral around field lines. The magnetic field of the galaxy consists of a large scale ordered component and a small scale random component[23]. The ordered component of the magnetic field extends through the plane of the galaxy and undergoes a series of reversals in direction as a function of galactic radius. To a first approximation, the field can be considered as a set of concentric rings in which the magnetic field lines are directed purely in the

azimuthal direction. Reversals in field direction occur between adjacent rings and have been measured at galactic radius of 5.5kpc and 8.1kpc[143]. The strength of the field in our local region is $\sim 2\mu$G which may or may not be aligned in the direction of the the spiral arm, within which it is thought to be stronger. The field strength is also thought to increase to $\approx$ 5-6μG in the inner region (R $<$ 5.5kpc) of the galaxy. In addition to the ordered component, the turbulent nature of the interstellar medium gives rise to a random component to the field. The random component of the magnetic field has a strength of $\sim 5\mu$G and is correlated in direction with a scale of $\approx$ 50pc, although this is probably overly simplistic and that there will be irregularties on many scales[144]. In addition to galactic fields in the plane of the galaxy, there may also exist a magnetic field in a spherical halo around the galaxy. Halos have been observed in several edge on spiral galaxies, and probably arise through dynamo effects arising due to chaotic motions and differential rotation of gas in the halo[42]. The actual situation is probably more complex than that presented here with active research being performed to extend and clarify our current understanding of magnetic fileds in the galaxy[23]. The extragalactic field is less well known but estimated as being $\approx 10^{-9}$ Gauss[17]. Magnetic fields tend to scramble the trajectories of cosmic rays, as non-uniformities will scatter cosmic rays by different amounts, thus randomising their trajectories. However at extremely high energies, charged particles (especially protons) are less affected by magnetic fields. Photons are of course unaffected, directly pointing back to their source, but observational evidence suggests that EHE cosmic rays are predominantly charged particles.

Universal Source Theories Universal source theories generally predict that the cosmic ray intensity is homogeneous and isotropically distributed. These theories propose sources such as shock acceleration in large scale structures such as in the jets or lobes of radio galaxies, galaxy cluster accretion shocks or perhaps via the decay of topological defects such as cosmic strings. Such theories predict a predominantly protonic composition above 10^{19}eV (topological defects models are the exception and predict a predominance of γ-rays[26]), a cut off in the energy spectrum at around 5×10^{19}eV and an isotropic distribution of arrival directions (due to the isotropic

nature of the sources)[162][17].

Infrared photons and photons from the 2.7 K Cosmic Microwave Background radiation field (CMB) cause photo-disintegration of cosmic ray nuclei as in the rest frame the nuclei they appear to be high energy γ-ray photons. For cosmological age cosmic rays this effect should produce a nearly pure proton spectrum above 10^{19}eV. The CMB photons also affect the propagation of EHE protons, with effects dependent upon proton energy E_p (since this governs how energetic the CMB photon will appear in the proton's rest frame). For $E_p \gtrsim 5 \times 10^{17}$eV the CMB photons appear as γ-rays with sufficient energy to undergo electron-positron pair production. The proton loses a small amount of energy in this interaction but the losses are cumulative[162][17]. For $E_p \gtrsim 5 \times 10^{19}$eV the CMB photons appear as γ-rays with energies in excess of the pion restmass so interactions lead to pion photoproduction degrading the energy of the proton by $\approx 20\%$[179]. The mean free path for a 10^{20}eV proton is about 30Mpc[119] – which is a small distance on the cosmological scale. These interactions lead to the Greisen-Zatsepin-Kuzmim (GZK) cutoff in the spectrum at around 5×10^{19}eV for sufficiently distant sources[93][179]. The actual shape of the spectrum is dependent upon the spatial and temporal source distribution used by the different models, but the general features are essentially model independent.

Quasi-local Extragalactic Sources These theories propose that there may be relatively local extra-galactic sources. The sources are likely to be similar to those of universal source models such as the lobes of radio galaxies. These sources are close enough that the effects of propagation through the background radiation fields will have limited effects on the spectrum or composition of EHE cosmic rays. Thus the strength of the GZK cut-off, and any associated pile-up of energy degraded cosmic rays prior to it, will depend on the source distance.

The closeness of such sources should also lead to some level of anisotropy. The effects of magnetic fields is dependent upon the energy and charge of the particle (see equation 1.1). High energy protons should be relatively undeflected by intergalactic or galactic magnetic fields. Iron (or heavy) nuclei will be more greatly affected, as will lower energy particles. Thus large scale anisotropy is expected at the highest energies

(10^{20}eV), and may also be present at lower energies (10^{18}eV) if the composition is light.

Galactic Sources Galactic sources are classed depending on whether the source is within the galactic disk or not. The most prominent theory for sources outside the disk involves acceleration in the termination shock of the outgoing galactic wind[108]. Interestingly the wind is powered by supernova explosions – which are thought to accelerate lower energy cosmic rays through Fermi acceleration in supernovae remnant shocks[80][71]. The large scale nature (200kpc) of the galactic wind would allow acceleration up to extremely high energies and, as heavy nuclei are most effectively accelerated, it would suggest a heavy composition in the high energy spectrum. Due to the large scale involved, anisotropies are likely to be relatively small, but may be detectable[108][162].

Galactic disk sources for EHE cosmic rays are possible but few theories are capable of accelerating the particles to the EHE range. One-shot acceleration *may* be possible in sources such as pulsars. It may be possible to accelerate EHE cosmic rays in binary systems containing a neutron star or black hole. Without details it is hard to know what the effects of galactic magnetic fields will be so that the spectrum and composition are model dependent. However such sources may also produce γ-rays or other neutral particles, in significant numbers to allow a point source detection. There are some models for diffuse acceleration by clusters of supernova remnants in the galactic disk – somewhat similar to that in the termination shock in the galactic wind[19]. However size constraints (the galactic disk is only 300pc thick) limit the possible acceleration to 10^{19}eV with a heavy composition again being favoured. Anisotropy will depend upon the galactic magnetic field structure, but, given the heavy composition, and the confinement of the accelerating region to the spiral arms, any anisotropy is likely to be very small[162].

1.3 Observational Extremely High Energy Cosmic Ray Physics

The different models predict different characteristics for the EHE comic ray spectrum, composition and anisotropy. Observations are needed to determine these observable quantities, as they can be used to rule out particular classes of models. Many of the fine details are still missing (especially at the highest energies), and observations can be used to develop and refine models, and hence allow us to to determine what the sources of EHE cosmic rays are. In this section I will outline recent results which will be used to illustrate our current level of understanding and what experiments are needed to improve and extend our knowledge.

Over the last thirty years several experiments have measured the shape of the cosmic ray energy spectrum in the EHE range. The differential energy spectrum is usually expressed in the form

$$J(E) = \frac{(dN/dE)E}{A_{eff}\Omega(E)T} = J_0 \left(\frac{E}{E_o}\right)^{\gamma} \tag{1.3}$$

where J_0 is the intensity at the energy E_0 and γ is the spectral index. The differential form takes into account the number of observed showers as a function of energy (dN/dE) and each detector's exposure which is defined as the effective area (A_{eff}) $\times$ solid angle (Ω) $\times$ running time (T). This allows a comparison of the measured spectrum between different experiments.

The spectral index γ is ≈ -3 from the energy range 10^{15}eV to 10^{20}eV, where statistics become too poor to determine the spectrum. As the spectrum is largely featureless it is commonly multiplied by a factor E^3 to enhance any features present. Figure 1.3 shows the individual and combined spectrum obtained from the four most recent experiments – AGASA, Fly's Eye, Haverah Park, Yakutsk[177]. The different spectra have been normalised to the Fly's Eye at 10^{18}eV. Table 1.1 lists the differential intensities at 10^{19}eV.

It is encouraging that the normalisation factors (at 10^{18}eV) between experiments (0.8, 1.0, 0.9, and 0.8 respectively) are all close to unity. This implies that despite different techniques used to detect EHE cosmic rays and estimate their energy, the

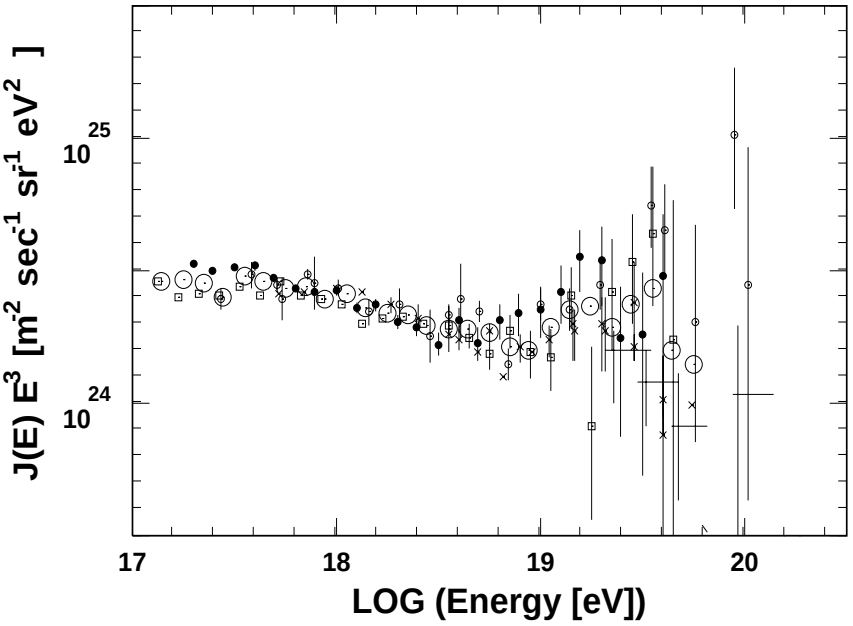

Figure 1.3: The EHE cosmic ray spectrum as measured by AGASA (□), Stereo Fly's Eye (●), Haverah Park (○), Yakutsk (×) and all experiments combined (⊙). Spectra are normalised to stereo Fly's Eye at 10^{18}eV, with energy normalisation factors of 0.8, 0.9 and 0.8 respectively. After S. Yoshida *et al*, [177].

Experiment	$m^{-2}s^{-1}sr^{-1}eV^{-1}$
AGASA	2.91×10^{-33}
Fly's Eye	2.38×10^{-33}
Haverah Park	2.22×10^{-33}
Yakutsk	3.39×10^{-33}

Table 1.1: Differential Intensities at 10^{19}eV for different experiments[17].

results from the different experiments are consistent. This gives us confidence that common effects seen are real effects. Two points of particular interest in this spectrum are a dip known as the "ankle" at about $10^{18.5}$eV and the existence of events beyond the GZK cutoff at 5.0×10^{19}eV.

The ankle in the spectrum is a feature that has been observed by all experiments in the field. It starts at about $10^{17.6}$eV where the spectral index γ steepens from -3.0 to -3.2. The dip appears to be centered at about $10^{18.5}$eV after which it flattens to -2.7. The structure of spectrum at the highest energies is limited by a lack of statistics[30].

A total of 9 cosmic ray particles with energies above 10^{20}eV have been collected since the first such particle by the Volcano Ranch Experiment[126]. These events are clearly well beyond the GZK cut-off. However whilst these events exist, the number of events above the GZK cut-off is less than that expected if the spectral slope remains unchanged after 10^{19}eV. This reduction was seen by the AGASA[177], Fly's Eye[32] and Yakutsk[72] but not Haverah Park[121]. However statistics are poor – the Fly's eye detected 10 events with energies above $10^{19.7}$eV, but expected 20.63 based on the spectrum between 10^{19}eV and $10^{19.7}$eV. New experiments to collect data at the highest energies are thus needed to clarify the nature of the GZK cutoff.

Mass composition studies attempt to determine the primary cosmic ray composition as a function of energy. Composition measurements are unfortunately indirect, relying on the detection of differences in the way EAS develop for different primary particles. However the exact hadronic interaction physics involved in EAS for EHE cosmic rays is unknown, as it is beyond the energies available in terrestrial accelerators. Thus we must use models to simulate EAS for EHE cosmic rays of different masses and energy, and examine the results of these models to determine any observable parameters. Comparison with experimental results can then be done to indicate the most probable mass composition. Such comparisons must be done statistically to overcome the effects of shower to shower fluctuations in the development of EAS and any detector biases that may exist.

Some mass composition studies use measurements of the depth of shower maximum (X_{max}) as an indicator of the primary cosmic ray composition. On average, EAS induced by heavy particles will reach maximum development at shallower depths than those induced by lighter particles (the absolute values must be estimated by EAS models). Additionally not all experiments are capable of measuring absolute values of X_{max}. However they can measure the rate of change in X_{max} with energy, which is known as the elongation rate. The elongation rate is useful as it can provide evidence for changes in composition.

Haverah Park used pulse risetimes in water Cerenkov tanks 500m from the EAS core, as an estimator of X_{max}. These estimates were used to study the elongation rate as it was unclear how to extract absolute values from the risetimes. Their results

implied a constant, possibly mixed (heavy and light components), composition up to about 5×10^{18}eV (the ankle) after which they saw tentative changes to a heavier composition[171].

The Fly's Eye experiment measured absolute values of X_{max} from shower development profiles (longitudinal shower size vs atmospheric depth)[50]. It was able to make good measurements up to 10^{19}eV and found that around the ankle, composition changed from heavy to light[32]. A QCD Pomeron model was used to estimate the elongation rate as a function of energy for a pure iron (heavy) composition, a pure proton (light) composition and a composition changing from heavy to light at the ankle. Good agreement was obtained with a composition that changed from iron at $10^{17.5}$eV to proton at 10^{19}eV.

AGASA is unable to measure composition directly. However Monte Carlo studies indicated that it should be possible to distinguish between proton and iron showers by measuring the ratio of muon to charged particle densities 600m from the core ($\rho_\mu(600)/S(600)$)[66]. It is expected that heavy nuclei will have a larger muon component and by studying the previous ratio as a function of energy it is possible to verify the Fly's Eye result[95]. Measurements of the ratio were compared to those expected from EAS simulations using the 1992 version of MOCCA (an EAS simulation program) assuming the composition proposed by the Fly's Eye experiment. They were unable to confirm the proposed composition change, instead suggesting a much smaller change in the elongation rate between $10^{17.5}$eV and $10^{18.5}$eV[95].

Yakutsk studied composition above and below 10^{18}eV using several different EAS models and (measured) parameters. They examined the ratios of total charged particle to muon numbers, total muon number and total charged particle number to Cerenkov light flux, and muon to charged particle densities at fixed distances from the core. They also estimated X_{max} from the Cerenkov light lateral distribution function. They obtained best agreement using the QGS-hadronic interaction model with a heavy composition before 10^{18}eV, and a proton composition above 10^{18}eV[10].

AGASA, Fly's Eye and Yakutsk all used different hadronic interaction models in EAS simulations making interpretation of the results is difficult, and leaving the proposed composition change undecided. In an attempt to resolve the issue a study

has been performed using a new interaction model and comparing the results with Fly's Eye data and the expected AGASA response[67]. The EAS simulation program MOCCA, with the SIBYLL hadronic interaction model was used to generate EAS for the comparison. These showers were passed through detector simulations of the Fly's Eye and AGASA to allow estimates of X_{max} and muon to charged particle densities. Encouragingly, when the same interaction model was used, the Fly's Eye and AGASA results showed good agreement (which they previously had not). However the evidence for a change in composition was less strong using the SYBILL interaction model, with the composition above 10^{18}eV best described by a 50-50 mixture of iron nuclei and protons and considerable uncertainty on the composition above 10^{19}eV[67].

All experiments in the field have failed to find any significant anisotropy at energies up to $\approx 10^{19}$eV (where statistics become poor). This is despite the use of several different analysis techniques. Harmonic analysis in right ascension was inconclusive and no signifcant galactic latitude dependences (deficiency or excess) have been found[162]. Targeted anistropy studies, where the sky is divided into expected excess and deficit regions (such as the galactic center and anticenter) have all failed to detect isotropy [118][48][49][59].

Whilst on the topic of anisotropy, searches for point sources of neutral particles should also be discussed. So far the only likely candiate has been Cygnus X-3. The Fly's Eye[47][49][59] and AGASA[167][134] reported significant excesses ($> 3\sigma$) between 1981 and 1988, after which the significance declined. Haverah Park[122] saw no significant signal over the same time. Yakutsk[89] saw a slight excess but noted that it was broader than expected and suggested the excess might be due to the influence of the magnetic field in the local arm of the Galaxy on charged particles. Additionally the source is thought to be episodic. It is fair to say that there exists no strong evidence for a point source of neutral particles. Detection of more showers with better angular resolution is needed to provide the sensitivity needed to detect such sources.

The spectrum, composition and anistropy measurements made by the Fly's Eye experiment led to them supporting the hypothesis that the change in the structure of the spectrum at the ankle is due to a change in the origin and composition of cosmic rays – from galactic (heavy particles) to extragalactic (light particles)[32]. The heavy

component is favoured below the ankle, as it is easier to accelerate and confine such particles in galactic magnetic fields. The galactic disk is only 300pc thick and thus protons are likely to leak out of the acceleration region or out of the galaxy due to the larger gyro-radii these particles have at the same energy. The lack of isotropy after the ankle implies that the light component at the highest energies is extragalactic. This is favoured over a galactic explanation essentially due to confinement problems. A proton at 10^{19}eV in a 2.2μG field has a gyro-radius of 4.5kpc and it is difficult to see how this can be confined for acceleration within the the galactic disk. Even the inclusion of the galactic halo (which might extend to a few kiloparsecs beyond the galactic plane) is probably not large enough to adequately confine protons[104].

The detection of particles with energies in excess of the GZK cutoff implies that at least some particles must originate from nearby sources. Despite thorough source searches for the highest energy events no suitable candidates have been found. Intriguingly, results have started to indicate a possible clustering of the highest energy events toward the supergalactic plane. A study of 143 events with energies greater than 20EeV from northern hemisphere surface array detectors (AGASA, Haverah Park, Volcano Ranch and Yakutsk) indicated a correlation with the supergalactic plane [163]. However, a study of data from the Sydney University Giant Airshower Recorder (SUGAR), the only southern hemisphere detector, did not detect any such correlation [114]. More recent results from AGASA have indicated that most EeV cosmic rays appear to be uniformly distributed across the sky. However above 40 EeV they also found that there were 3 pairs of showers with angular separation of less than 2.5 degrees, from a total of 35 events. There is a chance probability of 2.9% that this clustering is a random effect for a uniform distribution of cosmic rays[96]. A more detailed cluster analysis of 103 events with energies above 40EeV from AGASA, Fly's Eye, Haverah Park, Volcano Ranch and Yakutsk was performed[169]. No statistically significant clustering was found. However there were hints of possible clustering and future experiments with better angular resolution and higher statistics should yield more conclusive results.

Whilst much work has been done in attempting to answer questions about the EHE spectrum, composition and anisotropy, it is apparent that we do not yet have enough information to conclusively distinguish between competing source theories.

The Fly's Eye results add weight to the hypothesis that the source of EHE cosmic rays is changing from galactic to extragalactic around the ankle, but further information is needed. More data at the highest energies is also needed to distinguish between different possible extragalactic sources. It is apparent that more experiments with larger collecting areas and improved resolution are needed. Until we have more data from the highest energies, we can not measure the spectrum, composition and anistropy with the sensitivity needed to distinguish between competing source theories.

To achieve this goal, AGASA is currently operating with an area of $100km^2$ and $1.6°$ angular resolution above 4×10^{18}eV, and should provide important information. The High Resolution Fly's Eye (HiRes) is the improved successor to the Fly's Eye, featuring a much larger aperture and improved resolution. It has been operating as a prototype (which is the subject of this thesis) and is now being upgraded to the full detector. The full HiRes detector will improve experimental statistics around the ankle, with a reconstructible aperture of $360\,\mathrm{km}^2\,\mathrm{sr}$ at 10^{18}eV which increases to $10000\,\mathrm{km}^2\,\mathrm{sr}$ at 10^{20}eV. Despite the 10% duty cycle it will provide much needed data allowing us to refine and extend our measurement of the spectrum and composition and allow more sensitive anistropy or cluster studies at the highest energies.

Chapter 2

An Introduction to Extensive Air Showers

The detection of high energy cosmic rays relies upon the ability of the atmosphere to act as a transducer for cosmic rays, converting the energy contained by a single particle into a extensive air shower (EAS) of particles, each particle carrying some fraction of the initial energy. This conversion allows the indirect detection of high energy cosmic rays since the large particle numbers and their lateral spread make it feasible to construct efficient detectors for the very rare primary particles.

Through developing the theory of extensive air shower development, we can determine the best observable properties to be measured in our experiments. We can also use this knowledge to interpret our results and determine the primary cosmic ray spectrum, mass composition and arrival directions. Much of the interaction physics is uncertain at the high energies involved, so we must develop models to understand the details of EAS development. Observations must be used to distinguish between proposed shower models and so refine our theories of their development. Such a feedback process illustrates the importance of the interdependence between theory and experiment that exist in astrophysics and physics as a whole.

In this chapter I will examine the processes involved in EAS development to illustrate how they can be studied, and what measurements are necessary to determine the energy, mass composition, and arrival direction of the primary cosmic ray. I will

then discuss the types of experiments being performed to measure the properties of EAS, concentrating on the atmospheric fluorescence technique employed by the HiRes detector.

2.1 Extensive Air Shower (EAS) Development

An extensive air shower will develop when a primary cosmic ray particle such as a proton interacts with an atmospheric nucleus. This interaction will knock out a few nucleons from the target, and the primary particle will also lose some of its energy in the creation of new particles. These particles continue to interact as they move through the atmosphere, forming a tight core of hadronic particles. The continued interactions give rise to two other important components of the air shower - the muonic and electromagnetic components. The muonic component arises due to the decay of charged pions and kaons created in the hadronic core. Muons are important as they rarely interact, except by ionisation in which they slowly lose energy, allowing the majority of muons to penetrate to sea level. The number of muons can be used to infer the energy and composition of the primary particle. The electromagnetic component is continually fed by the decay of neutral pions (and to a lesser degree by other particles) which are produced by interactions within the hadronic core of the shower. The resulting γ-rays give rise to electromagnetic cascades – an alternating process of pair production and bremsstrahlung which continues until the ionisation losses of the cascade electrons are comparable to the energy loss due to bremsstrahlung. These electromagnetic cascades generate approximately 90% of the charged particles in the EAS and it is through the ionisation losses of these electrons that most of the shower energy is dissipated.

Prior to discussing EAS in detail it is worthwhile examining a simple model to illustrate their general features. The model by Heitler[100][84] can be generally applied to EAS and simply assumes that after a fixed interaction length (λ) a particle will undergo a collision and interact. After interaction it produces two particles, giving each particle half its energy. The branching process continues until the energy of a particle falls below some critical energy, after which it will lose energy through other

processes. Hence as the air shower develops through the atmosphere, the number of particles will initially rise to some maximum number after which the number of particles will decline (in this model to zero). Figure 2.1 illustrates the development of an electromagnetic cascade according to this simple model.

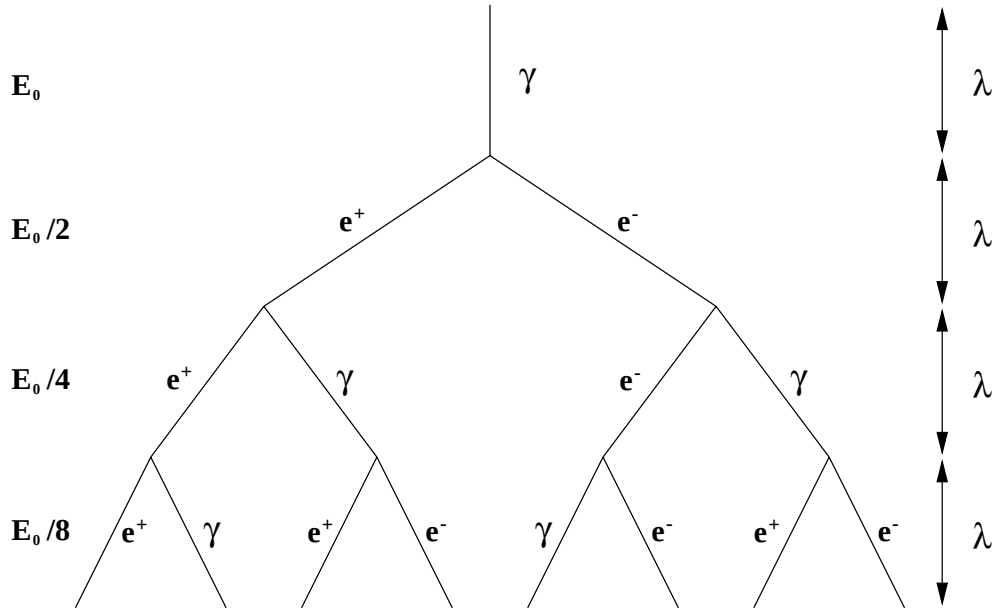

Figure 2.1: A simple model of the development of an electromagnetic EAS. A γ-ray starts with some initial energy E_0 and after a fixed interaction length λ, undergoes pair-production to produce an electron and a positron each with half the original energy. Electrons then produce a photon due to bremsstrahlung after another interaction length. These processes continue until the energy of the particles decreases to some critical value (Here $E_c = E_0/8$).

The number of particles after $n = X/\lambda$ branches (interactions) is

$$N(X) = 2^{X/\lambda} \tag{2.1}$$

where X is the distance traveled along the shower axis. X is referred to as the slant depth and is measured in grams per square centimetre along the track from the top of the atmosphere. The altitude of detectors is usually expressed in terms of the atmospheric depth, and it represents the minimum amount of mass that an EAS must pass through to reach the detectors. The (vertical) depth of the atmosphere at sea level, also known as the overburden, is roughly $1030\, g\, cm^{-2}$.

In this model the energy of a particle at slant depth X is

$$E(X) = \frac{E_0}{N(X)} \tag{2.2}$$

where E_0 is the initial energy of the particle.

The number of particles at shower maximum is then given by

$$N_{\max} = N(X_{\max}) = \frac{E_0}{E_c} \tag{2.3}$$

where E_c is the critical energy at which particle production ceases.

Combining equation 2.1 with equation 2.3 thus gives the depth of shower maximum:

$$X_{\max} = \lambda \frac{\ln(E_0/E_c)}{\ln 2} \tag{2.4}$$

This simple model illustrates two important features of EAS. First, that the number of particles at shower maximum is proportional to the primary particle energy, $N_{max} \propto E_0$, and that the atmospheric depth of shower maximum is proportional to the logarithm of the primary particle energy, $X_{max} \propto \ln E_0$. Thus this simple model illustrates the sort of measurements needed to obtain the primary cosmic ray energy and composition (which is related to X_{max}). However the model is very basic, thus we must now consider in detail how an air shower develops, and how the physics of the interactions shape the way air showers develop.

2.1.1 The Hadronic Core

When a extremely high energy cosmic ray particle enters the atmosphere, it will quickly undergo an interaction with an atmospheric nucleus. The exact physics of such an interaction is unknown, as it occurs at energies beyond those available in terrestrial accelerators. Nonetheless, we have a good picture of the situation, based on experimental data from lower energies, theoretical models of the interaction, and observed properties of air showers.

The initial interaction of a cosmic ray with an atmospheric nucleus can essentially be considered as occurring between the a single nucleon of the primary particle and a single nucleon of the target atom. The validity of this case, and how this case is applied to more general nuclei-nuclei interactions, will be discussed later. The interaction is inelastic, and we define the inelasticity (K_{inel}, measured in the laboratory frame) as the fraction of energy of the incident particle that is not carried out by the fragment. The inelasticity is of the order of 50%, and this energy is effectively available for

particle creation[87]. Particle production is normally considered in two regions – the fragmentation region and the central region.

The *fragmentation* region contains the remnant of the primary particle and other leading particles (such as nucleons) and accounts for the bulk of the energy. The *central* region corresponds to particles with small centre of mass momentum, and it is in this region that most of the particle production takes place. Pions form the majority of the particles created, but a small percentage of kaons and other hadrons will also be produced.

Particles from the two regions compose the hadronic core, and they will continue to interact as they move through the atmosphere. These interactions continually gives rise to new particles which feed the muonic and electromagnetic components of the shower. The core has a width of only a few metres, as the particles possess only small transverse momenta and are energetic and massive enough that any Coulomb scattering is minimised. This tight core forms the shower axis defined by the arrival direction of the primary cosmic ray.

2.1.1.1 Hadronic Interactions

Understanding the physics involved in the hadronic core is key to understanding how EAS development is related to the primary particle. It is possible to derive cascade equations that describe the development of EAS in terms of inclusive cross-sections and interaction lengths. As the exact interaction physics is unknown, we must rely on particle physics models to provide inclusive cross-sections for particle production. An inclusive interaction is one in which a specified particle is *always* produced – for particle c the interaction is simply $a + b \rightarrow c +$ anything. The Lorentz invariant inclusive cross section for this interaction is represented as

$$\sigma_1 = E_c \frac{\mathrm{d}^3\sigma_{ab}}{\mathrm{d}^3 p_c}(\sqrt{s}, p^*_{||}, p_T) \equiv f^{(b)}_{ac}(\sqrt{s}, p^*_{||}, p_T) \tag{2.5}$$

where $\sqrt{s}$ is the total center of mass energy of the initial system $a+b$. At high energies $\sqrt{s} \propto \sqrt{E_{Lab}}$. $p^*_{||}$ is the longitudinal momentum in the center of momentum frame (denoted by the asterix) and p_T is the transverse momentum of particle c. Models predict inclusive cross-sections for particles from interactions occurring within the EAS

core, and this allows estimations of the fluxes of measurable particles. Comparison between the observed EAS development and the predicted fluxes allows one to reassess the validity of the assumptions used in the interaction model.

Various models have been developed to predict the inclusive cross-sections. They can be tested at low energies available in accelerators, but the real challenge is to predict the behaviour at at the extremely high energies of interest in EAS development. Knowledge of how the cross-section changes with energy allows estimates of how the multiplicity, that is the number of particles produced in the interaction, changes with energy. The inclusive cross-sections also lead to estimates of the inelasticity as a function of energy.

The first interaction models for hadronic interactions were those based on statistical-hydrodynamical ideas of Fermi (1951)[79] and Landau(1953)[120]. A model that explained pion production (pionisation) in terms of 'fireballs' was developed by Cocconi, Koester and Perkins[57] in 1961. In this model, two fireballs follow behind the two nucleons involved in a collision. The short lived fireballs decay isotropically in their rest frames to emit mesons with an average energy of 0.5GeV. The two fireballs have different Lorentz factors, and in the lab frame appear as fast and slow fireballs that produce narrow and diffuse cones (respectively) of secondary particles[132]. The multiplicity suggested by these models has an energy dependence $< n > \propto E^{\frac{1}{4}}$[11].

By 1969, the quark model had been proposed and observations of high energy collisions were difficult to explain in terms of previous models. Experiments detected small values of transverse momenta and large values of longitudinal momenta for outgoing particles. Even when the multiplicity was low, the momentum distributions for outgoing particles reflected the longitudinal momentum of the incoming particle. This was intuitively understood in terms of two extended objects passing through each other but breaking into fragments in the process. This observation led to the hypothesis of limiting fragmentation by Benecke et al.[25]. They proposed that the inclusive cross-section for a given particle approaches a limit at high energies, with different limits for different particles. This hypothesis implies that as energy of the collision increases, the fragments will have finite momenta in either the lab or the projectile/beam system and that the inelasticity should approach a high energy limit.

Around the same time as the above hypothesis, Feynman[81] proposed that inclusive cross-sections might approach some limit with energy, and that this applies in fragmentation regions *and* the central region. Feynman scaling differs only from the hypothesis of limiting fragmentation in that it also applies in the central region. Both versions claim that if one measures the inclusive cross-sections in the high energy limit $\sqrt{s} \to \infty$ (which should be measurable in accelerators) then the cross-sections can be applied at higher energies.

The hypothesis of limiting fragmentation can be expressed mathematically in equation 2.5 for the inclusive cross-section (for $a + b \to c +$ anything) as

$$\sigma_1 \equiv f_{ac}^{(b)}(\sqrt{s}, p_{||}^*, p_T) \stackrel{\sqrt{s}\to\infty}{\longrightarrow} f_{ac}^{(b)}(x^*, p_T) \tag{2.6}$$

where $x^* \equiv 2p_{||}^*/\sqrt{s}$ and is limited to $-1 < x^* < 1$. The condition that x^* remains fixed as $\sqrt{s} \to \infty$ ensures that as the energy $\sqrt{s}$ increases, particle c will remain a fragment of either the incident (beam) or target particle, depending upon the sign of $p_{||}^*$. For $p_{||}^* > 0$ (the particle fragmentation region), equation 2.6 implies there is no dependence of the inclusive cross-section for particle c on the target b as energy increases. Similarly when $p_{||}^* < 0$ (the beam fragmentation region) the distribution is independent of the nature of the incident particle[84].

The Feynman x scaling variable is defined as

$$x^* = \frac{p_{||}^*}{p_{||}^*(max)} \cong \frac{2p_{||}^*}{\sqrt{s}} \tag{2.7}$$

and Feynman scaling differs from the hypothesis of limiting fragmentation only in the central region. Feynman scaling implies $f_{ac}^{(b)}(0, p_T) =$ constant, and that the multiplicity increases logarithmically with energy:

$$< n_{ac}^{(b)} > \propto \log s \tag{2.8}$$

Following the analysis of accelerator data, Yen[175] suggested a more suitable scaling variable in equation 2.6

$$x^* = x_R = \frac{E^*}{E^*(max)} \cong \frac{2E^*}{\sqrt{s}} \tag{2.9}$$

where x_R is known as radial x (and this case as radial scaling). x_R is simply the fractional energy of the particle in the center-of-mass system. Yen found that the

invariant cross-section approached the limiting function in equation 2.6 faster than the Feynman x case parameterisation. Yen's modification of x^* from the Feynman x scaling variable only modifies predictions in the central (low energy) region, obtaining better agreement with accelerator data. In the high energy limit $\sqrt{s} \rightarrow \infty$, radial scaling and Feynman scaling results are identical.

However investigation of the scaling hypothesis has shown that the inclusive cross-sections are not invariant with energy. Results from cosmic ray experiments[176][65] and accelerator data up to energies of $\sqrt{s} = 1.8$TeV[13] find the cross-section is not constant, instead increasing with energy at a rate $\propto \log^2 s$.

To account for such violations, and to more generally understand high energy interactions, QCD based quark models are used in hadronic interaction models to estimate inclusive cross-sections and their behaviour with energy. Such models predict scaling however such scaling is modified due to other QCD effects that become important as the energy increases (such as the production of jets). Scaling appears most strongly in the fragmentation region, with the scaling violations arising due to the production of minijets in the central region [84].

The inelasticity is an important parameter in the development of EAS[84]. Studying the inelasticity as function of energy relates the interaction between the energy consumed by minijets in the central region and the energy of the particles in the fragmentation region. Different models will have different inelasticity-energy relationships (see Shabelski *et al.*[155] for a comparison), and this will affect the way an EAS develops – a large inelasticity implies energy is rapidly lost leading to fast EAS development.

Models must also account for nuclear effects. Cross-sections for hadron-nuclei (such as the proton-air cross-section $\sigma_{p\ Air}$) and nuclei-nuclei interactions must be estimated. Hadron-nuclei interactions are based on hadron-nucleon interactions, but take into account possible interactions with extra nucleons in the target. The basis for this work is the multiple scattering theory of Glauber[88]. Essentially one must allow for possible reinteractions of the beam particle with other nucleons in the target. This will depend upon density of nucleons and the the hadron-nucleon cross-section[84][87].

Since we are interested in composition of EHE cosmic rays we are interested in the differences between proton initiated showers and those initiated by nuclei such as iron.

We thus need to determine models for nucleus-nucleus interactions. The simplest such model is the superposition model[69]. It simply assumes that a nucleus with energy E_0 and consisting of N nucleons is equivalent to N independent nucleons with energy E_0/N. Thus the cosmic ray nucleus can be thought of as a beam of nucleons. The effect on shower development can be inferred using our previous simple EAS model. If we substitute E_0/A for E_0 in equation 2.4, we get the result

$$X_{\max} \propto \lambda \ln \left(\frac{E_0}{A\, E_c} \right) \tag{2.10}$$

Thus EAS generated by cosmic ray nuclei will develop more rapidly than a proton of the same energy. Nuclei induced showers should also have less intrinsic fluctuation than proton showers. Fluctuations arise due to the probabilistic nature of cross-sections and particle interactions. Since nuclei can be thought of as a beam of nucleons, fluctuations are effectively averaged.

Whilst the superposition model is reasonable, it has been found to underestimate shower fluctuations[86]. Thus for composition work one really needs to use a more sophisticated model of nuclear-nuclear interactions. Engel *et al.*[76] proposed a semi-superposition model, in which they retain the idea that a nuclei is a superposition of nucleons, but use a more realistic distribution of the depth of first interaction. This model also handles fluctuations in the number of nucleons involved in each interaction (the wounded nucleons in the target nuclei) and fluctuations in fragmentation of the residual nucleus. The net result is that fluctuations in such parameters as $X_{\max}$ increase.

Work on hadronic models for use in EAS simulations is ongoing. Current hadronic interaction models in use at the highest energies (up to 10^{21}eV) include DPMJET[146], SIBYLL[82] and QGSJET[112]. SIBYLL is currently undergoing a significant upgrade, and upgrades to extend the energy range of the the VENUS model[137] are planned. Ranft[145] has compared the physics used by the different models, and compared them with accelerator data where it is available. The different models have developed due to uncertainties in the physics of high energy interactions, and thus it is important that any comparisons between experimental data and simulations use several different hadronic models. This should ensure that real effects can be distinguished from

simulation biases, and so the properties of EHE cosmic rays and the physics of EHE interactions can be determined.

A comparative approach was taken by Gaisser *et al.*[87] to interpret the the cosmic ray composition based on data from the Fly's Eye experiment. They considered three different interaction models in EAS simulations with each model differing in the way inelasticity relates to the energy dependence of the central region. The first model was a statistical model where the multiplicity was given by $< n >= \text{const} \times (K_{inel}\sqrt{s})^{\frac{1}{3}}$. Comparison with accelerator data leads leads to inelasticity decreasing with energy. The second model was the Kopeliovich-Nikolaev-Potashnikova (KNP) model in which the inelasticity increased with energy. The inelasticity rise is due to an increase in particle production in the central region and the KNP model was chosen as it gives an upper bound to the rate of increase with inelasticity. The final model was a minijet model in which the inelasticity increased slowly with energy. This model incorporates the production of jets in the central region which increase the multiplicity and bring about scaling violation by reducing the energy available to beam fragments. The study found that data were consistent with either the KNP or the minijet model but not the statistical model. This implies that one must take into account the high energy physics of the situation.

Finally the importance of the need to use consistent models was reinforced by the recent comparison[67] on composition studies by AGASA and the Fly's Eye. Different interaction models were initially used in EAS simulations and different interpretations of the composition were inferred. When the data were reanalysed using a common hadronic model (SIBYLL) the experimental results were found to be in agreement.

2.1.1.2 Secondary Particles

The fate of the secondary particles created in hadronic interactions is important in shaping the development of the shower. It is through the decay of these particles that the more easily observable components, namely the muonic and electromagnetic components, arise. Table 2.1 lists the rest mass, half lifes and major decay modes for some important secondaries (relative fraction of total modes $> 10\%$). Relative fractions are rounded to the nearest %.

Particle	Mass (MeV/c^2)	Half-life $t_{\frac{1}{2}}$ (s)	Decay Mode(s)	Relative Fraction
$e^{\pm}$	0.511	stable	stable	
μ^+	105.7	2.2×10^{-6}	$e^+ \nu_e \overline{\nu}_\mu$	100%
μ^-	105.7	2.2×10^{-6}	$e^- \overline{\nu}_e \nu_\mu$	100%
π^0	134.9	8.4×10^{-17}	$\gamma\,\gamma$	99%
π^+	139.6	2.6×10^{-8}	$\mu^+ \nu_\mu$	100%
π^-	139.6	2.6×10^{-8}	$\mu^- \overline{\nu}_\mu$	100%
K^+	493.6	1.2×10^{-8}	$\mu^+ \nu_\mu$, $\pi^+ \pi^0$	64% ,21%
K^-	493.6	1.2×10^{-8}	$\mu^- \overline{\nu}_\mu$, $\pi^- \pi^0$	64%, 21%
K^0_S	497.7	8.9×10^{-11}	$\pi^+ \pi^-$, $\pi^0 \pi^0$	69%, 31%
K^0_L	497.7	5.2×10^{-8}	$\pi^\pm e^\mp \overline{\nu}_e(\nu_e)$	39%
			$\pi^\pm \mu^\mp \overline{\nu}_\mu(\nu_\mu)$	27%
			$\pi^0 \pi^0 \pi^0$	22%
			$\pi^+ \pi^- \pi^0$	12%

Table 2.1: Summary of relevant particle properties. Half-lives are measured in the particle's rest frame. Time dilation extends this time in the laboratory frame. Decay modes are the predominant channels (fraction of total reactions > 10%)[133].

Pions constitute the majority of the secondary particles created with all species (π^+, π^0, π^-) created in equal numbers. The neutral pions have a very short half life so they rapidly decay via photo-production without interacting. The γ-ray photons produced then initiate electromagnetic cascades (see section 2.1.2). The charged pions, with a longer half-life have the opportunity to interact instead of decaying. This depends upon factors such as their altitude (atmospheric density increases as the shower develops) and energy (time dilation extends their life-time in the laboratory frame). If they do not interact they decay into muons, the fate of which will be discussed in section 2.1.3.

Kaons are produced at $\sim$ 10% the rate of pions, with all four species present ($K^+, K^-, K^0, \overline{K}^0$). The neutral kaons occur in two charge parity states distinguished by their half-lifes. Half the neutral kaons will be produced in each of the two states: the short $|K^0_S> = \frac{1}{\sqrt{2}}(|K^0> + |\overline{K}^0>)$, and the long $|K^0_L> = \frac{1}{\sqrt{2}}(|K^0> - |\overline{K}^0>)$. The charged kaons have similar half lives to charged pions, and so have the opportunity to interact instead of decaying.

Neutrinos are also produced but owing to their extremely low interaction cross-sections, do not play any further part in the development of EAS.

2.1.2 The Electromagnetic Component

The most numerous and observable component of EAS is the electromagnetic component. The electromagnetic component is composed of electrons, positrons and gamma-rays and arises from interactions in the hadronic core. In each hadronic interaction, approximately a third of the available energy goes in the electromagnetic component via production of neutral pions. As most hadrons in high energy showers reinteract, $\sim 90\%$ of the primary energy will eventually find its way into the electromagnetic component[84].

The development of the electromagnetic cascade is well understood and essentially very similar to the model of Heitler[100] discussed in section 2.1. The classic review paper on the development of the electromagnetic component of EAS was by Rossi and Greisen in 1941[150]. The subject has been well reviewed by Greisen in 1956[91] and 1960[92], Allan in 1971[11] and in the book by Gaisser[84]. Energetic gamma rays are produced via the decay of neutral pions created in the hadronic cascade. Various loss-mechanisms will give rise to lower energy electrons (positrons will be considered electrons for this discussion) and photons. Eventually the energy in this component is dissipated through ionisation losses of electrons, giving rise to fluorescence by atmospheric nitrogen.

The development of the electromagnetic cascade is controlled by the energy loss processes that dominate different energy ranges. Photons lose energy via pair-production, the Compton effect and the photo-electric effect. At high energies the dominant energy loss process is pair-production in the field of a nucleus. As the energy of the photon decreases, Compton scattering of atomic electrons (in which photons loses some but not all of their energy) dominates over the range 20MeV to 100keV. Below 100keV the photo-electric effect becomes the dominant energy loss mechanism, in which the photon is absorbed to knock out an atomic electron. Electrons predominantly lose energy via either bremsstrahlung or ionisation. Bremsstrahlung production of a photon in the field of a nucleus is the dominant process for electrons with energies above $E > E_c \sim 80$MeV[84]. Below E_c ionisation losses dominate, and it is through this channel that most of the energy of the EAS is eventually dissipated[172][84]. The

presence of ionising particles gives rise to fluorescence by atmospheric nitrogen at the rate of ~ 4 photons per metre of ionising track (with a slight pressure and temperature dependence)[110]

Understanding the energy loss processes enables us to construct a picture of shower development. The initial development is controlled by the high energy processes of pair production and bremsstrahlung. For energies large compared to E_c we really only need to consider these two processes. The case where we ignore other loss processes, where we assume complete screening of the nucleus by atomic electrons in bremsstrahlung production, and assume that the radiation length is independant of energy is known as approximation A of electromagnetic cascade theory[91]. Approximation B is identical to approximation A, but it also takes into account ionisation losses of electrons prior to shower maximum.

Approximation A is essentially similar to the simple model of Heitler discussed in section 2.1. A slight difference is that in the Heitler model the interaction lengths for pair production and bremsstrahlung were assumed to be the same. This is close to the true situation – the radiation (interaction) length for electrons in air is $x_o = 37.15 gcm^{-2}$[123], whilst for pair production the interaction length is $\frac{9}{7}x_o$. Approximation A also handles the decline of the shower after maximum by taking into account the actual energy loss processes. Despite these differences, the general results of the Heitler model still hold – that $N_{max} \propto E_0$ and $X_{max} \propto \ln E_0$.

Under Approximation B the ionisation losses of electrons in air is also taken into account. These losses are assumed to be continuous, and constant at $E_c = 81$MeV per radiation length $x_o = 37.1 gcm^{-2}$, giving a rate of $2.18\text{MeV}/gcm^{-2}$[162]. The total number of electrons at a depth X of a shower initiated by a photon of energy E_0 is given by [91].

$$N_e(E_0, X) \approx \frac{0.31}{\sqrt{X_{max}}} \exp\left[X\left(1 - \frac{3}{2}\log s\right)\right] \tag{2.11}$$

where $X_{max} = \log(\frac{E_0}{E_c})$ is the depth of maximum and
$s = \frac{3X}{X+2X_{max}}$ is the shower age parameter.
The shower age parameter varies from 0 to 2 and describes the state of the shower development: $s = 0$ is the origin of the shower, $s = 1$ is shower maximum, and by the time $s = 2$, there are no particles left in the shower.

Such models are of course an approximation. In reality, at a given depth the particles will have a distribution of energies, with lower energy particles being more abundant. There will also be fluctuations in the size of the shower at a given atmospheric depth, arising due to the probabilistic nature of interactions. Shower size fluctuations arise predominantly through fluctuations in the depth of the first pair-production, but other sources of fluctuations contribute as well[91].

The electromagnetic component of an EAS will be a superposition of many such showers, which leads to a more gradual development and decay than a photon-initiated shower. The longitudinal development can be well parameterised by the Gaisser-Hillas function[85] which estimates the number of particles in an EAS as a function of atmospheric depth:

$$\mathrm{N(X)} = \mathrm{N_{max}} \left(\frac{\mathrm{X} - \mathrm{X_0}}{\mathrm{X_{max}} - \mathrm{X_0}} \right)^{\frac{(\mathrm{X_{max}} - \mathrm{X_0})}{\lambda}} \exp \left[\frac{(\mathrm{X_{max}} - \mathrm{X})}{\lambda} \right] \tag{2.12}$$

$\mathrm{X_0}$ is the atmospheric depth of the initial interaction and $\mathrm{X_{max}}$ is the depth of shower maximum (both measured in g $\mathrm{cm^{-2}}$). $\mathrm{N_{max}}$ is the number of particles at shower maximum and λ is a model dependent constant which is $\approx 70\,\mathrm{g\,cm^{-2}}$. The formula effectively describes the build up of particles as the shower initially develops, before maximising at some depth after which the number of particles decrease as the ionisation losses increase[21].

2.1.2.1 The Lateral Distribution Function

Coulomb scattering of electrons will result in lateral spreading of these particles in the EAS. Since electrons compose ~90% of the particles in a shower, this lateral spreading effectively increases the size of the shower, making it measurable over large distances.

Rossi and Greisen[150] calculated the mean square scattering angle $< \delta\theta^2 >$ due to multiple Coulomb scattering in traversing a thickness δt (measured in radiation lengths) as

$$< \delta\theta^2 > = \left(\frac{E_s}{E} \right)^2 \delta t \tag{2.13}$$

where E is the energy of the particle and $E_s \approx 21\mathrm{MeV}$[150] (Allan [11] also provides a good description of the calculation). It can be seen that scattering is inversely

proportional to energy, implying that lower energy particles will be found at greater distances from the core. The additional trajectories that such particles have lead to longitudinal lagging compared to particles near the core. We thus gain a picture of the airshower as a curved disk (perpendicular to the shower axis) moving through the atmosphere at the speed of light. The thickness of the shower front will be of the order of a few metres, increasing with distance from the core.

The lateral distribution function describes the lateral extent of the charged particles in the shower as a function of distance from the core (R). This is obtained by solving the cascade equations for electrons that describe their development in an EAS (see Gaisser[84]). Approximate solutions were obtained by Kamata and Nishimura[113], and Greisen[91] leading to the NKG formula for the lateral distribution

$$f_{NKG}\left(\frac{R}{R_0}\right) = C(s)\left(\frac{R}{R_0}\right)^{s-2}\left(1+\frac{R}{R_0}\right)^{s-4.5} \tag{2.14}$$

where s is the shower age ($0.5 > s > 1.5$) and the coefficient, $C(s)$, is defined as[92]

$$C(s) = \frac{\Gamma(4.5-s)}{2\pi\Gamma(s)\Gamma(4.5-2s)} \tag{2.15}$$

R_0 is Molière unit, the characteristic unit of length for scattering defined as $R_0 = x_o(E_s/E_c) \approx 9.3g\ cm^{-2}$[84]. The Molière unit is 79m at sea level, but for equation 2.14 needs to be calculated at two radiation lengths prior to the observation height[92].

The importance of the lateral distribution function is that it is related to local density of charged particles (electrons and muons), which is a measurable quantity for ground arrays[92]:

$$\rho(N_e, R) = \frac{N_e}{R_0^2} f_{NKG}\left(\frac{R}{R_0}\right) \tag{2.16}$$

Comparison of the NKG formula with experimental and Monte Carlo results has indicated that, whilst the general form of the NKG formula is good, deficiencies have been found[84][77]. The NKG function is found to be too steep near the core and too flat at large distances. Photons near the core are from new (young) cascades, whereas photons at large core distances are from more fully developed electromagnetic cascades (old). These observations have led to a modification of the original NKG formula. The Japanses AGASA group modified the NKG formula by adding an extra term to give

the density at a distance r from the core

$$\rho(N_e, R) = N_e C_e \left(\frac{R}{R_0}\right)^{-1.2} \left(1 + \frac{R}{R_0}\right)^{-(\eta-1.2)} \left(1.0 + \left(\frac{R}{1000}\right)^2\right)^{-0.6} \tag{2.17}$$

where C_e is an normalisation factor, $\eta = 3.91 - 1.79(sec\ \theta - 1)$ and θ is the shower zenith angle.

The NKG formula is thus useful in fitting the measured density of particles as a function of distance from the core. This can then be related to the primary energy. Monte Carlo studies are required to determine the exact relationship between densities and primary energy, as fluctuations and different hadronic models influence the reliability of this method. This method will be discussed further in section 2.2.1.

2.1.2.2 Cerenkov Radiation

The presence of large numbers of relativistic electrons and charged particles in EAS will give rise to Cerenkov radiation. Emission of Cerenkov radiation arises when a charged particle passes through a dielectric medium, such as the air, with a speed greater than the speed of light in that medium. The molecules in the medium become temporarily polarised as the highly relativistic particle moves through their local region, and this temporary polarisation results in the emission of electromagnetic radiation. In effect, the electron's path can be considered as a series of short dipoles elements, each giving rise to electromagnetic radiation. The electromagnetic waves from small sections of the particles track can be coherently added using Huygens construction to obtain the wavefront. The wavefront appears as a 'shockwave', with emission in the forward direction of the particle at an angle θ given by

$$\cos\theta = \frac{c}{vn} \tag{2.18}$$

where c is the speed of light in a vacuum, n is the refractive index of the medium and v is the speed of the particle. Atmospheric Cerenkov emission is emitted as a continuous spectrum, with most of the energy in the UV/visible region. The threshold energy (E_0) for electrons in air is 21MeV at sea level which increases as the inverse square root of the atmospheric density such that at 7.5km it is 35MeV[92]. The energy loss

of electrons due to this process is proportional to $1-(E_0/E)^2$, and is much smaller than bremsstrahlung[172][128].

An important feature of Cerenkov emission from an EAS, is that the light flux is proportional to the integral number of particles in the EAS. The lateral distribution of Cerenkov light will be related to the lateral distribution of electrons, as they are the dominant charged particle component. We can use equation 2.18 to determine the maximum emission angle in a given medium by assuming $v = c$. For air at sea-level, $n = 1.0029$ and we obtain a maximum emission angle of 1.3°. Thus due to the small angles of emission, Cerenkov light from an EAS will tend to follow the lateral distribution of the electrons[92].

2.1.3 The Muonic Component

Muons form a small but important component of high energy extensive air-showers. They are generated primarily from the decay of charged mesons (see Table 2.1). Small contributions will come from pair production ($\gamma \rightarrow \mu^+\mu^-$) and via the decay of photo-produced pions ($\gamma \rightarrow \pi^+\pi^-$).

Muons are weakly interacting particles with a half-life of 2.2×10^{-6}s. Time dilation extends this lifetime in the laboratory frame, such that muons with Lorentz factors > 20 are able to reach sea-level before decaying. Ionisation is the dominant energy loss mechanism for muons due to their small interaction cross-sections for radiation and pair-production. Ionisation losses are $\sim$ 2MeV $(g\ cm^{-2})^{-1}$[101], so only muons with energies of $\approx$ 1GeV or more penetrate to sea level. The penetrating ability of muons has led to them being known as the the hard component of EAS.

Muons will spread laterally in a disk several metres thick as they move through the atmosphere[11]. The dominant cause of the lateral spread for muons is the transverse momenta of the parent particles from the hadronic core. Multiple scattering by air nuclei is a comparatively small effect, due to the large mass of the muons (the opposite is true for electrons where multiple scattering is dominant). Whilst the angle of emission may be small, muons are generated early in the shower, which results in large lateral spreading by the time they reach sea-level. Due to the different processes

causing lateral spreading, the muon lateral distribution function (LDF) is flatter than the electron LDF. At very large distances from the core, it dominates the charged particle (electron and muon) LDF[84].

Greisen[92] estimated the muon lateral distribution function as

$$\rho_\mu(N_\mu, R) = C_\mu N_\mu \left(\frac{R}{R_0}\right)^{-\frac{3}{4}} \left(1 + \frac{R}{R_0}\right)^{2.5} \tag{2.19}$$

where N_μ is the total number of muons in the shower, C_μ is a constant and $R_0 = 320m$ is the characteristic length. Akeno[95] examined the LDF at energies up to $10^{19.5}$eV and found that the Greisen form was valid out to distances of 800m from the core. Beyond 800m, the Greisen form overestimated the densities and thus Akeno proposed a modified form valid out to distances of 2000m

$$\rho_\mu(R) = N_\mu \left(\frac{0.325}{R_0^2}\right) \left(\frac{R}{R_0}\right)^{-0.75} \left(1 + \frac{R}{R_0}\right)^{-2.52} \left\{1 + \left(\frac{R}{800\text{ m}}\right)^3\right\}^{-0.6} \tag{2.20}$$

The characteristic length was determined for vertical showers as $R_0 = 266 \pm 32$m using information within 800m of the core (the zenith angle dependence was also investigated).

The composition of the primary cosmic ray will also affect the number of muons in the shower. This is qualitatively understood through the superposition principle. A heavy cosmic ray such as iron will interact much earlier than a light cosmic ray such as a proton. The number of muons in a shower as a function of energy goes as a power law with index slightly less than one. As the energy per nucleon for iron is A^{-1} lower than that of a proton, we get higher muon production. The ratio of the number of muons for iron to proton can be approximately calculated, although the exact ratio is model dependent. The number of muons in a shower of primary energy E_0 is related to the mass number of the cosmic ray by $N_\mu(> 1\text{GeV}) \propto A^{1-p_\mu}$[84]. If we take a value of $p_\mu = 0.86$ we get an enhancement factor for iron (noting that $A = 1$ for a proton) of $N_\mu(Fe, E_0)/N_\mu(p, E_0) \approx 56^{0.14} = 1.8$. A comparison of the measured number of muons in showers can be compared with the number from EAS simulations with an expected composition. However the effects of shower fluctuations and different hadronic models make such comparisons difficult.

Gamma ray induced showers will be muon poor, making gamma ray astronomy possible if a significant number of such showers can be detected. Muons are produced

in electromagnetic cascades primarily through the decay of hadrons produced by photoproduction (γ + nucleus $\rightarrow$ hadrons). The relative probability of photo-production to pair production is $\approx 2.8 \times 10^{-3}$[84]. The hadrons will interact resulting in the production of muons (as this branch of the cascade develops as a hadronic cascade). Fluctuations will thus give rise to a muonic component in the shower – with the shower being indistinguishable from an hadronic shower if the first interaction is via photoproduction rather than pair-production.

The importance of the muonic component of EAS arises from the physical properties of muons. Their weakly interacting properties means that the total number of muons in an EAS is related to the energy of the primary cosmic ray. Their penetrating nature means that they can be detected separately from other charged particles by placing an absorbing layer (such as earth or concrete) above detectors. The exact relationship between energy and number of muons depends upon the choice of hadronic interaction model and also the primary cosmic ray composition. The main disadvantage of measuring muons is that they are a much smaller component when compared to electrons, which implies larger detectors are needed (AGASA[95] measured the ratio of total muon to total electron number as $N_\mu \approx 0.01 N_e$).

2.2 Observing EAS

Now that we have a good picture of how the different components of EAS develop, we can put the picture together to determine what properties we should seek to observe to obtain information on the primary cosmic ray particles. Our picture is one in which a primary particle initiates an extensive air shower. This air shower begins as a core of high energy particles moving through the atmosphere close to the speed of light. Secondary particles are emitted due to interactions with atmospheric molecules. The secondary particles decay giving rise to electromagnetic cascades and muons. As the shower develops it spreads out laterally, forming a disk of high energy particles moving through the atmosphere. The number of electrons and muons grows as the shower reaches its maximum size, after which the number of electrons declines whilst the number of muons remains constant. Muons and electrons are constantly losing

energy via ionisation, which gives rise to isotropic fluorescence light. The passage of highly relativistic shower particles through the atmosphere gives rise to Cerenkov light which is beamed in the forward direction of the shower.

The more energetic the primary particle, the more energy is available to produce particles such as electrons and muons. Hence the more energetic the primary particle, the larger is the shower size (at maximum), and the shower will reach maximum at progressively deeper depths. Nuclear effects imply that EAS from heavy cosmic rays will develop more rapidly than those from light cosmic rays. However fluctuations in shower development blur these distinctions. Fluctuations arise due to the probabilistic nature of particle interactions, and early fluctuations in the depth of the first interaction play an important role in smearing the range of values at which the depth of shower maximum will occur.

The three basic quantities we wish to investigate are the cosmic ray spectrum, the composition and anisotropy. Thus we need to measure the energy of the primary cosmic ray, develop methods to distinguish differences between showers of different primary composition, and finally we need to determine the arrival directions.

Two basic techniques are used to detect and measure properties of EHE cosmic ray EAS. Ground arrays sample the lateral distribution function for various particle types within the shower, at one atmospheric depth. The atmospheric fluorescence technique detects nitrogen fluorescence caused by ionising particles in the EAS (mainly electrons) to measure the longitudinal shower profile. These two techniques, and the way they measure quantities of interest, will now be discussed with emphasis on the atmospheric fluorescence technique used in this thesis.

2.2.1 Ground Arrays

A ground array consists of separated detectors, which sample the shower front density at one atmospheric depth. These density measurements can then be fitted to the lateral distribution function which is used in determining the primary particle's energy. Composition estimates require knowledge of particle types present and must be compared with models. Arrival directions are determined by time of arrival measurements

of the shower front at different detectors.

One of the challenges with ground arrays is how to relate measurements of the number of particles in a shower (its size) to the primary energy. It is known that there was a simple relationship between energy and the number of particles at shower maximum. The problem is that ground arrays make measurements at some fixed depth, which is generally after shower maximum (and thus the shower size is decreasing). The position is further complicated due to variations in X_{max} due to shower fluctuations and the primary particle composition. Finally a hadronic model is needed to relate the total size and energy.

Hillas examined these problems through the use of Monte Carlo simulations and developed what is known as the $\rho(600)$ method for estimating energy[102][103]. He found that the density of particles at large distances from the core (500-1000m) was fairly insensitive to composition and shower fluctuations, and was thus a better parameter than total shower size. The particle densities at such distances are mainly affected by shower development near maximum, which is where fluctuations are the smallest. The actual distance at which fluctuations are minimised varies with energy, but studies over the energy range 10^{17}eV to 10^{20}eV indicate that the 600m from the core ($\rho(600)$) is a reasonable compromise[162]. Experiments use Monte Carlo studies to relate $\rho(600)$ to primary particle energy. Such studies are done using vertical showers, so $\rho(600)$ must be corrected for the zenith angle of the shower. Such a correction takes into account the additional attenuation of off–vertical showers. Haverah park obtain the relationship[103] $E = 7.04 \times 10^{17}[\rho_v(600)]^{1.018}$eV, Yakutsk[10] obtain $E = 4.8 \times 10^{17}\rho_v(600)^{1.00}$eV, and AGASA[62] obtain $E = 2.0 \times 10^{17}\rho_v(600)^{1.00}$. The three experiments agree reasonably well when the different types of detectors and detector related parameters are taken into account (Haverah Park used water Cerenkov detectors, AGASA and Yakutsk use scintillators, and the experiments operate at different atmospheric depths and operating which affects R_0). Yakutsk also measure the Cerenkov flux from EAS which can be used to estimate energy. This allows a cross check between the two methods which appears to agree well[162][9].

Composition studies generally require estimating the depth of shower maximum,

which can then be compared with Monte Carlo studies of different compositions. Absolute estimates of X_{max} are difficult with ground arrays, so some studies have investigated evidence for changes in composition (rather than a specific composition). Section 1.3 reviews the methods used in composition studies by different ground arrays.

Measurement of EAS arrival directions allows cosmic ray anisotropy studies to be performed. The use of fast timing between separated detectors allows the arrival direction of the EAS to be determined. Each detector records the time the EAS shower front passes through it, and by using the different time lags between detectors the shower direction can be determined. Obtaining the zenith angle is also important in adjusting $\rho(600)$ to the value for vertical showers $\rho_v(600)$ needed to estimate energy.

2.2.2 The Atmospheric Fluorescence Detection Technique

An atmospheric fluorescence detector measures the amount of isotropic nitrogen fluorescence induced by the passage of charged particles in an EAS. The amount of fluorescence light produced is proportional to the number of charged particles present in the EAS – an amount that rises and falls as the shower develops, maximises and is attenuated. Thus this technique utilises the absorption properties of the atmosphere (which give rise to fluorescence) to measure the longitudinal development of an EAS, which is known as the shower profile. As the majority of the primary particle's energy ends up being dissipated into the atmosphere, the energy can be obtained from the integral of the shower development curve (plus a small correction for unobserved components). The advantage of this method is that it allows estimation of the primary energy in essentially a model independant way, and in a way that is unaffected by shower fluctuations. Composition studies are also possible as X_{max} can be directly measured from the longitudinal shower profile. Shower arrival directions are determined geometrically, and thus allow anisotropy studies. The aperture of such detectors increases with energy – more energetic showers are brighter, and thus visible at greater distances. The main disadvantage of this technique is that it can only be used on clear moon-less nights, limiting the operating duty cycle to $\sim 10\%$[21][170].

Approximately 90% of the primary particle energy ends up in the electromagnetic

channel of an EAS. This is dissipated into the atmosphere via ionisation and excitation of air molecules which gives rise to isotropic atmospheric fluorescence. Bunner[44] measured the spectrum and yield as a function of altitude and temperature, measurements that have recently been extended by Kakimoto *et al.*[110]. Figure 2.2 illustrates the spectrum measured by Bunner.

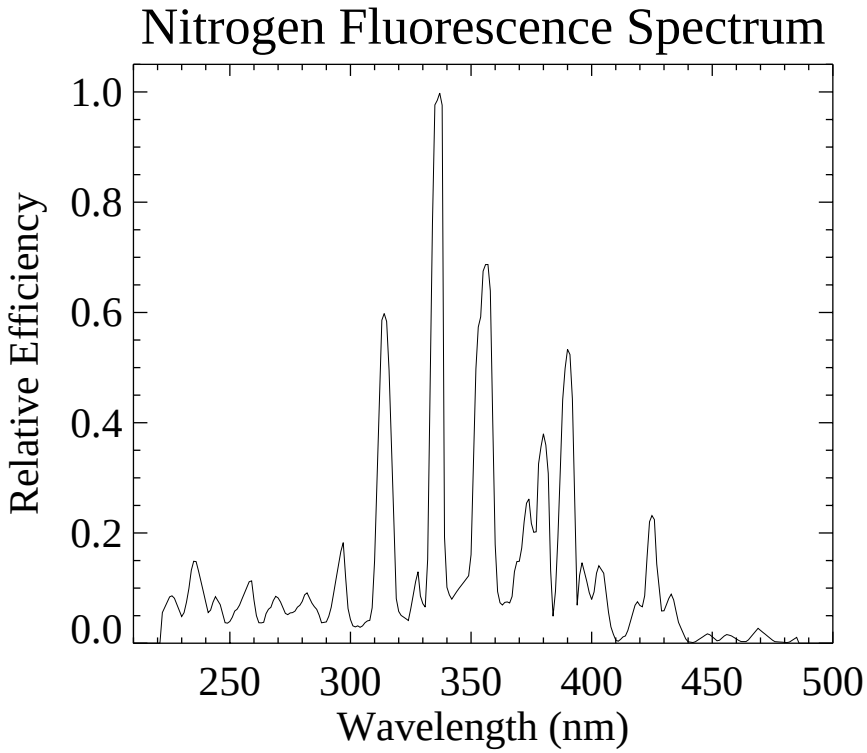

Figure 2.2: Atmospheric fluorescence spectrum which arises mostly from the 2P band of molecular nitrogen and the 1N band of the N_2^+ molecular ion as measured by Bunner[44].

Fluorescence arises primarily in the 300-400nm range from the 2P band of molecular nitrogen and the 1N band of the N_2^+ molecular ion (the decay time is less than 10ns)[44]. The yield has a very slight pressure and temperature dependence – at 20°C the yield ranges from 4 (360nm) photons per metre per electron at sea level to 5 at a height of 18km. A temperature decrease of 20°C only increases the yield by 0.2 photons at both heights. The light yield per particle is quite small, but the large number of particles in high energy EAS ($E > 10^{16}$eV) makes detection possible during dark sky conditions (no moon).

Atmospheric fluorescence detectors utilise large mirrors and photomultiplier tubes

(PMT) to detect the weak fluorescence signal. Each PMT has a fixed field of view on the sky and records the triggering times and the light intensity in a fixed time window. This effectively grids the sky like a composite eye, an effect which led to the first successful atmospheric fluorescence detector being named the Fly's Eye detector[21].

As the EAS develops it will move past the fields of view of a succession of PMTs as is indicated in Figure 2.3. The amount of light each PMT detects will depend on the stage of shower development the PMT views, as well as the distance and orientation of the shower with respect to the PMT. The fluorescence light will be attenuated by its passage through the atmosphere, and the PMT will also collect extra light due to the Cerenkov emission. This will come from directly viewed Cerenkov contamination (viewing angles of $< 30°$ from the shower axis) and indirectly from Rayleigh and Mie scattering of the intense Cerenkov beam along the shower axis (at sea level the beamed Cerenkov light per particle, per metre, is ~ 6 times more intense than isotropic fluorescence light over the same 300-430nm range[45]). To correctly determine energy and other shower properties we need to subtract out this Cerenkov light to obtain the fluorescence component as a function of shower development (since this is a direct tracer of the number of particles at any point in the shower).

The first step in determining the shower profile is to determine the shower orientation in space. Once this geometry is found (through the use of PMT pointing directions and triggering times), an iterative process can be begun to calculate and subtract the Cerenkov component. An iterative process is required because the shower longitudinal profile is needed to determine the Cerenkov beam and hence the scattered component. This also requires a thorough understanding of the state of the atmosphere. This task is accomplished by the use of such devices as Xenon 'flashers'[38] and 'Laserscope'[6], which fire collimated beams of UV light into the atmosphere. These produce air shower like signals, and the light scattered out of the beams can be measured by a fluorescence detector. A standard atmospheric model is used to determine the state of the atmosphere so that the amount of Mie (aerosol) and Rayleigh (molecular) scattering can be determined [5][6][7][68].

Once the fluorescence component is determined, the shower size as a function of depth ($N_e(X)$) is determined through measurements of the fluorescence efficiency [110].

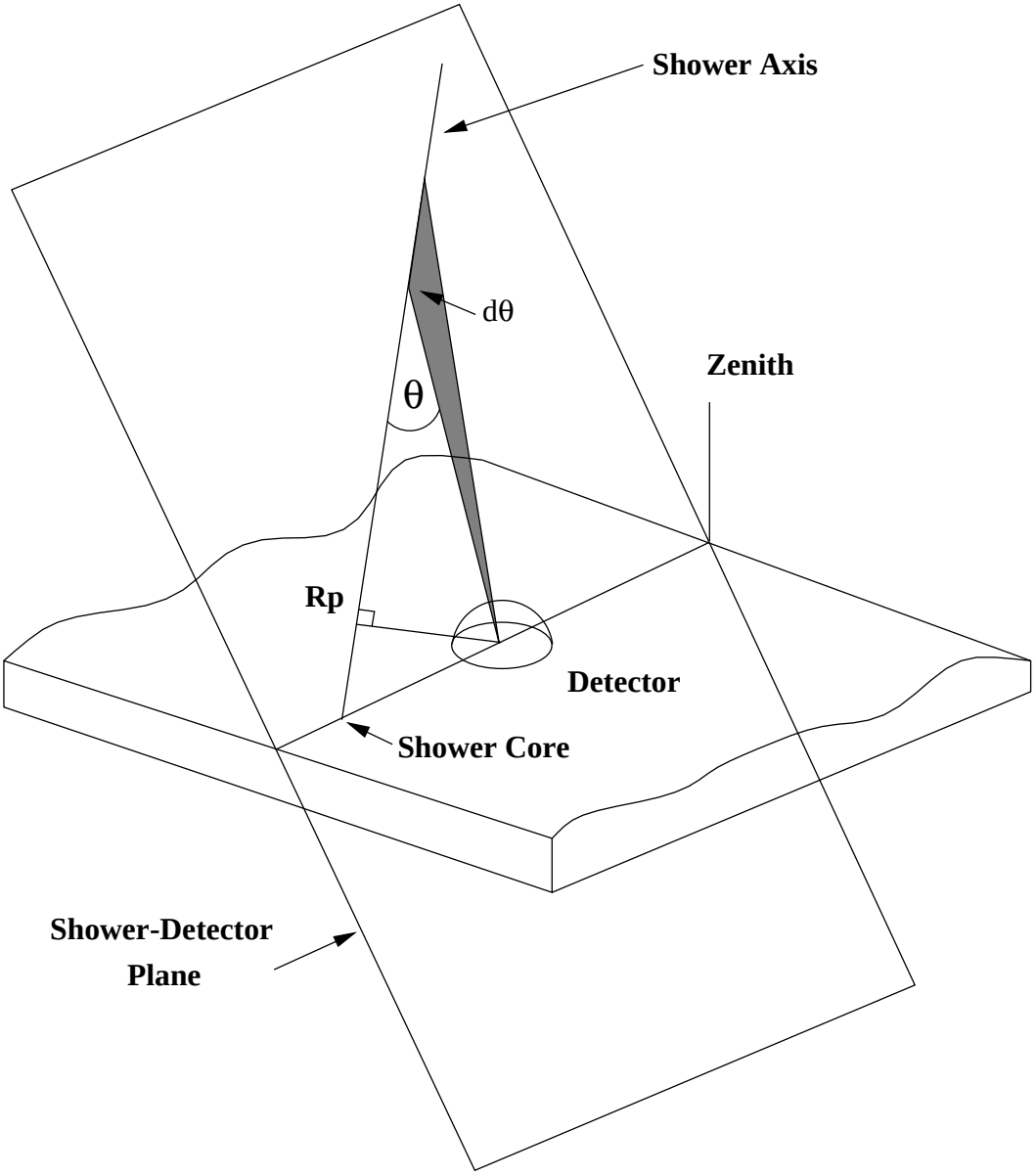

Figure 2.3: The fluorescence light generated by the passage of an extensive air shower is viewed by a succession of photomultiplier tubes. Each photomultiplier tube detects light from a small section of the shower (indicated by shading). Compensation is made for Cerenkov contamination and atmospheric scattering to allow a measurement of the shower light profile. This then allows measurement of energy and X_{max} (depth of shower maximum).

The shower size measurements are fitted using a Gaisser-Hillas functional form as described by equation 2.12 [85]. An example of of this fitting process is shown in Figure 2.4, which is the fit to the data from the Fly's Eye 3×10^{20}eV event. The Gaisser-Hillas fit provides estimates for X_0 and X_{max}, but more importantly it allows us to determine the primary particle's energy. The energy in the electromagnetic component can be determined is determined by integrating the shower development curve over the atmospheric slant depth X:

$$E = \frac{E_c}{x_o} \int N_e(X) dX \tag{2.21}$$

The E_c/x_o term is the ratio of the critical energy of an electron to the radiation length in air, with $E_c = 81\,\mathrm{MeV}$ and x_o=37.1 g cm^{-2} giving an energy loss rate of 2.18 MeV electron^{-1} g cm^{-2}. This ratio converts a track length integral into the total energy loss of the electrons by ionisation and excitation. A small correction (of order 10%) is added to take account of energy not accounted for here – neutral particles that fail to convert to detectable charged particles before hitting the ground, high energy muons, and nuclear excitation by shower hadrons. The 10% is a compromise between for what is expected for iron and proton initiated showers, with the proper correction being roughly 5% for protons and 15% for iron. This small correction is the only model-dependent factor in the energy assignment[21].

Atmospheric fluorescence detectors are capable of composition studies through their ability to directly measure X_{max}. The intrinsic fluctuations present in EAS development make the task of identifying the composition of individual cosmic rays difficult. Thus one must perform composition studies statistically on a large set of showers to overcome the effects of EAS fluctuations on X_{max}. Table 2.2 presents Monte Carlo simulations of some depth of shower maximum distributions illustrating the effect of fluctuations[170].

Arrival directions of cosmic rays can be determined using knowledge of PMT pointing directions and triggering times. The Fly's Eye experiment[21] found that simultaneous observations by two sites provided superior angular resolution (as well as improved energy and X_{max} estimation). EAS reconstruction methods will be a further subject of this thesis. Accurate determination of cosmic ray arrival directions allows

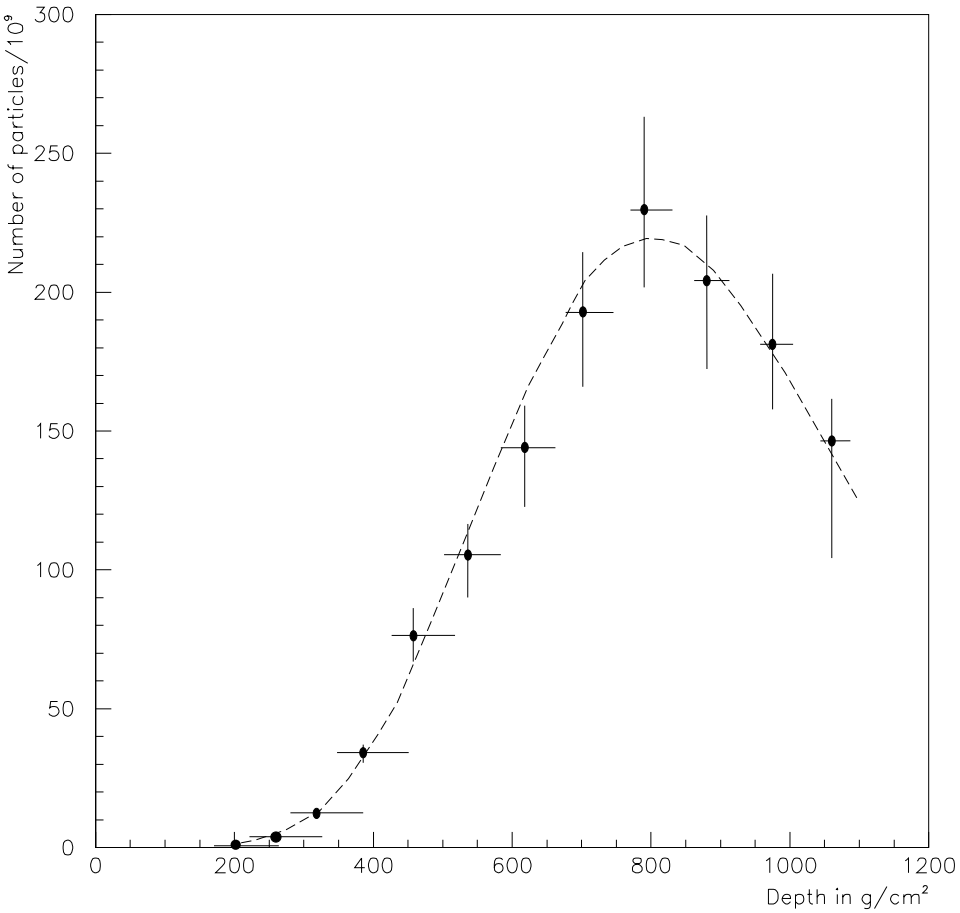

Figure 2.4: Longitudinal shower profile for the Fly's Eye 3.2×10^{20} eV event - the highest energy cosmic ray ever detected. The points represent the number of particles at a given atmospheric depth, and the dotted line is a Gaisser-Hillas fit to these values. N_{max} was in excess of 200 billion particles. Energy is obtained by integrating the curve over the atmospheric slant depth. [33]

Primary Nucleus	$< X_{max} > \, g\,cm^{-2}$	$\sigma\,(X_{max})\,g\,cm^{-2}$
p	726	50
C,N,O	681	38
Fe	640	34

Table 2.2: Mean and standard deviation (σ) depth of shower maximum (X_{max}) from Monte Carlo simulations for different primary cosmic ray particles at 10^{19}eV. The 1σ widths arise due to intrinsic fluctuations in EAS development[170].

sensitive anisotropy and clustering studies to be performed.

The next chapter discusses the HiRes detector prototype - an atmospheric fluorescence detector used by the author. It is building upon the success of the original Fly's Eye detector, providing increased resolution, sensitivity and greater collection area.

Chapter 3

The HiRes Prototype Detector

The High Resolution Fly's Eye cosmic ray detector (HiRes) has been developed to detect a significant number of cosmic rays at energies around the GZK cutoff using the atmospheric fluorescence technique. The detector is building upon the experience gained with the Fly's Eye detector[21] and has been designed with the specific goals of:

- Increasing the data rate above 10^{19}eV by an order of magnitude over the Fly's Eye to > 200 events per year,
- Improving the depth of shower maximum (X_{max}) resolution to a mean of 15 to $20 g cm^{-2}$ from $90 g\ cm^{-2}$ for the monocular Fly's Eye and $45 g\ cm^{-2}$ for the stereo Fly's Eye, and
- Improving the angular resolution and acceptance in the EeV range to increase sensitivity to point sources.

These goals will be achieved through the construction of a two site detector utilising improved optics, electronics and analysis techniques[170].

The Fly's Eye detector was the first successful air fluorescence detector, beginning operations in 1981 and collecting data up until July 1992[32] (thorough reviews may be found in Baltrusaitis *et al.*[21] and Cassiday[46]). The HiRes detector is the successor to the Fly's Eye, achieving a seven fold increase in signal to noise predominantly through decreasing the field of view of each photomultiplier (PMT) from $5.5° \times 5.5°$

down to $1^\circ \times 1^\circ$ and increasing the mirror size from 1.5m to 2m. The improved signal to noise significantly increases the triggering aperture of the detector, since light signals can travel further through the atmosphere before being attenuated to the noise level[68][170]. The smaller pixel size also allows finer sampling of the EAS longitudinal shower profile, improving energy and X_{max} resolution as well as allowing measurement of shower profiles for short (and often distant) EAS. Simulations[170] indicate that 90% of showers viewed by HiRes will have tracks which bracket shower maximum, which will allow excellent composition studies helping to resolve this current issue. Further improvements in sensitivity and resolution will be achieved through the operation of two separated detectors to simultaneously observe cosmic ray EAS (known as stereo observing).

The HiRes detector is being constructed in stages through the use of modular mirror detector units. Each mirror unit has a field of view of 16° in azimuth and 13.5° in zenith with independent electronics to allow progressive integration into detector operation. The HiRes detector began operating as a 2 mirror prototype in 1991 at the site of the original Fly's Eye experiment[16]. The two mirrors were orientated to overlook the Fly's Eye II detector, the Chicago Air Shower Array (CASA) and the Michigan Muon Array (MIA). A further 12 mirrors were gradually added with the HiRes 1 prototype becoming fully operational in March 1993[35]. The 14 detectors were arranged in 5 elevation bands, covering elevation angles from 3° to 70° overlooking CASA/MIA. The Hires 2 site was then developed, with a 4 mirror prototype becoming operational in September 1994[37]. The HiRes 2 site is located 12.6km to the south-west of HiRes 1, with the 4 mirrors of the prototype arranged within 2 elevation bands to overlap the field of view of HiRes 1 and CASA/MIA. The geometry of the two HiRes sites and the fields of view of the prototype detectors is illustrated in Figure 3.1.

Data were collected from the two site prototype for a period of just over two years, with the prototype being shutdown in November 1996 to allow reorganisation of mirrors and electronics for the full HiRes detector. Operation of the prototype detector allowed testing, development and optimisation of detector hardware and software. It is on this 18 mirror HiRes prototype detector that the author has been involved with (covering detector operation and maintenance, installation of hardware, development

of analysis routines and data analysis) and which will be described in detail in this chapter.

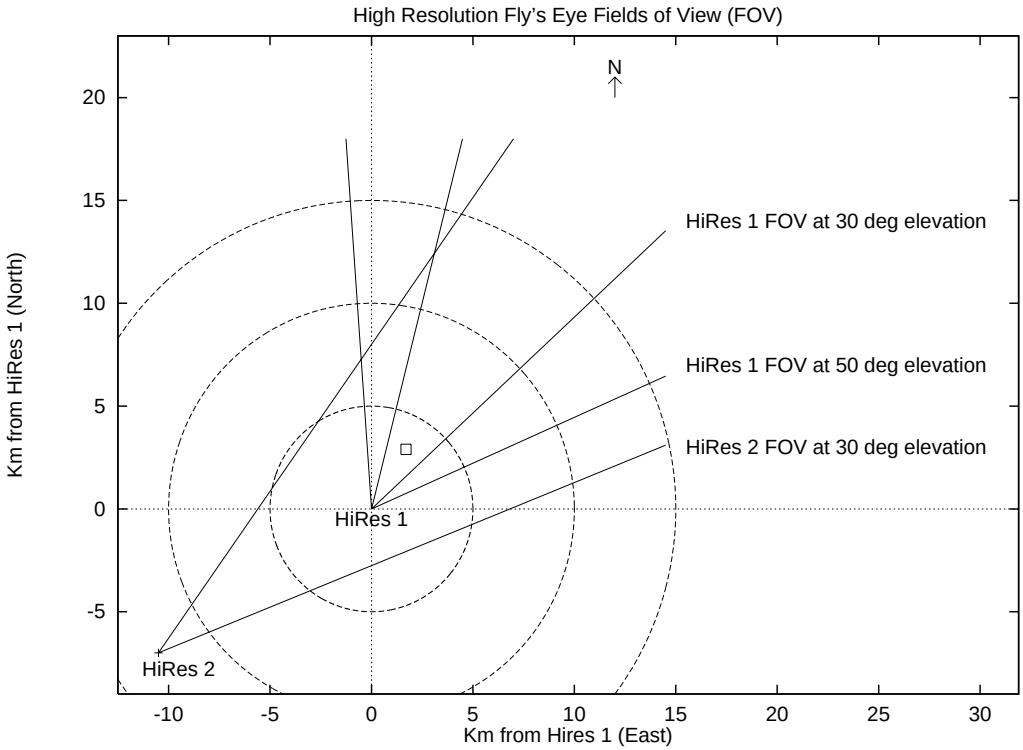

Figure 3.1: A plan view of the location of HiRes 1 and HiRes 2 at Dugway Proving Ground and their fields of view. The square in the centre of the field of view denotes the site of the CASA/MIA arrays and Fly's Eye II.

The HiRes detector has been operating in the Stage 0.5 configuration since July 1997[1]. This configuration consists of 22 mirror units at HiRes 1 arranged in a single azimuthal ring (covering 352° of azimuth) to observe elevation angles from 3° to 17°. This configuration optimises the high energy aperture whilst the detector is upgraded to the full Stage 1.0 configuration. Stage 1.0 configuration comprises the Stage 0.5 detector at HiRes 1, with two azimuthal rings of mirrors at HiRes 2. The 42 mirror units at HiRes 2 will cover an azimuth angle of 336° and elevation angles from 3° to 30°, and use newly developed Flash ADC electronics[2]. The expected *reconstructible* aperture of HiRes stage 1 ranges from $360\,\mathrm{km}^2\,\mathrm{sr}$ at 10^{18}eV to $10000\,\mathrm{km}^2\,\mathrm{sr}$ at 10^{20}eV. Thus we can expect to detect approximately 2200 showers per year above 10^{18}eV, 220 showers per year above 10^{19}eV and 16 showers per year above 10^{20}eV[2].

The results from operation of the stage 1 detector will then be used to determine the configuration of additional mirrors in stage 2. If the flux of cosmic rays extends beyond the GZK cutoff, then the high energy aperture will be increased through two more two-ring sites. If, however, the cutoff is present, then a further two high elevation rings will be added to each existing site to improve measurements of early shower development. HiRes Stage 2 may also involve collaboration with the Telescope Array[1].

3.0.3 Layout of the Prototype Detectors

The HiRes 1 prototype detector is situated on the Five Mile Hill site of the original Fly's Eye detector within the U.S Army's Dugway Proving Grounds in Utah, U.S.A. The GPS determined coordinates are a longitude of $112°50'08.8764''$ W, latitude of $40°11'42.6156''$ N and an altitude of 1597m above mean sea level ($-112.835799°$, $40.195171°$). This is a mean atmospheric depth of $860 gcm^{-2}$. The 14 mirrors of the prototype were arranged in 5 elevation rings with a 0.81 steradian field of view that overlooks the CASA/MIA detectors. Figure 3.1 illustrates the geometry, and figure 3.2 illustrates the field of view of the mirrors. HiRes 1 is also used as the centre of a local cartesian coordinate system. Coordinates are specified in metres in terms of (East, North, Up) with respect to the top of the roof of a building adjacent to the central observing hut (ie a plane tangential to the surface of the earth at this point).

Figure 3.3 illustrates the site layout of HiRes 1. A total of seven buildings each house two mirrors and their electronics. Five of the seven buildings are prefabricated steel buildings with electronically controlled roller doors. The remaining two buildings were corncrib silos whose front face and roof slid back to permit viewing at the highest elevation angles.

The experiment is run from the central trailer, which houses the central computing facilities (computers, hard disks, network routers), timing electronics, YAG laser (used for calibration purposes) and operator quarters. A single ethernet line is used for communication between the control software and the mirrors.

HiRes 2 is the second site of the detector. It is located on Camels Back Ridge, 12.6 km to the south-west of HiRes 1 (see Figure 3.1). The GPS determined coordinates

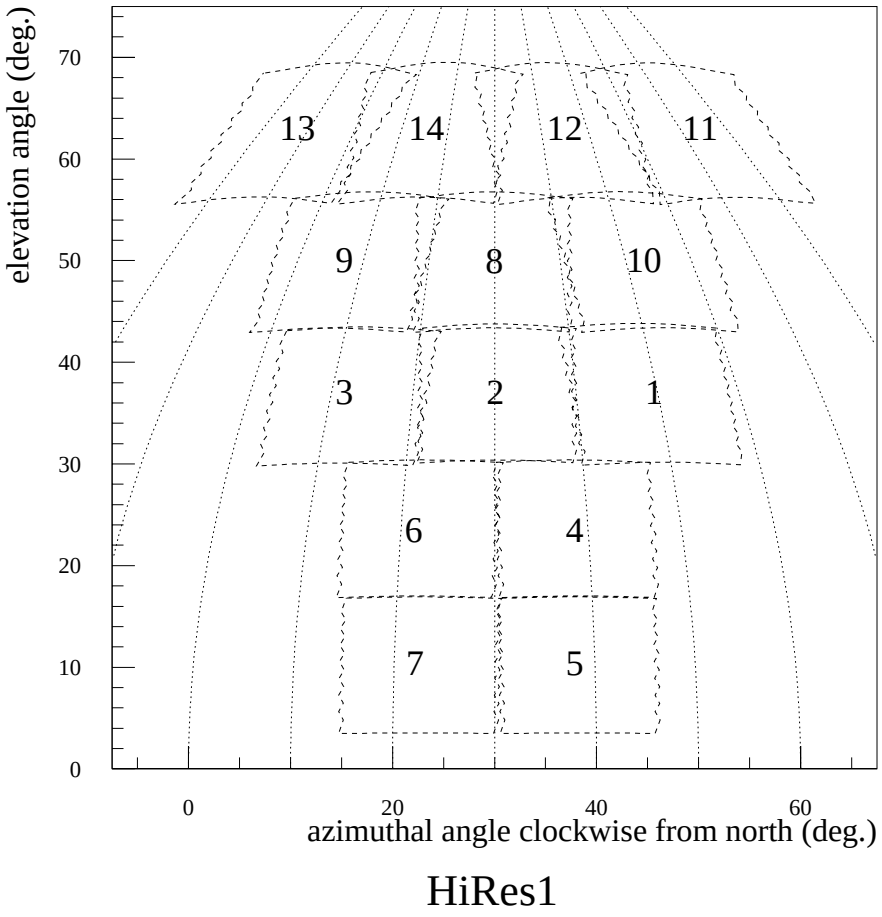

Figure 3.2: Fields of view of the HiRes 1 prototype mirrors.

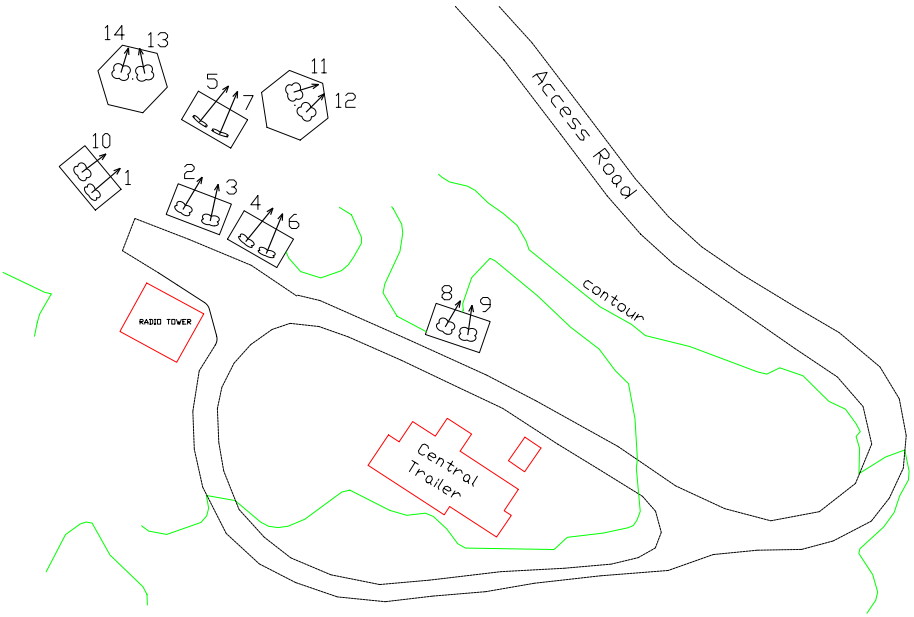

Figure 3.3: Physical layout of mirror at HiRes 1[115].

are a longitude of $112°57'32.292''$ W, latitude of $40°07'55.452''$ N, and an altitude of 1553m above mean sea level ($-112.958970°$, $40.132070°$). In standard HiRes (East, North, Up) cartesian coordinates this is (-10500.3m,-7001.0m,-56.5m). The 4 mirrors of the prototype were arranged in 2 elevation rings with a field of view that overlaps the HiRes 1 field of view and the CASA/MIA detectors as is illustrated in figure 3.1. Figure 3.4 indicates the specific field of views of the mirrors.

The stereo aperture is not optimal for event reconstruction, but it does allow significant testing of event reconstruction. It allows the resolution for events with small opening angles to be examined and the ability to check reconstruction at both small and large distances simultaneously (by doing mono reconstruction at both HiRes 1 and HiRes 2 and comparing with stereo reconstruction)

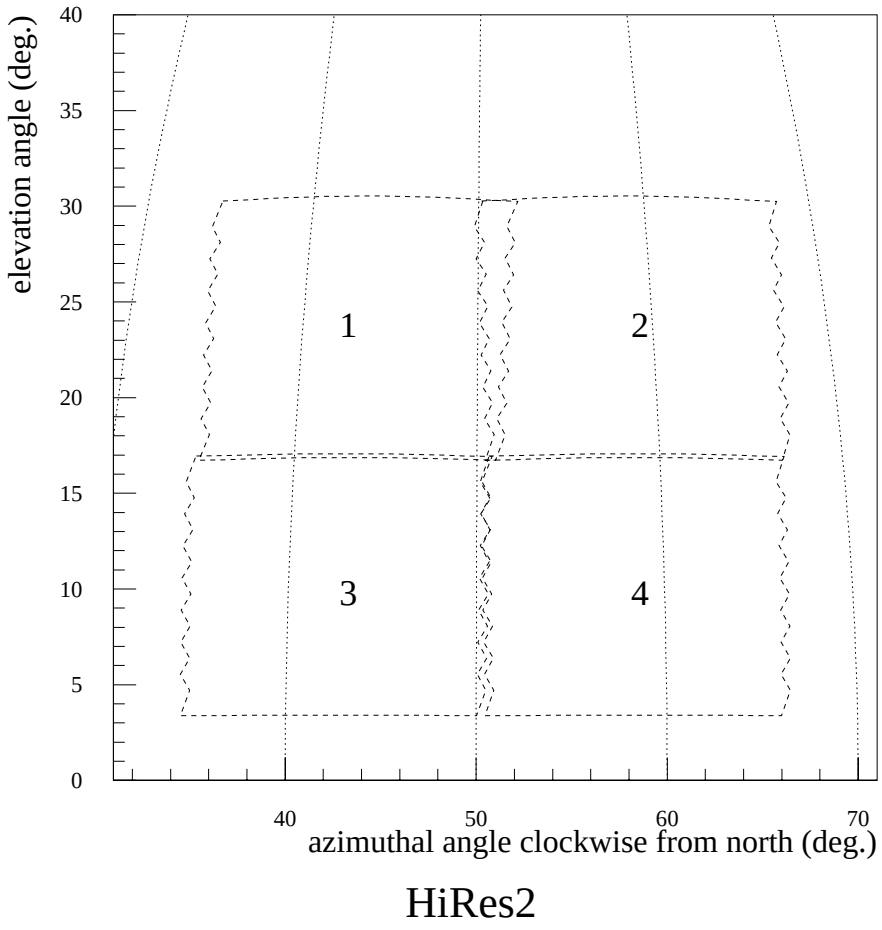

Figure 3.4: Fields of view of the HiRes 2 prototype mirrors.

3.1 Detector Components

The HiRes detector is being constructed through the use of modular mirror detector units. Each mirror unit consists of a an optical system, photomultiplier tube cluster and data-readout electronics, all of which is housed in a mirror building (with two mirror units per building). The rest of the data acquisition system is housed in a central facility, comprising the central timing electronics used to record absolute mirror triggering times, and the central computer which collects the data and controls its acquisition.

The basic system is illustrated in Figure 3.5 – fluorescence light is collected by the mirror, focused onto the PMT cluster and digitised by the electronics. The absolute triggering time is recorded by the central timing crate, and the control software collects the information via ethernet and stores it to disk.

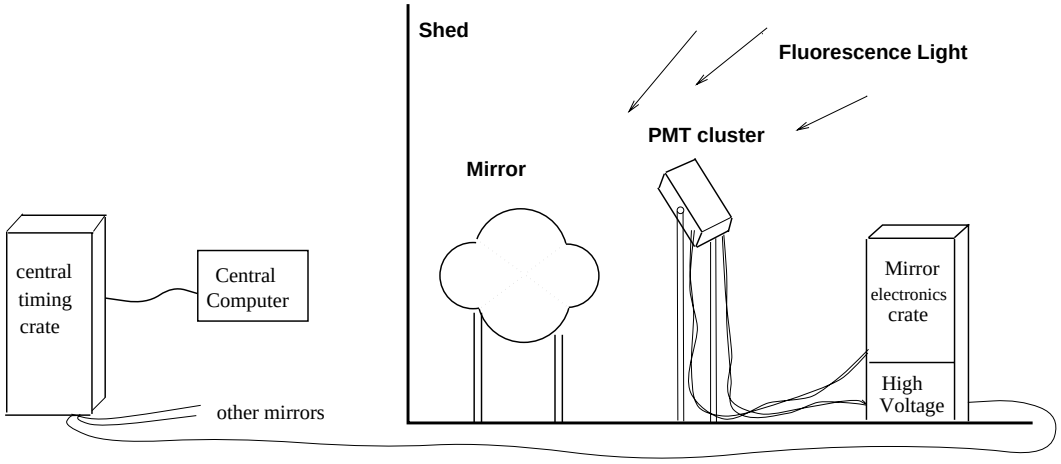

Figure 3.5: The basic HiRes data acquisition system[115]

The data acquisition system is almost identical at each HiRes site and a detailed block diagram of the detector components is presented in Figure 3.6. These components will now be discussed in detail with the improvements between HiRes 1 and HiRes 2 being indicated.

3.1.1 Mirror Unit

The mirror unit is the basic component of the data acquisition system. Each mirror unit consists of a 2m diameter mirror which focuses light onto a cluster of 256 PMTs

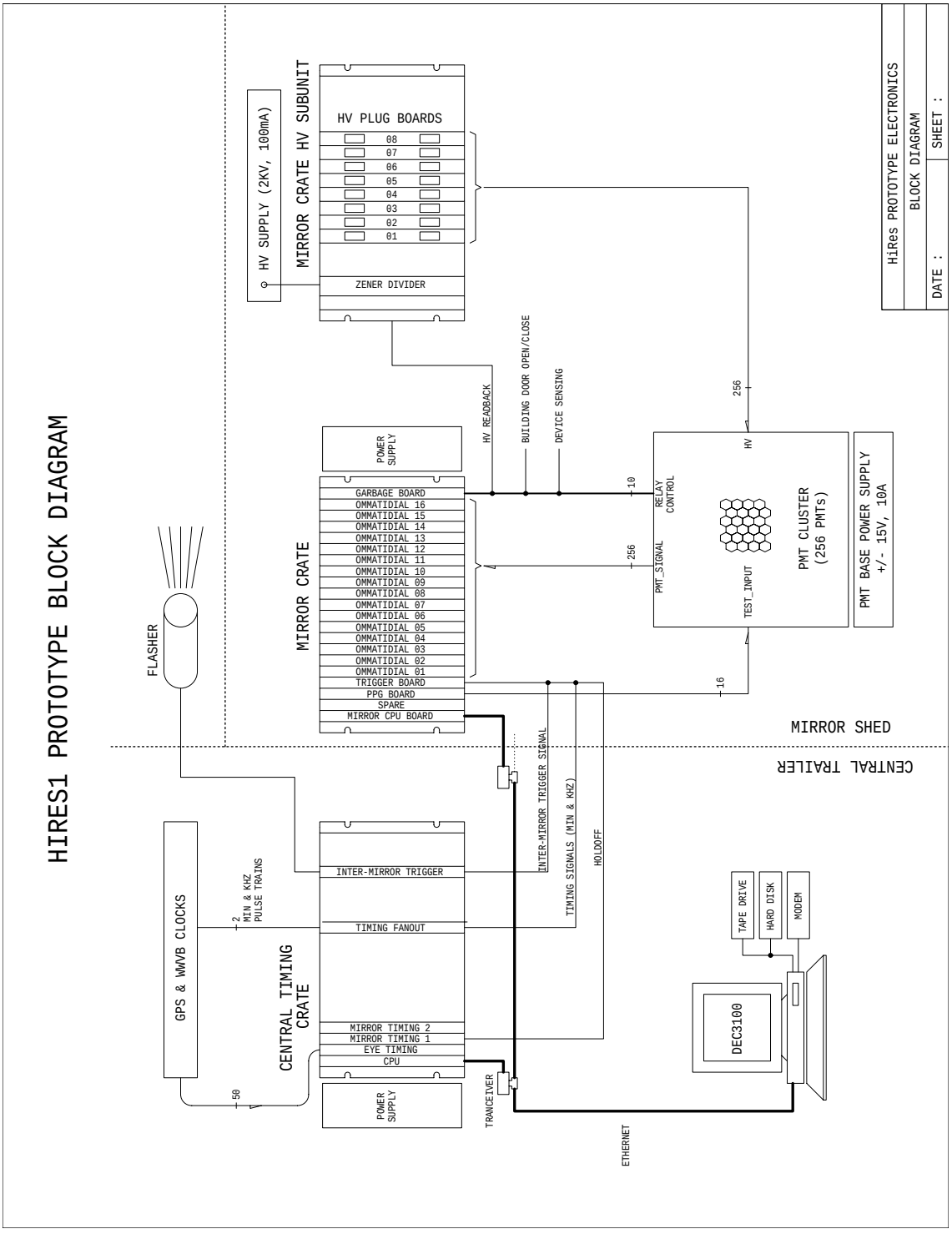

Figure 3.6: Block Diagram of HiRes 1 Prototype components[115]. HiRes 2 is essentially identical.

placed behind a UV bandpass (300-400nm) filter. Each heaxagonal PMT has a fixed field of view of approximately $1^\circ \times 1^\circ$, with each mirror having a total field of view of 16° in azimuth and 13.5° in zenith. The PMTs convert the fluorescence light into an electrical signal which is sent to the mirror electronics rack for measurement of the total signal.

The mirror electronics are housed in a VME crate within the mirror buildings to minimize cable lengths to less than 10m/channel. The VME crate contains a 68030-based processor board, 16 data acquisition boards (known as 'ommatidial' boards), a trigger board, a programmable pulse generator board (PPG) and a sensor/relay board (known as a 'garbage' board). The mirror electronics also include a power supply for the PMT preamps, the PMT high voltage supply and the high voltage distribution system.

Each ommatidial board processes the individual signals of a subcluster of 16 PMTs. A sample and hold system is used to measure the total signal in a fixed time window, along with the relative PMT triggering time. The mirror CPU is the primary interface between the central computer and the ommatidial board with data being sent between the central computer and the crate over an ethernet line. The trigger board determines when triggering criteria have been met, and has a direct (twisted pair) line to the central timing electronics to allow recording of the absolute triggering time. The PPG is used to generate calibration pulses, and the garbage board performs a variety of different tasks such as monitoring the high voltage system and opening/closing the building door. Each component of the system will now be discussed.

3.1.1.1 Optics

The optics comprise a 2m diameter composite spherical mirror having an effective area of $3.75m^2$ which focus light onto a cluster of 256 photomulitpliers placed behind a UV bandpass filter. The mirrors have a radius of curvature (R) of 474cm and a f-stop of 1.16. For ease of fabrication each mirror is composed of 4 segments in a clover leaf pattern. Each mirror segment was slumped from a 0.375 inch glass blank which was cut to size, aluminised and then anodised. Details of the fabrication process may be found in Loh[127].

The mirrors have deliberately been designed to have a finite spot size. A finite spot size reduces the variation in PMT response along the track owing to dead space between PMTs and also gain variations across the face of PMTs. Mirrors were accepted if more than 70% of light was focused down to spot with a diameter of less than 1cm. Initial average reflectivity was measured as 85% at 355nm.

As the mirrors must focus light onto the PMT cluster which extends 8° off axis, a ray tracing program was developed to calculate the spot shape across the cluster. It was found that the shape of the spot depends most strongly on the angle away from the mirror axis. Figure 3.7[115] shows the ray tracing results. It can be seen that as one moves towards the edge of the cluster, the spot coma grows worse and the central spot size grows slightly larger.

Mechanical support for the prototype mirrors used a aluminium hexcell honey-comb structure that was glued to the backs of mirrors. However this support structure was found to have a large thermal expansion co-efficient, resulting in the radius of curvature decreasing with temperature by as much as 3mm/°C[168]. Thus the individual mirror segments would all flatten as the temperature decreased and the blur spot would increase. All HiRes 1 mirrors, and HiRes 2 mirrors 2 and 4 had this problem. The remaining two HiRes 2 mirrors utilised a simple three point mechanical support structure that overcame this problem. The honeycomb structure was replaced after the prototype was shutdown to prevent this problem affecting the full HiRes detector.

The mirror focuses light onto the photomultiplier tube cluster which is situated behind a UV filter used to reduce background light and so improve the signal to noise. The face of the PMT cluster was placed at a distance of $0.97 \times (R/2)$ (where R is radius of curvature of the mirror), which was found to minimise the spot size variation across the field of view. The filter is a single sheet of UG-1 glass which passes light in the 300-400nm range with a transmission factor of 80%[170]. The measured transmission curve is shown in figure 3.8. The absorption filter used was found to enhance the signal to noise over the no filter case by a factor of 1.7[74]. This was found to be a cost effective improvement. More expensive interference filters would only increase the S/N ratio by 10%.

The pointing directions of the mirrors and clusters are important parameters in

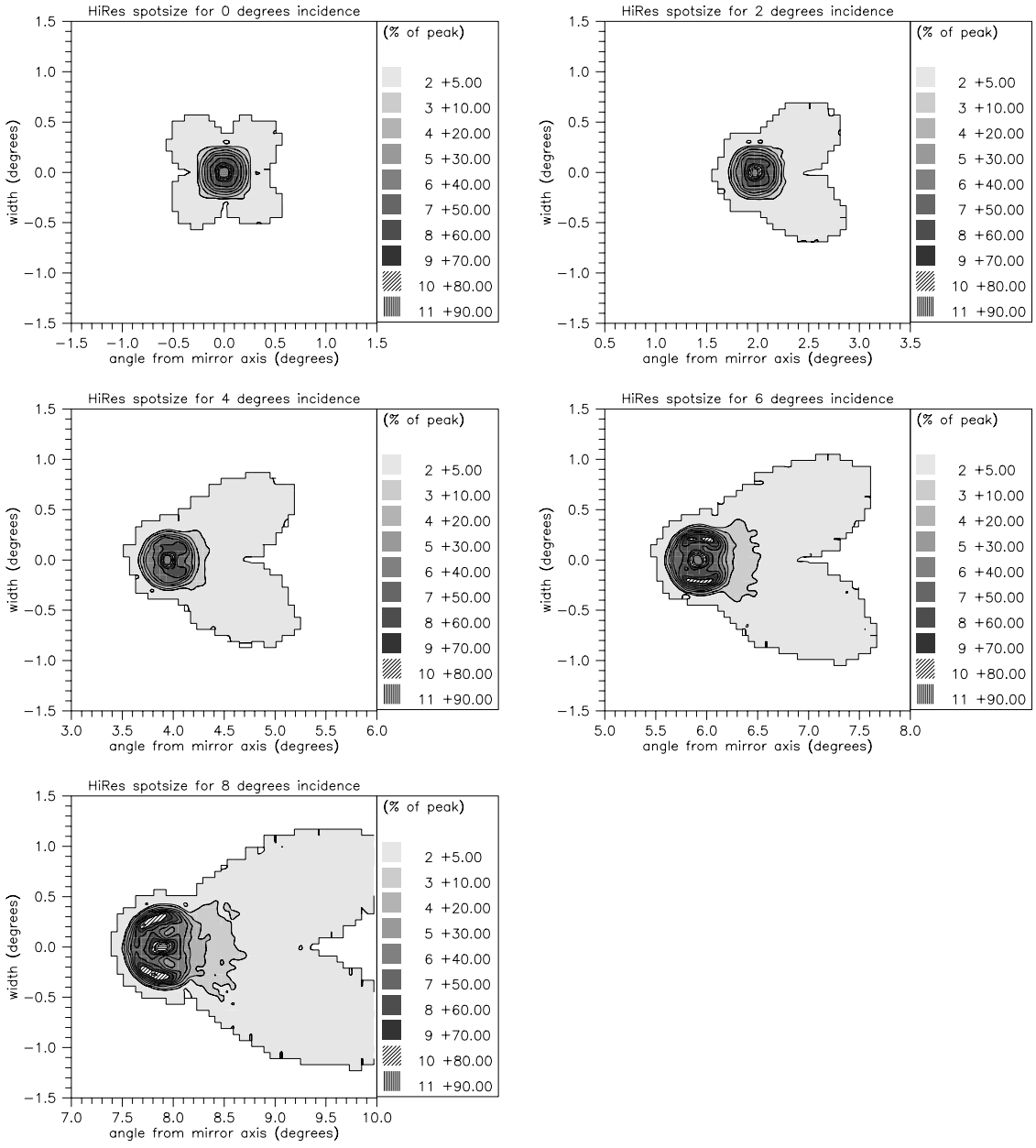

Figure 3.7: Mirror spot patterns for points laying 0,2,4,6, and 8 degrees away from the center of the cluster[115]

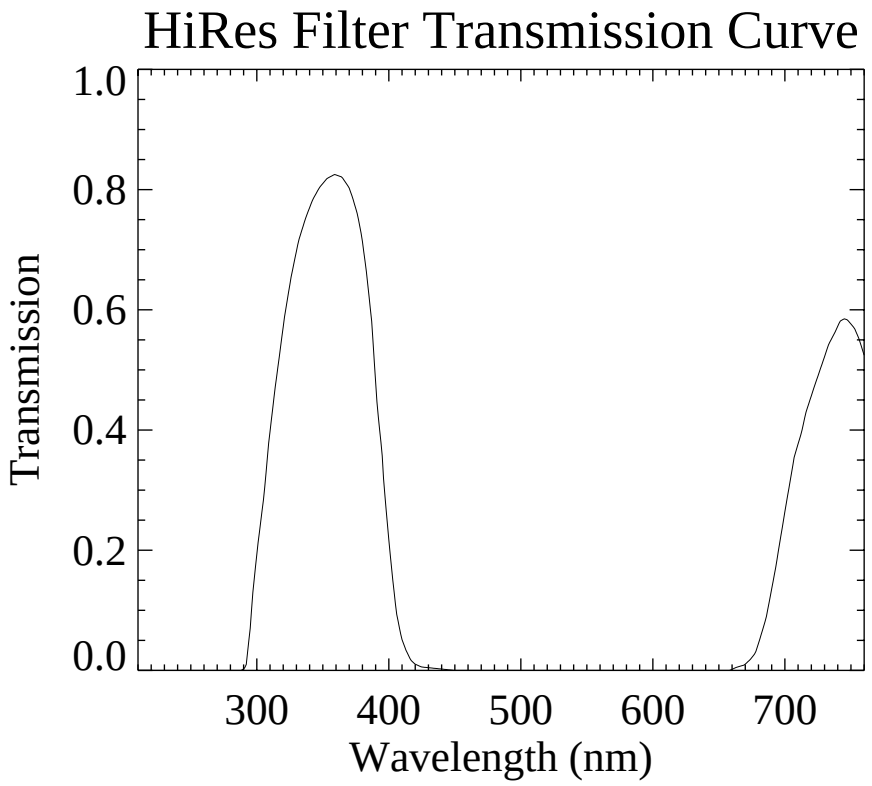

Figure 3.8: Transmission curve for HiRes UV bandpass filter[4].

reconstructing EAS events. During installation the mirror and cluster were carefully surveyed into position, and the location and pointing directions were then recorded[4]. These directions change slightly as building foundations settle and equipment is accidentally knocked. Thus prior to decommissioning the prototype the positions were resurveyed to determine the amount of movement experienced.

Surveying is conducted using a theodolite which is levelled and referenced to a common distant point whose position is well known (surveying at HiRes 2 used the power pole at HiRes 1). A target is placed in the centre of the cluster, and the location of the reflected image on the surface of the mirror is found. The angle between the reflected image on the mirror surface and the reference point is recorded, as is the distance from the theodolite to the mirror and the position of the image on the mirror. Figure 3.9 illustrates the geometry of the survey process. The theodolite is moved, and the process is repeated so that four points on each mirror segment are surveyed. The measured distances and angles can then be used to determine the average pointing

direction of the mirror.

The surveying process is a difficult and time consuming process, with the difficulty increasing with the elevation angle of the mirror. Mirrors are surveyed after installation, and all mirrors were resurveyed when the prototype was shut down in December 1996. Comparison found that some of the mirrors, and in some cases the entire buildings, had undergone shifts of up to 0.1°. Alternative surveying methods such as the use of precision laser shots are being investigated[6][4].

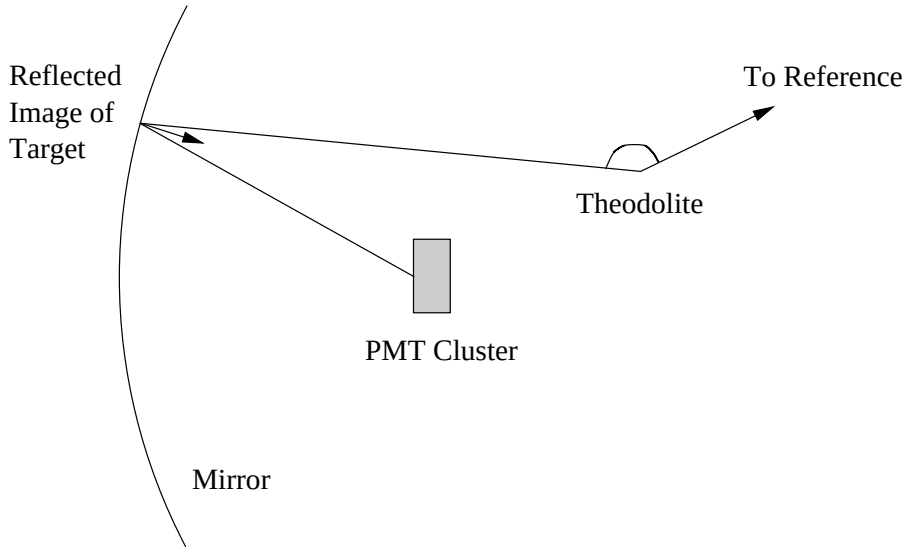

Figure 3.9: Geometry of the surveying process. The theodolite is used to measure the angle between a reference point and the centre of the tube cluster via the reflection of the mirror surface. Measurement of angles and relative positions of reflected image, cluster and theodolite allow determination of mirror pointing direction.

3.1.1.2 Photomultiplier Tube Cluster

The photomultiplier tube cluster is held in the focal plane by a structure designed to minimise obscuration of the mirror field of view. The cluster consists of 256 close packed 40mm diameter hexagonal photomultiplier tubes each having a 1° field of view. Half of the mirrors (1,3,9,10,11,12,14) at HiRes 1 use Philips XP3062/FL PMTs and the other half use EMI 9974KAFL PMTs. At HiRes 2, mirror 4 uses EMI PMTs and the other three mirrors use Philips PMTs. The Philips PMTs will be used in all future mirrors. A test facility[31] was constructed to measure the absolute gain and quantum efficiency for all PMTs. The facility was able to perform two-dimensional scans across

the face of the PMTs, so that PMTs with greater than 10% non-uniformity could be rejected. This is discussed in more detail in section 3.2.1.

Each PMT is soldered to a high voltage bleeder chain and a preamp circuit. The preamp adds a gain of 100 onto the PMT pulse and generates a differential signal which removes the DC night sky background. This ensures that only fluctuations in the night sky background contribute to the noise signal, rather than the full background. The preamp circuit also has an identification chip (used to keep track of PMTs in the clusters) and an external test input. Test pulses from the PPG board are injected via this input and are used to calibrate the data acquisition electronics without high voltage applied to the PMT.

The PMTs are arranged in 16 subclusters of 16 PMTs each, as illustrated in Figure 3.10. The entire PMT/circuit board assembly mounts in the cluster frame with a 256 socket backplane. The backplane distributes high voltage (HV) and test signals, and transmits PMT pulses from the preamp to the data acquisition boards. At HiRes 1 high voltage is supplied to each PMT through 256 20 gauge high voltage wires. At HiRes 2 the PMTs were sorted into groups of 16 with similar gains (prior to installation). Each group of 16 tubes formed a subcluster which could be operated at the same high voltage which simplified the HV distribution system (to be discussed).

The PMTs are wrapped in magnetic shielding metal and closely packed within the cluster. To prevent a buildup of heat a cooling fan is located at the top of the cluster. The sides of the cluster box are bonded with a heat conducting paste, and an aluminium sheet runs vertically through the center of the cluster. A temperature sensor is located in the centre of the cluster to allow monitoring of the effectiveness of these measures.

3.1.1.3 Mirror Electronics

The mirror electronics (in a VME crate) and the high voltage supply and distribution system are contained in an electronics rack in the mirror sheds (one rack for each mirror). The electronics consists of 16 data acquisition (ommatidial) boards, a trigger board, a 68030-based VxWorks Force controller board (the mirror CPU), a programmable pulser generator (PPG) board, and a sensor/relay (garbage) board.

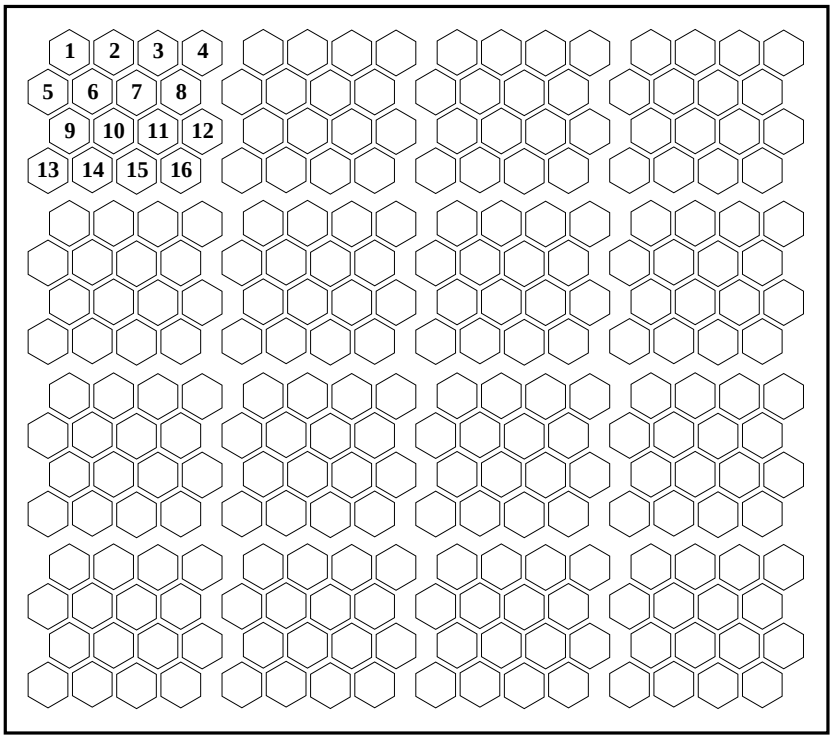

Figure 3.10: Arrangement of PMTs within subclusters and cluster. The numbering system of PMTs within the top left subcluster is used to number subclusters within the PMT cluster. The seperation between subclusters has been exaggerated.

The PPG board produces square pulses of varying width and amplitude and is used in diagnostic and calibration processes to be discussed in section 3.2. The 'garbage' board handles a number of unrelated systems. It handles the high voltage read-out system, controls pre-amp power to individual PMT subclusters through the cluster relay board, opens and shuts shed doors and monitors the crate temperature.

High Voltage Supply and Distribution The high voltage distribution system provides power for the PMTs in the cluster. The system is a powered by a single 2kV 100ma supply which is fed into a simple zener voltage divider chain which provides twenty-five voltages in 20V steps to cover a 500V range. The voltage range was individually set for each mirror (as different PMTs had different optimal high voltage values), with the middle of the range generally around 1100V. The zener taps are fed into a matrix plug board which allows each PMT (HiRes 1) or subcluster (HiRes 2) to be tapped to within 10V of the optimal voltage/gain. PMT gains have been found to be very stable, generally requiring adjustment less than once per year. A VME crate

controlled high voltage readback system is also incorporated to allow checking of the voltage on each PMT/subcluster.

Ommatidial Board The ommatidial boards handle triggering of PMTs and the digitisation of their signals. Each ommatidial board records and stores the integrated charge waveform and the time the waveform's leading edge rises above threshold for the 16 PMTs in each subcluster[158][115][37]. The sample and hold electronics used at HiRes 1 and HiRes 2 are presented as flow charts in Figure 3.11 and Figure 3.12.

It is desired to maximise the sensitivity to cosmic ray EAS signals whilst minimising the effects of the night sky background noise. The pulses generated by EAS have the property that the pulse time width is roughly proportional to the distance from the shower to the detector, due to each PMT subtending a fixed angular range on the sky. Thus two channels are used for each PMT – channel A optimised for fast, close pulses and channel B for more distant wider pulses. The night sky background has a power law pulse height spectrum, which intensifies with decreasing pulse width. Thus triggering thresholds can be reduced by the inclusion of filters to remove pulses with widths shorter than the expected signal pulse widths. A 100ns single pole RC filter is optimised for channel A and a 375ns 3-pole LC Bessel filter is optimised for channel B to help filter out noise signals. At HiRes 1 only one filter may be selected for both channels (this is software controllable) whilst at HiRes 2, Channel A and Channel B each have their own filter and can trigger independently of each other (see Figures 3.11 3.12). HiRes 1 almost exclusively used the 100ns filter so that the detector would be sensitive to close showers that might trigger CASA/MIA.

The triggering rate of each PMT is measured using a 16 bit scaler and is monitored by an 80188 microcontroller chip. The microcontroller maintains a constant triggering rate through the use of a digital to analogue converter (DAC) to dynamically adjust the trigger threshold every 4 seconds. The choice of triggering rate is a compromise between sensitivity and PMT trigger dead time. At HiRes 1 a trigger rate of 200Hz was chosen and at HiRes 2, rates of 50Hz for channel A and and 300Hz for channel B were chosen to maximise sensitivity for distant EAS (so as to maximise stereo aperture).

Once a PMT has triggered, the triggering time and the integrated charge in the

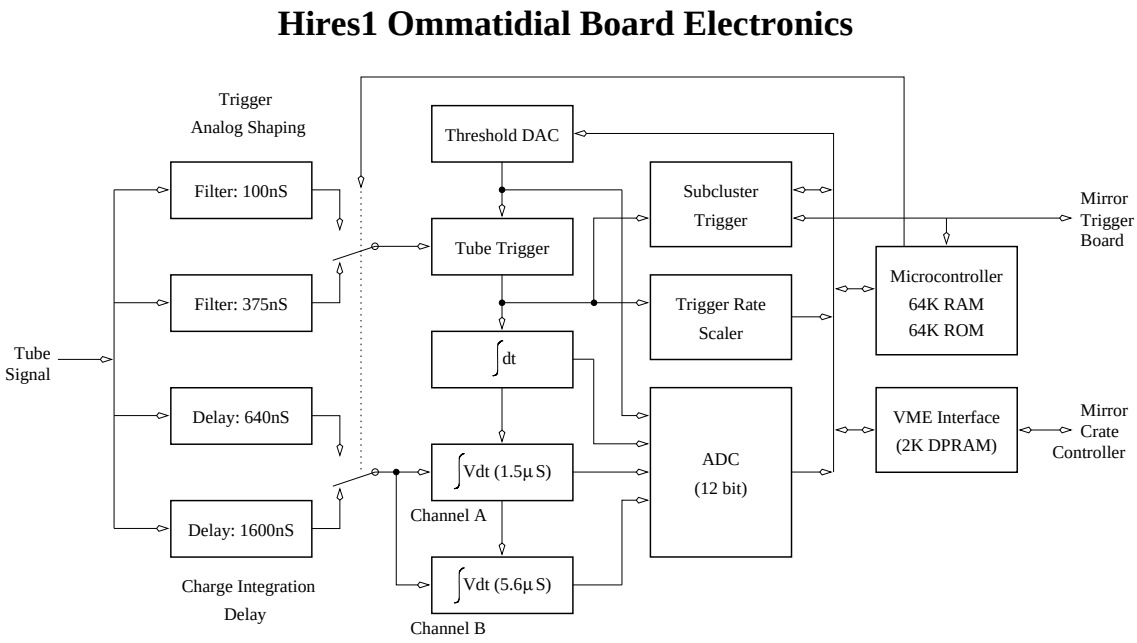

Figure 3.11: HiRes 1 Data Acquisition 'Ommatidial' Board. After Kidd[115].

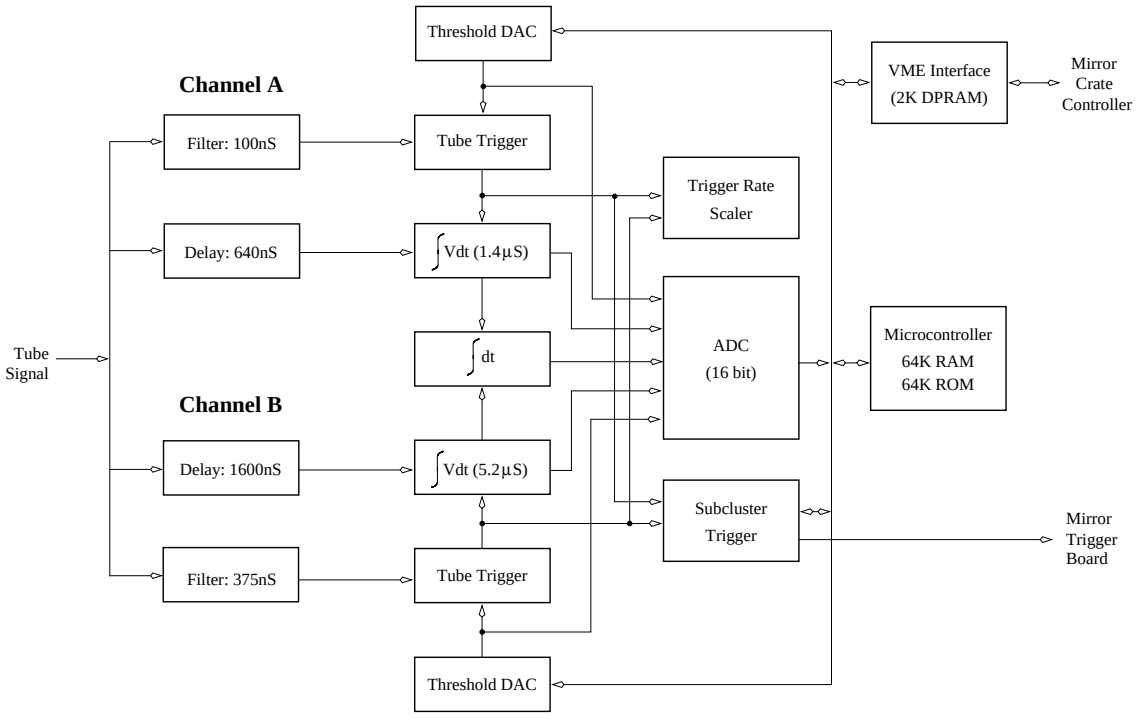

Figure 3.12: HiRes 2 Data Acquisition 'Ommatidial' Board

PMT is measured. PMT timing is measured using a time to digital converted (TDC). The TDC consists of a capacitor which is charged with a constant current source from the time the PMT triggers until a common stop signal is issued approximately 10μs after a full mirror trigger has occurred. The charge is then measured by a 12 bit (HiRes 1) or 16 bit (HiRes 2) analog to digital converter (ADC) and cleared. If no mirror trigger occurs the charge is cleared after 25μs. The HiRes 1 TDC's had a resolution of approximately 5ns thus having a dynamic range of 2000 (10ns to 20000ns). The HiRes 2 TDC's initially had a resolution of 0.65ns/count which was increased to 2ns/count in March 1995. This increased the dynamic range from 2000 to 6000 (the maximum time increased from 20μs to 60μS). The linearity of the TDCs is better than 0.2%.

To ensure that the full waveform is measured, the PMT signals are sent through delay lines whilst triggering is determined. A delay line of 640ns was used for the 100ns filter and 1600ns for the 375ns filter. Channel A and Channel B are integrated for two different time periods, with charge to digital converters (QDC's) being used to measure the integrated charge in each channel . The linearity of the integrators is better than 1%. At HiRes 1, channel A uses a 1.5μs gate, and channel B used a 5.6μs gate. HiRes 2 uses a 1.4μs gate for channel A, and a 5.2μs gate for channel B. The two different gate lengths correspond to crossing times optimised for near and far showers, providing a compromise between skynoise contamination of short pulses (close EAS) and clipping of long pulses (distant EAS). At HiRes 2 the triggering of each channel is done independently so that it is possible for only one channel to trigger, and thus only one charge integral to be stored. At HiRes 1, the triggering channel is fixed, and both charge integrals are stored. As is the case with TDCs, QDCs are cleared after 25μs if no mirror level trigger occurs. An analog multiplexor fans the 48 storage capacitors (QDCA, QDCB and TDC for the 16 PMTs in a subcluster) into an ADC for readout by the 80188 microcontroller chip.

Trigger Board The ommatidial boards store the time and charge integrals for each PMT in each of the 16 subclusters. When a PMTs signal rises above threshold, the PMTs trigger flag is set for at least 25μs. During this time the integrated charge is saved and the PMT may not retrigger. A subcluster trigger is formed when a pattern of

PMT triggers within a subcluster matches a pattern in a trigger lookup table. The 16 PMT trigger flags (25μs pulses) form an input address for a 64K, 8 bit EPROM. Each bit of the address corresponds to a given trigger flag pattern, thus indicating when a subcluster has triggered according to one of the preprogrammed patterns. The specific bit used is software selectable with the different patterns being used for data collection, diagnostics and testing purposes. Normal operation defines a subcluster trigger as three triggering PMTs, with at least two hexagonally adjacent. Other patterns include any one tube, any two tubes, any three tubes, any two hexagonally adjacent tubes and all tubes.

The output of the subcluster trigger lookup table is reshaped into a 25μs pulse and is used as an input to a second lookup table to generate a mirror trigger. Normal operations require at least two subclusters to trigger in the 25μs window to generate a mirror trigger (a minimum of 6 PMTs). A mirror trigger is also sent to adjacent mirrors. This allows adjacent mirrors to drop their triggering requirements down to a single subcluster, so that EAS which clip the edge or corner of a mirror may still cause a trigger.

A mirror trigger generates a mirror save condition in the detector electronics which prevents the PMT charge integrals from being cleared. New PMT triggers may continue to save integrals for a further 10μs after a mirror trigger to allow the EAS to finish crossing the mirror. At the end of this period, a holdoff condition is set to prevent any new PMT triggers and stop the TDC integrators. At HiRes 2 the 10μs was found to be an insufficient time and in March 1995 was increased to 25μs. When holdoff is set, a signal is sent to the central timing crate to record the absolute mirror holdoff time, and then the PMT charge and time integrals are digitised and saved as a mirror event. The mirror holdoff time is also recorded locally by latching scalers which count the one kilohertz and one minute pulsetrains from the GPS clocks. The latched minute and millisecond values of holdoff are used to match the mirror event data to the central timing holdoff latch time for a much more precise mirror event time. Event processing takes $\sim$ 8ms after which the mirror save and holdoff conditions are cleared, resetting the mirror electronics for the next EAS event.

Mirror CPU The mirror CPU is the primary interface between the central computer and the mirror electronics (the 16 ommatidial boards, the trigger board, the PPG board and the garbage board). The central computer sends commands to set up the mirror for tasks such as calibration and data collection, and the mirror CPU sends back event and mirror status data. An ethernet link using UDP protocol is used for communications between mirrors and the central computer.

The mirror CPU is a Force computers 680303 CPU card using the Wind Rivers System's VxWorks real time operating system. VxWorks provides a fast operating system with Unix like function libraries and multitasking. The HiRes specific software is maintained on the central computer and is downloaded to each board when it is rebooted. This allows global changes to the operating software to be made and easily propagated to each mirror unit. The system also allows logins, so operators can login to individual mirrors to check the status and diagnose any problems that arise.

The main task of the mirror CPU is to collect the TDC and QDC information from PMTs in a mirror event. It attaches an event number (using a scaler) and the minute/sec/msec time using scalers synchronised by the master clock at the start of the night. The information is placed in an event packet, and several mirror events are collected before they are sent to the main computer for storage. The CPU also gathers information on trigger rates, thresholds, network performance and deadtime and checks local time scalers (the CPU checks that there were exactly 60000 kiloHertz scaler counts in the last minute). Every minute this is packaged and sent to the main computer to be incorporated into the data stream. The CPU receives control packets from the central computer, which are then sent to the relevant boards. Thus the ommatidial boards can be instructed to set thresholds or disable/enable triggering for individual tubes (useful when stars enter a PMTs field of view), triggering requirements may be set on the trigger board, and the PPG board can be made to fire pulses with specified shapes and rates.

3.1.2 Central Timing

The central timing crate (CT) provides the master clock which is used to record mirror triggering times, and to provide timing pulses to the mirrors. The basis of the timing system is a 24 bit, 40MHz scaler (25ns resolution) which is synchronised to absolute UTC to within 340ns (2σ) by a global position system (GPS) clock. Relative timing between the two HiRes sites is much better and is of the order of 10ns for the majority of the time. The author was responsible for the development and testing of the GPS clocks used by the two HiRes sites which are the subject of chapter 4.

The GPS clocks produce a synchronisation pulse at the start of the UTC second. This is used to latch the 40MHz scaler, so that the scaler value at the start of each second can be recorded. This allows a measurement of the scaler drift, which can then be corrected for later in the analysis stream. The GPS clock is also used to fan out minute and millisecond pulse trains to each mirror, which are used to assign event times (to the millisecond level) in event packets.

The 40MHz scaler is used to provide inter-second times with a resolution of 25ns. When a mirror trigger holdoff is raised, a signal is sent down a dedicated line to latch the value of the 40MHz scaler (the ethernet is too slow). The tens and ones of the absolute millisecond time are also recorded from the GPS. The mirror that triggered, the scaler value and lower digits of the millisecond time are packaged together and placed in a timing packet. If additional mirrors trigger within 50ms of the first mirror, their triggering information is added to the timing packet, up to a maximum of 128 triggers. The timing packet is then sent to the central computer via ethernet and added to the data stream. Event and timing packets are matched later in software.

The prototype detector initially used WWVB clocks which only had a resolution of 1ms. The WWVB clocks were replaced in November 1994, and all data analysed for this thesis was taken using GPS clocks. At HiRes 1, the central timing crate is also used to produce a pulse to fire a Xenon flasher (flashers are described in section 3.2.5.1) which is used to alert CASA/MIA of a HiRes 1 trigger[115].

3.1.3 Control Software

The central computer is a DecStation 3100 workstation and is used to control data collection for the detector[159]. The central computer makes network connections to each mirror and handles the initialisation of each mirror for data collection. The control software includes a user interface so an operator can issue commands and view the detector response (such as PMT count rates, trigger rates, and any warnings or alarms). The operator can issue diagnostic calibration and detector operation instructions, which are then sent via the ethernet to each mirror. Event, timing and status packets from the mirrors and the control program are collated and written to a local hard disk.

3.2 Calibration

Calibration is an important component of data collection. To extract useful information from EAS we must understand how the different detector components function (such as response of individual PMTs) and how to convert this to useful information. HiRes calibrations can be broken into five components: PMT response, mirror behavior, filter response, electronic response, and the atmosphere. Calibration parameters are obtained for the different components (some occasionally, some nightly), and are combined to enable us to calibrate data from normal detector operation. The calibration components will now be discussed.

3.2.1 Photomultiplier Tube Response

A computer controlled testing station to measure the response of PMTs was built at the University of Utah and is well described in [31]. The test bed was designed to measure the PMT quantum efficiency, the gain as a function of voltage and the uniformity across the PMT face. The test bed is shown in figure 3.13 and it was used to measure all PMTs in the HiRes prototype.

Most components are located in a light tight box, with the lasers outside the box for easy access. Area A was used to measure the anode sensitivity and cathode quantum

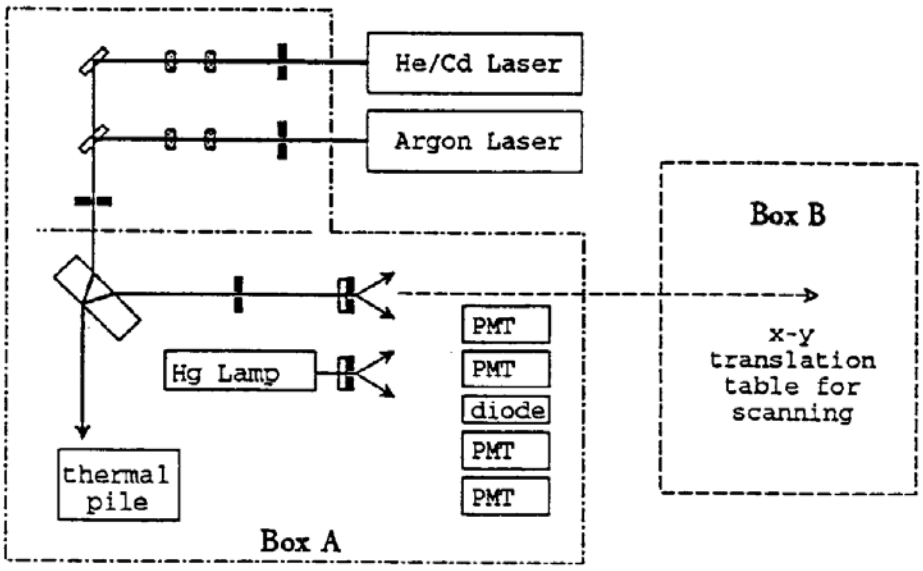

Figure 3.13: Photomultiplier Tube testing setup[31]

efficiency, and area B was used to measure the spatial uniformity of gain and quantum efficiency. Three different monochromatic light sources were used in the testing – an Argon laser which provided wavelengths of 351nm or 364nm, and a He-Cd laser which provided a wavelength of 325nm. The light beam is attenuated and split, with one beam being sent to thermopile as a monitor of the beam intensity. Attempts were made to minimise and absorb any stray light. For measurements of PMTs in area A, the attenuated beam is passed through a teflon diffuser to uniformly illuminate four PMTs and a diode calibrated by the U.S. National Institute of Science and Technology (NIST). The NIST calibrated diode provides an absolute calibration for the system. The typical light intensity for testing the PMTs was 8×10^6photons/cm^2s (4.5 picoWatts/cm^2 at 350nm). A computer was used to perform the measurements and record results. Scanning of the PMT faces used computer controlled stepper motors to allow X-Y scanning. The teflon diffuser was removed for scanning measurements, and up to 16 PMTs can be measured in a single cycle.

PMT Quantum Efficiency PMT quantum efficiency was measured for all PMTs used in the HiRes detector. The quantum efficiency was found to vary little from PMT to PMT and a sample plot of the PMT quantum efficiency for one of the Philips

PMTs is shown in figure 3.14.

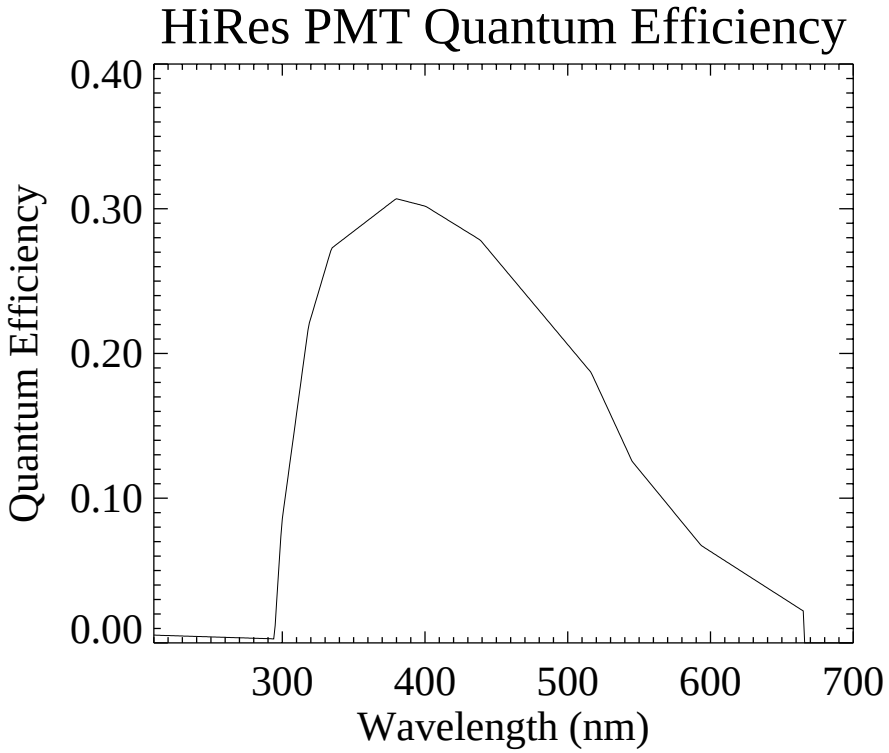

Figure 3.14: Typical quantum efficiency as a function of wavelength for Philips XP 3062 PMT used in the HiRes detector[38]

The PMT quantum efficiency and the HiRes filter affect the sensitivity of the detector to the atmospheric nitrogen fluorescence spectrum. Measurements of the filter response and quantum efficiency as a function of wavelength can be combined to obtain the resultant sensitivity to the spectrum and is presented in figure 3.15

Gain as a function of Voltage The gain as a function of voltage (V) is well described by the functional form

$$gain = \exp(\alpha) \times V^{\beta} \tag{3.1}$$

where α and β are measured for each PMT. The distributions of α and β for all PMTs at HiRes 1 were roughly gaussian with $\alpha = -31.70 \pm .77$ and $\beta = 5.89 \pm .14$ (1σ errors)[115]. PMTs are operated at a gain of approximately 10^5 electrons per photoelectron[158][37].

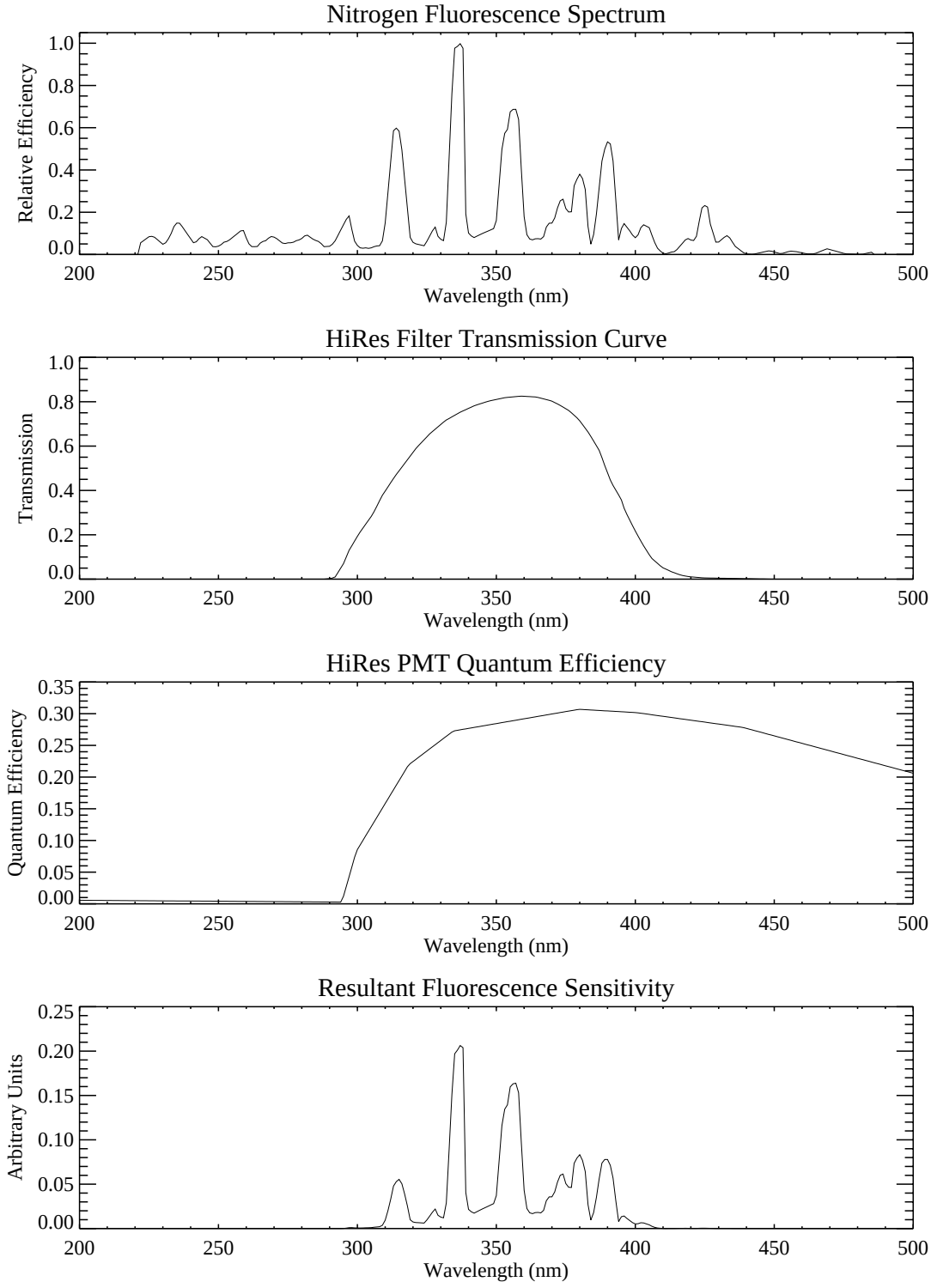

Figure 3.15: Resultant fluorescence spectrum after taking into account HiRes filter and PMT quantum efficiency.

Temperature Dependence The PMT gain temperature dependence is roughly 0.5%/°C which is significant given the detector operates in ambient temperatures from -15°C to 40°C. The PMT clusters are cooled with a fan in an attempt to maintain a uniform cluster temperature, but the actual temperature is allowed to vary. A temperature sensor is located in the centre of each cluster and two additional sensors record the shed and crate temperature. Measurements are recorded using the garbage board.

PMT Response Profile HiRes PMTs are checked to ensure they have a uniform response to within ±10% over the face of the tube, except for within 3mm of the edge. A selection of HiRes 1 PMTs were scanned, and all HiRes 2 PMTs were scanned in this way.

UV Light Delivery Systems The response of the PMTs to UV light is monitored each night using a YAG laser system[166] at HiRes 1, and a similar system using a Xenon flash bulb system[38] at HiRes 2. These systems are used in nightly calibrations and mirror reflectivity measurements (to be discussed in section 3.2.2).

The system consists of a light source and optics located in the central trailer, which focus light into one of two bundles of fibre optic cables that then pipe the light out to each mirror. Fibres in the first bundle terminate in the centre of each mirror, so that light from the fibre will illuminate the PMT cluster. Fibres in the second bundle are attached to the cluster, so that their light must first reflect off the mirror before arriving at the cluster. Each fibre terminates at the base of a cup where it encounters teflon sheets which diffuse the light so that it will uniformly illuminate the mirror. The light entering the fibre bundles is monitored with silicon photodiodes. A solenoid is used to select the bundle that the light source fires into. A Macintosh computer is used to trigger the light source, operate the solenoid, calibrate the monitor photodiodes and record the diode measurements which are then sent to the central computer where they are recorded in the data stream. Pulse to pulse variations at the fiber bundles are approximately 1% at HiRes 1 and 5% at HiRes 2. The variation at the cluster is probably slightly larger due to small variations in the light intensity entering the

different fibres.

Two sets of calibration data consisting of 50 shots are taken each night. The calibration systems at HiRes 1 and HiRes 2 are slightly different with the information being used differently at each site. At HiRes 1 the relative response of each PMT to the average response of the cluster is measured, and is used to weight the electronics gain which is measured nightly using the PPGs (to be discussed in section 3.2.3). This calibration is done on the assumption that the response of PMTs will not vary much between absolute calibrations.

At HiRes 2, the average QDCs and the average intensity measured by the photodiodes are used with measurements of the electronic constants (determined using the PPGs). Constants obtained from the absolute calibration are used to convert the diode measurements into numbers of photons, which can then be used to determine the gain of the electronics and PMTs.

Intermirror and Absolute Calibration The intermirror and absolute calibration is performed using four standard tubes which are moved from mirror to mirror[4]. These four PMTs were selected from those which had been fully scanned, and were chosen based on their having similar gains and response profiles. A portable calibration system consisting of an ommatidial board, PPG board, a high voltage supply and monitor was constructed so that the standard tubes could be operated with standard electronics. The standard tubes are calibrated to 2%[115]. The standard tubes are placed in a subcluster of a mirror and illuminated with the UV light source (a YAG laser at HiRes 1, a Xenon Flasher at HiRes 2). The response of the standard PMTs and the PMTs in all other subclusters are compared. Details may be found in Abu-Zayyad *et al.*[4]. The sensitivity of the full cluster was calculated using the gains of the standard tubes, the filter transmission and the PMT response to the UV light. The mean sensitivity for PMTs in all clusters was found to be 12160 A/W.

3.2.2 Mirror Reflectivity

The relative night to night variation in the mirror reflectivity is measured by comparing the average PMT response to directly viewed and reflected UV light. The light

monitoring system previously discussed (YAG laser/Xenon flash bulb) is used to provide a light source. Unfortunately a series of tests conducted just before the prototype was disassembled revealed that small flexing of the teflon diffusers within the cups could affect output on a nightly basis by 10% or more, thus affecting the accuracy of the mirror reflectivity tracking.

The absolute mirror reflectivity starts at $\sim$ 90% when the mirrors are washed, a twice yearly occurrence. Experience with the Fly's Eye mirrors indicated that dust accumulation occurs rapidly in the first month or two after washing reducing the reflectivity to $\sim$ 80%. After this time, the rate of accumulation drops off and reflectivity only decreases slowly[115].

The output of the fiber optic cups is measured using a special device which covers the cup and measures the light at a photodiode which is a fixed distance from the teflon diffuser. This provides one method of measuring mirror to mirror gain variations, but it is subject to the flexing problem mentioned above.

In addition to reflectivity from the mirrors, the walls of the sheds will reflect a small component of light onto clusters. For the sheds the crosstalk between neighbouring mirrors is less than 1%. However For the silos at HiRes 1 (mirrors 11-14) the problem was originally between 5% and 10%. After painting the interior a UV absorbing green, the problem was reduced to less than 1%[115].

3.2.3 Electronics Response

The electronic system for each channel consists of a preamp on the PMT and one ommatidial board for every 16 tubes. A programmable pulse generator (PPG) board in each crate allows a square pulse of varying width and amplitude to be injected into the input of the preamp of each PMT. Software is used to vary the pulse width and amplitude so that the electronics constants can be calculated. For QDCs the task is to relate the PPG pulses with QDC charge, and for TDCs it involves fitting TDC values to known different length holdoffs. Electronics calibration is done at the start and end of each night.

PMT Pedestals, Electronic Noise and Sky Noise "Snapshots", where all PMTS are forced to repeatibly trigger (and integrate) for a period of roughly one minute, are used to measure PMT pedestals, electronics noise and sky noise. The mean value of the QDCs give the PMT pedestal, and the rms variation provides a measure of the electronics and sky noise. Pedestal values should be the same whether taken in a dark shed with the doors closed, or taken when viewing the night sky. This has been observed to be true to within 0.2QDC counts at HiRes 1. The noise contribution will differ depending upon whether the shed doors are open or closed. Snapshot data taken with shed doors closed is used to indicate electronics noise. Snapshot data taken with shed doors open indicate the electronics noise combined (in quadrature) with the night sky noise. At HiRes 1, the combined electronics and sky noise was found to be 40 photoelectrons in channel A and 200 photoelectrons in channel B. Unfortunately problems with the HiRes 2 electronics has prevented snapshot measurements from being used. However the similar integration times imply that skynoise in each channel is probably similar.

TDC calibration The TDC calibration is performed by using snapshots to start the TDCs and the holdoff counter (when the counter reaches a specified value it issues a signal to stop TDC integration). The holdoff times used range from 500ns to 18000ns in 500ns steps, with 20 TDC integrations performed at each step so that the mean and standard deviation of the TDC counts can be determined. A function is then fitted to relate TDC values with physical times.

Ideally the holdoff time should be increased so that the entire TDC range may be directly calibrated. At HiRes 1, the 12 bit TDCs are set at approximately 5ns/TDC count, and thus the holdoff times used in calibration range from 500ns to 18000ns in 500ns steps. A linear least squares fit is used to determine the gain and pedestal values for the TDCs.

A similar calibration range was initially used at HiRes 2, where the 15 bit TDCs were set at 0.65ns/TDC. In March 1995, the length of holdoff during data collection was increased from 10μs to 25μs, and thus the TDCs were changed from 0.65 to 1.5ns/TDC count. Later that year, the TDC calibration was re-examined by the

author (see section 4.7) and some further changes were made. In December 1995, the maximum holdoff time in TDC calibration was extended from 18μs to the hardware limit of 25μs, so as to calibrate as much of the TDC range as possible. The hardware was then modified, and the calibration changed to measuring the average TDC count for times from 1μs to 50μs in 1μs steps, allowing the full TDC range to be calibrated. Thus for data taken between March 1995 and February 1996, the last half of the TDC range must be extrapolated based on the first 18μs. The best function to fit to the calibration data was also examined. A linear least squares fit was initially used, but investigations showed non-linearities in the TDC and thus a more suitable quadratic function was chosen instead. Additionally, about half the TDCs used at HiRes 2, were found to have leaky capacitors, which were thus replaced in March 1996. Details of this investigation are presented in section 4.7. All stereo data have been calibrated using the quadratic form. Calibration fit residuals (mean TDC value - fitted value) for most of the data is 10ns, but for TDCs with the leaky capacitors it is 50ns for the period March 1995 to February 1996 (the time calibration was not done over the full TDC range).

3.2.4 Calibration of Raw Data

Calibration data (PPG data, snapshot data, YAG/Xenon flasher data) are collected at the beginning and end of each night. Either data set may be used in calibration, and the redundancy allows calibration data to be obtained when problems arise. In the event of no data set being available (due to problems such as the YAG intensity dropping or a board failing), data from the next or previous night are used. Standard programs were developed to combine the calibration data so that it could be used on data from normal operations. The calibration of all the stereo data from the prototype was performed by the author.

3.2.5 Atmospheric Monitoring

Effective monitoring of the atmosphere is a difficult and important challenge for the HiRes detector. The effective aperture, EAS light production and light propagation are

affected by clouds, temperature variations, pressure variations and the distributions of aerosols. Atmospheric monitoring is performed through operator observations, an array of collimated UV light sources known as flashers, a permanent YAG laser system, and a portable telescope-mounted laser known as the Laserscope. Meteorological data is also available from the Dugway meteorological department, and a basic weather station that measures temperature and wind velocity is located at HiRes 2.

An important task in atmospheric monitoring is to measure the atmospheric extinction length of UV light. The horizontal attenuation length of a beam of light is given by

$$I = I_0 e^{-\tau/\tau_0} \tag{3.2}$$

where τ_0 is the horizontal extinction length. The uncertainty in the intensity of the beam (in our case light from an EAS) is then a function of our uncertainty in the extinction length

$$\frac{\Delta I}{I} = \left(\frac{\tau}{\tau_0}\right)\left(\frac{\Delta\tau_0}{\tau_0}\right) \tag{3.3}$$

We wish to know $\Delta I/I$ to 10% for distances out to 20km or more. This means we must know our extinction length very well (a few percent for τ_0 =10km). The extinction length depends on both molecular and aerosol scattering. However in the dry desert air of Dugway, the aerosol content is often low enough that the extinction length depends solely on Rayleigh scattering.

Molecular or Rayleigh scattering is well understood[27]. The scattering probability is proportional to $1/\lambda^4$ and the scattering angular (θ) distribution goes as $1 + \cos^2\theta$. The atmospheric molecular density decreases exponentially with a scale height of 7.5km, and variations can be tracked with radiosonde data. Thus the effect of Rayleigh scattering on the transmission of light can be well understood using easily available meteorological data. Typical sea level horizontal attenuation lengths are 7km at 300nm and 22km at 400nm[161][27].

Aerosol scattering of light in the atmosphere is an important but less well understood effect. Variations in size, shape, dielectric constant and vertical distribution all contribute to making estimates of the effect of scattering by aerosols difficult. In an attempt to characterise aerosol scattering, the Mie scattering approximation is used

in which the particles are assumed to be dielectric spheres. In Mie scattering the wavelength dependence and angular distribution of scattering, depends on the size distribution of particles. For desert aerosol particles the scattering probability goes as $1/\lambda$, and the angular distribution is strongly peaked in the forward direction. The vertical distribution is also important and depends upon local meteorological conditions. It is typically an exponential falloff with a scale height of 1-4 km, or a constant distribution confined in a mixing layer up to some height (the height of the inversion layer). Given that aerosol distribution and densities may vary rapidly in time by orders of magnitude, it is important that measurements be made to characterise the aerosol content of the atmosphere.

To assist in understanding atmospheric effects a computer model known as MODTRAN has been used. MODTRAN was developed by the U.S.A.F.[116] and provides a set of standard atmospheric models – such as a standard desert atmosphere which may be applied at Dugway. MODTRAN can be incorporated in Monte Carlo code and can be used to examine the effects of different aerosol distributions on the atmospheric extinction lengths. It thus provides a comparison for data obtained with local monitoring systems such as flashers and lasers.

An array of flashers, the fixed YAG laser and the Laserscope are all used to monitor the aerosol content so as to estimate the horizontal extinction length on a nightly basis. All systems are used to generate a collimated beam of UV light into the atmosphere. Light will be scattered out of the beam and then be viewed by the HiRes detector at a variety of emission angles. The intensity of light at different emission angles provides information on aerosol content and the horizontal extinction length due to the different angular distributions of Rayleigh and Mie scattering. Light viewed at small angles is dominated by aerosol scattering whilst light viewed at large angles is dominated by Rayleigh scattering. Hence by knowing the orientation of the original beam, the emission angles of observed light can be determined, and thus it is possible to characterise the state of the atmosphere. Clouds and fog that cause large amounts of scattering can also be detected.

3.2.5.1 Xenon Flashers

Xenon flashers consist of Xenon flash bulb located at the focal point of a 20cm spherical mirror contained in a cylindrical steel housing and hermetically sealed[38]. Flashers act as reverse telescopes with light from the flash bulb being collimated by the mirror to produce a beam that travels into the atmosphere through a pyrex window. The flashbulb produces a 1μs 0.8J light pulse of which approximately 10% falls in the 300-400nm range. After taking into account geometrical effects and reflection and transmission losses, the pulse energy exiting the flasher is 0.2mJ. Shot to shot variation is $5\%(1\sigma)$.

The flasher units are designed to operate independently with power and electronics located in an adjacent box. Solar panels are used to charge the batteries that supply the power. A heater unit prevents the buildup of frost or snow on the window. The original flashers have circuits that will trigger the flasher to fire at a rate of $\sim$ 1Hz for 10 seconds, every $\sim$ 7 minutes. Radio controlled flashers have recently been developed and allow much greater flexibility in the use of flashers, allowing computer or operator control of triggering (and heating). Full details may be found in Bird*et al.*[38].

Vertical flashers were developed for use by the Fly's Eye experiment and several flashers located around CASA and in the HiRes 1 field of view were maintained. An array of vertical flashers was placed in the HiRes 2 field of view specifically for atmospheric monitoring[38][7]. Flashers are aligned along two legs at distances of 1,2,4,8 and 10km from the detector, and along a given leg all flashers are viewed by the same set of PMTs (covering elevation angles from 3° to 30°).

Light from vertical flashers must scatter at angles close to 90° to be viewed by HiRes 2. Since the aerosol phase function is relatively independent of the details of the aerosol size distribution in this angular region, the received light intensity is primarily sensitive to the horizontal extinction length. Signals from flashers at different distances but the same emission angles are compared with reference nights and MODTRAN results to allow a measurement of the extinction length and aerosol content[161][38].

An inclined flasher, known as the intersite flasher (ISF), is located at the centre of CASA and aligned so that scattered light is visible by both detectors[27][5]. PMTs view

light with scattering angles from 30° to 70°. Around 30° the intensity of the scattered light is strongly dependent on the density of aerosols whilst at viewing angles of 70° the intensity is mostly sensitive to Rayleigh scattering. Thus a quality ratio (QR) has been defined that compares the intensity in the first 5° of the track with the last 5°. MODTRAN has been used to relate QR measurements to the atmospheric extinction length.

Quality ratio measurements are made every 7 minutes and measurements are available for all stereo data. The majority of nights have good atmospheric conditions (a selection effect of running the detector) with 90% of the nights with horizontal extinction lengths between 18km (purely Rayleigh) and 7km (aerosol extinction length of 13km). The variation over the night has also been studied and was generally found to be small (generally less than 1%). Not surprisingly nights with larger quality ratios tend to be more unstable. The data from the intersite flasher has also been compared with that from the HiRes 2 flasher array. The two independent measurements of extinction length are well correlated, with the intersite flasher being more sensitive to nights with low aerosol content (which is expected due to the different viewing angles of the two techniques)[27].

3.2.5.2 Fixed YAG Laser system

A steerable YAG laser system has been constructed at the centre of the Fly's Eye II/CASA site and is used in nightly atmospheric monitoring[161][8]. Its position in standard HiRes (East, North, Up) coodinates is (1648.6, 2966.6, -129.5). The system consists of a YAG laser which is frequency tripled to 355nm. The YAG fires 10ns pulses with energies up to 50mJ, at a rate of 1Hz. The beam is well collimated with a divergence of 10mrad, and is directed to the atmosphere using a series of mirrors. Mirror directions are controlled by stepper motors which allow pointing to any azimuth or zenith angle to within 0.1°. A personal computer is used to control and monitor the system, and is setup so that it may operated remotely by the HiRes operators.

Each hour, the laser fires 0.4mJ shots in a pattern of eight equispaced azimuthal directions at zenith angles of 0°, 30°, 45° and 60°. The laser is powerful enough that scattered light is visible by both detectors. The laser can also be set up to do other

tests, such as repeatedly firing in a fixed direction so that large datasets with fixed geometries can be obtained. Such a set was used in testing the accuracy of the GPS clocks (chapter 4) and is discussed in section 4.5. The system was also trialed as a LIDAR[160] for the first six months of 1995 when sets of 20mJ laser shots were taken each hour in addition to the 0.4mJ laser shots. However the information was found to not be sensitive enough in characterising the aerosol content of the atmosphere (a larger mirror, higher powered laser and more accurate stepper motors would be needed).

3.2.5.3 Laserscope

In addition to the fixed YAG laser system, a portable laser system known as the Laserscope has been developed[6]. The Laserscope consists of a commercial YAG laser (frequency tripled to 355nm) mounted on a commercial Meade LX-200 200mm telescope. The laser produces a 5ns pulse with a nominal energy of 4mJ, with the direction given by the telescope which has a pointing accuracy of 5 minutes of arc. An energy probe and radiometer are used to measure the energy of each pulse.

The head of the laser, the optics and energy probe are contained in a custom made box mounted on the telescope. The laser is aligned with the telescope at the start and end of each night, and the telescope is aligned with several stars to check its absolute pointing accuracy. A personal computer is used to control and log telescope pointing, laser triggering and energy monitoring. Triggering time is recorded to the nearest second. A GPS system has been developed to to trigger the laser on the start of each UTC second.

The Laserscope was designed with several applications in mind. In addition to atmospheric monitoring, it can be used to generate a set of reference events for testing reconstruction resolution and for checking PMT pointing directions[5]. The flexibility and portability of the system allows probing of the atmosphere at large distances from the detector. The Laserscope can also be used to determine PMT pointing directions in addition to traditional surveying methods. This is achieved by performing a series of fine scans across a mirror aperture from two different sites (the laserscope grids the field of view in 0.1° steps, with shots taken from two sites to generate sets of

approximately orthognal grid lines). The PMT response as a function of the angle between the PMT pointing direction and the Laserscope track can be examined to determine to determine the true pointing direction and the effects of optical aberrations and photocathode response[6].

Some of the first uses of the Laserscope was to provide reference events for testing EAS reconstruction techniques which are discussed in 5. Problems with pointing direction and laser energy were found and are discussed in section 5.2. A temporary fix has been applied, and work is underway to improve the system through mounting the laser in the more controlled environment of the trailer, and using a fibre optic link to pipe the light to the telescope. This will lighten the load on the telescope and should fix the problems found.

The fixed YAG laser, and the Laserscope have both been used to check the quality of data from the prototype. The next chapter covers the development of GPS clocks for the two HiRes sites, and the subsequent testing of the timing system. The fixed YAG laser was used to generate large sets of test data that enabled the discovery and fixing of previously hidden problems with the system.

Chapter 4

GPS Clocks and the HiRes Timing System

The use of timing information provides important constraints on EAS trajectory reconstruction (reconstruction methods are discussed in chapter 5). With EAS viewed by a single site, timing information is necessary to determine the orientation of the EAS in space[21][90]. The Fly's Eye found that reconstruction could be greatly improved using purely geometrical fits if the EAS was viewed simultaneously by two sites (stereo observations)[30][90]. Simulations of the full HiRes detector[73] indicated that it should be possible to improve stereo reconstruction by incorporating timing information, provided that the two sites were synchronised to within 100ns and timing systematics were well understood. Hence one of the aims of the prototype detector was to upgrade and improve upon the timing system used by Fly's Eye so that timing information could be used to further improve stereo reconstruction of EAS.

The timing system is of great importance in the operation of the HiRes detector. However the separation of the two sites leads to potential difficulties in maintaining synchronised timing systems. Initially, the prototype used WWVB clocks (as had the Fly's Eye) which only provided absolute timing accuracy to a millisecond. A 40MHz oscillator at each site provides a 24 bit scaler counter which is used to provide more accurate mirror triggering times. The scaler was not synchronised with the WWVB nor was the frequency monitored. Thus, whilst mirror to mirror times were quite precise,

comparing two sites was a difficult task. It was decided to investigate the use of clocks using Global Positioning System (GPS) receivers to maintain site synchronisation and allow accurate event time tagging. The author's entry into the HiRes project was in helping to design the GPS clocks, and then conduct the testing and monitoring of the system. This chapter gives an overview of the timing system followed by details of the testing of the GPS clocks. This covers both initial laboratory testing and then the *in-situ* testing after the installation of the clocks at the HiRes sites. Finally the chapter covers the testing and calibration of the rest of the timing system which followed from installation of the GPS clocks.

4.1 Overview of the current timing system

To best understand the timing system it helps to understand the overall HiRes design. Essentially each mirror has been designed to act independently of other mirrors and to communicate with the control software over ethernet. This approach has the advantage that new mirrors may be easily brought on line, and that any mirrors with problems can be shut down without affecting the rest of the system. Each mirror has a rack of electronics (physically in the mirror building) that contains a VxWorks CPU board, a mirror trigger board and other electronics such as tube QDC's and TDC's (see chapter 3 for more details). There is also a special "mirror" in the central observing hut which contains the central timing electronics (mirror 0). Central timing consists of the GPS clock, the eye timing board and the mirror timing board. As mentioned, communication is done using UDP packets over ethernet, with the control software issuing commands to the mirrors and the mirrors sending data packets to the control software for logging to disk.

Due to the distributed nature of the system, assigning accurate event times is a multistep process requiring communication between a mirror and central timing. Central timing (CT) contains the reference 40MHz oscillator which drives a free-running 24 bit (now) graycode scaler (nominally 25ns ticks). This scaler is latched whenever a mirror event occurs so that an accurate time may be assigned. To ensure times are accurate the 40MHz frequency is monitored by the custom built GPS clock. The GPS

clock produces a pulse synchronised to the start of the UTC second. This pulse is latched by CT so the actual number of scaler clock ticks in one second can be measured, and thus the actual oscillator frequency. Originally, full time information (year down to millisecond level) was obtained from a 50 pin connector on the WWVB clock and when a mirror latch occurred the time was read off these pins. The WWVB was also used to provide 1/60Hz (minute) and 1kHz pulsetrains which were fanned out to all the mirrors as timing reference signals. Now, as the GPS clocks were designed to smoothly replace the WWVB, this 50 pin connector was incorporated, but only with minutes down to millisecond so that the above pulsetrains could still be supplied to the mirrors. The rest of the time information (years down to seconds) was supplied over a serial port from the GPS receiver to the mirror timing board. More generally this serial connection was used to send and receive information from the GPS receiver (the heart of the clock). Thus it is possible to get the absolute UTC time of a mirror latch to roughly the 25 nanosecond level.

A serial line connects the mirror to CT and it is used to latch the 40MHz scaler a fixed time (known as the holdoff time) after the mirror triggers (this allows other PMTs within the mirror to trigger). After holdoff, the mirror reads TDC and QDC information of triggered PMTs along with the time from its local clock (minute, second and millisecond). Each mirror assigns event times by counting the one kilohertz and the one minute pulsetrains (from the GPS clock) and latching the value from a scaler when holdoff occurs. The minute pulse also generates an interrupt at which point mirror event rates and deadtime are calculated (and sent back to the control software), and a check is made that there was exactly 60,000 kilohertz counts in the last minute. The TDC, QDC and time information is stored in an event packet which is sent to the control software.

Whenever the scaler in central timing is latched, the lower 8 bits of the GPS clock's 50 pin D connector is read to get the millisecond time (to tenths of millisecond). A timing packet stores the 40MHz latch value of the start of the second, and the corresponding time (hour, minute, second) from the GPS. Mirror event latches (recording the mirror, scaler latch value and millisecond) are added to the timing packet which is then sent to the control software. The time packets and event packets are then

matched at a later point and an accurate PMT trigger time can be determined by subtracting the calibrated TDC time (ns) from the scaler latch time (also converted to ns) as is illustrated in figure 4.1.

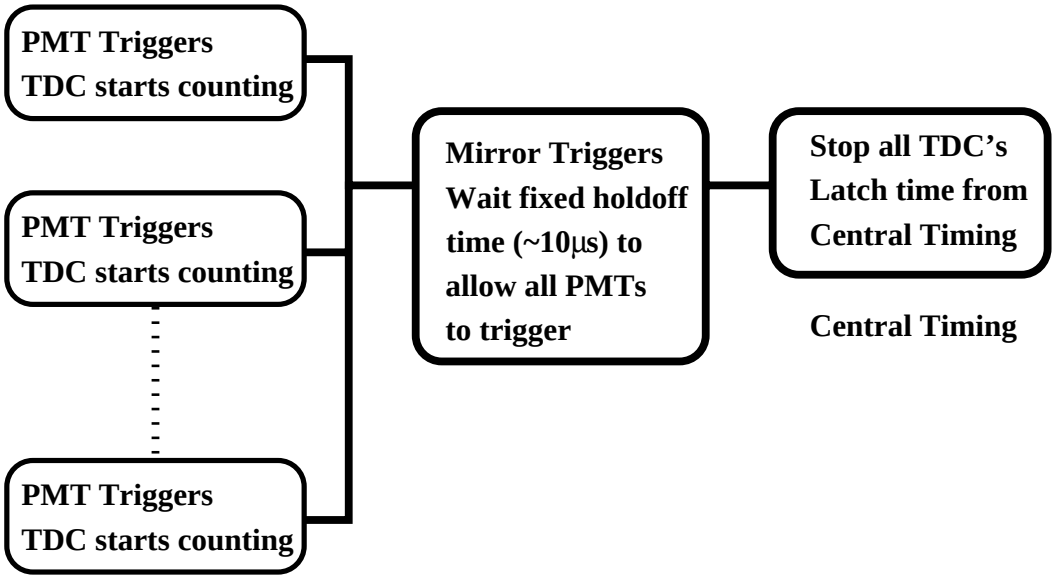

Figure 4.1: An overview of the mirror level timing system.
PMT Trigger Time = Mirror Latch Time (ns) – TDC (ns).

4.2 GPS Based Clocks

The GPS clock systems were designed in Adelaide where initial testing was done. These were then taken to Utah for installation at the two HiRes sites, where their performance was again tested. However before going into detail on the actual clocks we will review the Global Positioning System to understand why it is useful in an experiment such as HiRes.

4.2.1 The Global Positioning System

The Global Positioning System (GPS) was developed by the U.S.A.'s Department of Defense to allow accurate determination of position, velocity and time anywhere in the world. It consists of an active constellation of 21 satellites (plus at least 3 spares) in 12 hour orbits distributed in 6 orbital planes (inclined at 55° to the equator) and at altitudes of approximately 18000 km. The distribution of satellites was designed so

that 4 or more satellites (enough to allow an accurate determination of position) are visible at any given time, anywhere in the world. Full details of the system may be found in appendix A

Each GPS satellite carries an atomic clock which is synchronised daily to within 100ns of UTC, and each satellite continuously transmits its current position in space (their orbital emphemeri are recalculated and uplinked every 4 hours by ground stations). GPS receivers obtain their position by measuring the distance to each of four satellites, and using the received positional information from each of the satellites, solve for receiver position and clock bias (see section A.1 for details). A useful corollary is that if the receiver's position is known, then the receiver may synchronise its clock to UTC by tracking a single satellite. It is thus also possible to synchronise two separated receivers to within 10ns by having them track the same satellite (assuming that the positions of both receivers are well known)[64]. It is this feature that has been exploited in the development of GPS clocks for the HiRes project.

4.2.2 Design of the GPS Clocks

It was desired that the change from WWVB to GPS clocks be as smooth as possible. To achieve this, the GPS clocks were required to supply BCD millisecond information, a 1kHz pulse train and a 1/60Hz (minute) pulse trains. GPS receiver boards (and antennas) were purchased and integrated with additional electronics to produce the desired clock units which could be placed in a standard equipment rack. Figure 4.2 illustrates the front and rear panels of the GPS clock and the three basic internal sections which will now be described.

4.2.2.1 The GPS Receivers

Several different GPS receivers were considered on the basis of their ability to act as a source of UTC synchronised pulses, their cost and availability. The receiver chosen was the Scientific Time Recovery model of the GPS Engine manufactured by Leica (previously Magnavox). Receiver specifications may be found in appendix B of the Magnavox GPS integration guide and applications manual[131]. This receiver was

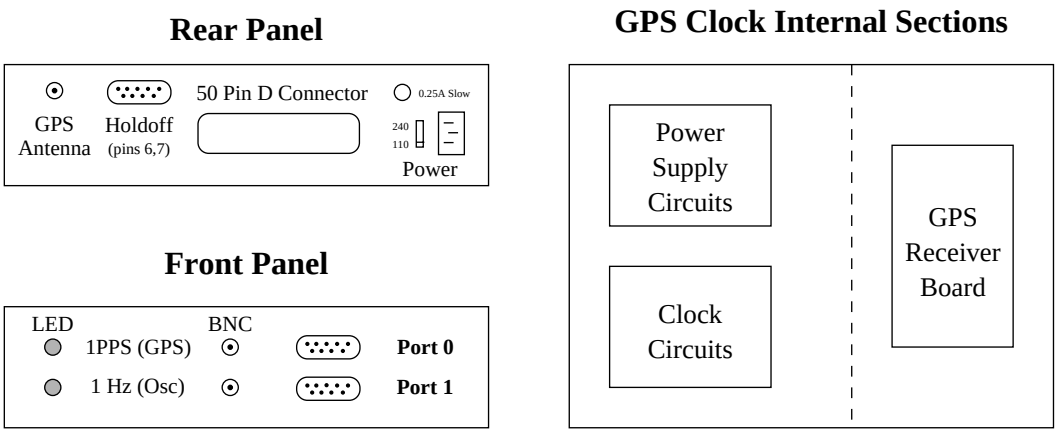

Figure 4.2: GPS Clock Schematic.

designed with timing applications in mind, producing timing pulses synchronised with the start of every UTC second. An additional factor that influenced their selection was that the receivers are the same model as used by Pryke and Lloyd-Evans in a similar timing application[141].

The chosen GPS receivers allows operation in known position mode, where the receiver solves only for the bias between its local oscillator and the satellite oscillator so that the synchronisation pulses can be steered to UTC. This mode allows the choice of the specific satellite to be used to extract timing information, as well as the option of using all satellites being tracked and then averaging over the timing solutions ("all" satellite mode). Further, the receiver produces an estimate of the error in the previous synchronisation pulse which can be used to improve the timing accuracy for post event processing.

The receiver uses flash EPROMs to store software for the navigation processor which is an Intel S80C186EB chip (the use of EPROMs allows *in-situ* software upgrading). On board RAM stores information such as last position, date, time, current satellite almanac and ephemerides and last operating mode. The RAM has a battery backup to prevent loss of information and to allow rapid satellite re-acquisition and receiver operation after periods of (main) power loss.

The receiver board has a coaxial RF connector for the antenna, and a 20 pin interface connector for power and communication with pin connections illustrated in figure 4.3. The RF connector provides power to the GPS antenna and preamp via

the centre pin of the BNC connector with the preamp boosting the satellite signals to overcome any cable losses. A Magnavox AT575 patch antenna[131] and a cheaper Furuno AU-6 patch antenna[75] are in use at the HiRes sites and both have found to be perform satisfactorily. The 20 pin interface has pins for the serial ports and the UTC synchronised timing pulse. The CMOS serial ports 0 and 1 have buffered input and output lines to protect the receiver against any potentially damaging signals. Pin 17 is used for the UTC synchronised 1 Pulse Per Second (1PPS) output, which is 8-9.5V, 500μs wide pulse with a 25ns risetime.

Communication with the receiver is via two RS-232 CMOS level bidirectional ports using an 8 bit no parity protocol at 150-19200 baud (configurable). Port 0 is the raw data and reprogramming port which operates at a default baud rate of 9600. Port 1 is the control and data port, with a default baud rate of 4800 baud which is normally increased to 9600 baud by the HiRes detector software. Port 1 is used to exchange control and data messages with a host CPU using the National Marine Electronics Association (NMEA) 0183 interface standard. Each data sentence consists a start delimiter character, the message body of no more than 79 ASCII printable characters in at least two fields, and is ended by carriage return and line feed characters. Input messages are stored in a 1000 byte buffer which is processed once per second. The total number of characters in all messages in a one second time frame must not exceed 350 characters or data will be lost.

The GPS manual[131] provides a full list and the syntax of input and output messages (the second field of each messages contains the message ID). Input messages allow selection of the navigation mode, time recovery mode, the satellites to track and the current time and position. Output messages include the current time and error in the last GPS pulse, the satellites currently being tracked, the current position and the GPS status. Of most importance is the time recovery message (ID 830). This message is output prior to each synchronisation pulse and provides the exact time of the next pulse (year down to second) and an estimate of the error in the previous pulse (due to its local oscillator). Serial port 1 of the GPS is connected to the central timing CPU board, so that all messages can be incorporated into the data stream (and importantly current time information in timing packets).

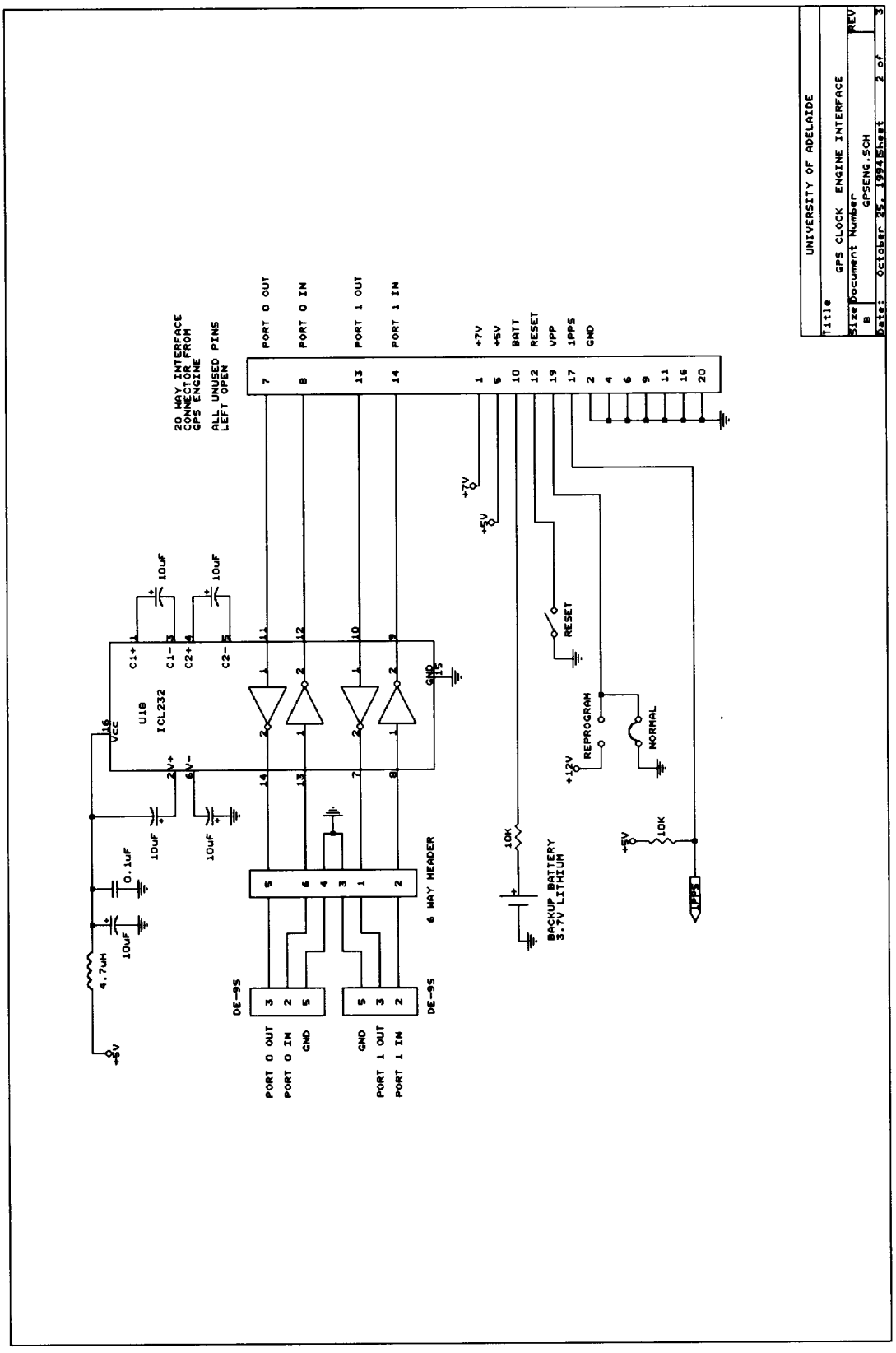

Figure 4.3: GPS Engine I/O Connections

4.2.2.2 Power Supply

The GPS receiver draws a current of approximately 200mA for its digital section from the 5V supply and 180mA from the 7V supply for the regulators in the RF section of the receiver. The +5V and +7V power supplies are derived from stepping down the mains power supply (either 110V or 220V) with the circuit diagram shown in figure 4.4. A +12V supply is also provided to allow reprogramming of the GPS receiver EPROMs, should it ever be needed. Within the GPS clock housing, the receiver section is physically mounted apart from the rest of the clock electronics to provide shielding between the two sections and to also allow easy access to the receiver board.

4.2.2.3 The Clock Circuits

The primary role of the clock is to provide a time stamp when a mirror triggers. In the previous WWVB system the millisecond and second information were read via a 50 pin port at the rear of the WWVB clock when a mirror triggered (along with the 40MHz latch value). To provide a similar system, the 1PPS from the GPS receiver is used to synchronise a local 10MHz oscillator, which is then used to provide the desired clock functions. Additionally the 1PPS is used to produce a (phantom) mirror holdoff pulse to central timing so that the exact frequency of the 40MHz oscillator may be monitored. Figure 4.5 illustrates the circuit diagram of the clock section.

To produce the desired pulse trains, a 10MHz local oscillator is progressively stepped down by factors of 10 using binary-coded decimal (BCD) counters. The "10" count output of BCD counters is used to produce frequencies from 1MHz to 0.1Hz (8 decades). The 1/60Hz pulsetrain is then produced from the 0.1Hz signal using a similar step down system. The output of the counters are then placed on the pins of the 50 pin D connector at the rear of the GPS (see figure 4.2).

To ensure the BCD counters rollover synchronously and avoid any potential propagation delays, all pulsetrains lower than 1kHz (millisecond and above times) are advanced by 0.5ms. This is achieved by inverting the 1kHz pulse train sent to the subsequent BCD counters. This inverted pulsetrain is then used to force the update

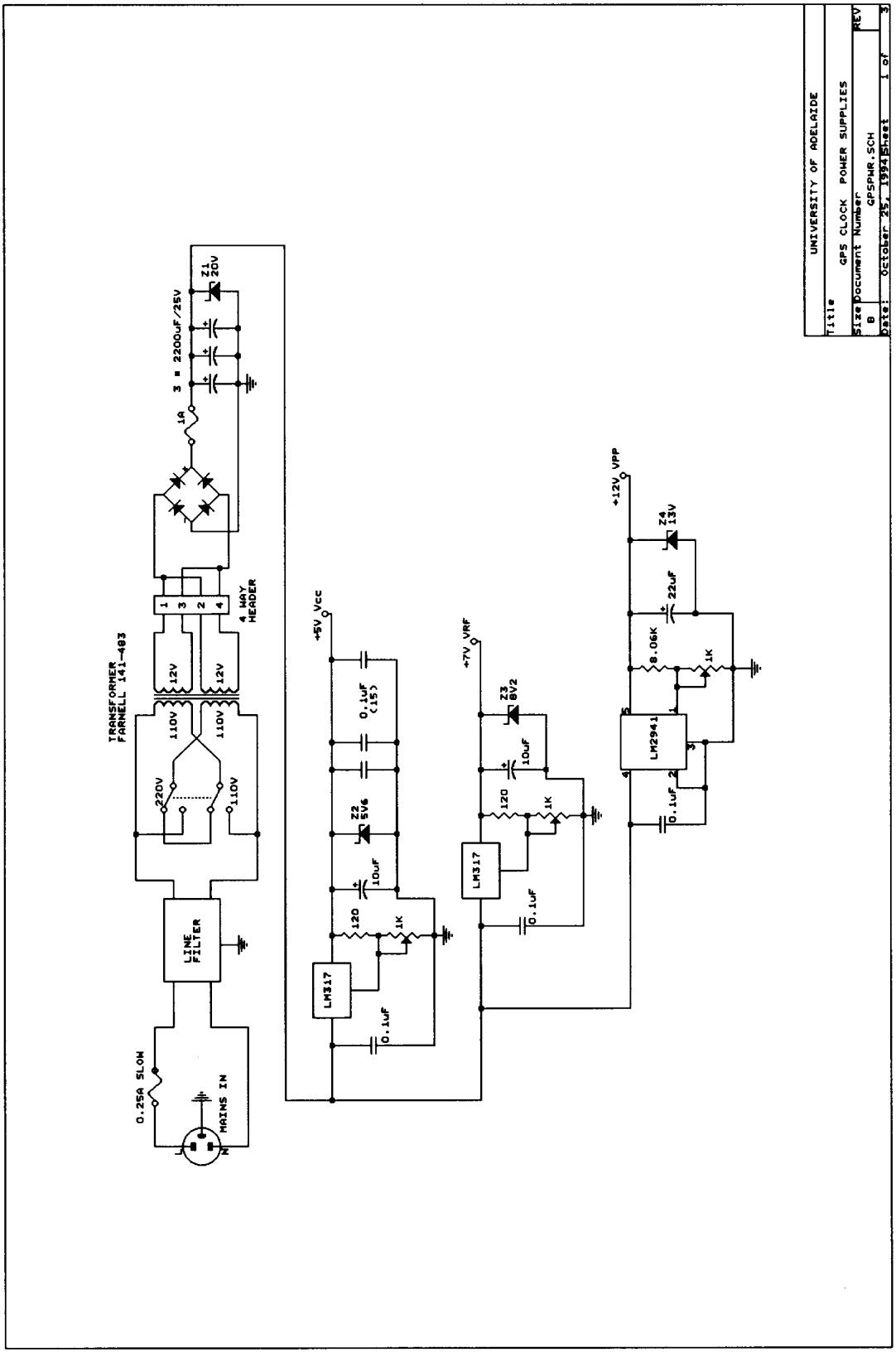

Figure 4.4: GPS Clock Power Supply Circuit.

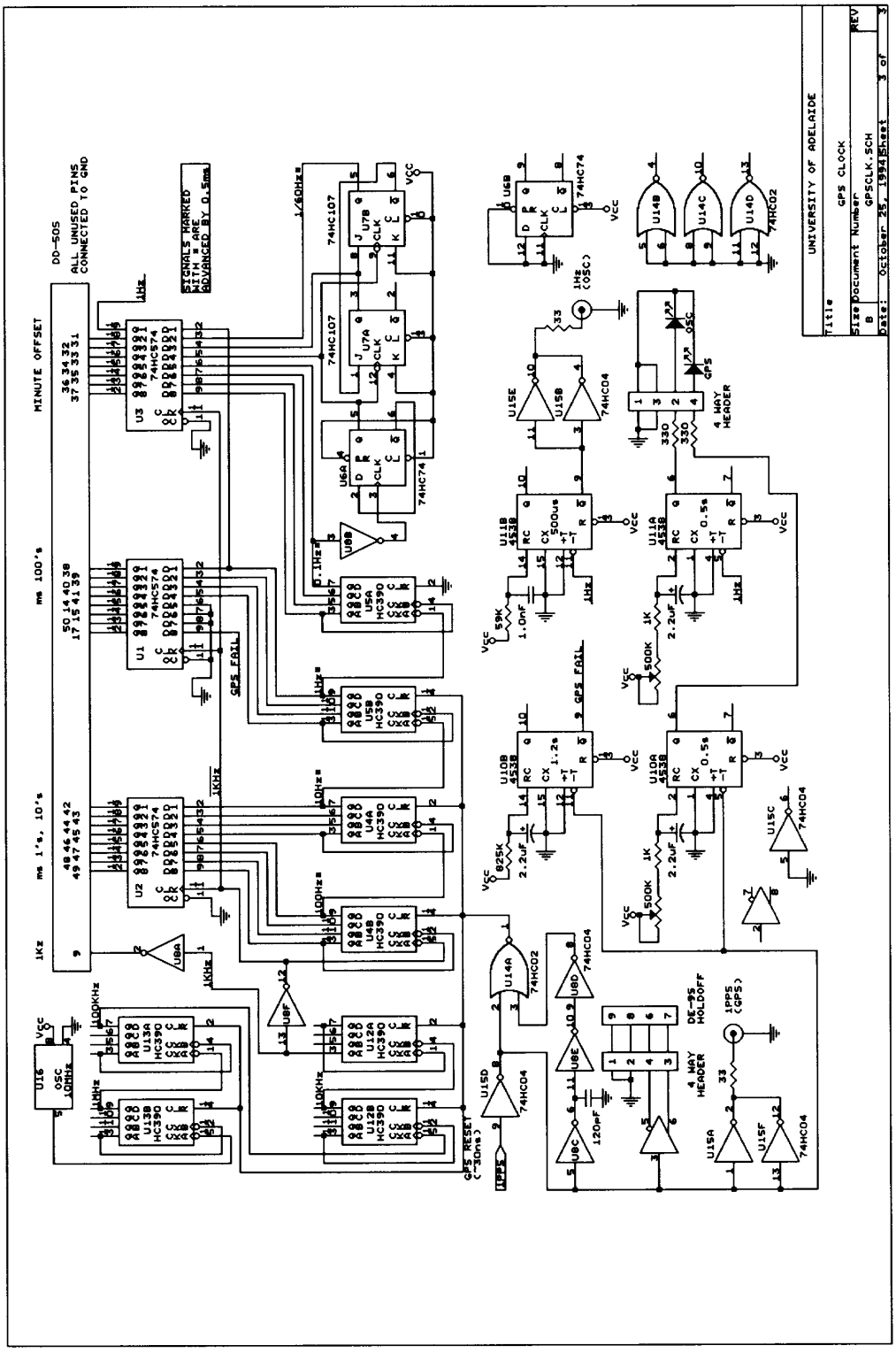

Figure 4.5: GPS Clock Circuit

of the output register at the correct time (ie when the inverted 1kHz pulse train goes low).

The BCD counters are reset every second through the use of the GPS 1PPS output. The GPS output is split, and one arm is delayed by 30ns. The two arms are used as inputs to a NOR gate which then produces a 30ns pulse used to reset the BCD counters. Thus by resetting the counters every second, the local oscillator is only required to keep accurate time for one second intervals.

As our synchronisation pulse comes every second, and we seek to provide a seconds counter and minute pulse (1/60Hz signal), these BCD counters are not reset but left free running. Thus our minute pulse will not be on the true minute but at some fixed integer second offset from the start of the minute, with the offset dependent upon the time the GPS clock unit is powered up. As each mirror unit latches event times from the GPS clock, their holdoff times recorded in event packets will be offset from the true time by this minute offset. This minute offset is not really a problem though, as the event times are only used to enable matching of mirror events with more accurate time information stored in timing packets.

The 1PPS output of the GPS receiver is split to provide various other functions besides resetting the BCD counters. It is sent through a buffer to a 9 pin connector on the rear of the GPS unit which is connected to central timing to latch the 40MHz scaler value every time the 1PPS occurs. In this way the actual frequency of the 40MHz oscillator can be measured, and thus the scaler tick length is measured so event times can be accurately determined. The 1PPS is also sent to a counter that raises the GPS FAIL signal if no pulse comes within 1.2 seconds. This is extremely unlikely to happen as the GPS is instructed to put out a pulse every second regardless of whether it is tracking satellites. In addition the GPS unit raises a warning via port 1 if it believes the pulse is inaccurate by more than some specified amount (currently set at 300ns). Thus the GPS fail line only indicates when a catastrophic problem occurs such as 20 pin port on the GPS receiver board failing.

Two BNC connectors are provided on the front panel of the clock. One is the 1PPS signal passed through some buffers, and the other is the 1Hz signal (produced by the clock) which is stretched to 500μs (the same length as the 1PPS) and buffered.

Finally the 1PPS and 1Hz pulses are stretched to 500ms and sent to two LED's on the front panel. These LED's thus provides a visual check that the system is functioning properly.

4.2.3 Installation at HiRes

The GPS clocks were installed by the author in November 1994 at both HiRes sites in the central electronics rack following laboratory testing of the system. GPS antennas were mounted on poles on top of the central observing huts and are connected to the receivers by approximately 10m of coaxial cable. The 9 pin holdoff port was connected to the mirror 0 latch position and the control software modified to recognises latches on the 40MHz scaler from this phantom mirror as the 1PPS GPS timing pulses. The 50 pin D connector was connected to the central timing board which fans out the 1KHz and 1/60Hz pulsetrains to each mirror. Serial port 1 of the GPS was connected to serial port 3 (second port from top) of the central timing CPU board, and the software modified to handle communications with the GPS receiver. Each night the HiRes control software issues initialisation commands to ensure the GPS receiver is operating in the correct mode and then listens to all output messages from the GPS. All messages except for the 830 time recovery messages are sent to the HiRes control software for incorporation into the data stream. The date and time information is extracted by the central timing software and temporarily stored until the next 1PPS, when it is copied to the variables storing the current time. Following final in-situ testing and software debugging the GPS based timing system was used for all data collection after December 1994.

4.3 Testing the GPS clocks

The implementation of a new timing system would be incomplete without thorough testing. Thus the GPS receivers and the GPS clocks were extensively tested both before and after installation at the HiRes sites.

Once the receivers were obtained testing was performed to explore the accuracy of the system and to explore the capabilities of the receivers. This testing began by

looking at the jitter of the 1PPS output by comparing it with the 1Hz output from a Rubidium oscillator. This moved onto looking at the relative time accuracy between two co-located GPS receivers. A rough estimate of the relative timing accuracy of two separated receivers was obtained by recording position data at two sites and looking at the instantaneous relative separation of the receivers. *In situ* monitoring of the timing accuracy at HiRes was performed by looking at trigger times of the separated detectors to commonly viewed atmospheric laser shots.

4.3.1 Initial tests with GPS Receivers

4.3.1.1 Familiarisation with GPS Receivers

Upon the arrival of the first GPS receiver, tests were begun to familiarize ourselves with its operation. Software accompanied the receiver so that an immediate interface with a personal computer was possible. This software enabled the user to view and reset various parameters of the receiver (such as output messages, navigation mode, which satellites to track, etc) and provided a basic interface before the testing software was written.

The antenna was later moved on top of the physics building at the University of Adelaide which ensured a field of view of 300 degrees above an elevation of 15 degrees (a nearby tall building blocked out about 60° in azimuth and up to about 60° in elevation). A rough estimate of receiver position was then obtained using the supplied software. This provided a continuous track of the estimated position on a 100m by 100m grid. The receiver was left for several hours so that a good position distribution could be obtained. Visual inspection allowed an estimation of the mean position to be made and this was then used as the initial position of the receiver until a more thorough position test could be done.

4.3.1.2 Comparison with a 1Hz Rubidium oscillator

Once an initial position was obtained the receiver was put into "known position time recovery mode". In this mode the receiver assumes it is at the user specified position and synchronises its output 1PPS (Pulse per Second) to UTC. When used in this

mode, the receivers could be instructed to use either a single satellite, or all satellites to produce the synchronised 1PPS output. The 1PPS should be within 340ns of UTC 95% of the time (due to the degrading effects of selective availability), although it may have actually been slightly worse due to errors in the estimation of the true antenna position.

A Rubidium oscillator with a 1Hz output was obtained for use as a reference oscillator. The 1Hz output from the Rubidium oscillator and the 1PPS output from the GPS were sent into a Tektronix TDS350 digital (1Gigasamples/sec) oscilloscope. This was set up to trigger off the Rubidium oscillator and measure the delay between the two pulses (the pulse width of the sum of the inverted Rubidium and GPS pulses). This delay gradually increases due to drift in the Rubidium oscillator. To prevent the Rubidium-GPS pulse delay from becoming greater than 20μs (and thus increase the absolute error in the pulse width measurement) the Rubidium was routinely resynchronised to the GPS output.

To allow automated data logging a GPIB card was inserted into the PC to allow an interface between the PC and the oscilloscope. A program to measure the Rubidium–GPS pulse delay was written both as a monitoring test, and to gain experience with the "c" programming language. This program allowed an examination of the jitter in the GPS 1PPS and also in the long term drift of the Rubidium oscillator. The program was run mostly at night (work on other programs was done during the day) throughout August and September 1994 taking one data point per minute. Results for the month of September are shown in figure 4.6.

The week of September 20-25 is of particular interest because Selective Availability (SA) was turned off due to the invasion of Haiti by the USA. This meant that the satellite signals were undegraded and thus the 1PPS output was of much greater precision and with much reduced jitter – the accuracy should be close to the military level service which has a 2σ error of 100ns. Figure 4.7 shows two 10 hour periods where SA was on and off. The GPS jitter with respect to the Rubidium oscillator for SA off is about half that of SA on. Overall the GPS appears to follow the Rubidium oscillator very well indicating that it should be a good reference for UTC time.

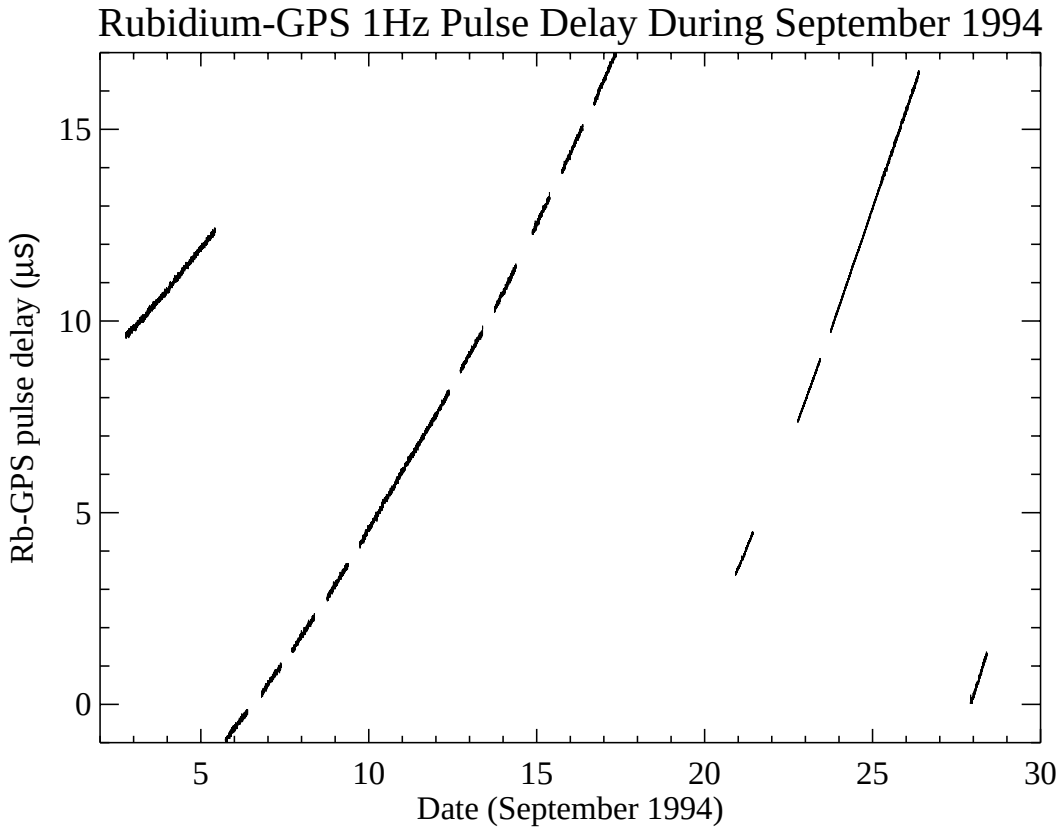

Figure 4.6: Plot of the Rubidium–GPS pulse delay over the month of September 1994. Plot illustrates the drift of the Rubidium oscillator over time. The region from the 18th–25th is of interest as selective availability was deactivated due to the US invasion of Haiti, improving the accuracy and reducing the jitter of the GPS timing pulse.

4.3.1.3 Initial Position Determination

The initial position determination in Adelaide was performed over the period 19-22 September 1994. This also happened to be the week of the US invasion of Haiti, during which SA was turned off. Thus determination of position was done under extremely favourable conditions.

The program used was designed simply to obtain a continuously improving estimate of the mean and standard deviation of latitude, longitude and altitude (the statistics assume a Gaussian position distribution, which is reasonably accurate). The GPS produces a position estimate each second and each data point was used to continuously improve mean and error position estimates. Each minute one data point was recorded so that some raw data was retained. It should be noted that occasionally the GPS

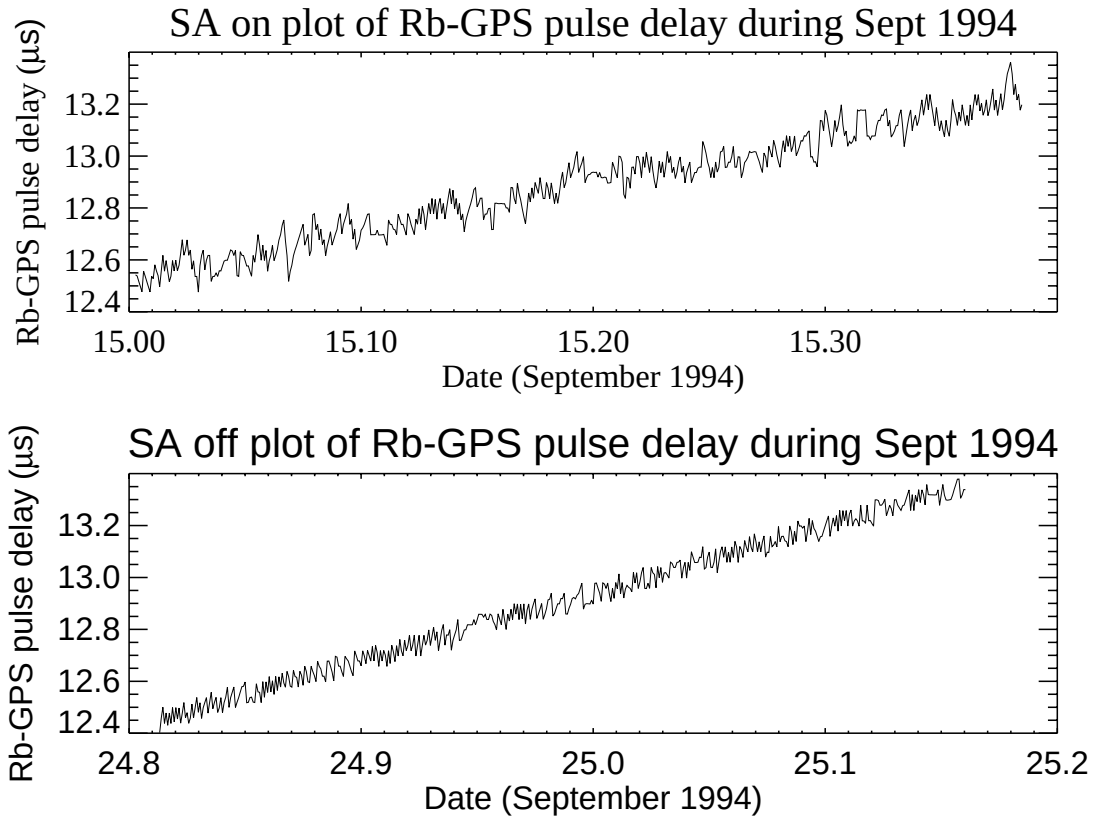

Figure 4.7: Plot of the Rubidium–GPS pulse delay comparing selective availability (SA) on with SA off data. Intervals are 10 hours long to show the fine detail of the variations present.

receiver resorted to 2D position mode (generally when there were insufficient good satellites to track) where it assumed altitude was fixed, and solved for latitude and longitude. The initial program did not distinguish between 2D and 3D mode, so there are slightly fewer altitude points than latitude and longitude. Results of position integration data taken over the period from the 18th to the 20th of September 1994 at the University of Adelaide are presented in table 4.1.

The standard deviation (σ) about the mean latitude can roughly be turned into a distance using the equation for the arc length(d) of a circle of radius R subtended by an angle θ (in radians), $d = R\theta$. Thus $d = R_e\sigma\pi/180$ where R_e is the earths radius (approximately $6.371 \times 10^6 m$ at the above latitude. The standard deviations thus correspond to approximately 5m (and $0.000001^\circ \approx 0.1m$). The SA off data in table 4.1 can be compared to data taken with SA on, presented in table 4.2, where the errors are 4-5 times larger. The mean position shifted in latitude by about 3m

Position data taken with Selective Availability (SA) off			
	Mean	1σ	N
Results after 16.75 hours			
Latitude	34.919631° S	0.000047°	60277
Longitude	138.602957° E	0.000057°	60277
Altitude	$59.1m$	$9.0m$	55582
Results after 26.5 hours			
Latitude	34.919629° S	0.000040°	95300
Longitude	138.602961° E	0.000049°	95300
Altitude	$59.7m$	$8.3m$	85998
Results after 34 hours			
Latitude	34.919633° S	0.000047°	122863
Longitude	138.602946° E	0.000051°	122863
Altitude	$58.7m$	$8.3m$	113362

Table 4.1: Progressive position integration results taken when SA was temporarily switched off. Note how the mean remains relatively stable as the amount of data increases.

whilst the standard deviation increased from 5m to 23m. Note that this 3m variation is larger than that estimated using the standard error in the mean ($\sigma/\sqrt{N}$). However long integration tests do seem to indicate that good positions can be obtained even when SA is on (to within a metre or two of the true position).

Position data taken with Selective Availability (SA) on			
University of Adelaide, 7th October 1994			
	Mean	σ	N
Latitude	34.919603° S	0.000205°	83626
Longitude	138.602945° E	0.000197°	83626
Altitude	$58.0m$	$37m$	76306
Author's Residence 1st–3rd October 1994			
Latitude	34.998624° S	0.000183°	204625
Longitude	138.517405° E	0.000188°	204625
Altitude	$11.4m$	$37m$	204625

Table 4.2: Position integration results at two locations with SA on. Note the larger errors when SA is on compared to when SA is off (table 4.1)

4.3.2 Preinstallation Tests

Once a reasonable interface capability between the GPS, Oscilloscope and PC had been developed, more serious testing began. The broad aim of the testing was to check that the GPS receivers were working as expected and that the they would act as good time references. This was achieved by first checking a receiver in single satellite mode against the Rubidium oscillator. Then two co-located receivers were compared. The comparisons were done with the receivers in single satellite and in "all" satellite mode so that an estimation of how they would perform when separated could be obtained.

4.3.2.1 Single Satellite Mode vs Rubidium Oscillator

The GPS receiver was tested in single satellite mode taking into account the corrections the GPS issued to account for drift in its own local oscillator. The program was designed so that every two hours the highest satellite in the sky would be chosen as the time recovery satellite. However a programming bug meant that the receiver was instructed to change satellites more frequently than this. Despite this bug the results are interesting as they illustrate that selective availability is the dominant error source in timing results, and show the magnitude of its effects. Typical results are presented in figures 4.8 and 4.9.

Figure 4.8 shows a plot of the corrected GPS 1PPS – Rubidium pulse delays over Sept 30^{th} 1994. It shows the deviation of the GPS about the drift of the Rubidium oscillator after applying the correction term estimated by the GPS receiver (issued after each pulse to correct for the effects of the GPS receivers local oscillator – see section 4.2.2.1). Most interestingly, it shows the case of a satellite with SA off in which the signal is very stable. A linear fit for the drift rate of the Rubidium was performed (the assumption of linearity appears to be approximately true over periods of a day based on figure 4.6), and this drift rate subtracted to obtain the residual spread in the GPS 1PPS. Figure 4.9 presents the GPS residuals as a function of time and a histogram of the residuals using a 1ns bin width.

The most interesting results are those obtained when the receiver was tracking a satellite with selective availability disabled. In these cases the variation from the

mean drift rate (determined from the full data set) is $\sim \pm 15$ns. When this is compared against satellites with selective availability imposed, their variations are larger by a factor of approximately 10. Overall through the timing distribution is quite good. If one subtracts off the peak due to the satellite with SA off, the FWHM is 182ns, and 95% of the data is within ± 170ns of the mean. Given that the peak due to the satellite with SA off is 10ns from the mean, we can have confidence that drift correction applied is reasonable. Thus it appears that the GPS receiver was performing well within timing specifications (1PPS within ± 340ns of UTC, 95% of the time, and ± 100ns for the satellite with SA off).

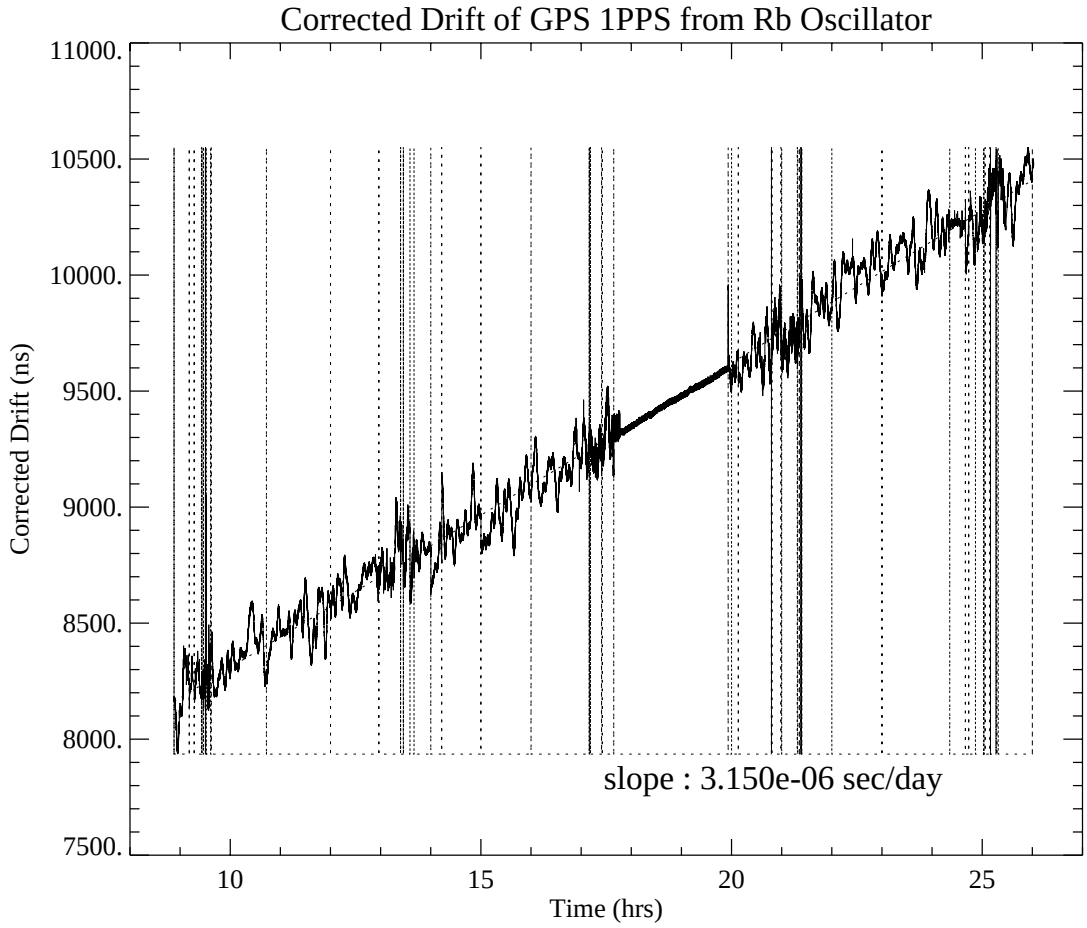

Figure 4.8: Plot of the corrected GPS–Rubidium pulse delay whilst GPS was operating in single satellite mode with average drift rate plotted. Vertical lines indicate when time recovery satellite was changed. Variations are essentially due to SA. Note region of low variation corresponding to the tracking of a satellite for which SA had been deactivated. Data taken on Sept 30th 1994.

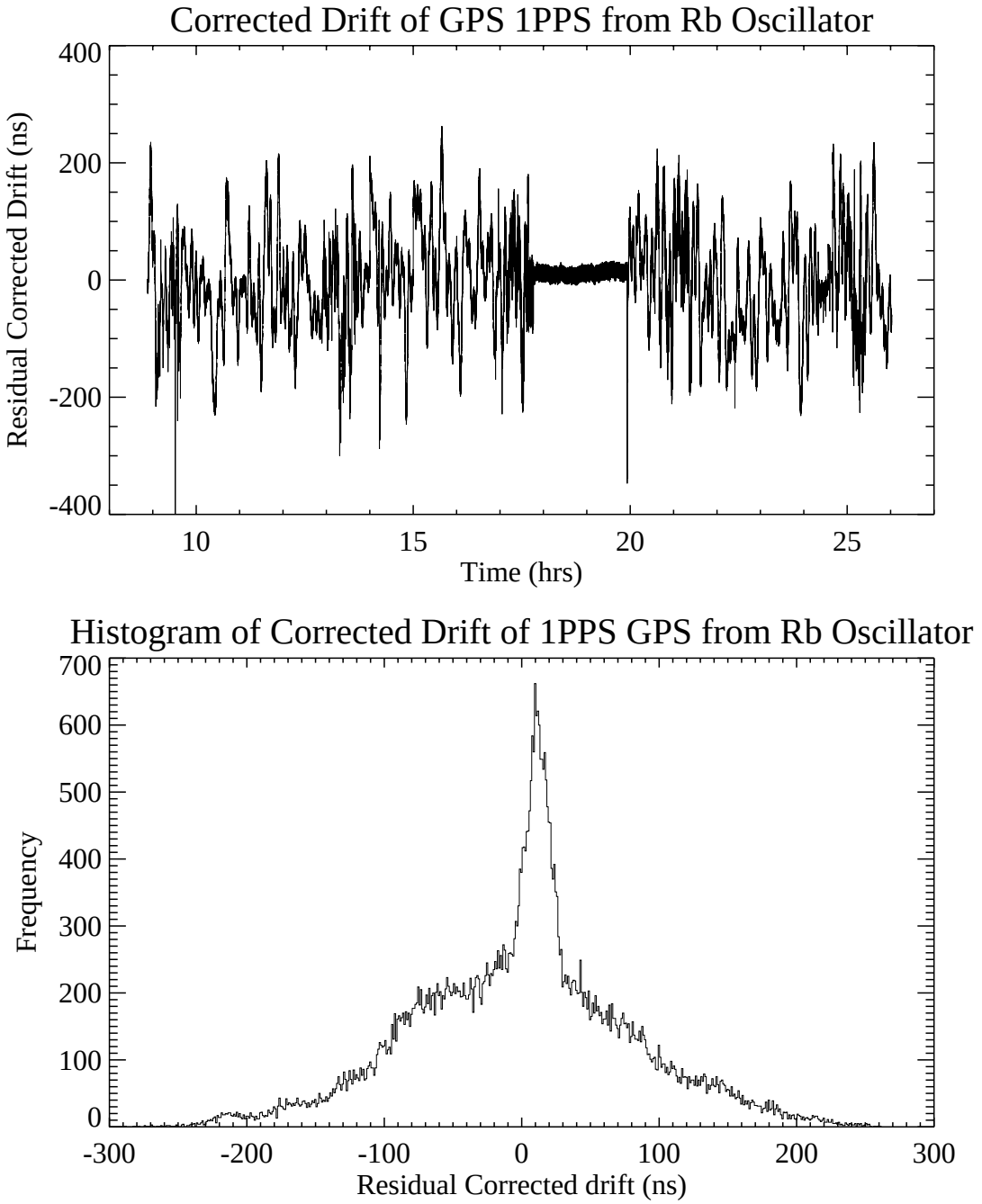

Figure 4.9: Plot of the residual corrected GPS–Rubidium pulse delay after the average drift rate of the Rubidium oscillator was subtracted. A histogram of this data has also been plotted (1ns bin size).

4.3.2.2 Co-located Receiver timing comparisons

The next set of tests were to compare the timing distributions between two co-located (adjacent) receivers. This work was initiated at the University of Adelaide and followed

up at the University of Utah. The initial testing was conducted with the receivers operating in single satellite mode but was extended to investigate the use of "all" satellite mode.

Testing at the University of Adelaide was performed using a 1GHz digital oscilloscope to measure the time delay between the two 1PPS from the two co-located receivers. Antennas were placed side by side on the roof of the physics department so as to give approximately identical fields of view. The antenna positions used in calculations by the two GPS receivers were identical. Cable lengths were identical to within 2m. A GPIB board was used to interface a PC with the oscilloscope and communication with the two GPS receivers was via both PC serial ports. Later, when problems were encountered, another PC was used to control and log data from the second GPS. These problems were eventually tracked down to a buffering problem with the communications port, complicated with occasional GPIB problems. The testing setup at the University of Utah was slightly different. The Oscilloscope was replaced with the 40MHz scaler system used in the HiRes detector. The 1PPS from each GPS were used to latch the 40MHz scaler, and the difference between the two latch values was multiplied by 25ns (approximate scaler tick length) and recorded. Relative antenna positions, and cable lengths were similar to those used at the University of Adelaide. Antenna positions were obtained from integrating the position for 16 hours and were probably accurate to approximately a metre. The Utah setup proved to be more reliable and thus results taken with this setup are presented below.

The receivers were operated in two different time recovery modes so that the modes could be compared. The first mode was the single satellite time recovery mode, in which up to six satellites are tracked but only one satellite is used to extract timing information. The second or "all" satellite mode averaged the timing solutions of all satellites being tracked. If both receivers track the same satellites then the results should be identical to those in single satellite mode. Receivers were instructed to track the satellites with the 6 highest elevations. The time recovery satellite used in the single satellite mode was chosen by using the satellite with the highest elevation at the start of each hour. If two satellites were within 1° of elevation the satellite with the largest azimuth was used. Histograms of the timing differences are plotted

in figure 4.10 and table 4.3 summarises the results.

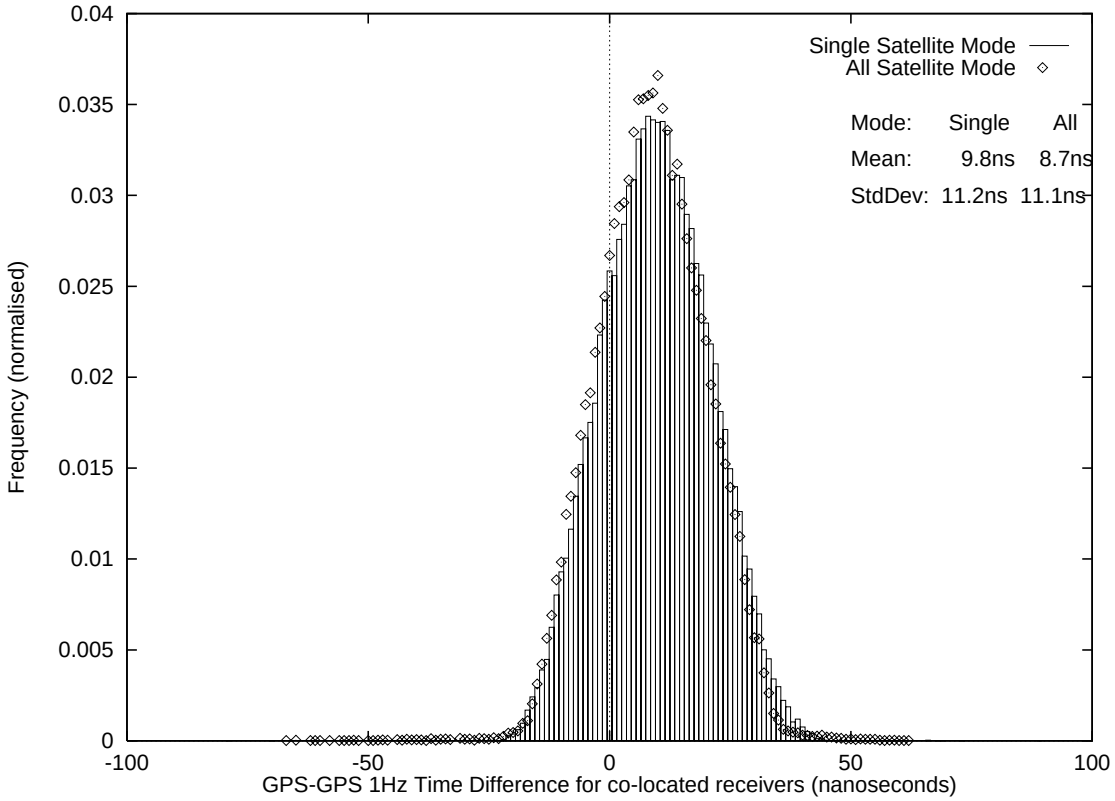

Figure 4.10: Relative time differences for 1PPS timing output (1 Hz) from two co-located GPS receivers operating in single and "all" satellite time recovery modes. Frequencies for each distribution were normalised to the number of data points. A significant contributor to the width of the distribution in all cases is the granularity of the 40MHz oscillator used to make the measurements.

The results for "all" satellite mode and single satellite mode are both encouraging and interesting due to their similarity. When one takes into account the coarseness of the 40MHz oscillator (25ns ticks), the distributions appear essentially identical with means of 10ns and standard deviations of 11ns. The only differences come when we examine the tails on the distributions. In single satellite mode, only 0.02% of data points lay outside $\pm$50ns of zero difference. Investigation showed that all such points occurred within 15 seconds of a satellite change. Such behaviour was seen previously in comparisons with the Rubidium oscillator and previous single satellite tests (performed at the University of Adelaide). This behaviour was also seen by Pryke and Lloyd-Evans[141] who used the same receiver model in a similar application. They advised ignoring the first minute after a change of satellite if relative timing accuracy of better

than 25ns is required. It is thought this behaviour arises due to the different receivers switching at slightly different times combined with errors in initially determining the clock bias between receivers and the new satellites.

In "all" satellite mode, a total of 0.08% data points lay ±50ns from zero. These points are probably due to the receivers tracking different satellites which would start to degrade the relative timing accuracy. To check the extent of this degradation, another test was performed in which the receivers were again operated in "all" satellite mode. However for this test, one receiver was forbidden from tracking two satellites so that the two receivers could only track (at most) 4 common satellites. This was essentially a test of the worst case scenario of receivers tracking different satellites. In our application at Dugway, this would be expected to happened only rarely since the HiRes sites are relatively close, and receivers are instructed to track the 6 satellites with the largest elevations. Figure 4.11 shows the variation as a function of time and figure 4.12 compares the results from this test with those from normal "all" satellite mode. Results are also summarised in table 4.3. The time series plot shows SA-like variations rather like those in figure 4.8, although in this case the amplitudes are much smaller.

The distribution from this test was broader although this was still relatively small (23ns). However a greater proportion of the events (6%) had differences greater than ±50ns from zero. Only one point had a difference of greater than 100ns and given that this was the first data point (see figure 4.11) taken it appears to be a startup glitch. Thus the results of this test seem to indicate that even in the case where there are only 4 common satellites the relative timing accuracy is still very good.

Satellite Mode	Min	Max	Mean (ns)	σ (ns)	N
Single	-79	100	9.76	11.22	56710
"All"	-67	62	8.67	11.09	58516
4 common	-66	126	16.28	23.35	7377

Table 4.3: Relative Time differences for 1PPS timing output from two co-located GPS receivers operating in different time recovery modes. A significant contributor to standard deviation (σ) in all cases is the granularity of the 40MHz oscillator used to make the measurements.

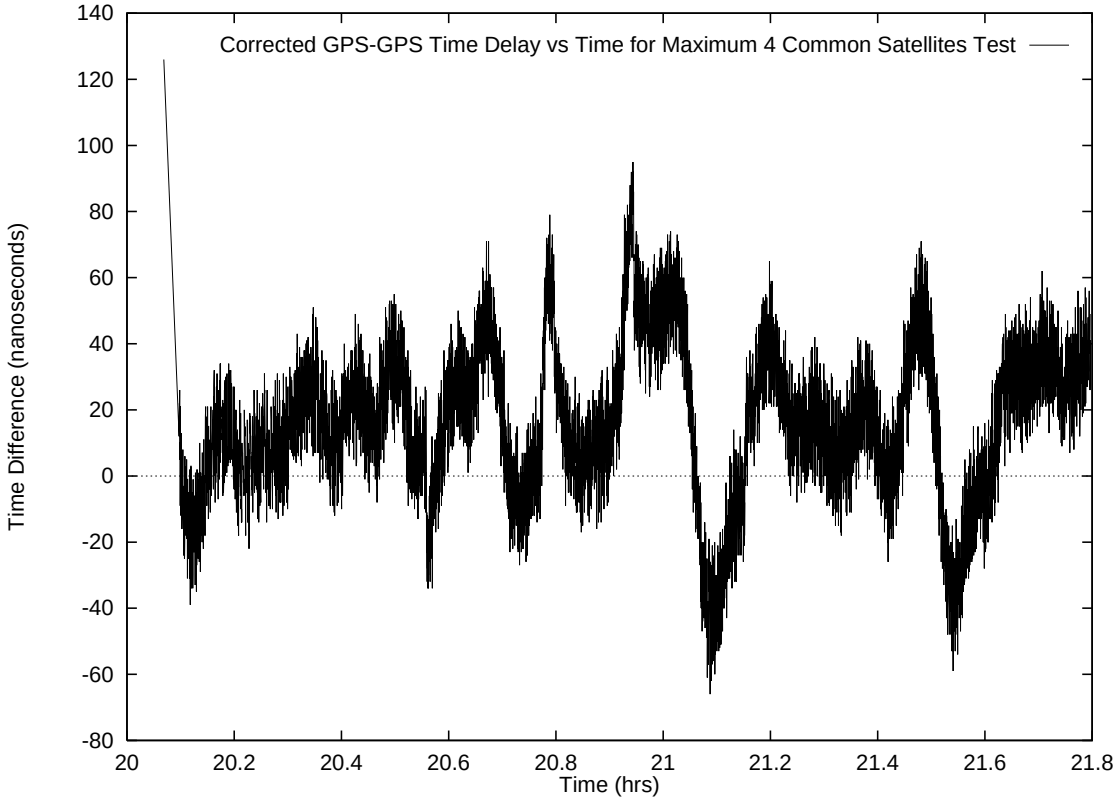

Figure 4.11: Relative time differences for 1PPS output from two co-located GPS receivers operating in "all" satellite time recovery mode but limited to no more than 4 (of 6) satellites in common. The variation is similar to that seen in figure 4.8 and thus is probably due to selective availability effects.

On the basis of these results it was decided to operate the GPS receivers in "all" satellite mode rather than the single satellite mode as used by Pryke and Lloyd-Evans[141]. This mode was chosen as it is considered more robust than single satellite mode with an identical distribution. It requires less intervention (we do not have to plan the satellites to use in advance) and importantly we also avoid the risk of losing all timing if tracking of the time recovery satellite is lost. Given that satellites are sometimes lost (due to effects such as obstruction by buildings, low signal to noise ratios or other reasons) this does represent a small but serious risk. We also reduce the deviations that occur when the receivers change satellites (these are of the order of 100ns or more in single satellite mode). The risk with "all" satellite mode is that receivers may use different satellites (the satellites being used are logged every five minutes, so to some extent we can monitor this potential problem). However given the relative closeness of HiRes sites (12.6km), this is thought to be fairly unlikely, and

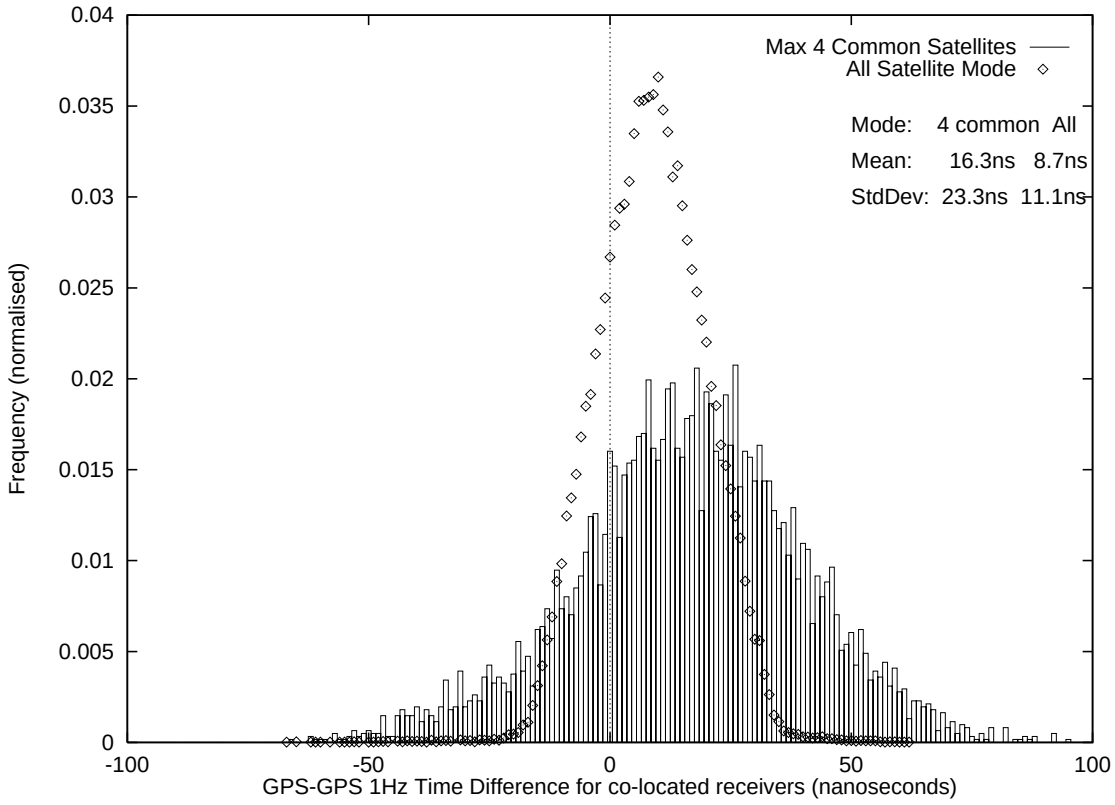

Figure 4.12: Relative time differences for 1PPS output from two co-located GPS receivers operating in "all" satellite time recovery modes. The plot compares "all" satellite mode from figure 4.10 with the distribution when receivers could track at most 4 common satellites. Frequencies for each distribution were normalised to the number of data points. A significant contributor to the width of the distribution in all cases is the granularity of the 40MHz oscillator used to make the measurements.

thus the overall benefits of "all" satellite mode are considered to outweigh the small risk that they may track different satellites.

4.3.3 Installation Tests

4.3.3.1 Simultaneous Position Integration Tests

To obtain a high degree of relative timing accuracy, the antenna locations must be well known. As the receivers being used are not differential models, the instantaneous position accuracy is only about 100m, and several days worth of data is required to obtain positional accuracies to the level of 1 metre. It was also realised that if two receivers are relatively close ($\sim$ 10km), the same satellites should be visible to both receivers at approximately similar elevations and zeniths. Thus identical satellites are

likely to be used in solving position solutions (they should have the same selection algorithm when multiple satellites may be used) and thus the instantaneous positions of the two receivers should move synchronously (which also implies that the timing solutions should as well). Three position integration tests were performed, one in Adelaide and two at the HiRes sites at Dugway. Results from the 10 hour integration test and 30 hour integration tests at Dugway are presented in table 4.4. These results backup the initial behaviour observed in the test conducted in Adelaide. The data was analysed by converting the geodectic coordinates (latitude, longitude and height) to geocentric (XYZ) coordinates (see appendix A). This allowed the individual X, Y and Z distributions to be determined as well as a distribution of the relative separation. The mean X,Y and Z coordinates were then converted back to give mean geocentric coordinates. Figure 4.13 illustrates the measured X, Y and Z distributions for the 30 hour position integration test performed.

Information on the satellites being tracked, along with their azimuth, elevation and signal to noise was recorded every minute. On average, satellites were tracked for a period of 5 hours and the elevations and azimuths of the satellites with respect to each site were identical to within 1-2°. Six *identical* satellites were tracked by both receivers over 90% of the time and satellite tracking statistics are presented in Table 4.5. Satellite drop outs were generally temporary - with satellites missing for only one data point. Thus in all cases where one site was tracking more satellites than the other site, it was because the other site had either temporarily lost tracking, or not yet acquired the new satellite. Thus 99.9% of the time the receivers are tracking at least 5 if not 6 common satellites.

The mean positions of both sites between the 10 hour test and the 30 hour test moved by 13m, presumably due to the effects of selective availability. The effects of SA are likely to be worse on the 10 hour integration test, as each satellite was visible for ~ 5 hours, so the number of *different* satellites used to estimate the position is not as large as that used in the longer test. Thus it is probable that the position determined in the longer integration test is more accurate but probably not by a large amount. If we examine the distributions in figure 4.13, we can estimate the uncertainty in the means as about 5 metres in X and 10 metres in the Y and Z. Thus the overall absolute

10 Hour Integration Test (26th November, 1994)			
	Mean	1σ	N
X Site 1	-1893868.9 m	10.5 m	33612
Y Site 1	-4497479.7 m	17.6 m	33612
Z Site 1	4095589.1 m	25.9 m	33612
X Site 2	-1905283.1 m	22.5 m	33612
Y Site 2	-4497529.4 m	27.4 m	33612
Z Site 2	4090205.7 m	25.9 m	33612
Site Separation	12620.0 m	11.6 m	33612
	Min	Max	FWHM
Site Separation	12551.1 m	12669.2 m	4 m
	Latitude	Longitude	Altitude (msl)
HiRes 1	40.195162° N	112.835745° W	1591.2 m
HiRes 2	40.132066° N	112.958916° W	1547.9 m

30 Hour Integration Test (January 19th, 1995)			
	Mean	1σ	N
X Site 1	-1893869.4 m	20.4 m	105279
Y Site 1	-4497469.1 m	30.8 m	105279
Z Site 1	4095582.2 m	28.0 m	105279
X Site 2	-1905283.5 m	20.6 m	105279
Y Site 2	-4497518.6 m	31.6 m	105279
Z Site 2	4090198.1 m	28.4 m	105279
Site Separation	12620.3 m	2.4 m	105279
	Min	Max	FWHM
Site Separation	12610.5 m	12640.4 m	3
	Latitude	Longitude	Altitude (msl)
HiRes1	40.195171° N	-112.835799° W	1596.8m
HiRes2	40.132070° N	-112.958970° W	1553.0m

Table 4.4: Relative positions statistics from 10 hour and 30 hour position integration test with a receiver at each HiRes site. Altitudes are specified with respect to mean sea level (msl) (note that msl altitude differs slightly from the geodectic height). Note that the mean position of both sites changed by $\sim$ 13m between the two tests.

uncertainty in the mean position of each HiRes site is about 15m.

It is also worth considering the distribution in the instantaneous relative separation of the two sites. The distribution of the instantaneous relative separation for the 30 hour integration test is presented in figure 4.14 and table 4.4 lists statistics for the 10 hour and 30 hour test. The mean instantaneous site separation was 12620m in both tests and full width at half maxima (FWHM) was 4m and 3m for the two tests.

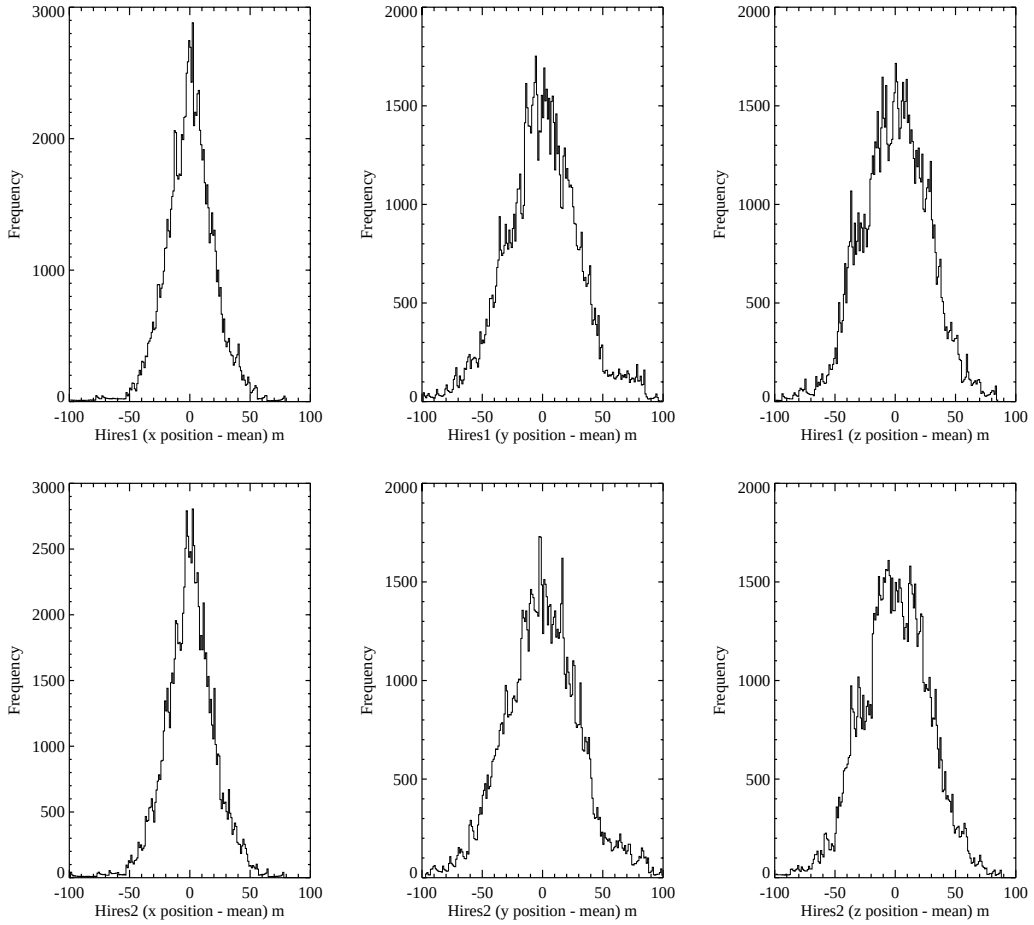

Figure 4.13: Histograms of X,Y and Z geodectic coordinates for both HiRes Sites for data taken on January 19th, 1995.

Thus the instantaneous separation is well measured – as would be expected since the receivers are using the same satellites to determine their position the majority of the time. The spread of the distribution is presumably due to fewer satellites being used by one of the two sites, but is quite small with the maximum width being 30m. This is consistent with the $\sim$ 100ns total width of the timing distribution from co-located receivers using a maximum of four common satellites presented in figure 4.12.

4.3.3.2 Relative Timing Accuracy between the HiRes Sites

The quantity that we seek to measure is the relative timing accuracy between the two HiRes sites. The 12.6km site separation makes a direct measurement of this quantity difficult, so indirect methods have been used to estimate it. However a

Number of Satellites Tracked		Percent
HiRes 1	HiRes 2	of time
6	6	91.5%
5	6	3.8%
6	5	3.0%
5	5	1.6%
4	6	0.05%
4	5	0.05%

Table 4.5: Number of satellites tracked by both HiRes sites during 30 hour position integration test performed on January 19th, 1995. Satellite information was logged each minute, and in the cases where fewer satellites were used at a given site, all the satellites tracked where also tracked by the other site.

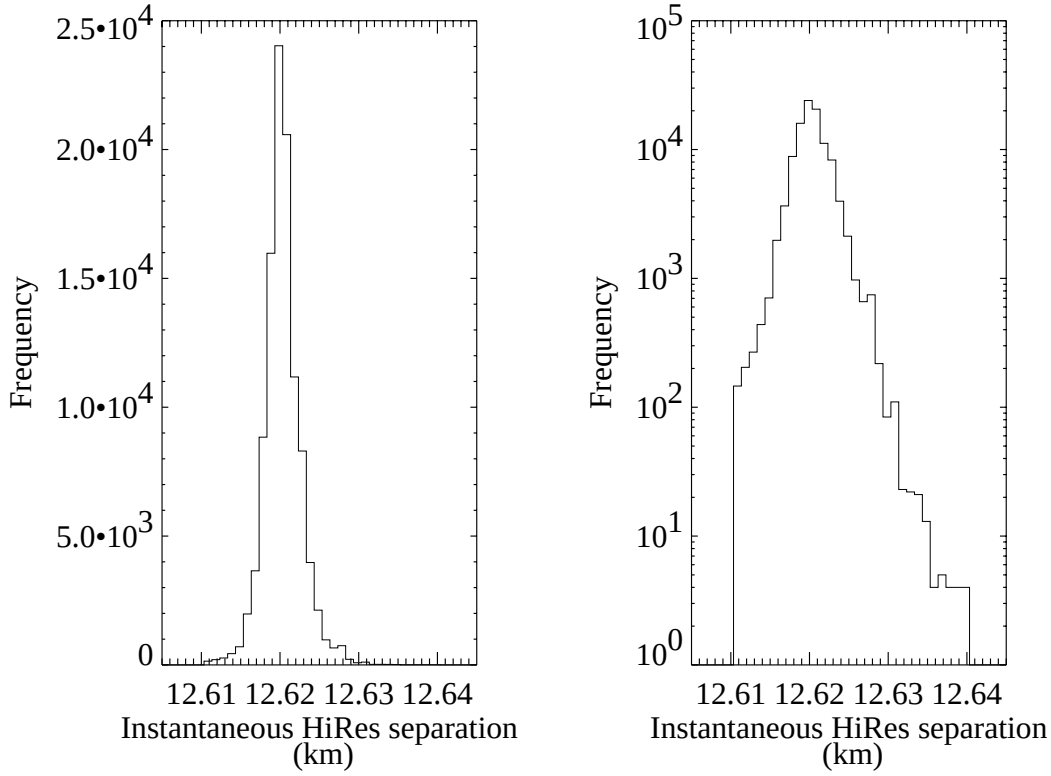

Figure 4.14: HiRes instantaneous relative separation. Both plots are of the data from the 30 hour integration test, with the log plot emphasising the small width of the instantaneous separation (always less than 30m)

direct measurement is not impossible, and such a relative timing test using separated receivers was performed by Pryke[142] as a follow up to earlier work by Pryke and Lloyd-Evans[141]. The two receivers (identical receiver models to those used at HiRes)

were separated by 11.2km and made use of an L-band radio phase transfer link which forms part of the Multi-Element Radio Linked Interferometry Network (MERLIN) at Jodrell Bank, UK. They obtained time difference distributions that were very similar to the distributions using co-located results, with the distribution in this case having a standard deviation of $\approx$ 7ns. This is to be expected, as the same satellites appear in the same region of sky whether receivers are co-locatd or 10km apart, and the receivers act independently, regardless of their separation. Thus it is not suprising that the results are identical when receivers are co-located and separated by $\sim$ 10km.

An added complication with separated receivers, is the effect due to errors in position (in co-located tests the receivers use the same position, so a position error is common and can be ignored). An error in position, directly translates to a systematic error in determining the receiver clock bias, and thus in the 1PPS timing pulse. Satellites are normally distributed reasonably equally over the sky, thus in "all" satellite mode where the different biases are averaged, we expect that the positional errors should be largely averaged out. In the case of the HiRes sites, the absolute position uncertainty of both sites is about 15m, whilst the relative position uncertainty *between* them is about 3m. The relative position error increases when the sites track different satellites so we do expect some broadening of the relative timing distribution similar to that seen with the co-located timing test when a maximum of 4 common satellites was used (figure 4.12).

The final effect to consider is the synchronisation error between the two 40MHz scalers used at each site to record the value of the 1PPS output. We expect a one clock tick, or $\sim$ 25ns error between the two sites due to this effect. Thus combining all these effects, the synchronisation error between the two sites is probably of the order of 1-2 clock ticks, or 25-50ns, the majority of the time. Satellite drop outs are likely to occasionally cause of the degradation of this accuracy out to at worst case of $\sim$ 100ns. Absolute timing accuracy is expected to be that due to selective availability, which is within 340ns of UTC, 95% of the time.

4.4 *In-Situ* Testing of GPS Clocks

It was desirable to perform a further check on the accuracy of the overall timing system once the GPS clocks were installed. Due to the difficulty of doing a direct timing comparison, it was decided to examine triggering times of laser shots viewed by both HiRes sites. These were performed using the steerable YAG laser system located at Fly's Eye II (approximately 3km from HiRes 1 and 16km from HiRes 2) and described in section 3.2.5.2. The usefulness of the YAG laser results from the well known (and fixed) relative position and the repeatability (both intensity and geometry) of the system.

At the time of this testing, the laser was firing a set pattern of shots at the start of each hour. This pattern consisted of stepping through 8 azimuthal directions at 4 zenith angles taking several shots at each point. For this initial analysis, a specific orientation of shots with a zenith angle of 25° and an azimuthal angle $\simeq$ 120° clockwise with respect to East were chosen. Simulations were performed to identify pairs of PMTs at HiRes 1 and HiRes 2 which observed identical sections of the track. The simulation was performed by sampling the track at 50 metre intervals and then determining the two PMTs at each site which most closely viewed this point in the sky. Due to the proximity of the shot to HiRes 1, the angular velocity and brightness of the track is much higher at HiRes 1 than that at HiRes 2. As a result of this, for each PMT at HiRes 2 there are several matching PMTs at HiRes 1 and trigger time slewing effects are likely at HiRes 2. These trigger time slewing effects arise because the time a PMT fires is affected by the amplitude and shape of the pulse. As a result, determining the exact triggering time is sometimes difficult. PMT selection was based on which PMTs were expected to be brightest at HiRes 2 and for simplicity were chosen so that all PMTs came from the same mirror at each site (mirror 6 at HiRes 1 and Mirror 4 at HiRes 2). This gave three PMT pairs for comparison (the PMTs used are given in table 4.6 in mirror-subcluster-tube numbering as per figure 3.10). Data were taken from 18 shot sets over 4 nights giving approximately 390 events for each PMT pair. Some events were excluded due to bad TDC times (noise triggers) and obviously bad mirror scaler latch values.

PMT Set	HiRes 1	HiRes 2	Mean (ns)	FWHM (ns)	N
1	06-04-07	04-13-06	39889.1	250	388
2	06-08-15	04-13-09	40196.0	250	393
3	06-16-03	04-13-13	40393.0	200	390

Table 4.6: HiRes 2 – HiRes 1 trigger delays for 3 PMT pairs (numbering system as per figure 3.10). Data taken from 18 sets of YAG laser shots over 4 nights (25th, 30th March; 3rd, 4th April 95).

Figure 4.15 and table 4.6 shows the results from combining the 18 data sets. These results combine the effects of slightly different YAG laser directions and trigger time slewing effects (it can take up to a 1μs for the signal to cross the face of a PMT at HiRes 2) which should explain the main broadening of the distribution. Figure 4.16 illustrates the extent of the variation amongst the laser shot sets. The individual laser shot sets, whilst hampered by low statistics, showed some very interesting behaviour. Distributions varied from the best case of distributions being well peaked with standard deviations of 80ns, to cases where the distribution appears bimodal (and give rise to the sidelobes in figure 4.15). Shot by shot investigation of the bimodal and outlying events showed that this behaviour occurred simultaneously in each of the three PMT pairs, so it seems likely that the problem was arising at the mirror level.

To interpret this information, it is worth while considering the stages involved in assigning a PMT trigger time:

$$\text{Mirror Holdoff Time (ns)} = (\text{Mirror Latch} - \text{GPS Latch}) * \text{Avg Freq} \quad (4.1)$$

$$\text{PMT Time} = \text{Mirror Holdoff Time} - \text{PMT TDC (ns)} \quad (4.2)$$

Thus given that the observed behaviour was common to all PMTs in a mirror, it points to a problem with latching the mirror holdoff time from the 40MHz scaler. Latching problems had previously been suspected, and are easily detected in the higher order bits as the resultant trigger times are unphysical (provided the track spans more than one mirror). Problems with the lower order bits are much more difficult to detect since they only affect the time by small amounts (smaller than the resolution of the previous WWVB based system). The results of combining the 18 shot sets implied that times were generally good, and that the GPS clocks were working as expected.

However the observed sidelobes and bimodality implied the need for a more indepth study, which is described in the next section.

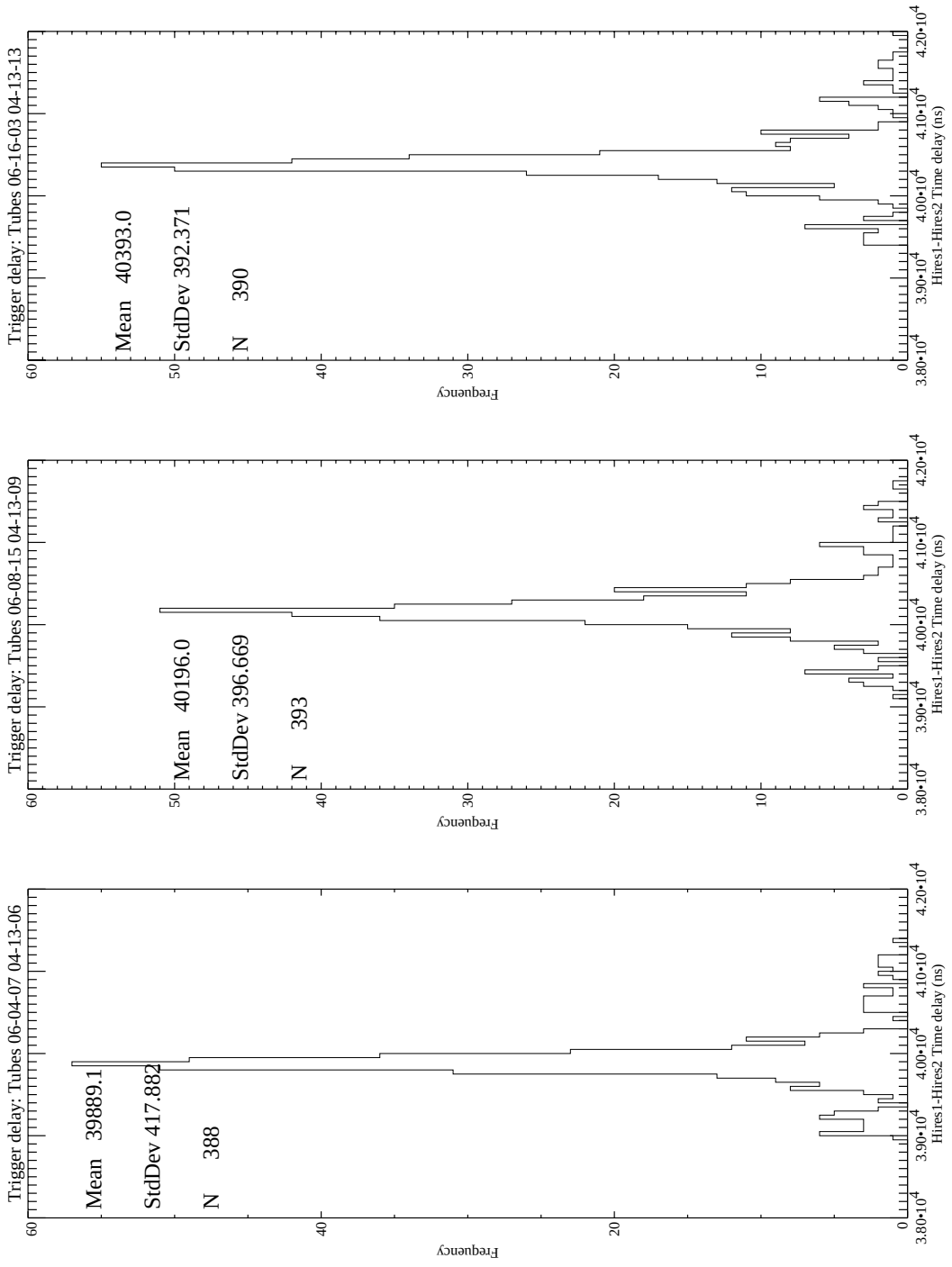

Figure 4.15: HiRes 2 – HiRes 1 time delay for a series of YAG laser shots over 4 nights. Night to night pointing direction changed by up to 1°. Sidelobes are believed to be due to problems with latching the 40MHz scaler used to determine mirror trigger time.

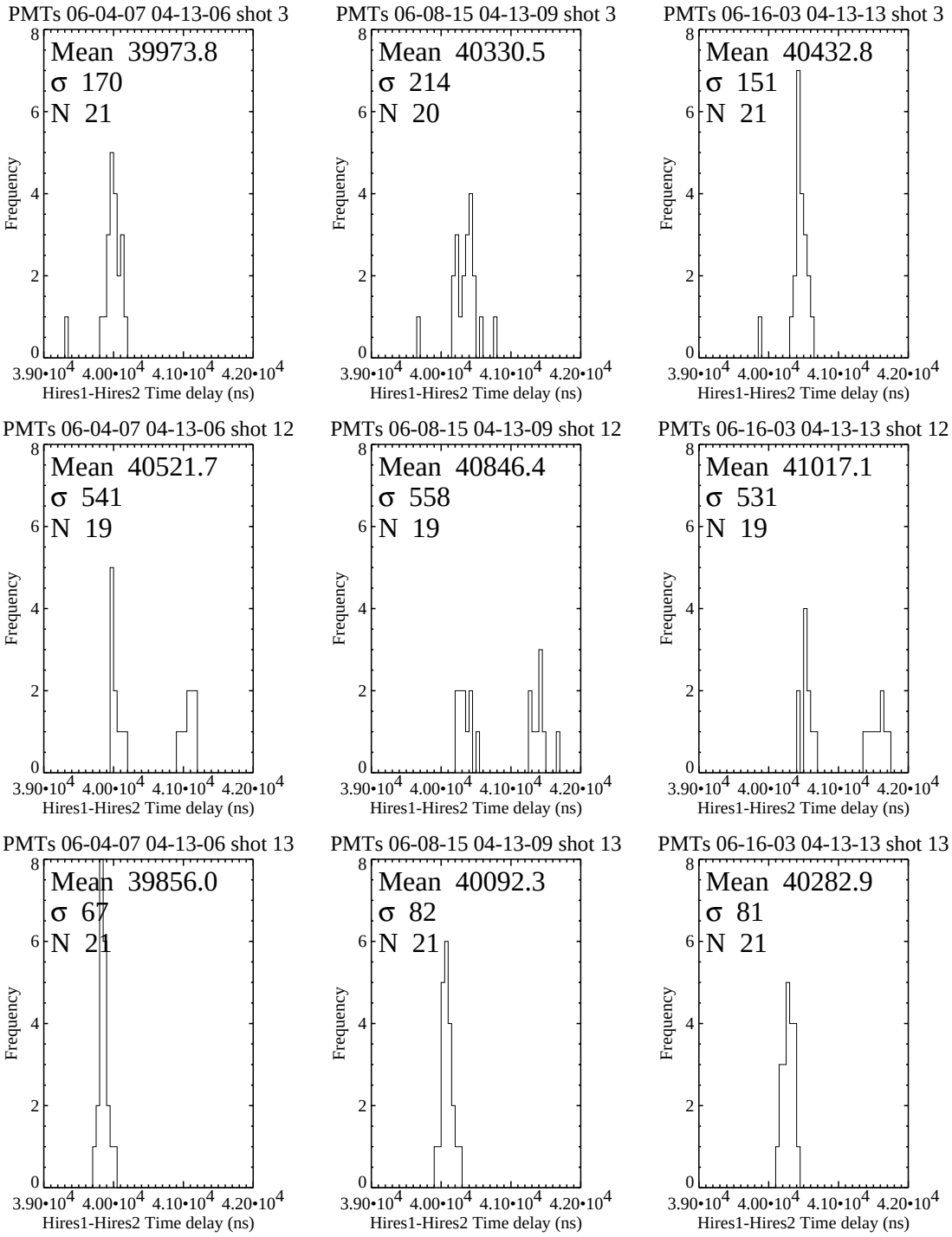

Figure 4.16: HiRes 2 – HiRes 1 time delay for 3 individual sets of YAG laser shots illustrating the range of variation between shot sets. The top set of 3 plots shows average behaviour, the middle set show worst case bimodal distributions and the lower set show best case tightly peaked distributions.

4.5 Investigating 40MHz Scaler Latch Problems

The initial investigation using nightly atmospheric YAG laser shots indicated a problem with latching the mirror holdoff time from the 40MHz scaler at central timing following a mirror event. However better statistics were needed to pin down the exact problem so a further, higher statistics test was conducted on the third of May 1995.

4.5.1 Generating the Data

To obtain data to investigate the latching problem, the YAG laser was fired at a rate of about 1Hz for 30 minutes in a fixed direction. The nominal direction of the YAG was an azimuth angle of 140° (anticlockwise with respect to east) and at a zenith angle of 15°. Events observed at HiRes 1 and HiRes 2 were then matched, using the criteria that:

- at least 3 HiRes 1 mirrors triggered,
- the Julian day event times at HiRes 1 and HiRes 2 were within 1ms.
- the earliest triggering HiRes 2 mirror fired no more than 100μs later than the earliest HiRes 1 mirror.

These criteria matched a total of 1704 events from 21745 HiRes 1 events and 54358 HiRes 2 events. The satellites used by both sites were recorded every 10 minutes (this is standard operational practise) and the six satellites tracked by the receivers were identical over the half hour period. The HiRes 1 operator noted in the nightly logfile that there were patches of rapidly moving low level cloud that passed through the field of view of the detector during some parts of the night.

4.5.2 Analysis of the matched YAG Laser Events

Following from previous work it was decided that the best way to analyse the data was by choosing pairs of PMTs and looking at the delay between the PMT triggering times. In an effort to select the events with the strongest signals (and thus reduce the

effects of time slewing or clouds) a simulation was again performed using the nominal pointing direction to determine the PMTs most directly viewing the laser track.

The track was sampled every 50 metres to determine the two PMTs most directly viewing the track, and a parallax was taken into account using the surveyed mirror positions and site locations. As a further check, a program was written to count the number of times each PMT actually fired, which was useful when the track split adjacent PMTs (as the PMT most directly viewing the track tended to trigger more often). The azimuth and zenith values of the laser were varied slightly to try and obtain the best match between the PMTs that actually fired and what the simulation predicted.

The next stage was to select PMT pairs (one PMT from each site viewing the same section of track) and look at the distribution of the HiRes 2 – HiRes 1 PMT triggering delay times. After some initial investigation a set of 56 PMT pairs were chosen. This was done by taking two PMTs from each mirror and matching them with PMTs from mirrors of the opposite site (HiRes 1 mirrors 7,6,2,3,9,14,13 and HiRes 2 mirrors 3,1). Thus each PMT from HiRes 1 was paired with 4 PMTs at HiRes 2, and each PMT from HiRes 2 was paired with 14 PMTs from HiRes 1. The selection of the two PMTs for each mirror was based on taking the most often triggered PMTs from two different subclusters.

Only events that contained all 56 PMT pairs were used in the analysis which further reduced the data set to 1389 events. For each event and PMT pair, the HiRes2 – HiRes 1 triggering time delay was determined. Figure 4.17 is a representative plot showing the triggering delays between PMT number 159 in mirror 3 at HiRes 2 and the 14 PMTs chosen at HiRes 1, as a function of event number. The delays between each pair were reasonably stable, but obvious deviations do occur. The data were binned to obtain the time delay distributions for each of the 56 pairs, and a subset of 6 pairs (all involving PMT number 159 in mirror 3 at HiRes 2), are shown in figure 4.18. For each distribution the mean value and the full width at half maximum (FWHM) were determined, with FWHM for all data varying between 250-450ns. The sidelobes seen in the preliminary investigation were again seen and it was found that for any given pair of PMTs, the delay value would be greater than 1 FWHM from the mean

($\sim 2.3\sigma$) anywhere from 10% to 30% of the time. This is definitely more than would be expected through just random errors.

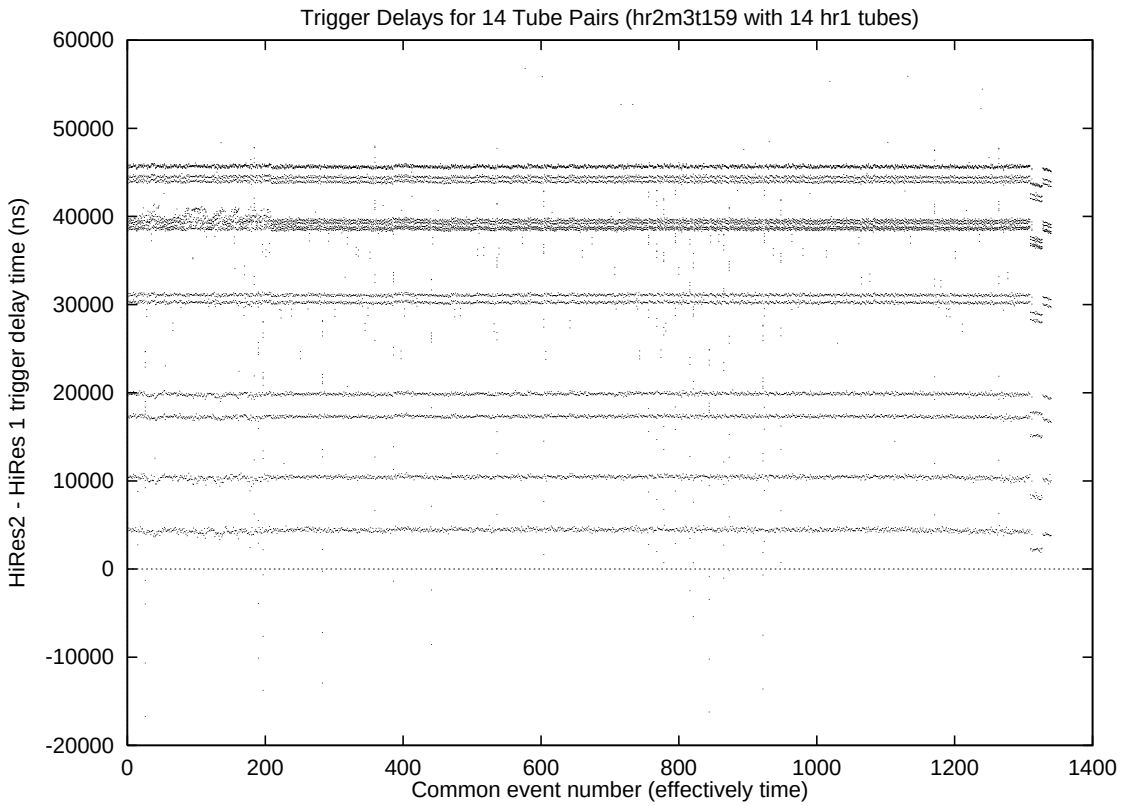

Figure 4.17: A representative plot of the HiRes 2 – HiRes 1 triggering delays. For each event the delay between HiRes 2 mirror 3 PMT 159 and two PMTs from each of the HiRes 1 mirrors (that triggered) is plotted.

An investigation into these "bad" cases was then launched. This was conducted by looking at which PMT pairs were bad in any given event where a "bad" PMT pair is defined as any pair whose time is more than 700ns from the mean. The choice of 700ns was fairly arbitrary but chosen so it was at least 3σ from the mean. These bad events were then split up into the cases where all 56 pairs were bad (implying all times at one site where bad), all occurrences where a single mirror was bad and all occurrences where a single PMT was bad (implying a noise trigger). There were also some events (52) with bad times that could not be classified in any of the above categories, most often because at least one of the pairs fell inside the 700ns window whilst other pairs did not.

Plots of the quantity "bad" delay – mean delay time for the bad events for each of the

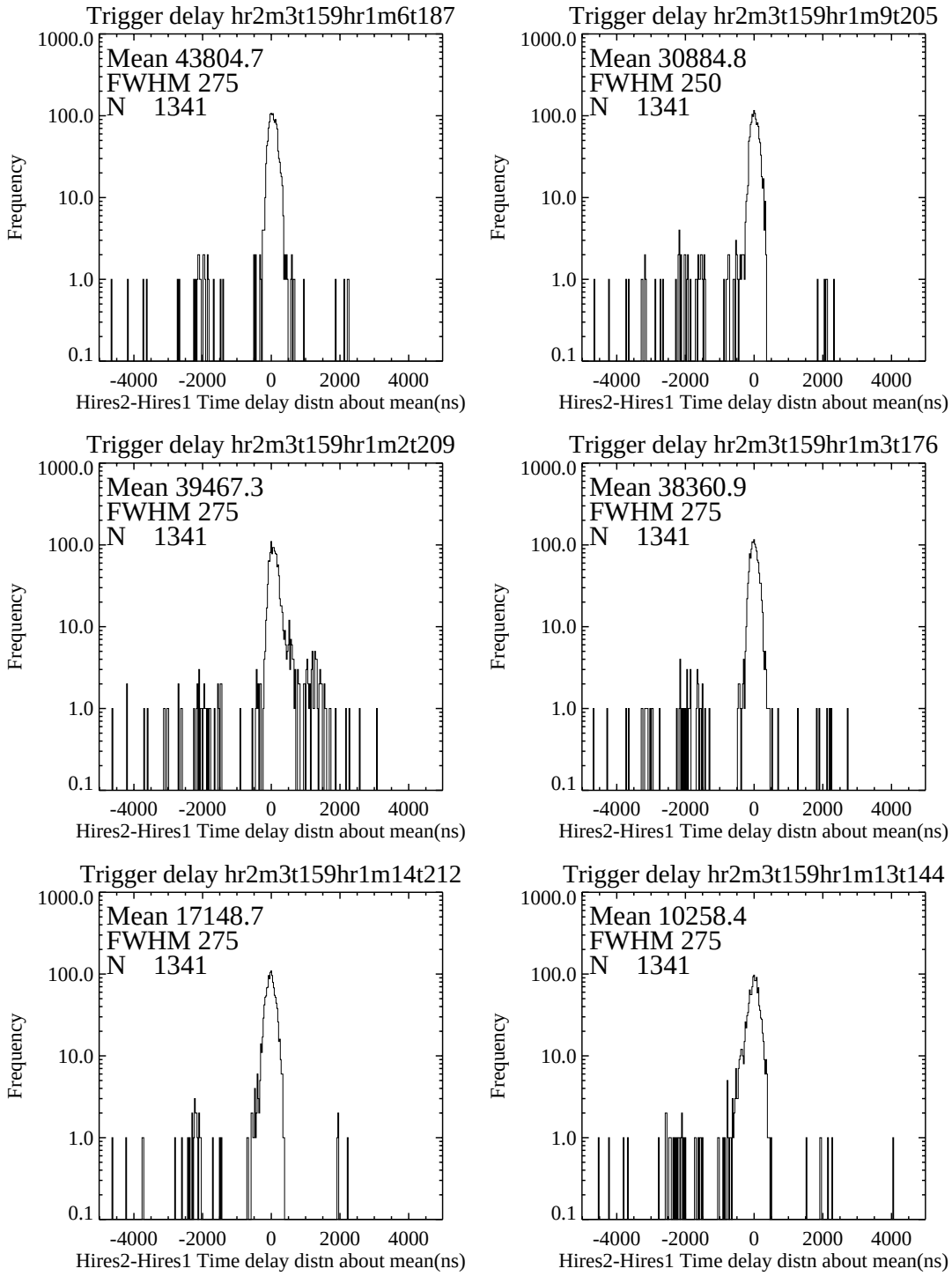

Figure 4.18: A selection of the histograms showing the distributions in PMT triggering times.

three categories were produced to examine patterns in the deviation of PMT triggering times from their mean values. Figure 4.19 shows the cases where all mirrors were bad, figure 4.20 shows the cases where only a HiRes 1 mirror was bad and figure 4.21 shows

the cases where only a HiRes 2 mirror was bad. As we were interested in looking for evidence of scaler latch problems, the PMT delay times were divided by the nominal tick length of 25ns so that the plots of deviation from the mean delay is in units of scaler clock ticks, not nanoseconds. Each data point in the plot correpsonds to one PMT pair, and a grouping of points thus represents one event. In figures 4.20 and 4.21 points were placed at $y = 0$ to designate the end of an event. Also note that due to the 700ns selection window there should be no events within about 28 ticks from the mean value of 0.

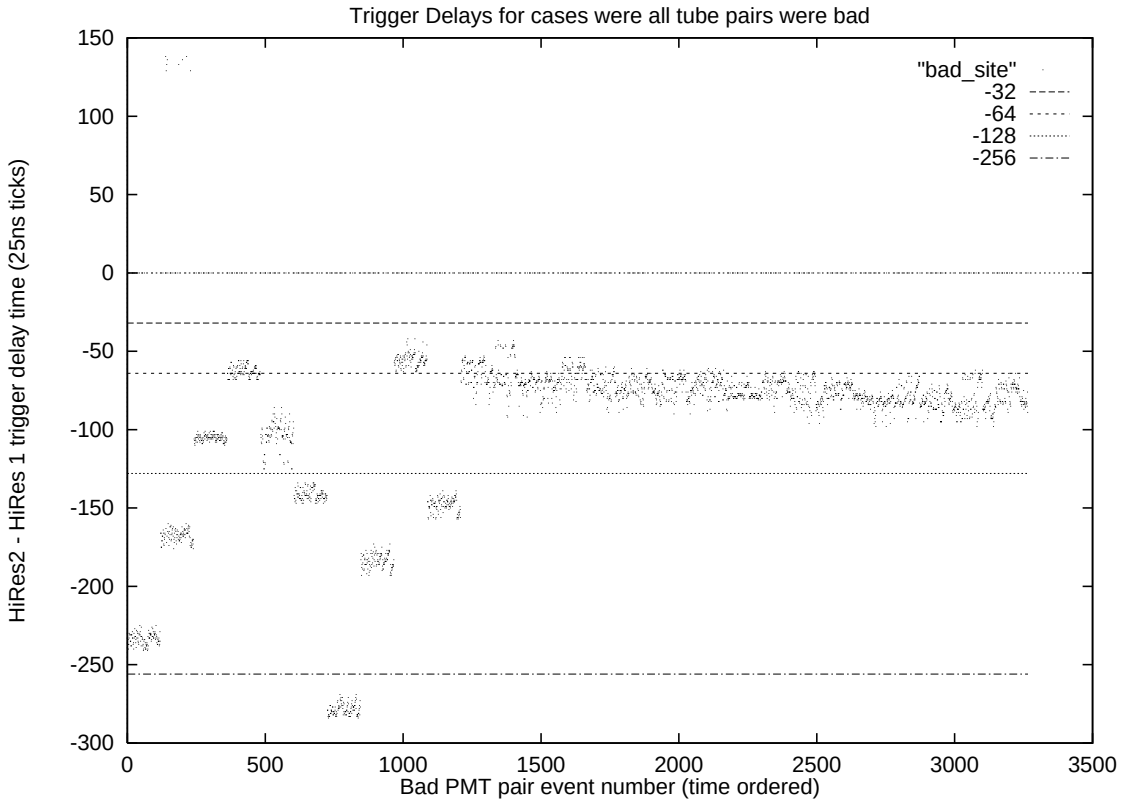

Figure 4.19: Plot of Deviation of HiRes 2 – HiRes 1 delay from mean for the case where all 56 PMT pairs were greater than 700ns from the mean (implying all times at one site where bad. Each point represents a PMT pair and 56 such points form one event. Note the y axis is in units of scaler clock ticks, and lines showing powers of two were over plotted to look for bit associated problems.

4.5.2.1 Investigation of the cause of all times "bad".

A total of 27 events in which all 56 pairs were bad were found (see figure 4.19). Since the times for all PMT pairs were bad, it points to a problem occurring with times at

the entire site. If we refer to equation 4.2, we see that this case would occur if the GPS 1PPS synchronisation pulse was incorrectly latched by central timing. Further investigation indicated that most of the observed cases occurred in a period of 20 consecutive seconds. Given that the minimum deviation was at least 64 clock ticks, or 1.6μs, it is unlikely that this was due to a GPS problem such as the use of different satellites (all indications were that the GPS receivers were functioning normally and tracking the same set of satellites).

4.5.2.2 Investigation of the cause of "bad" mirror times

The next case considered were those where all pairs using PMTs from a given mirror were considered bad. Consulting equation 4.2, we see that if the mirror holdoff time is incorrectly latched, it will affect the triggering times of all PMTs within that mirror by the same amount. Table 4.7 illustrates the number of times a mirror was classed as bad. Note that due to the presence of clouds the frequency of HiRes 1 mirrors 2 and 3 is elevated beyond the effects due to a scaler latching problem (this is discussed later).

HiRes Site	Mirror	No. times mirror bad
1	7	0
1	6	0
1	2	52
1	3	19
1	9	22
1	14	0
1	13	1
2	3	4
2	1	8

Table 4.7: Number of times all PMTs within a mirror were bad (triggering delay more than 700ns from the mean value). Mirrors are arranged in order of triggering and the total number of events examined was 1389.

We now turn our attention to figures 4.20 and 4.21. Each HiRes 1 mirror event has 8 points (2 HiRes 1 PMTs $\times$ 4 HiRes2 PMTs) and each HiRes 2 mirror event has 28 points (2 HiRes 2 PMTs $\times$ 14 HiRes 1 PMTs). The plotting order (within an event) was the first PMT from HiRes 2 mirror 3 with 2 PMTs from HiRes 1 mirrors 7, 6, 2,

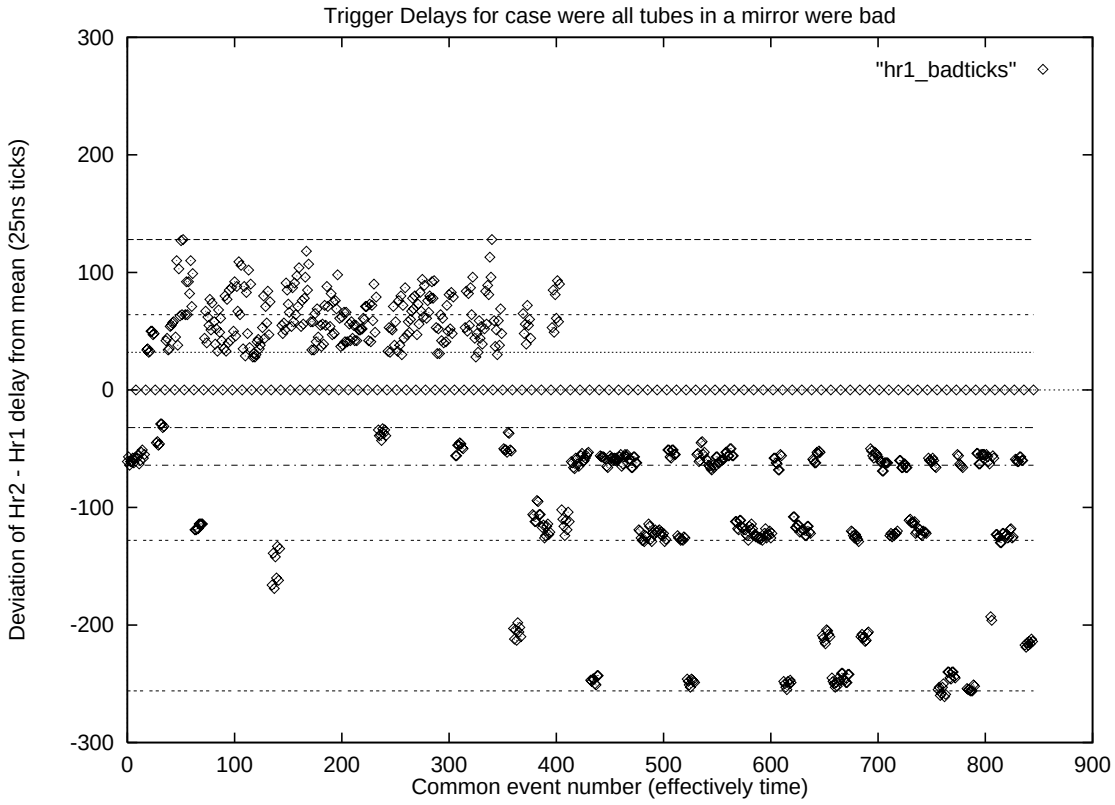

Figure 4.20: Plot of Deviation of HiRes 2 – HiRes 1 delay from mean for the case where all PMTs in a HiRes 1 mirror were greater than 700ns from the mean. Each point represents one PMT pair, with 4 consecutive points representing one YAG laser event (points at zero delimit the events). The clustering of points with positive delays are due to cloud scattering effects in mirrors 2 and 3.

3, 9, 14 and 13. This was repeated for the second PMT from HiRes 2 mirror 3 and then again for the two PMTs from HiRes 2 mirror 1.

Analysis of the plots seems to indicate the presence of a scaler latching problem. Events seem to cluster around the values of ($\pm$) 64 128 and 256 ticks. There are also events which seem to cluster around values such as 64+32+16 – although some care must be exercised in classify a cluster since the intrinsic spread is $\sim$ 10 ticks (FWHM = 250ns = 10, 25ns ticks). This is well explained if there is a latching problem so that bits are set when they should not be thus making times appear later than than they otherwise should. Additional evidence comes from examining the effect at HiRes 1 and HiRes 2. If the scaler is incorrectly latched for a HiRes 1 mirror, the quantity HiRes 2 – HiRes 1 will be more negative than usual, which neatly explains the predominantly negative bias seen in bad HiRes 1 mirrors in figure 4.20.

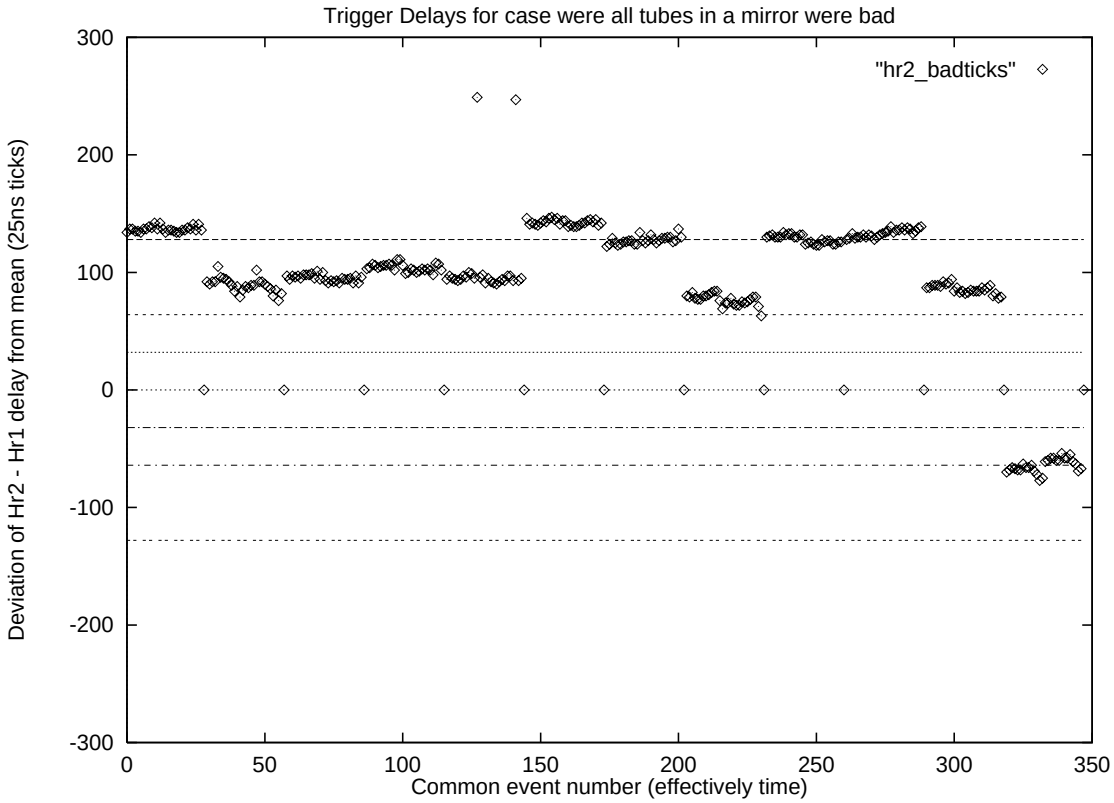

Figure 4.21: Plot of Deviation of HiRes 2 – HiRes 1 delay from mean for the case where all PMTs in a HiRes 2 mirror were greater than 700ns from the mean. Each point represents one PMT pair, and points at zero delimit events.

A similar argument is applicable for HiRes 2 mirrors where the bad delays should be predominately positive, as is observed in figure 4.21. We can also apply this hypothesis to the previous case where all PMTs were bad. By equation 4.2 a bad latch of the GPS 1PPS would mean that all times at one site would be bad for the *next* second, which is quite a serious problem. This does seem a likely explanation because from figure 4.19 we see that all the events (bar a few PMTs) have negative deviations. This would be the case if the problem was located at one site, namely HiRes 1.

A possible explanation of how this latching problem is occurring is that the scaler is being read whilst it it in the process of rolling over. In this case, the latch value read will be larger than it should, as the new highest order bit would be set high but as the change has not propogated down, some lower order bits will be still be high as well. Lower order bit problems are likely to be more frequent since they are set more often, but are also the hardest to detect. The lowest order bits may not be noticed if

it only shifts the time by a few clock ticks. This may also explain some of the width of the timing distributions (see figure 4.18).

Finally the problems with mirror 2 seem to be mostly due to clouds. All the positive delay times in figure 4.20 were from mirror 2 within the first 6 minutes of the data file. Examination of the triggering patters of PMTs at HiRes 1 indicated "mushrooming" of the YAG laser shot at the top of mirror 6 and into the bottoms of mirrors 2 and 3. This mushrooming, so called because a narrow track suddenly balloons as many adjacent PMTs trigger is indicative of the YAG laser been scattered by clouds so that light will reach PMTs not directly viewing the track. The presence of rapidly moving low level cloud was mentioned in the nightly log of the HiRes 1 operator indicating the presence of clouds that can cause such effects. What is unusual about the problems of mirror 2 (compared to the other mirrors) was that the PMTs were triggering $1-2\mu$s *early*, with significant variation between when the two PMTs triggered. Thus it was hypothesised that light from earlier in the track, where mushrooming was concentrated, was getting scattered by the clouds into mirror 2.

4.5.2.3 Investigation of the cause of "bad" PMT times

In this section we discuss the cases where all occurrences of a single PMT gave bad times, distinct from the cases where all PMTs in a mirror give bad times. It was considered that these cases arose due to the PMTs triggering on noise. The investigation began by by obtaining the frequency that PMTs were bad, which is presented in table 4.8, and by plotting the delays for each of the bad PMTs. It was soon noted that almost all the HiRes 1 cases had positive delays and all the HiRes 2 cases had negative delays. By equation 4.2 this seems to imply that the PMT TDC values were larger than normal which implies that the PMTs were triggering early than normal.

An investigation of the raw TDC values indicated that these bad PMTs were among the first PMTs to fire for the given mirror. Also many of the PMTs had saturated TDC values, indicating they had indeed fired early (these PMTs were removed from the analysis as their times were not usable). Figure 4.22 shows a histogram of the relative firing rank within a mirror for all the "bad" PMTs (relative to the total number of PMTs that triggered in the mirror). The histogram is skewed towards the first few

HiRes Site	Mirror	PMT	No. times PMT bad
1	7	28	5
1	7	29	5
1	6	220	0
1	6	187	3
1	2	209	32
1	2	177	29
1	3	208	23
1	3	176	6
1	9	205	3
1	9	189	4
1	14	245	3
1	14	212	3
1	13	144	2
1	13	110	4
2	3	159	10
2	3	110	4
2	1	203	11
2	1	138	12

Table 4.8: Table indicating how often all occurrences of a specific PMT had a bad time. Total number of events was 1389.

ranks, but does have a long tail. This is mainly due to the effect of mirrors 2 and 3 which were being affected by scattering from clouds. Their contribution to the total has been plotted as impulses within the bins.

Thus it would appear that the majority of bad PMTs were simply noise triggers that were included within the event. The PMT trigger rates at HiRes 1 are set to be around 200Hz, and if a trigger lasts 10μs, there is a 0.2% chance that any given PMT will trigger off noise rather than the event. If we look at the actual statistics we see that any given PMT was bad for about 0.4% of events which is a reasonable comparison. Thus it seems reasonable that these bad PMTs can simply be explained as noise triggers.

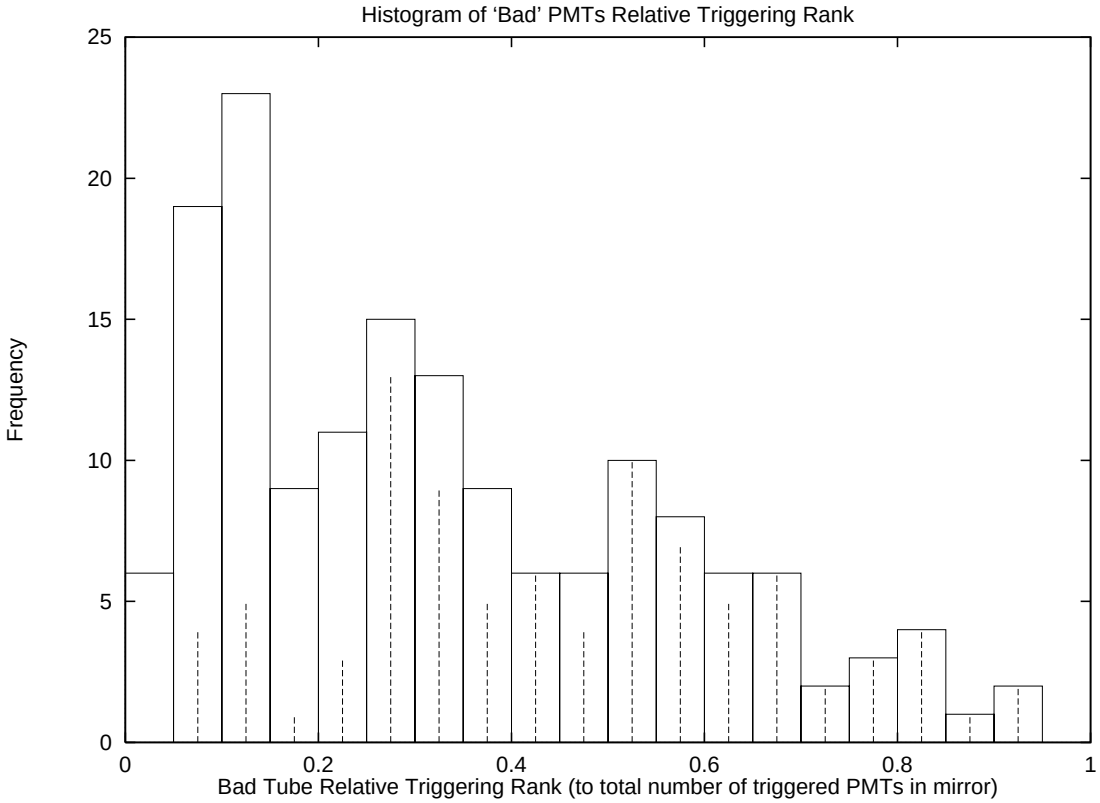

Figure 4.22: A histogram of the firing rank within a mirror for the case where a single PMT within a mirror was classed as "bad" (firing rank is relative to the total number of PMTs that triggered in the mirror). Mirrors 2 and 3 were affected by cloud scattering and their contribution to the total bin is indicated by the impulses. Note how the majority of PMTs from other mirrors triggered in the first 25% of PMTs.

4.5.3 Summary

The analysis of the YAG laser data seemed to indicate that there was a hardware related problem with the 40MHz scaler in the central timing unit. Based on the above analysis it appears that the 40MHz scaler is getting latched whilst in the process of changing. This has the effect of making event times later appear than they actually are. This problem was reasonably serious as it had the potential to affect the times for an *entire second* if it occurs when the GPS 1PPS latches the scaler. Degradation in timing was also seen to be due to noise triggers within events and due to scattering of the YAG laser track by clouds.

4.6 Fixing The 40MHz Scaler Latch

The analysis of the YAG laser data seemed to indicate that there was a hardware related problem with the 40MHz scaler in the central timing unit. The most likely explanation was that the 40MHz scaler was getting latched whilst it is in the process of changing, thus making event times appear later than they should. This problem was reasonably serious as it had the potential to affect the times for an *entire second* if it occurred when the GPS 1PPS latched the scaler.

Once the likely source of the problem was found we examined ways to fix the problem. The scaler was using a binary counter which meant that each time a higher order bit changed, lower order bits were forced to change as well, and problems arose if it was latched whilst in the process of changing. A graycode scaler latch was then considered as the best way to fix, or at least minimise the problem. A graycode scaler counter is a counter in which only one bit changes at each change of state. This avoids the previous problem since there is no flow on effect when the counter changes state. This fix does not actually remove the problem, but it does reduce the effect so that if the scaler is read in the process of changing, it will only be wrong by one clock tick (25ns). The necessary circuit and software changes were made and testing began on the electronics test rack at the University of Utah. Initial results were favourable so the changes were then implemented at the HiRes sites on September 16th 1995. Data (time and event packet) matching went from 97% to 100% overnight suggesting that the change had been effective.

As a follow up, a set of laser shots in a similar geometry to the first set was taken on the 29th of September 1995. The analysis used was identical to that for the pre-graycode lidar shots. The brightest tubes along the track were found and then two tubes from different subclusters were chosen for each mirror using this information. This once again gave 56 HiRes2-HiRes1 tube pairs for comparison. Only events containing all of the desired tubes were used which gave a data set of 1477 events. The distribution of the HiRes 2 – HiRes 1 tube trigger times were produced and figure 4.23 illustrates some of the histograms obtained. The distribution of FWHM for all 56 PMT pairs reduced by roughly 100ns from 327 ± 53ns to 238 ± 41ns with the gray

code scaler. Importantly, in contrast to the pre-graycode test, there were no cases where all PMTs in a mirror were bad, where bad was defined as when both tubes in a mirror had hr2-hr1 delays that were more that 700ns from the mean delay. Thus it appears that the graycode scaler fixed the latching problem with the binary scaler.

Whilst there were no cases were a mirror or an eye were bad there were still 159 cases where individual PMTs were bad. The expectation was that this was due to noise triggers and thus a similar investigation to that performed on the pre-graycode scaler test was performed. For almost all PMTs that were bad, that PMT was within the first 5% of triggering PMTs within that mirror, implying that they are indeed noise triggers Thus in summary the problem with the 40MHz scaler appears to have been fixed. This investigation would not have been possible without the installation of the GPS clocks, as their accuracy allowed a sensitive test to be conducted.

4.7 TDC calibration

Following the work on the scaler latch problem, I began work on reviewing the TDC calibration for HiRes 2. The TDC calibration is described in section 3.2.3. Briefly, the TDC calibration was a modified version of that used at HiRes 1. Snapshots were used to simultaneously start all TDCs integrating for a fixed time set by the holdoff counter. TDC counts were recorded for each holdoff time from 500ns to 18000ns in 500ns steps and a linear regression performed to determine the gain and pedestal for each TDC. In addition, twenty TDC values are taken at each holdoff time enabling the mean and standard deviation number of counts to be determined, but these values were not initially used. Originally a 10μs holdoff time was used during data collection, but it was soon found to be not long enough to allow distant EAS (or laser shots) to cross the mirror, and thus tracks were being clipped. Thus in March 1995, the holdoff delay was increased from 10μs to 25μs, and the TDCs from $\sim$ 0.65ns/count to $\sim$ 1.5ns/count. The maximum TDC count then increased to a value of $\sim$ 50μs. However the timing calibration at the time was not changed, so that at the time I began this work only the range from 0–18μs was being used to calibrate the HiRes 2 TDCs.

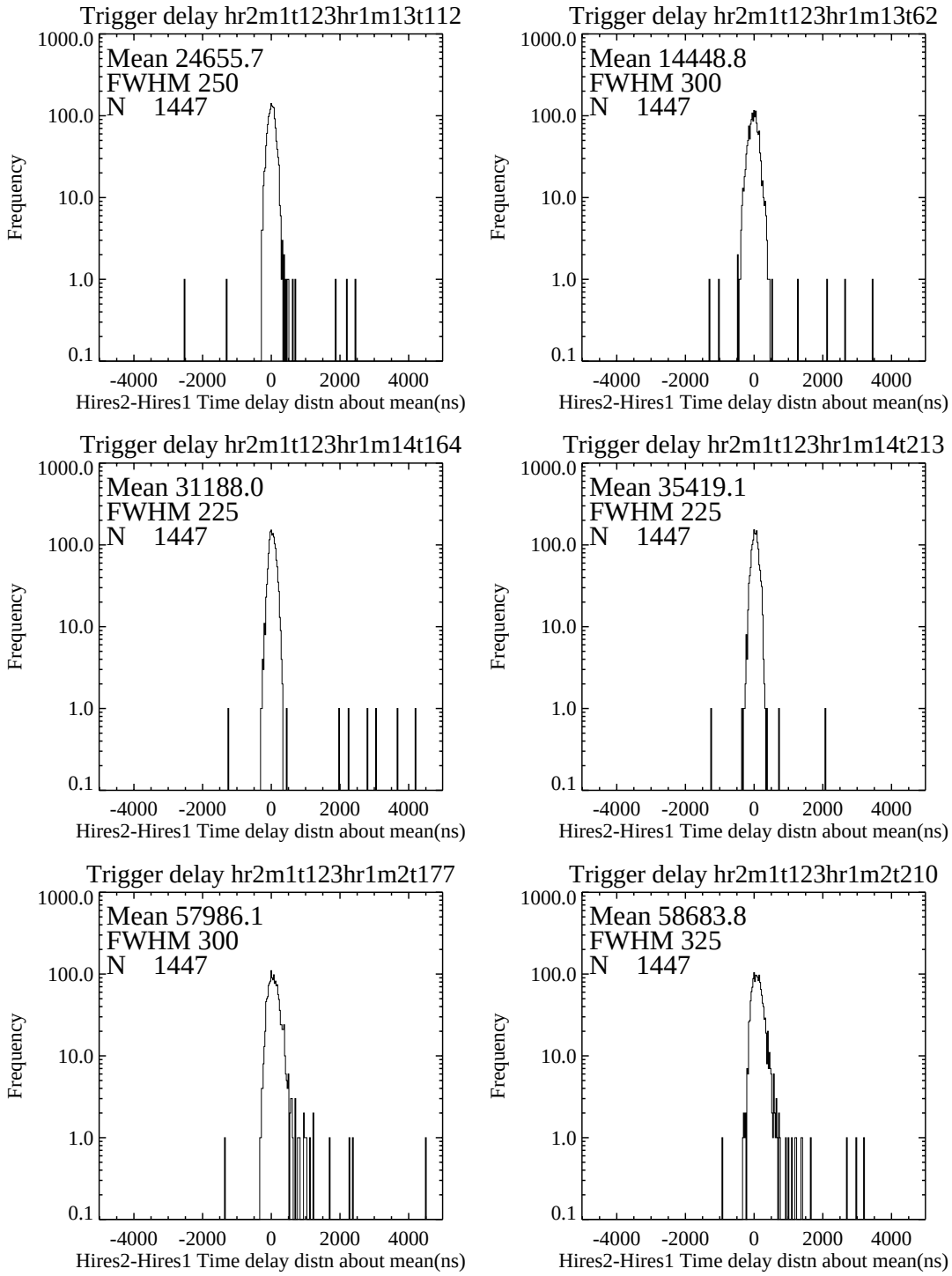

Figure 4.23: A selection of post gray code histograms showing the distributions in tube triggering times (HiRes 2 – HiRes 1). Note the relatively fewer outlying points compared to those in figure 4.18. These outliers are mostly due to noise triggers.

The investigation began by examining the linearity of the TDCs. I decided to compare the linear least squares fit being performed with linear fitters (a least squares

χ^2 fitter and a robust linear fitter[139]) that used the mean and standard error number of counts for each holdoff time. We wish to obtain

$$\text{Time} = \text{Gain} \times \text{TDC} + \text{Ped} \tag{4.3}$$

We can not directly fit this as we have the standard error in the TDC rather than time. Thus we fit

$$\text{TDC} = a \times \text{Time} + b \tag{4.4}$$

for a and b and note that the gain $= 1/a$ and the pedestal $= -b/a$ (and thus the errors in a and b can be used to get errors in the gain and pedestal).

Calibration data were fitted using the different methods, and the resultant gains and pedestals compared. In addition residuals between fitted and actual times were calculated. Results indicated that the χ^2 and robust fitter tracked each other closely but both differed from the simple least squares regression originally used. It was also obvious that there was a bimodality in the data - some subclusters had small residuals ($\sim 10ns$) over the 18μs whilst others were larger by a factor of approximately four. Also the χ^2 values for linear fits was ~ 30 in good subclusters but ~ 300 in 'bad' subclusters. In addition, it was noted that there was significant curvature in the residuals over the 18μs range. Instead of the residuals being randomly distributed about the mean, they were largely positive near 0μs and 18μs, and negative near 9μs. This implied that the function relating time and TDC counts was non-linear. Finally it was realised that the calibration process was not fully covering the range of the TDCs. Ideally we wish to map the response over the full range of the TDCs, but as the calibration was not changed when the holdoff and TDC count size was increased, this was not being performed. Thus in December 1995 the calibration range was increased from a maximum of 18μs to the hardware limit of 25μs. The hardware on each ommatidial board was then modified in February 1996 to increase the range from 25μs to 50μs, which is roughly the time equivalent to the maximum TDC value. Thus twenty calibration points are now taken every 1μs over the full range of the TDCs.

The observed bimodality was correlated with subcluster (the residuals in a given subcluster were either all large, or all small) – implying that it was probably due to a component on some ommatidial boards but not others. This was tracked down to the

capacitors used to store charge in the TDCs. Approximately half the TDCs at HiRes 2 used low leakage capacitors, like those in use at HiRes 1. However during board construction the supply ran out, so capacitors with slightly larger leakage values were used. Leaky capacitors allow the loss of charge prior to reading the TDC, thus the number of TDC counts will be less than it should. This effect was obvious as the subclusters with larger residuals were those using the the leakier capacitors. In March 1996, all the leaky capacitors at HiRes 2 (some 1700 used in TDCs and QDCs) were replaced with the original low leakage capacitors.

The structure of the residuals implied a non-linear relationship between time and TDC counts. Thus the use of quadratic, quintic and quartic polynomial functions were investigated. Also as approximately one year of calibration data was taken over only 18μs rather than 50μs, it was desired to examine how extrapolation of data fitted over 18μs compared with fits over the full 50μs range. We should also note that there is a slight problem in performing polynomial fitting – we wish to fit $\text{time} = a_0 + a_1\text{TDC} + a_2\text{TDC}^2$ when we have measurements of time, TDC and the standard error in TDC. To avoid the problem we faced earlier with linear fitting, in that we have errors for TDC values rather than time values (see equations 4.3 and 4.4), it was decided to convert the TDC errors into time errors using the gain information from the linear fit. Thus the standard error in the time measurement is $\sigma_{\text{Time}} = \sigma_{\text{TDC}} \times \text{LinearGain}$. The gain used was that obtained with the robust fitter – which in most cases is identical to that found using the χ^2 linear fitter.

Quadratic fitting was found to be the best choice for polynomial fitter. In the cases where we had calibration data over the 50μs range there was essentially no difference between quadratic and higher order polynomial fitters. In the cases where data are available only over the first 18μs, quadratic fitting performs the best, as is illustrated in figures 4.25 and 4.24. Table 4.9 summarises the results of the comparisons.

In the majority of cases the TDC times are accurate to $15ns$. In the worst case where the capacitors were leaky and the fit only over 18μs the times are quite good out to $\sim 30\mu$s after which they become systematically poor. Overall, the timing accuracy is extremely good – the accuracy in mirror holdoffs post latch fix is one scaler tick or 25ns which combined with 15ns TDC resolution gives roughly 30ns. The clock

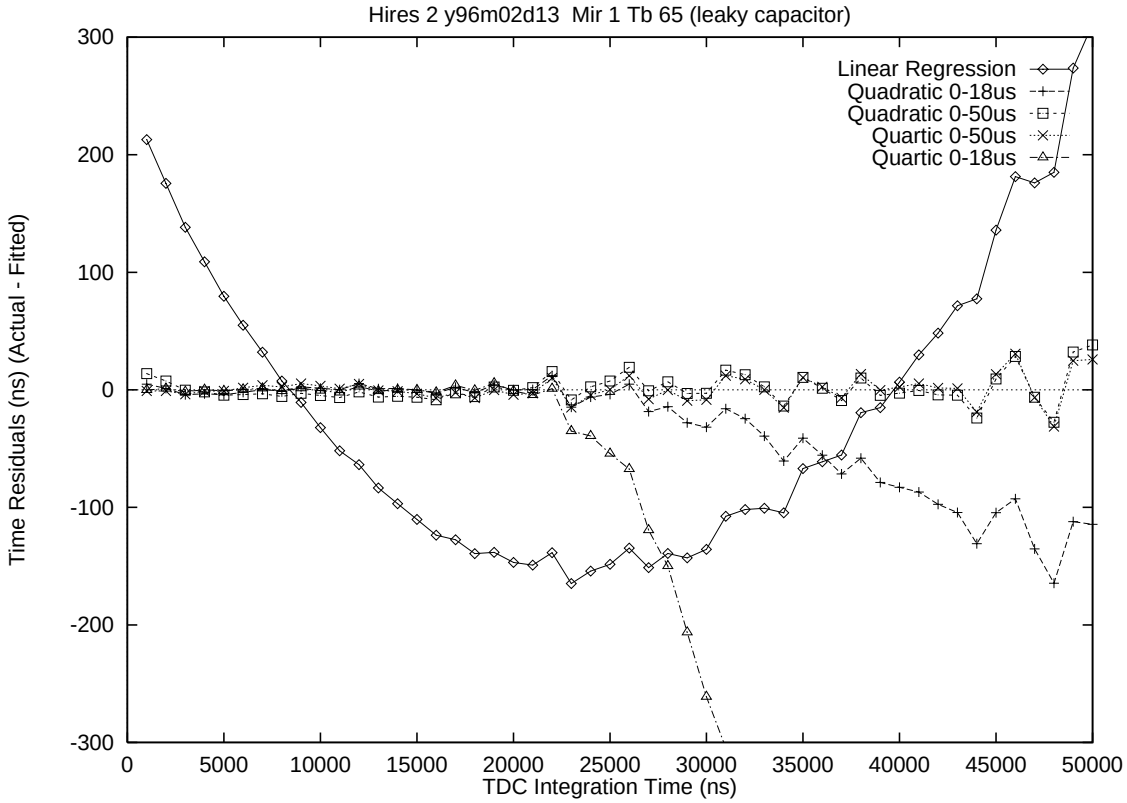

Figure 4.24: Residual TDC fitting results for several different fitters on data from a subcluster using leaky leakage capacitors in the TDCs. Note the poor performance of linear regression, the nearly identical residuals when data is available over 50μs, and how quadratic fitting out performs quartic fitting when data is only available from the first 18μs.

synchronisation errors between HiRes 1 and HiRes 2 probably increase this to $\sim 50ns$. This is still much smaller than the effects such as time slewing, which will effectively increase the triggering time uncertainty to the order of 100ns or more in most cases. Thus in the cases where TDCs times are poor (large TDC values) and the binary scaler was in use, it is likely that PMT trigger times are still accurate to the order of 100ns. In the next chapter I develop stereo event reconstruction methods, which incorporate PMT triggering times to improve EAS reconstruction.

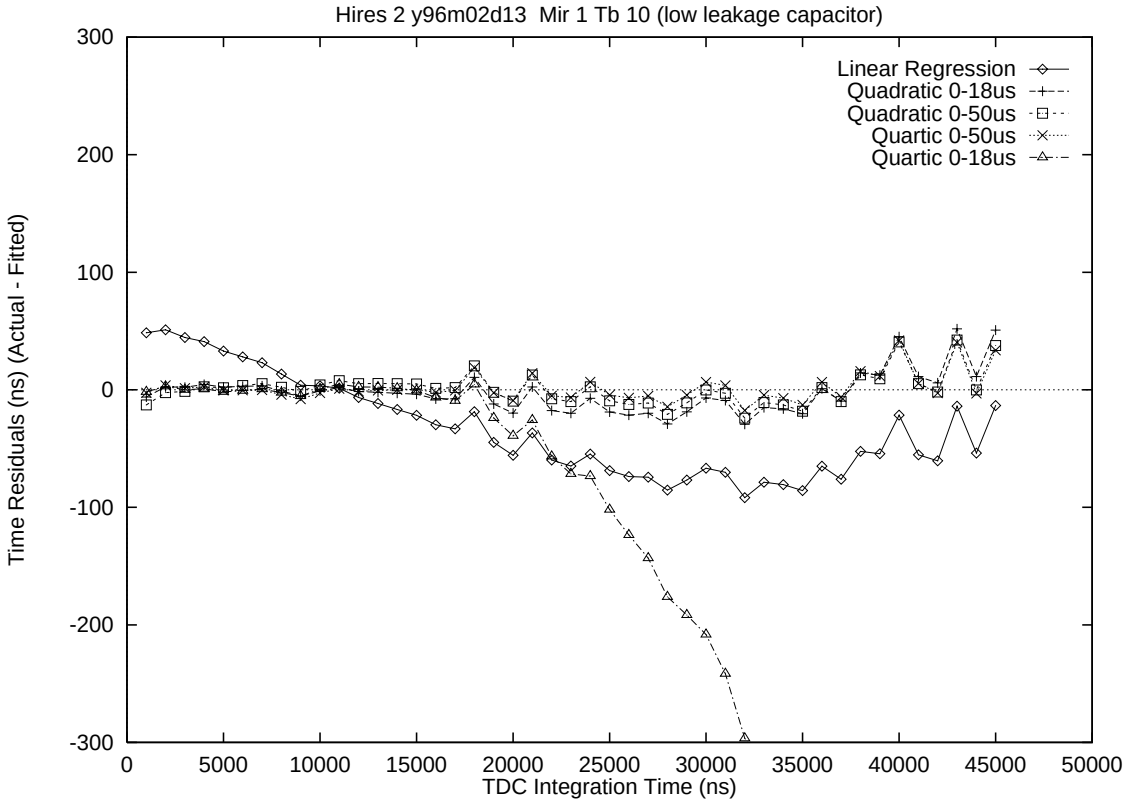

Figure 4.25: Residual TDC fitting results for several different fitters on data from a subcluster using low leakage capacitors in the TDCs. Compare the performance of the different fitters when leaky capacitors were used and also note that the quadratic fitter performs well irrespective of the use of data from 18μs or 50μs.

Calibration Range	Subcluster Classification	TDC Fit Type	Residuals (ns)	
			Mean	1σ
Limited 18μs	Good	Quadratic	-2	18
		Linear Regression	-33	41
	Bad	Quadratic	-35	47
		Linear Regression	-18	127
Full 50μs	Good	Quadratic	1	14
		Linear Regression	-33	41
	Bad	Quadratic	1	12
		Linear Regression	-18	127

Table 4.9: Typical TDC calibration fitting results for quadratic and original linear regression method. Fit residuals (actual – estimated times) show the improvement obtained with using quadratic fitter to relate TDC counts and times. The 1σ residual errors indicate that quadratic fitting is quite good for most cases, with the worst case for TDCs which used leaky capacitors and could only be fitted over 18μs.

Chapter 5

EAS Reconstruction

The results from the Fly's Eye detector illustrated the ability of the stereo atmospheric fluorescence technique to reconstruct EAS with good energy and spatial resolution. Good trajectory resolution allows us to determine the primary particle energy and arrival direction with confidence. We can then search for point sources or in fact, any anisotropy of EHE cosmic rays as a function of energy. Whilst the method was proved by the Fly's Eye experiment, the improved electronics and resolution provided by HiRes requires a fresh look at reconstructing the trajectory of EAS. This chapter examines the analysis methods used to reconstruct events observed in stereo by the HiRes prototype.

The starting point for this analysis were the results of a Monte Carlo study of EAS reconstruction with the (then proposed) full HiRes detector performed by Elbert[73]. The Monte Carlo simulations were conducted assuming two detector sites with each HiRes site covering 360° in azimuth and $3 - 30°$ in elevation (2 elevation rings of mirrors). These Monte Carlo studies illustrated that EAS events observed in stereo by such a detector might be reconstructed with a median (50%) angular error of 0.1°, and 90% to better than 0.6°.

The challenge was to take the techniques used to reconstruct the Monte Carlo data, and see how well we could adapt them to real data taken by the prototype detector. Real data has many added complications due to atmospheric effects (such as scattering), noise triggers, and any other detector systematics. Importantly, the

prototype has fewer mirrors than the simulation, and they are arranged such that the two sites have near coincident fields of view. This configuration contains geometries that pushes two site or stereo reconstruction to its limits (for reasons which will be discussed later). Hence the Monte Carlo studies represented something of a best case reconstruction scenario for the current prototype detector.

Whilst these limitations may prevent us from reconstructing prototype data with the angular resolution obtained with the Monte Carlo simulations, it is worthwhile to consider what level of angular resolution we require. Our current understanding of high energy cosmic rays is that they are charged particles, and as such their trajectories are affected by the galactic and intergalactic magnetic fields they pass through on their journey to us. It is estimated that a 10^{20}eV proton at 50Mpc is likely to be bent by intergalactic magnetic fields by 2.1° and as little as 0.6° by galactic magnetic fields[17]. We thus need to reconstruct EAS with an accuracy better than the amount they are likely to be deflected (ie we want the statistical error in determining the arrival direction to be smaller than the search area for sources). It must also be remembered that resolution is a function of instrument design. HiRes is designed to have good angular resolution – hopefully achieving the levels indicated by Monte Carlo simulations. It could have been designed to have better resolution, but this would taken more time, effort and money. The challenge in developing the reconstruction techniques is try and achieve an angular resolution as good as (if not better) than the Monte Carlo resolution.

In this chapter I will give an overview of the different fitting methods available to reconstruct an EAS trajectory, and how they can be implemented. This involves taking into account the effects of real data, and the optimisation done on the different methods as a result. I will cover the programs I developed, the comparisons performed and the level of accuracy I obtained.

5.1 Reconstruction Methods

An extensive air shower moves through the atmosphere at the speed of light, isotropically emitting fluorescence light as the shower develops along some axis that points

back to the arrival direction of the primary particle. This axis, or trajectory, can be parameterised by a point in space (chosen to be in the tangential plane to the earth containing HiRes 1) and a pointing direction defined by a zenith and azimuth angle. The HiRes detectors consists of individual PMTs, each having a fixed 1° field of view on the sky which trigger as the EAS travels across their fields of view. Each PMT records the triggering time, and the light received in two time windows of different lengths (one optimised for signals from nearby showers, the other for more distant showers). At each site, the collection of triggered PMTs defines a great circle on the celestial sphere. It is then possible to define a Shower-Detector Plane (SDP) as the plane containing this great circle and the detector. The shower trajectory may then be found using information from either a single HiRes site (mono reconstruction) or both HiRes sites (stereo reconstruction). However, complications due to effects such as atmospheric scattering, finite shower width and optical aberrations make this determination of the SDP difficult, so some fitting is necessary to determine the true SDP and trajectory.

There are three basic fitting techniques that will be discussed. The first two, amplitude weighting and amplitude fitting, are used to determine the Shower-Detector Plane, and the third, time fitting, is used to determine the orientation of the EAS trajectory within a given SDP. Following discussion of these techniques I will discuss the way these techniques may be used to determine the EAS trajectory.

5.1.1 Determining the Shower-Detector Plane (SDP)

The passage of an EAS will trigger a series of PMTs at each site. Each PMT has a unique pointing direction, and records the light intensity in its field of view. The more directly the PMTs view the EAS, the larger the light signal should be. Figure 5.1 illustrates the SDP and a PMT viewing a section of the EAS track. Two basic χ^2 fitting methods, known as amplitude weighting and amplitude fitting, for obtaining the SDP were developed and will now be discussed.

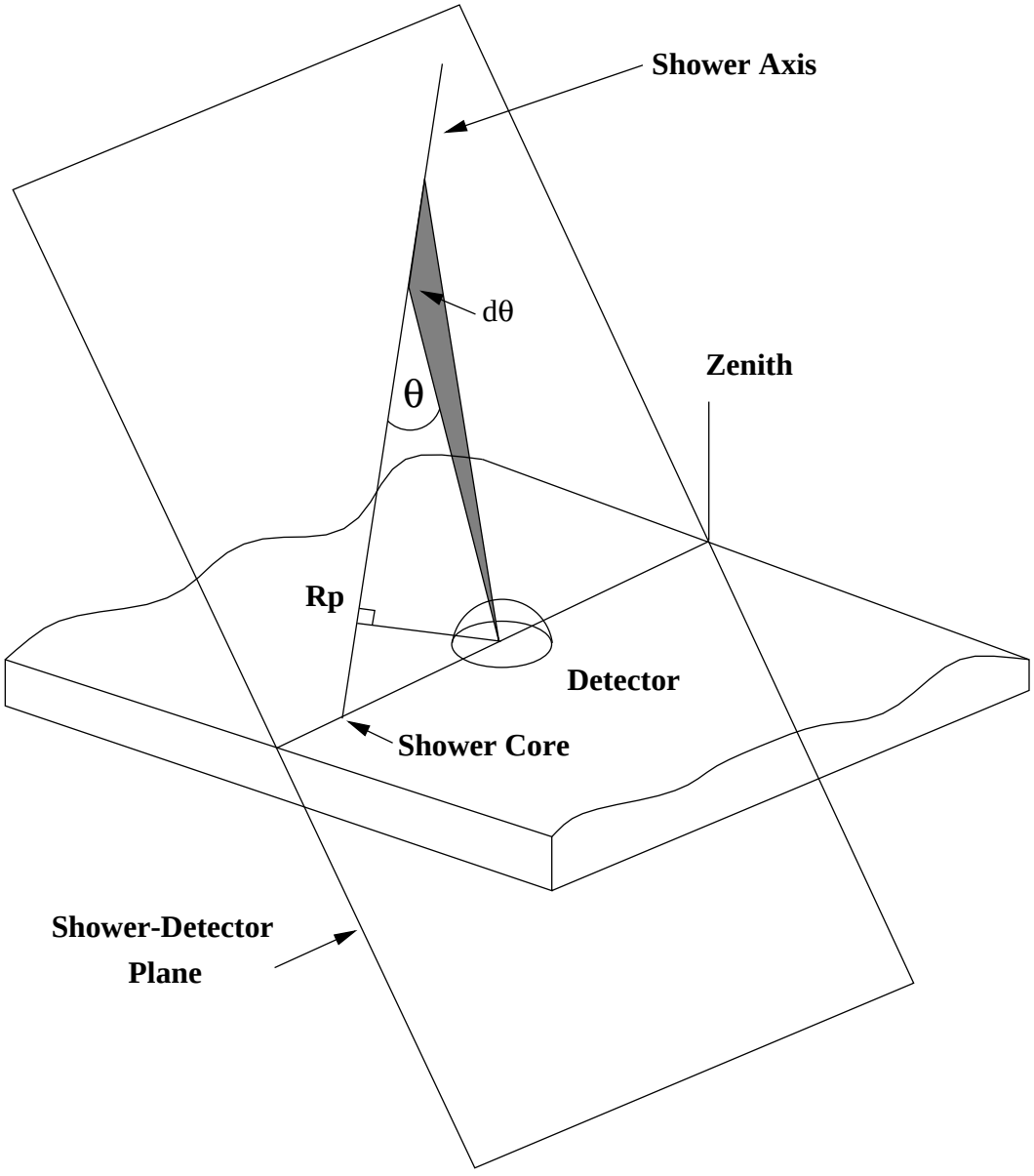

Figure 5.1: Geometry of an EAS illustrating the Shower-Detector Plane (SDP) for a single site. Light is emitted from the EAS and is viewed by a PMT with a light emission angle theta. Each PMT has some fixed field of view, so it will actually view a section of the EAS, denoted by dθ. A succession of PMTs will view the EAS, and their pointing directions combined with their light intensity information can be used to determine the SDP.

5.1.1.1 Amplitude Weighting

Amplitude weighting is a fairly simple way of using the available PMT triggering information. The effects of a finite mirror spot size are ignored, such that a PMT is assumed to trigger if the EAS passes through its field of view. Under this assumption the mean off plane angle of triggered PMTs should be zero (the off plane angles should be randomly distributed between $0.5°$ and $-0.5°$) and the standard deviation should be $0.3°$[115]. This method further assumes that those PMTs with the largest amplitudes are those most directly viewing the central axis of the EAS. An individual χ^2 component for a PMT can thus be simply determined using the offplane angle of the PMT and weighting the χ^2 component by the PMT's amplitude relative to the average amplitude:

$$\chi_i^2 = \omega_i \frac{(\text{PMT}_\text{i} \text{ off plane angle})^2}{\sigma^2} \tag{5.1}$$

$$\begin{aligned} \text{where } \omega_i &= \frac{\text{PMT}_\text{i} \text{ Amplitude}}{\text{Average PMT Amplitude}} \\ \text{and } \sigma &= 0.3° \end{aligned}$$

The SDP is then the plane that minimises the χ^2 function formed from the sum of individual PMT components. The individual PMT weighting factors are large for bright PMTs and small for dim PMTs, which forces the fitter program to choose a plane that is close to the bright PMTs to minimise the total χ^2, rather than fitting the plane purely on minmising the offplane angles. Amplitude weighting thus seeks to prevent the fitter from being misled due to the effects of atmospheric scattering (which may be non-uniform about the track), noise PMTs (which are weak but randomly placed), and when the light intensity is weak (often at the start or end of a EAS) and the finite spot size is important (as optical effects may degrade the symmetry of triggered PMTs about the shower axis).

5.1.1.2 Amplitude Fitting

Amplitude Fitting is a more sophisticated and, in principle, a more powerful χ^2 fitting technique than amplitude weighting as it attempts to take into account optical effects which affect the amplitude recorded by a PMT viewing the EAS. Amplitude fitting

compares the measured amplitude with that expected, based on how the light spot crosses the PMT (such as through the center or just clipping the edge) and how distant the PMT is from the EAS track (the off plane angle of the PMT). Ray tracing calculations and empirical measurements of the PMT photocathode have been performed and combined (by other collaboration members) to produce the estimated response of a PMT to a constant light flux over a mirror for a given trial plane[115]. These estimated responses are then scaled to to the actual light flux over the mirror when a given PMT triggered. This flux is estimated by averaging the flux from all PMTs within 3° of current PMT on the assumption that the flux should change smoothly along the track (and avoiding any assumptions about the development of the EAS). We can thus construct a χ^2 component for each PMT and fit for the SDP that minimises the sum of the individual χ^2 components:

$$\chi_i^2 = \frac{(\text{PMT}_\text{i} \text{ amplitude} - \text{Expected Amplitude})^2}{\sigma^2} \tag{5.2}$$

$$\begin{aligned} \text{where Expected Amplitude} &= \text{Ray Tracing Response} \times \text{Average Flux at PMT}_\text{i} \\ \text{and } \sigma^2 &= \text{PMT}_\text{i} \text{ Amplitude} + \text{Sky Noise} + 0.05\text{Expected Amp} \end{aligned}$$

The amplitudes and errors are given in units of photo-electrons. The error takes into account poisson fluctuation in the PMT amplitude, the effect of skynoise during the PMT integration and an arbitrary 5% error in the estimated amplitude. This last term is due to uncertainty in the estimated flux and errors in the calculated PMT response. Recent work with the Laserscope to measure the response profile of PMTs (see section 3.2.5.3 and Abu-Zayyad *et al.*[6]) has indicated some deficiencies with the PMT response parameterisation used[156]. Further work is underway to improve the PMT response profile estimates, but for this analysis the original response profile results have been used together with the above 5% error term.

5.1.2 Orientation of EAS within the SDP – Time Fitting

The final fitting technique discussed here is that of time fitting, in which PMT triggering times are used to constrain the orientation of the EAS within the SDP. The

EAS moves through the atmosphere at essentially the speed of light, triggering a succession of PMTs. The relative times that a set of PMTs trigger is dependent upon the geometry of the EAS within the SDP. Figure 5.2 illustrates the geometry of the EAS trajectory within the SDP which is defined by R_p, the distance of closest approach of the shower, and Ψ, the angle between the trajectory and the ground. From figure 5.2 it can be seen that it is relatively simple to derive the time lag between when a PMT triggers and the time of the closest approach of the shower. This is equivalently the time the EAS shower front would pass through the detector assuming that the shower front was infinite in extent and had zero curvature. Now for a given orientation of the trajectory within the SDP we can develop an individual χ^2 component for each PMT by comparing the expected PMT triggering time against the actual time (t_i) that the PMT triggers (with respect to an appropriately chosen reference t_{ref}):

$$\chi_i^2 = \frac{(t_i - t_{ref} - \frac{R_p}{c}\tan\frac{\theta}{2})^2}{\sigma_t^2} \tag{5.3}$$

The orientation of the EAS within the SDP can thus be obtained by minimising the sum of the individual χ^2 components in equation 5.3.

This technique relies upon a good knowledge of PMT triggering times. As indicated by figure 5.2, each PMT actually views an extended section of the EAS trajectory. To correctly estimate the triggering time of a PMT, one must estimate what fraction of the PMT crossing time has elapsed before the PMT triggers (this is analogous to knowing the exact emission angle of light from the EAS at the time of triggering). To a first approximation this is can be set to the 50% point. However, bright tracks will trigger the PMT soon after they start crossing the PMT, whilst dim tracks may trigger later than the 50% time. This problem gives rise to a systematic error known as time slewing (since a bright close shower will systematically trigger PMTs early and a dim distant shower will systematically trigger PMTs late). To properly compensate for this systematic effect one must know the pulse shape in the PMT, which is affected by the energy (amplitude) and distance (crossing time) of the EAS. This information was unavailable with the sample and hold electronics used by the prototype detectors, but should be available with the new FADC electronics of the full HiRes detector. This problem, and possible solutions will be further discussed later.

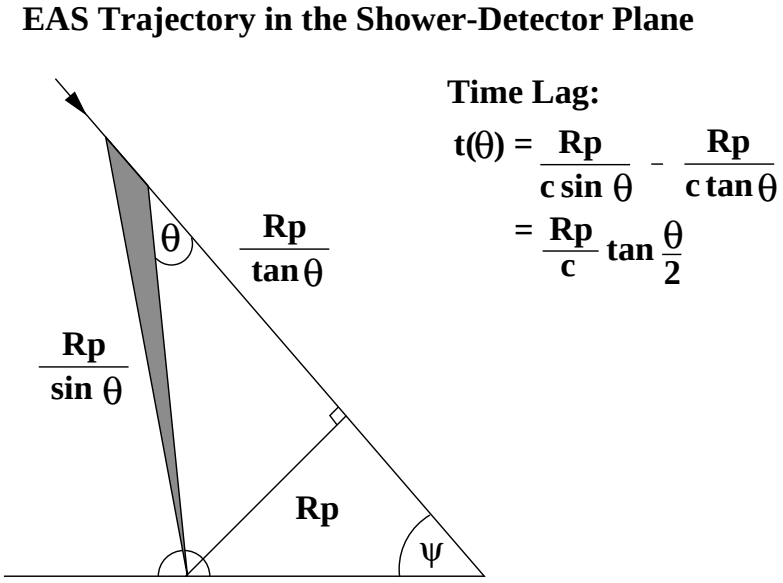

Figure 5.2: Determining the time lag for a PMT with an emission angle of θ within the SDP. The time lag represents the delay between light from an angle θ arriving at the detector, and the time of closest approach of the shower (when it is a distance of R_p from the detector). The shaded region represents the field of view of the PMT, illustrating the need for an accurate estimation of the emission angle θ at the time of triggering. The orientation of the trajectory within the SDP is defined by the R_p distance and Ψ, the angle between the trajectory and the ground.

It should be noted that timing fitting performs poorly for EAS with small observed track lengths. In such cases the tan function is approximately linear over the small angular range of emission angles, and errors in fitting for R_p and Ψ become correlated (see Kidd[115] for details). For timing fitting to be effective, we require that the data exhibit curvature in $(\theta, (t_i - t_{ref}))$ space. Finally we should note that σ_t represents the uncertainty in the triggering time of the PMT. Whilst within a mirror relative PMT triggering times are accurate to several nanoseconds, mirrors are only synchronised to within 25ns (one clock tick of the 40MHz scaler) increasing the triggering uncertainty. Determining the triggering time error σ_t will be discussed later in conjunction with accounting for triggering time slewing (which systematic affects PMT triggering times).

5.1.3 Mono Fitting

Mono fitting is used when the EAS is viewed by a single site. Either amplitude weighting or amplitude fitting can be used to determine the shower-detector plane,

and a timing fit must be performed to determine the orientation of the EAS within this plane. This can produce reasonable fits, but is subject to problems such as trigger time slewing[21][115].

The fitting problems of this method may be overcome through the use of information from multiple sites. This was illustrated by the Fly's Eye detector, and underlay the choice of using multiple sites for the HiRes detector. I have been primarily interested in the analysis of the stereo data set, and as such have concentrated my efforts in that area.

5.1.4 Stereo Fitting

Stereo fitting uses information from two sites and utilises the geometrical effect that the intersection of two planes is a line. Each site determines a shower-detector plane, and the intersection of the planes is the EAS trajectory, as illustrated in figure 5.3. Results from the Fly's Eye indicated that the stereo method performs better than mono fitting, producing smaller errors and reducing the tails in error distributions[30].

Stereo fitting performs well in most cases. However as the angle between the two planes approaches zero (denoted as α in figure 5.3, strictly it is the angle between the plane normals), the accuracy of stereo reconstruction degrades. In these cases, small errors in determining either shower-detector plane can lead to a large error in determination of the EAS trajectory. The geometry of the HiRes prototype is such that both sites have near coincident fields of view. As a result, many of the EAS will lie close to the line joining the two sites, and will thus have small opening angles. Hence reconstruction of prototype data serves as a tough testing ground for any reconstruction programs developed.

5.1.5 Timing Fitting

Timing Fitting implements the time fitting discussed in section 5.1.2 at both sites and requires excellent relative timing accuracy between the two sites to ensure that the trajectory is tightly constrained. A first guess of the trajectory is made using a the intersection of the two SDPs (defined by the triggered PMT pointing directions),

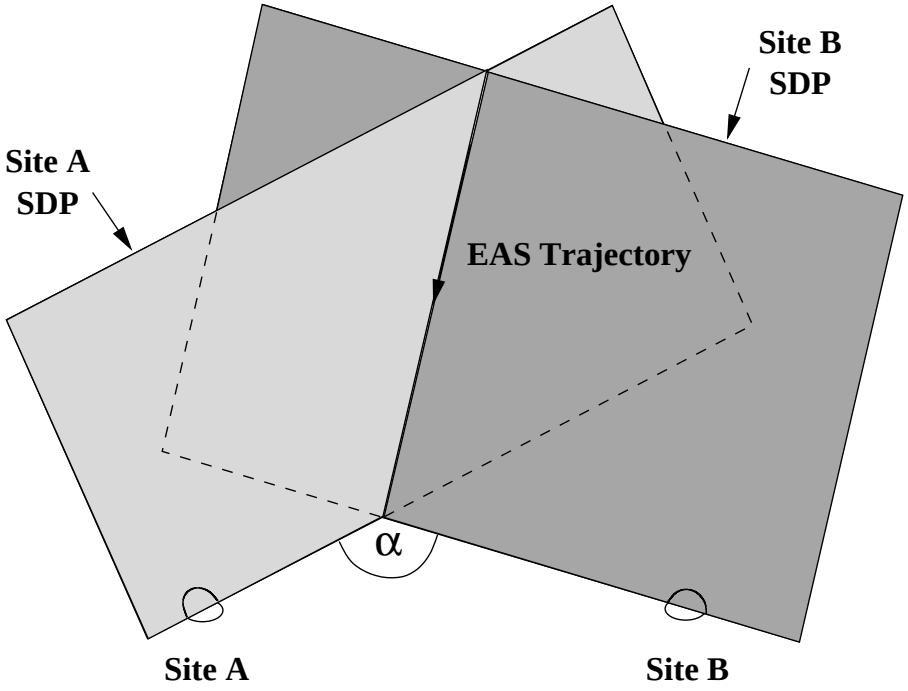

Figure 5.3: The stereo method for estimating the shower trajectory. The shower is viewed by two sites which each determine a shower-detector plane. The EAS trajectory is then the intersection of these two SDP's. The Stereo opening angle α is indicated, and is actually the angle between the normal vector for the two SDPs.

after which timing information alone is used to constrain the trajectory. The use of two synchronised sites effectively provides timing measurements over a large range of emission angles overcoming the problems of mono fitting where data is often sampled over only a narrow range of emission angles. However time slewing is still an important effect that must be taken into account for time fitting to be effective.

5.1.6 Stereo-Timing Fitting

Stereo-Timing fitting utilises all the available information from multiple sites to reconstruct the EAS trajectory. It combines stereo fitting with time fitting at both sites, to reconstruct the trajectory. The stereo component effectively limits the possible trajectories of the EAS whilst the timing component is able to distinguish between this reduced set of possible trajectories, thus utilising the power of both techniques. One of the big advantages of this method is that it can overcome the opening angle problems of stereo fitting by using the PMT triggering times to constrain the orientation of the

trajectory within a site's SDP.

5.1.7 Multi-dimensional Fitting for the EAS Trajectory

A trajectory in three dimensional space can be specified by a point in space and by its (unit) direction vector. We define our co-ordinate system as being centred on HiRes 1, with East as the x-coordinate, North as the y-coordinate, and z as the local normal. We then perform a 4 parameter fit for the trajectory by searching for the core location in the x-y plane, and for the zenith and azimuth angles that specify the arrival direction. Timing fits require an additional parameter to specify the clock offset between the two sites. Hence fitting for the trajectory requires the use of a multidimensional fitter to minimise our chosen χ^2 function.

The downhill simplex method[139] was used to minimise the χ^2 function over 4 or 5 dimensional space. The downhill simplex method proceeds by defining some initial simplex, where a simplex in N-dimensional space is defined by N+1 vertices and encloses some region of space assuming that the vertices are nondegenerate. The method proceeds by evaluating a given χ^2 function at each vertex. The method then tries a series of reflections, expansions and/or contractions to move the simplex away from the highest (largest) point. The method continues repeating this until all χ^2 values at each of the vertices are within some minimum range. It is then generally wise to restart this process with N of the N+1 vertices at the minimum to try and ensure that the minimum is truly the minimum. The book Numerical Recipes[139] provides an implementation of this method in its Amoeba routine - so named to describe the movement of the simplex.

Use of this technique requires a certain amount of care. Generally, the better the initial guess of the first vertex (the initial point to search around), the faster the convergence and the greater chances of finding the global minimum. The size of the initial simplex influences the size of the space searched over, and one must keep in mind that the larger the initial simplex size the greater the risk that a local rather than a global minimum will inadvertently be found. Finally it is worth noting that the downhill simplex method only requires a function (and no information on its

derivatives) to minimise.

5.1.7.1 The Fitting Process

To obtain an initial guess of the EAS trajectory, a simple estimate was made using the pointing directions of triggered PMTs to determine two SDPs which were intersected to obtain a trajectory. A routine based on the Amoeba routine of Numerical Recipes[139] was then used to search for the trajectory that minimised a chosen χ^2 function.

Separate χ^2 functions were developed to implement stereo, timing and stereo-timing fitting. I will consider the χ^2 function for stereo-timing fitting first as the χ^2 function for the other two methods are subsets of this function. The Amoeba routine searches over 5-dimensional space - 4 parameters for the trajectory and one for the timing offset between the two HiRes sites. The χ^2 function takes the trajectory and timing offset supplied by Amoeba and PMT triggering and amplitude information to calculate a reduced χ^2 value which is returned to Amoeba .

The stereo-timing χ^2 is a composite function given by

$$\chi^2_{\text{Total}} = \chi^2_{1\ \text{Stereo}} + \chi^2_{2\ \text{Stereo}} + \chi^2_{1\ \text{Time}} + \chi^2_{2\ \text{Time}} + \chi^2_{1-2\ \text{Offset}} \tag{5.4}$$

The $\chi^2_{1\ \text{Stereo}}$ and $\chi^2_{2\ \text{Stereo}}$ components represent the stereo components from both sites, and are determined using either amplitude weighting (equation 5.1) or amplitude fitting techniques (equation 5.2). The $\chi^2_{1\ \text{Time}}$ and $\chi^2_{2\ \text{Time}}$ components represent time fitting components at the two sites and $\chi^2_{1-2\ \text{Offset}}$ represents a component to take into account any clock offset between the two sites. This last component has the form

$$\chi^2_{1-2\ \text{Offset}} = \frac{(\text{HiRes 1} - \text{HiRes 2 Clock Offset})^2}{\sigma_{1-2\ \text{Offset}}} \tag{5.5}$$

where $\sigma_{1-2\ \text{Offset}}$ is an estimate of the synchronisation error between the two sites.

Stereo fitting utilises the first two terms of equation 5.4 and timing fitting utilises the last three terms. It is possible to perform mono fitting by only using the stereo and timing terms from a single site, but the method used here is not optimised for this approach as our initial guess assumes stereo information and further constraints are probably needed to ensure reliable fitting. The implementation and optimisation of these fitting methods is described later in section 5.3.

5.1.8 Monte Carlo comparison of Fitting Methods

The Monte Carlo simulations performed by Elbert [73] for the (then proposed) HiRes detector provide a good benchmark to compare our fitting accuracy against. Elbert tested the reconstruction accuracy of the various fitting techniques on a set of 300, 3EeV Monte Carlo generated showers. The simulation used 54 mirrors (two rings) at each of two sites separated by 13.2km thus providing very favourable opening angle coverage. It was also assumed that systematic timing effects were understood and that timing errors between predicted and actual times would be purely statistical. The fitting methods compared were stereo, timing, and stereo-timing. Amplitude weighting and amplitude fitting within stereo-timing were also compared. The space angle error distributions (angle between fitted and actual trajectory) were obtained and are presented in table 5.1

Fit Type	Space Angle Error	
	Median (50%)	90% Level
Stereo	0.5°	5°
Timing	0.7°	4°
Stereo-Timing Amplitude Weighting	0.24°	0.8°
Stereo-Timing Amplitude Fitting	0.12°	0.6°

Table 5.1: Reconstruction results for stereo, timing and stereo-timing techniques on 300, 3EeV Monte Carlo showers performed by Elbert[73]. Amplitude weighting and amplitude fitting methods used in stereo-timing fitting are also provided for comparison. Reconstruction was performed assuming the HiRes detector consisted of 54 mirrors in two elevation rings at each of two sites, and that all timing systematics were understood.

The results indicate the general trends expected. Stereo fitting performs better than timing fitting for most events, with both methods having larger tails whilst stereo-timing fitting is able to combine and improve these methods. Concentrating on stereo-timing indicates that amplitude fitting performs better than amplitude weighting which is not surprising given the greater detail involved. The simulation results presented in table 5.1 are expected to be better (smaller errors) than those using prototype data. This is because the use of sample and hold electronics limits our ability to account for time slewing properly (the simulation assumed all timing systematics

were accounted for), and our field of view has poorer opening angle coverage than this simulation.

5.2 Testing reconstruction with Laserscope data

The Laserscope, described in section 3.2.5.3, was used to produce a set of laser shots with known geometries for reconstruction tests. The laser shots appear very similar to EAS and were able to trigger the HiRes detector. The two main differences between EAS and laser shots are that laser shots are upward going instead of downward going, and the shower profile is different from that of a cosmic ray induced EAS. The advantage of the system is that it is capable of producing a large data set of events with accurately known geometries. These events can be reconstructed, and the space angle between the actual and reconstructed trajectory can be determined. The distribution of space angles thus provides an indication of the accuracy of the fitting process, and the fitting method can be optimised by comparing space angle distributions. This section details the generation of the data that formed a set of standard events that were used to optimise the reconstruction programs discussed later in section 5.3.

5.2.1 Generating the Laserscope Reference data

Two data sets were obtained on the nights of the 12th and the 15th of October 1996, for the dual purposes of generating data for testing event reconstruction and to help determine the PMT pointing directions and response profiles[6]. Unfortunately problems were encountered with maintaining a constant intensity – which was important for the PMT response profiles work, so the YAG laser was swapped with a more stable 337nm Nitrogen laser (which also required removal of the radiometer). Hence data from the 12th was taken with the YAG laser whilst data from the 15th was taken with the Nitrogen laser. It was also later discovered that the lasers were not sufficiently rigidly mounted on the telescope, leading to sagging of the laser with respect to the telescope – with maximum sagging of the laser occurring when the telescope was near zenith. The effect has since been corrected (and work is underway to replace the laser

with a fiber optic system) but it places an additional uncertainty on the pointing direction of the laser. This is approximately $0.1° - 0.3°$ for the YAG and $0.1° - 0.5°$ for the Nitrogen laser (the effect was larger as the Nitrogen laser was heavier than the YAG).

The positions of the Laserscope were marked and surveyed with a GPS unit and an electronic distance measurer, and thus are known to within 1m on both nights. The positions are indicated in figure 5.4 and in standard HiRes (East, North, Up) coordinates were (1.459km, 6.709km, -0.002km) on October 12th, and (4.924km, 4.072km, -0.068km) on October 15th.

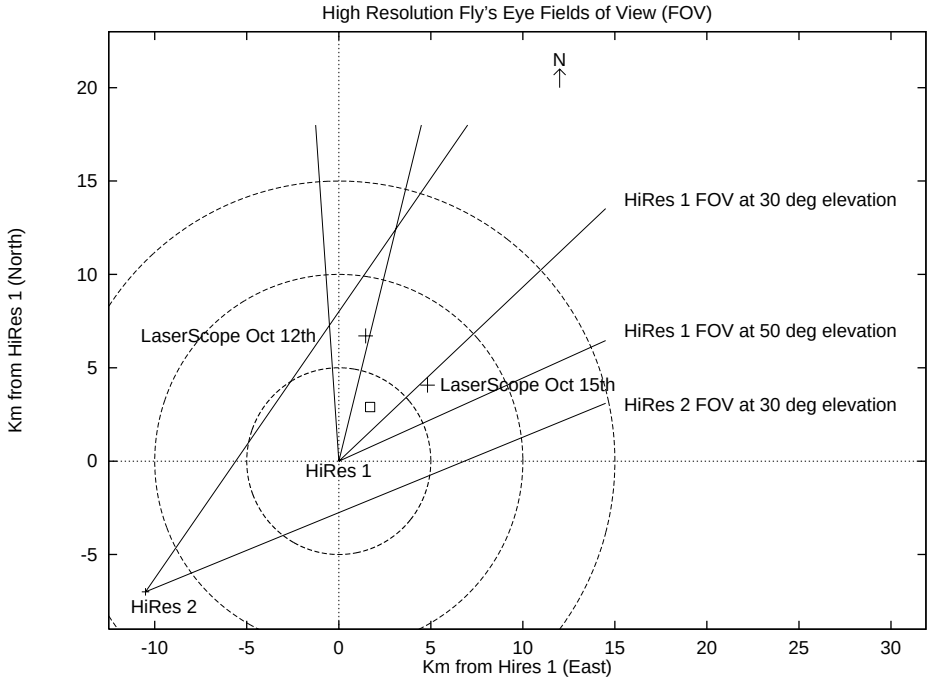

Figure 5.4: Map of HiRes detectors illustrating the Laserscope positions (crosses) used for testing reconstruction programs. The square in the centre of the field of view indicates the location of CASA/MIA/FE II.

A wide variety of geometries was obtained (in part due to use of this data to obtain PMT response profiles for many different mirrors – see section 3.2.5.3). To generate the data, the Laserscope was fired in the plane perpendicular to a given mirror's pointing direction. The Laserscope was progressively fired in this plane in 0.3° steps so as to scan across the mirrors field of view. Ten Laserscope shots were taken at each position at approximately two seconds intervals, with the time recorded to the nearest second by the PC clock. There was a delay of 15-20 seconds between each scan position to

allow for movement and stabilisation of the Laserscope, and larger delays occurred between scanning different HiRes mirrors.

The data taken on the 12th covered stereo opening angles of 7° to 35° whilst data on the 15th covered opening angles of 2° to 11°. On the night of the 12th, mirror 9 of HiRes 1 was not operational, and on the 15th mirror 2 of HiRes 2 was not operational. Plots of stereo opening angle as a function of HiRes 1 and HiRes 2 track lengths (the angular length of the Laserscope track observed by the HiRes site) for the two nights are shown in figure 5.5, and between opening angle and average photons per PMT in figure 5.6. These plots indicate the wide range of opening angles, observed EAS track lengths and intensities obtained using the Laserscope.

5.2.2 Event Matching

The Laserscope PC recorded the time, azimuth, elevation and intensity of each laser shot. The firing times of the laser were recorded to the nearest second by the PC clock whilst events that trigger the HiRes detector were recorded to an absolute accuracy of 300ns (UTC). In order to compare the reconstructed trajectory with the actual trajectory, the HiRes event times were matched with the PC times in a semi-automated process.

The HiRes events were first scanned to remove any non-Laserscope events. The initial offset between the PC clock and HiRes was determined by hand matching the first observed Laserscope event with the PC log time. A simple program to match times assuming a ± 0.9 second window around this offset was then developed. This attempted to detect the 15-20 second gap between shot sets, at which point the PC-HiRes offset was recalculated. This worked well for the data from the 12th but was less successful for the 15th due to drift in the PC clock and long gaps in Laserscope data. An alternative approach for the 15th was to break the data into 10 sections - each corresponding to a major time gap when the Laserscope was undergoing a large slew to a scan a new mirror. This enabled confident hand matching to determine the clock offset at the start of each event subset. These offsets allowed a measurement of the drift of the PC clock, which was found to be about 1 second every three hours. The data

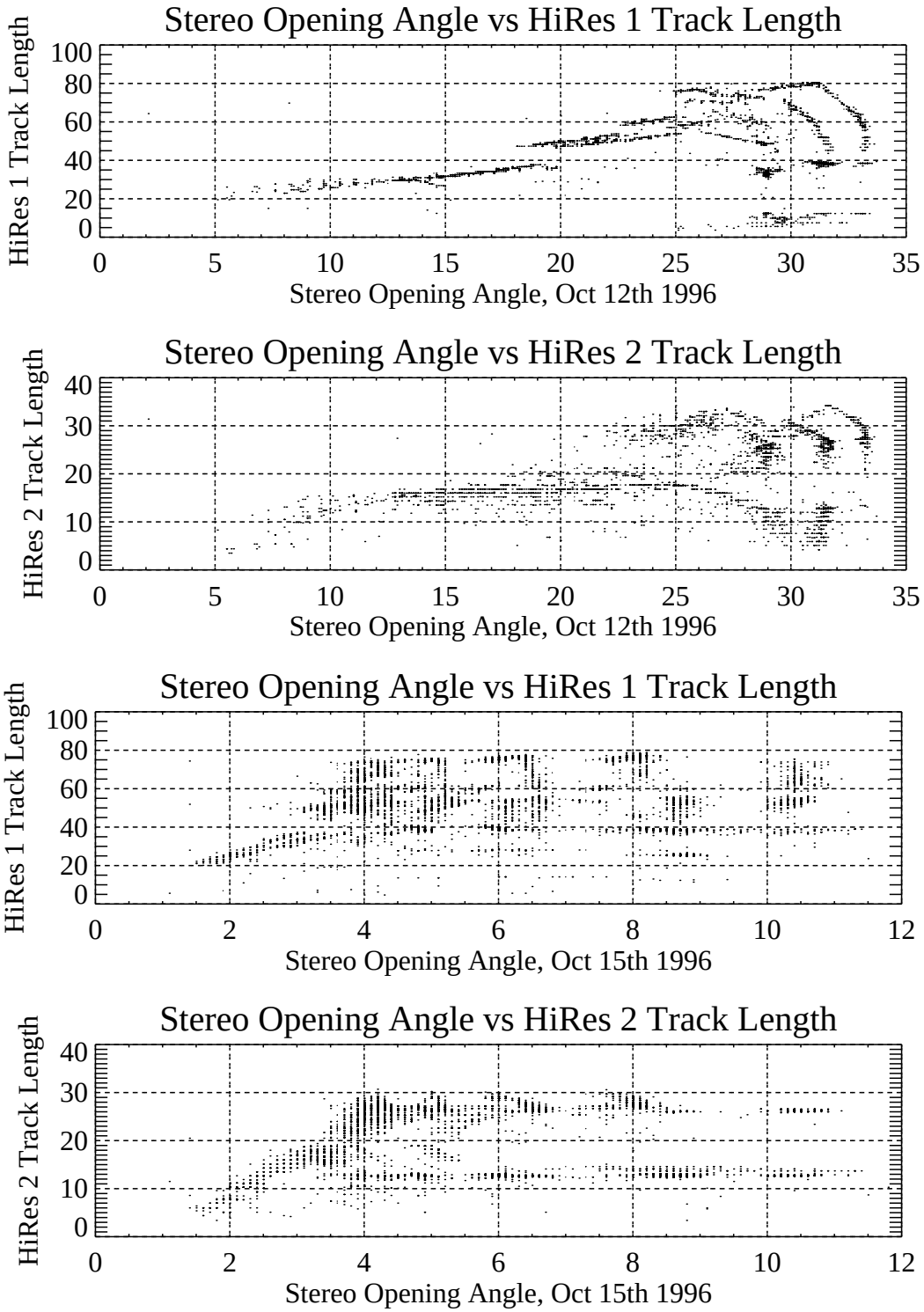

Figure 5.5: Plots of stereo opening angle vs HiRes 1 and HiRes 2 tracklength for Laserscope data from the 12th and the 15th of October 1996 (both in units of degrees). Note the wide range of tracklengths and opening angles obtained. The large number of laser shots in HiRes 2 on the 15th with tracklengths around 12° are due to the loss of mirror 2 for this night.

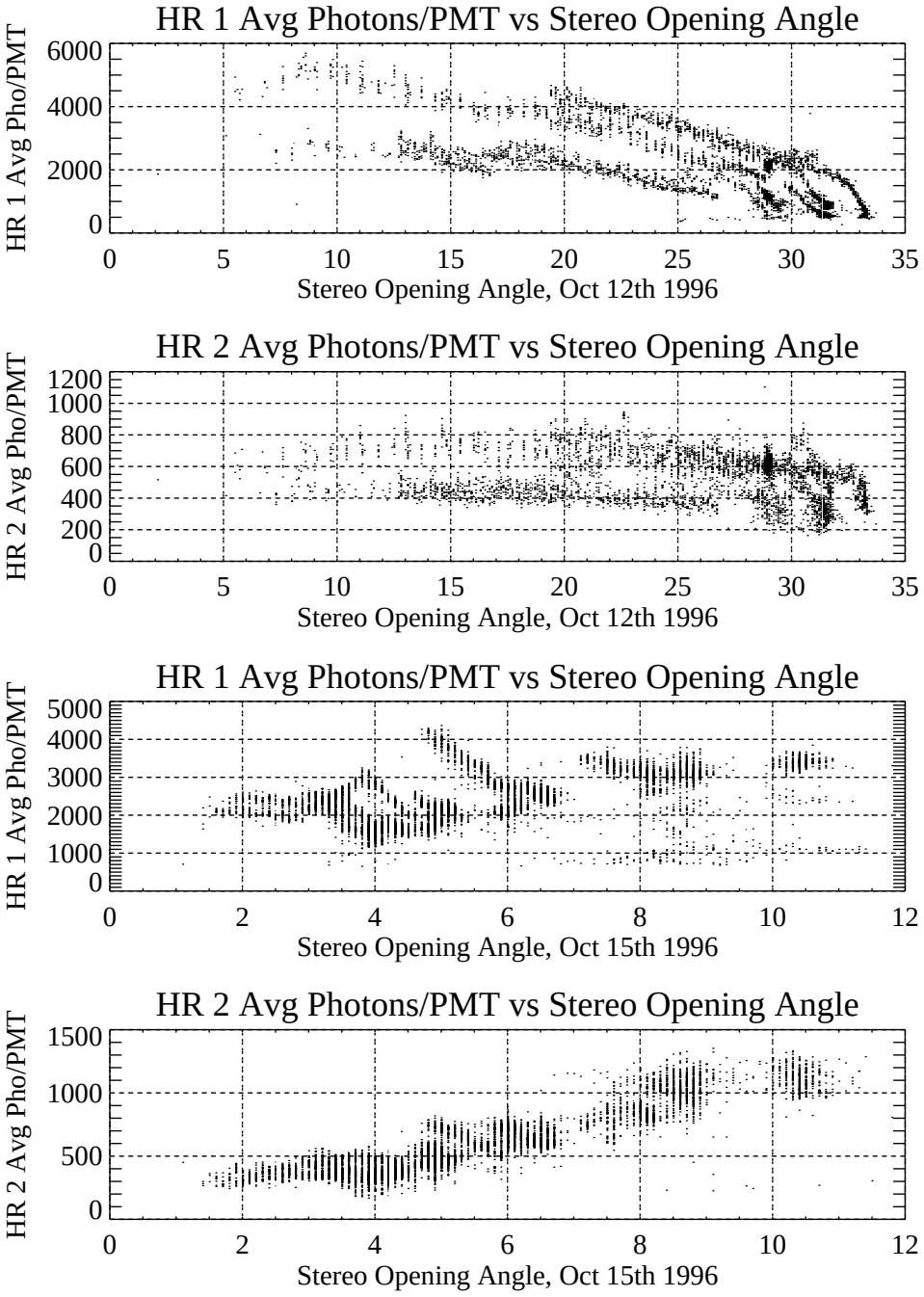

Figure 5.6: Stereo opening angle vs HiRes 1 and HiRes 2 Average Photons (350nm equivalent) per PMT for data from October 12th and 15th, 1996. Integration Channel A (1.5μs) was used at HiRes 1 and integration Channel B ($5,4\mu$s) at HiRes 2 (see section 3.1.1.3).

was matched in sections using a ± 0.9 second window and assuming that the offset did not change, which was considered reasonable as no section was longer than 1.5 hours. As a final check on the matching program, the data set was scanned to remove any non-Laserscope events and several randomly selected events were rechecked. At the end of the matching process there were 4343 events for the 12th and 6811 events for the 15th for which confident reference positions, azimuth angles and zenith angles were known.

5.3 Optimising the Reconstruction Program

A trajectory reconstruction program was developed to implement the reconstruction techniques described earlier in this chapter. This program reads in matched, calibrated HiRes1 - HiRes 2 events and reconstructs the event geometry. Reconstruction is achieved through the use of a χ^2 fit to determine the shower parameters: X and Y core location in the Z = 0 plane, and the Zenith and Azimuthal angles from this point. The program consists of modules which can be broken up into several broad areas. These are event preparation (reading the data in, initialising variables), selection (noise filtering) and geometrical fitting. These sections will briefly be described before concentrating on the work performed to optimise the fitting program.

5.3.1 Event Preparation

Event preparation consists of initialising variables, reading an event from a data file, and doing any other required bookkeeping. Data is stored in bank structures (common blocks in fortran, structures in 'C'). "RAW" banks contain raw data such as triggering time, QDCA, QDCB, and TDC values for all triggered PMTs. "PHO" banks contain calibrated information for all PMTs in the "RAW" banks, such as the number of equivalent 350nm photons collected in integral channels A and B, and the calibrated TDC triggering time with respect to holdoff for each triggered PMT. These routines read in the event information and do basic processing such as determining the PMT triggering order.

5.3.2 Event Selection

Event selection is handled by several functions. These functions look for evidence of Cerenkov blasts, muon tracks, and noise-triggered PMTs within each mirror, and then decide if there are enough PMTs to warrant event reconstruction.

Cerenkov blasts or muon tracks within a mirror are identified by requiring that the time difference between the first and last PMT to trigger in a mirror be greater than 300ns. Fluctuations in the night sky noise background will randomly trigger PMTs whilst a more ordered series of PMTs will (progressively) trigger as the EAS develops. If we time order the triggered PMTs, then those close in time should also have small angular separations (their pointing directions should be similar). The presence of PMTs with saturated TDCs makes this identification difficult, as their true triggering times are unknown. Noise triggered PMTs often have saturated TDC's. However we do not wish to rule out all PMTs with saturated TDC's, as there are sets of PMTs with saturated TDC that form part of the EAS track, and their pointing directions may still be used in stereo fitting.

The approach taken was to flag any PMTs that either had saturated PMTs, were physically isolated triggers or were obviously out of time and angular sequence. This provided a set of trusted PMTs. Fits of direction cosine against time were performed on these trusted PMTs, and the fit parameters used to more rigorously reject out of time and angular sequence PMTs (with the test being loosened slightly for saturated PMTs). This approach was tested on a series of events containing noise triggered PMTs and saturated PMTs forming a section of the track, and appeared to work satisfactorily.

5.3.3 Fitting the Shower Trajectory

The final and most important section of the program is the actual trajectory fitting stage. The trajectory fitting was performed by first estimating the initial trajectory, defining an approximate region to search over, and passing this information, together with a function to calculate a χ^2 value to a multi-dimensional fitting program (described in section 5.1.7). The task was thus to determine how best to estimate the

initial trajectory and starting simplex for Amoeba , as well as optimising the χ^2 function used. This work will now be discussed.

5.3.3.1 Selecting the initial trajectory

The initial trajectory is estimated using a simple geometric method which is at the heart of stereo reconstruction. Shower-detector planes (SDPs) are determined from the good PMT pointing directions at each site, and the initial shower trajectory is defined by the intersection of these two planes. To ensure the initial guess is reasonably accurate, checks are made for the cases where this simple method may be sensitive to errors. In such cases attempts were made to estimate alternative initial trajectories.

The basic method used to estimate the SDP at each site is well described by Elbert[73] and Kidd[115]. This method is based on the premise that the triggered PMTs are just points on the unit sphere, and that with an appropriate transformation, the plane can be found by a straight line fit to triggered PMTs directions. The amplitude weighted centroid direction of all the triggered PMTs is first found. The centroid direction is the mean pointing direction of all PMTs weighted by their amplitude – as bright PMTs are presumably seeing the central track and should be weighted accordingly. Given that the initial guess is quite important for the later fitting process, the effect of different weightings (such as the square root of the amplitude) were considered. For most tracks any reasonable choice of the weighting factor was found to work well. Amplitude weighting was chosen as it found to work the best with some of the more difficult tracks. For long tracks (tracklengths $> 60°$), the centroid used was the just the midpoint of the track.

The pointing directions of the PMT form an arc on the surface of the unit sphere – figure 5.7 (a). If these PMTs are projected into the plane whose normal is perpendicular to the centroid vector, the arc formed is nearly straight – figure 5.7 (b). PMT directions are projected into this plane, and each PMT is now defined as a (s,p) cartesian point with s along the projected arc and p perpendicular to this as illustrated in figure 5.7 (c). By performing a simple linear fit in this coordinate system a refined estimate of the track direction can be obtained. The plane normal can then be estimated as it is simply the cross product of the centroid and the track direction.

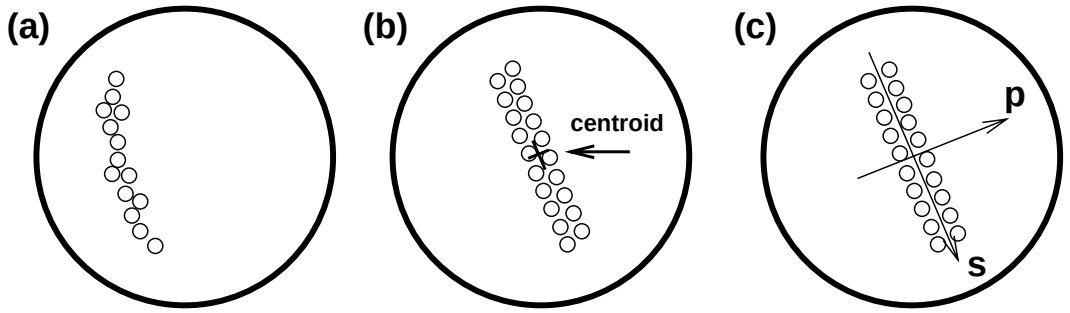

Figure 5.7: Determining the initial shower trajectory. (a) Projection of PMT pointing directions onto the surface of the unit sphere. (b) Projection of PMTs into the plane whose normal is perpendicular to the centroid direction. (c) The new coordinate system defined by the basis vectors.

The plane normals are found for each shower-detector plane and the cross product taken to give the initial trajectory. The core location is then estimated by assuming the two sites lie in the x-y plane, and solving for the intersection of the vectors defined by the intersection of the SDP and the x-y plane. This provides a reasonable estimate of the initial trajectory in most cases.

5.3.3.2 Optimising the Fitting Process

The optimisation of the fitting process was a complex process. To ensure the reconstructed trajectory is the true trajectory, we require the χ^2 function to be as accurate as possible. Developing a composite χ^2 function thus required examining each component carefully to ensure that the fitter worked reliably on a wide range of data. Laserscope data from the 12th of October consisted mostly of stereo events with opening angles $> 10°$ (see figure 5.5) and provided a useful dataset for optimising the χ^2 function. Laserscope data from the 15th was concentrated at small opening angles (see figure 5.5), where the size of the initial simplex was more crucial in accurately reconstructing events. This data provided a further test of the fitting process under tougher reconstruction conditions. This section describes the effects that were taken into account in optimising the fitting process, and the final set of parameters used in the fitting process.

The Stereo Component Stereo amplitude weighting and amplitude fitting were initially investigated and compared. Amoeba passes the trial trajectory to the χ^2 function, and the trajectory is converted into two SDPs for each site from which the stereo χ^2 components are calculated. With either stereo method, it is necessary to restrict the use of PMTs far from the trial plane as they unlikely to be part of the track, and are more likely to be due to noise, or large scattering effects. An off-plane cut of 2.1° (seven 0.3° off plane angular bins – see section 5.1.1.1) was found to work well. A smaller value could be used, but the fitter then tended to push the trajectory to one side of triggered PMTs rather than centering it. Presumably this effect arose because in some cases it could then use substantially fewer PMTs in the fit and thus get an overall reduced χ^2 value.

The effective use of amplitude fitting required some optimisation. As was discussed in section 5.1.1.2, amplitude fitting requires scaling of the estimated PMT response to the actual flux incident over the mirror when integration time of the PMT (it is assumed that the flux is constant over this time period). To obtain an estimate of the actual flux, the average flux over several PMTs surrounding the given PMT was calculated. Averaging over all PMTs in a mirror was initially investigated but was found to perform poorly, presumably due to a significant change in the flux between light triggering the first and last PMTs in the mirror. The best results were found when the flux was averaged over all PMTs within a 3° space angle (radius) of a given PMT. Presumably this angular range is large enough to provide a reasonable number of PMTs to average over, but is not so large that the flux is likely to changes significantly.

There were also occasional large differences between the estimated amplitude and the actual amplitude in a PMT. In such cases the χ^2 component could be extremely large, potentially excluding an otherwise good trajectory (trajectories could be pushed off the centre of the track in a bid to avoid a problematic PMT). Thus individual χ^2 components for each PMT were limited to the 7σ level ($\chi^2_{\mathrm{PMT\,i}} = 49$). This value was large enough that bad trajectory estimates, would still give large overall χ^2 values, but not so large that otherwise good fits would be rejected.

Recent work with Laserscope data has also indicated that the response profiles from the Monte Carlo deviate slightly from those measured (work is underway to improve

the response profile estimates)[6]. Thus the overall reduced χ^2 will not provide a true reduced χ^2 value because, strictly speaking, we do not have the true expected function (our function is also likely to include some error due to the normalisation used). This has the net result that the reduced stereo χ^2 component in equation 5.4 were generally around values of 5 rather than 1.

Stereo reconstructions using amplitude weighting and amplitude fitting were compared, with the two techniques achieving a similar level of reconstruction accuracy. When stereo-timing reconstructions using amplitude weighting and amplitude fitting was compared, amplitude fitting was found to provided greater reconstruction accuracy. An amplitude weighted, amplitude fit was also investigated. In such a fit, the amplitude fitting χ^2 component for a PMT (equation 5.2) was weighted by its relative amplitude (the weighting factor ω_i in equation 5.1). This amplitude weighted, amplitude fit was found to slightly reduce the tail of the error distributions over those obtained with amplitude fitting, and thus was chosen as the stereo χ^2 function in stereo-timing fitting.

The Timing Component The optimisation of the timing section of the total χ^2 is a more difficult task. Stereo-timing fitting was never successfully implemented on Fly's Eye data. This was largely due to the poor timing synchronisation between the two sites (1ms) but it was also due to trigger time slewing effects which are also present in the HiRes prototype data. Trigger time slewing arises due to the variation in triggering time due to the shape of the light pulse in the PMT. If we are viewing a bright track, the pulse will be large and so the PMT will trigger early. Alternatively if we are viewing a dim or distant track, the pulse will be small and/or long and so the PMT may take some time to rise above the threshold level.

Attempts were made to assume that the PMT triggered at some fixed time (such as when the track passed through the centre of the PMTs field of view) with some error, but results were found to be no better than pure stereo reconstruction. Essentially the problem was that the error had to be large enough to account for triggering before and after the assumed point, and this large error meant that the timing component had very little weight in the overall fitting process. Hence an attempt to parameterise

time slewing was made, so that more accurate estimates of the PMT triggering times could be made.

Investigating Time Slewing Time slewing was investigated through a set of laser shots taken on the 6th of May 1997. They were taken using the Laserscope at the site of the 8km-north flasher in the HiRes 2 flasher array (this position was known to within a metre – see section 3.2.5.1 and Bird *et al.*[38]). The Laserscope was triggered by the 1PPS output of a GPS receiver allowing easy identification of Laserscope events in the HiRes datastream.

The laser shots were all taken in the same shower-detector plane as is indicated in figure 5.8. Laser shots were taken at elevation angles of 10° to 90° in 10° steps. Time slewing was investigated through the use of transmission filters placed in front of the Laserscope beam. At each elevation angle, 50 shots were taken with no filter, 50 shots with a 40% transmission filter and 50 shots with a 10% transmission filter. The use of the filters allowed the effect of amplitude to be investigated, and the different elevation angles allowed the effects of PMT crossing time to be investigated.

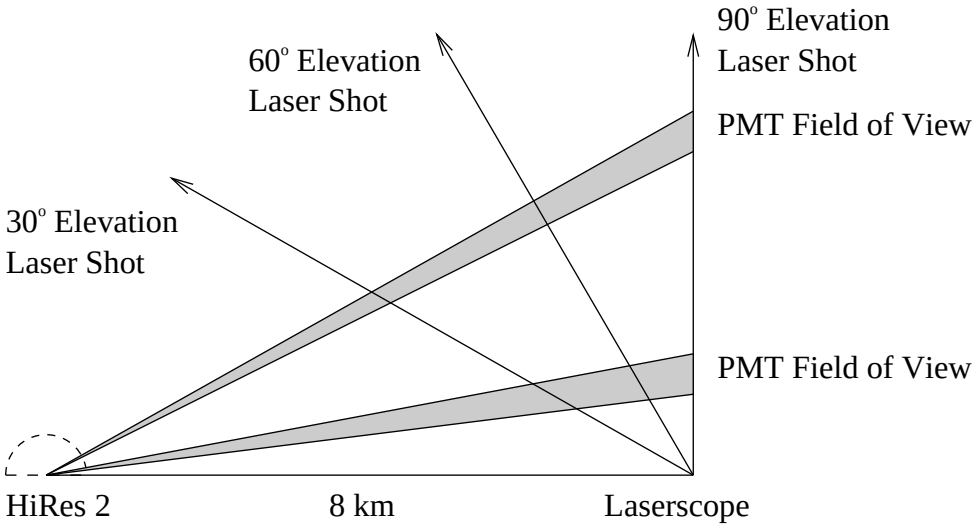

Figure 5.8: Geometry of Laserscope shots taken for the investigation of trigger time slewing. The Laserscope was located 8km to the north of HiRes 2 and laser shots were taken at elevation angles from 10° to 90° in 10° steps. 50 laser shots were taken at each elevation angle and using no filter, a 40% transmission filter and a 10% transmission filter. The triggering time of a set of PMTs was then studied as a function of amplitude and the time taken for light to cross the face of the PMT.

The data was analysed by choosing a set of PMTs from HiRes 2, mirror 3 that

Laser Shot Elevation	Mirror Crossing Time (ns)			Amplitude Range (350nm Photons)		
	no filter	40%	10%	no filter	40%	10%
30°	1485ns	1674ns	1662 ns	3836–7527	1488–3004	517–1012
40°	2273ns	2301ns	2333 ns	2389–4553	955–1806	304–612
50°	2875ns	3033ns		1621–2947	668–1169	
60°	3794ns	3864ns		1225–2143	491–825	
70°	4761ns	4853ns		1004–1617	373–625	
80°	5891ns	5996ns		904–1378	314–545	
90°	7240ns	7413ns		830–1414	323–553	

Table 5.2: Observed average crossing times (ns) and average amplitude ranges in HiRes 2 mirror 3 for time slewing laser shots taken with no filter, 40% and 10% transmission filters. Laserscope was 8km from HiRes 2 and all shots were in the same shower-detector plane. Only PMTs within 0.5° of the SDP were considered. The mirror crossing time were the time difference between the average triggering time of the lowest and highest elevation PMT in the mirror. Average amplitudes were used to determine the amplitude range (using the dimmest and the brightest PMT in the mirror). Laser shots taken with the 10% transmission filter were only able to trigger the detector at elevation angles of 30° and 40°.

had off plane angles of no more than 0.5° to ensure they were directly viewing the track. The mean triggering time and amplitude (expressed as the number of 350nm photons) measured by PMTs was calculated for each set of 50 shots. Standard errors in the mean for PMT triggering times were in the 10-15ns range for most amplitudes and geometries, whilst the 1σ variation of amplitudes varied from around 4% at high amplitudes ($\sim$ 6000 photons) to 15% at low amplitudes ($\sim$ 400 photons). Table 5.2 summarises the observed mirror crossing time (the difference between the average triggering time of the lowest and highest elevation PMT in the mirror) and amplitude ranges (the number of 350nm equivalent photons).

It had been hoped that for a given elevation angle the triggering delay between the start of the second and the laser triggering would be constant (so that the time at which light entered a given PMT would be the same for a given elevation angle, and different filters could be directly compared). However the different intensity laser shots were taken at different stages of the night and it was found that the jitter in the laser triggering time was large (500-1000ns) and such a comparison was not possible. The jitter was thought to arise due to jitter in the actual time of lasing after the laser

received the trigger pulse (which is thought to have a temperature dependence) as well as some jitter in the circuit that produced the triggering pulse for the laser (from the GPS 1PPS). The triggering time of each PMT for a set of 50 consecutive shots was generally quite stable – with most PMTs having standard error in the mean of 10–15ns.

Knowledge of Laserscope position and pointing direction allowed the expected time for light to enter a PMT, and the PMT crossing time to be calculated. This calculation provided a set of reference times that light would enter each PMT in the mirror for a given elevation angle (ignoring the finite spot size). These times were referenced to when light entered the first PMT, so there was an unknown offset between when light entered the first PMT and when it triggered.

To look for time slewing effects, the absolute triggering times for all elevation angles and filters were plotted. For the larger elevation angle shots, it could clearly be seen that for the same set of PMTs, lower amplitudes corresponded to later triggering (as would be expected). Plots of the reference times were overlaid, and slid forwards and backwards in time in an heuristic fitting method. Essentially one tried to fit PMT triggering time as a function of crossing time for different amplitude ranges by adding a (fixed) absolute offset to the calculated time at which light entered each PMT. PMTs with large amplitudes could be expected to trigger soon after light entered their field of view (the 100ns low pass filter had to be taken into account though) whilst progressively lower amplitude PMTs would trigger at progressively larger fractions. The fitting method is illustrated in figure 5.9, where the time at which light enters each PMT (relative to light entering the first PMT) is plotted below the mean triggering times of the PMTs using three different absolute offsets. The requirement of fitting a set of 16 PMTs at different elevation angles and amplitude ranges tended to restrict the range of possible time slewing parameterisations. However it is acknowledged that this technique is heuristic, so two different parameterisations were estimated for use in the fitter programs.

The two parameterisations differed in estimating the fractional crossing time at which PMTs would trigger for a given amplitude. In the "fast" approach, PMTs were allowed to trigger quickly, with the lowest amplitude PMTs (< 300 counts) triggering

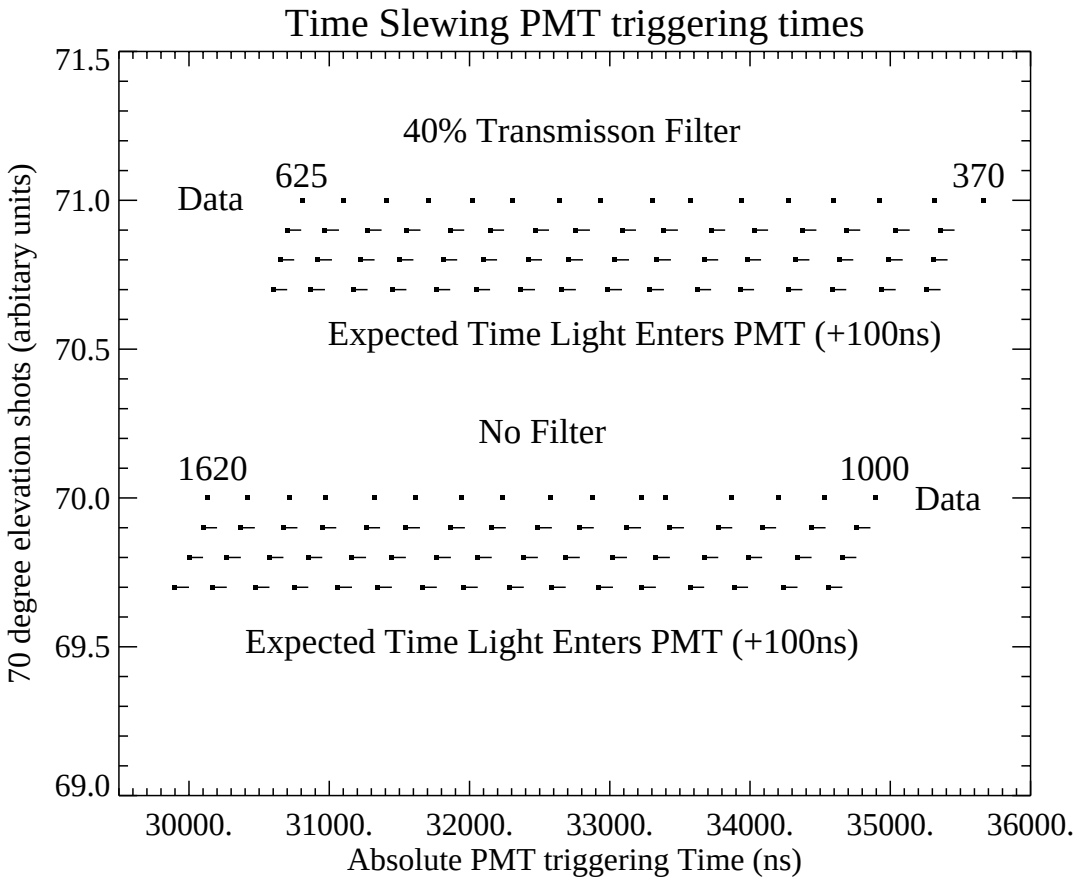

Figure 5.9: Plot showing average triggering time of 16 PMTs viewing a set of 50 laser shots taken with at an elevation angle of 70°. Standard errors in the mean triggering time are not shown but they were generally about 15ns. The average number of 350nm photons for the first and last PMT in the mirror are indicated. Note that as the amplitude decreases, the time between successive PMTs triggering increases (compare the end points between the two data sets). A simulation was performed to determine the expected time at which light should enter each PMT. The absolute offset was unknown and the three sets of data below the actual mean triggering times (marked as data) represent three different values for this offset. We are attempting to estimate how a PMT triggers soon after light enters it. Thus, by varying the absolute offset, noting the amplitude range of the data, and through applying this technique on different elevation angle data, it was possible to roughly estimate possible trigger time slewing parameterisations.

at a fractional crossing time of 65%. In the "slow" approach, the fractional crossing times at which PMTs triggered was larger with the lowest amplitude PMTs triggering at a fractional crossing time of 90%. Both parameterisations were compared, with the "slow" parameterisation performing consistently better than the "fast". The final "slow" parameterisation used is:

- PMT amp < 300 : triggering time = 90% of PMT crossing time
- PMT amp < 600 : triggering time = 60% - 90% of PMT crossing time
- PMT amp < 1000 : triggering time = 50% of PMT crossing time
- PMT amp < 1500 : triggering time = 40% of PMT crossing time
- PMT amp < 3000 : triggering time = 30% of PMT crossing time
- PMT amp > 3000 : triggering time = 20% of PMT crossing time

Time fitting used the time slewing parameterisation to improve its estimates of the expected PMT triggering time. The error in the triggering time for each PMT was fixed prior to calling the timing fit. Due to the problem of not knowing the shape of the pulse in the PMT, it was difficult to estimate the true uncertainty in the triggering time. It was decided to fix it to 10% of the PMT crossing time, with a lower limit of 25ns. A problem arises because we wish to have the error fixed for the entire fitting process (so different trajectories can be compared under standard conditions). Hence, prior to calling stereo-timing fitting, a stereo amplitude weighting fit was performed to improve the estimation of the true trajectory. This trajectory was then used to estimate PMT crossing times and thus PMT triggering errors. Due to the difficulties involved in estimating triggering times, a tighter off-plane cut of 0.45° was used for the timing component of the χ^2 . This ensured that for a given trajectory, only PMTs directly viewing the track would be considered. This cut restricted any slightly off-plane PMTs that may include a scattered light contribution (which complicate the time of triggering issue) from being used.

It is also worth considering the choice of the timing synchronisation error $\sigma_{1-2\,\mathrm{Offset}}$, which effectively limits the range of timing synchronisation offsets between HiRes 1

and HiRes 2 (as value much larger than this will have large $\chi^2_{1-2\ \mathrm{Offset}}$ values in eqn 5.4). Large choices of the error ($\sim 5\mu$s) tended to occasionally allow large values of the time synchronisation parameter that corresponded to a bad overall fit. In this case the timing information became nearly useless, providing little constraint on the fits and occasionally allowing bad overall fits. Small choices ($\sim$ 100ns) tended to prevent larger synchronisation values (200ns or more) from being considered as their χ^2 components would be large, and the fitter could usually find a trajectory that was close to the true trajectory and had a smaller time synchronisation error. A timing synchronisation error estimate of 500ns was found to perform the best. For the Laserscope data this produced a distribution of timing synchronisation values centered on 0ns with a FWHM of 190ns.

Determining the Initial Simplex Size Prior to calling Amoeba to find the best trajectory, we must set the size of the initial simplex about the initial trajectory (see section 5.1.7). The size of the initial simplex loosely corresponds to the range of parameter space that Amoeba searches over. The larger the space, the greater the risk of Amoeba finding some local minimum rather than the global minimum, hence choosing the size of the initial simplex passed to Amoeba was carefully examined. Optimisation of the search space was performed in conjunction with optimising the χ^2 fitting function.

The choice of the size of the initial simplex is usually not crucial, provided that it is not too large. However as the opening angle and the effectiveness of stereo fitting decreases, the sensitivity to the choice of search size increases. Several different simplex sizes were investigated before it was decided to take an iterative approach. The simplex size about the was initially set to be small, and was progressively increased. The final simplex sizes used were:

1. 1° zenith angle range, 1 km in x and y coordinates
2. 3° zenith angle range, 3 km in x and y coordinates
3. 10° zenith angle range, 10 km in x and y coordinates
4. 10° zenith angle range, 15 km in x and y coordinates

5. 40° zenith angle range, 50 km in x and y coordinates

6. 90° zenith angle range, 150 km in x and y coordinates

The azimuth angle search space was based on the zenith angle search size, but corrected for zenith angle effects (the azimuthal range was increased as zenith angle decreased to maintain a constant solid angle search size). The χ^2 value and fitted trajectory was recorded after each search. If the smallest χ^2 was less than 50 after trying the first three simplex sizes, the corresponding fitted trajectory was recorded, and the larger simplex sizes were not tried. The larger simplex sizes were generally only useful at small opening angles or large zenith angles when the initial estimate was poor.

Given a initial simplex and trajectory, Amoeba was called in a two step process. Amoeba was first called in stereo amplitude weighting mode to refine the initial trajectory. If the refined estimate was good (defined as $\chi^2 < 50$) it was used as the initial guess for the next stage, otherwise the original guess was used. Amoeba was then called using the refined trajectory as the initial guess to perform an amplitude fitted stereo-timing fit. Note that in both cases Amoeba was called twice, with the result of the first fit used as the input to the second fit, in an attempt to ensure a global, rather than local minimum is found. The decision to perform a stereo fit prior to the stereo-timing fit was based on the experience gained in optimising the program, and the need to provide good error estimates for PMT triggering times as discussed above.

The downhill simplex method requires a good choice of the initial trajectory.However, when the opening angle between the two SDPs is small, small errors in the plane normals can have a large effect on the initial trajectory. Similarly in cases where the zenith angle is large (highly inclined showers), errors can cause large shifts in estimations of the the core location. Hence if the initially estimated zenith angle was greater than 85° or if the opening angle between the plane normals was less than 15°, further estimates of the initial trajectory were made.

Handling Situations where the Initial Trajectory may be Poor The downhill simplex method requires a good choice of the initial trajectory.However, when the opening angle between the two SDPs is small, small errors in the plane normals can

have a large effect on the initial trajectory. Similarly in cases where the zenith angle is large (highly inclined showers), errors can cause large shifts in estimations of the the core location. Hence if the initially estimated zenith angle was greater than 85° or if the opening angle between the plane normals was less than 15°, further estimates of the initial trajectory were made.

New estimates of the trajectory were made by adding a random error to the normal vectors for the HiRes 1 and HiRes 2 shower detector planes and recalculating their new intersection. The errors were selected so that the space angle between the old and new plane normal were sampled from a gaussian with a standard deviation of 1.0°. This sampling was done 15 times for both the HiRes 1 and HiRes 2 plane normals and the resultant trajectories calculated. The trajectories with the maximum and minimum zenith angles (as these were generally the most different from the original trajectory), along with the original estimate of the trajectory, were then stored.

The next step was to decide upon the best initial trajectory to be used by the main fitting process. It was decided to use Amoeba in a stereo-timing mode using approximate triggering time errors. Triggering time errors for each PMT were simply set to be 10% of the time difference between the current PMTs triggering time and the next PMTs triggering time, with a lower limit of 100ns. The initial simplex size (about the initial trajectory) was set to 10° in zenith and azimuth angles (with the azimuth range adjusted for large initial zenith value), and 20km in the x and y core parameters. For the cases where the initial zenith angle was large ($> 85°$), small changes in zenith angle could move the core location by tens of kilometres. Thus to allow Amoeba full freedom to alter the trajectory such that the zenith angle might change slightly whilst the core location may change significantly, the x and y search space was set to be the size of the initial x and y core guesses. For each of the three initial guesses, Amoeba was called to search for the trajectory that minimised the stereo-timing χ^2 function. The initial trajectory that resulted in the smallest χ^2 value was then used as the initial trajectory in the main fitting stage.

This method achieved some degree of success, but was by no means guaranteed to recover all poor initial guesses. Often the poor trajectories were associated with short tracklengths in the top elevation ring of the HiRes 1 mirrors. It was then possible to

have degenerate situations where a trajectory that had a very large zenith angle and a core location 200km from HiRes 1 was as acceptable as a trajectory that had a smaller zenith angle and a core location 5km from HiRes 1. With further work, it should be possible to develop more robust techniques for these cases. However, as the number of cases in which the initial trajectory is poor is not large, it was decided to leave such work to another time.

5.4 Reconstruction Results

The optimised reconstruction program was used to reconstruct the two nights of Laserscope data. The Laserscope data provide a wide cross-section of events whose position and trajectories were well known, allowing a good comparison between stereo, timing and stereo-timing reconstruction techniques. The reconstructed trajectories were compared with the Laserscope data to obtain space angle error distributions which provide a direct measure of the reconstruction accuracy (these distributions were used to optimise the reconstruction techniques). Space angle integral error distributions for the different reconstruction techniques applied to data from the 12th and 15th of October are presented in figures 5.10 and 5.11 and summarised in tables 5.3 and 5.4 respectively.

Distributions of the component χ^2's and the total χ^2's (equation 5.4) were also obtained with results for the total χ^2 summarised in tables 5.3 and 5.4. Well reconstructed events had small χ^2's and approximately balanced components. These reduced χ^2's were generally larger than 1, indicating that the expectation functions used were not perfect. Poorly reconstructed events generally had large χ^2's , allowing quality cuts to be made on the data by rejecting events with large χ^2 values. Placing a cut of $\chi^2 < 50$ on stereo-timing data was found to suppress the tail in the space angle distribution as seen in figures 5.10 and 5.11 and tables 5.3 and 5.4. Such a cut reduced the number of reconstructable events from 4343 to 4110 (5%) on the 12th and 6811 to 5743 (16%) on the 15th.

Stereo fitting performed quite well for large opening angles, with the accuracy degrading as opening angle decreased. This opening angle effect is clearly visible

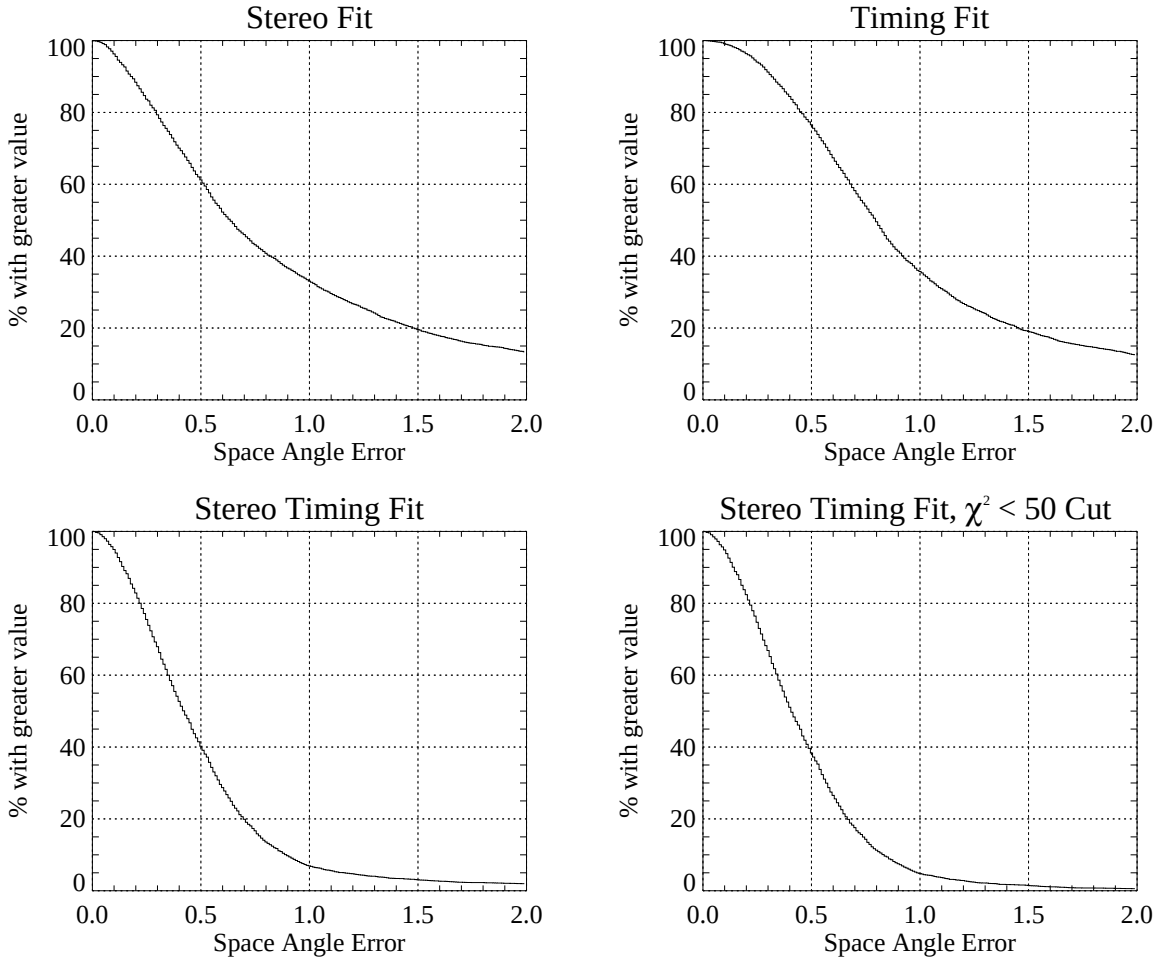

Figure 5.10: Space angle integral error distributions for different fitting techniques based on the nominal directions of the Laserscope for data taken on the 12th of October 1996. Note how stereo and timing perform equally well, and how reconstruction accuracy improves when they are combined in stereo-timing fitting.

when comparing space angle distributions from the two nights. Reconstruction of data taken on the 12th has a much tighter space angle distribution than data taken on the 15th. Apart from any opening angle effects, the distribution from the 15th is expected to be slightly worse than that from the 12th as it corresponds to the use of the Nitrogen laser. As was discussed earlier in section 5.2.1, the pointing accuracy of the Nitrogen laser was worse than that for the YAG laser, an effect contributing to the space angle error.

At small opening angles stereo fitting was found to systematically shift the core location away from the detectors (by as much as 1km in the data from the 15th) in conjunction with increasing the zenith angle (with respect to the Laserscope value

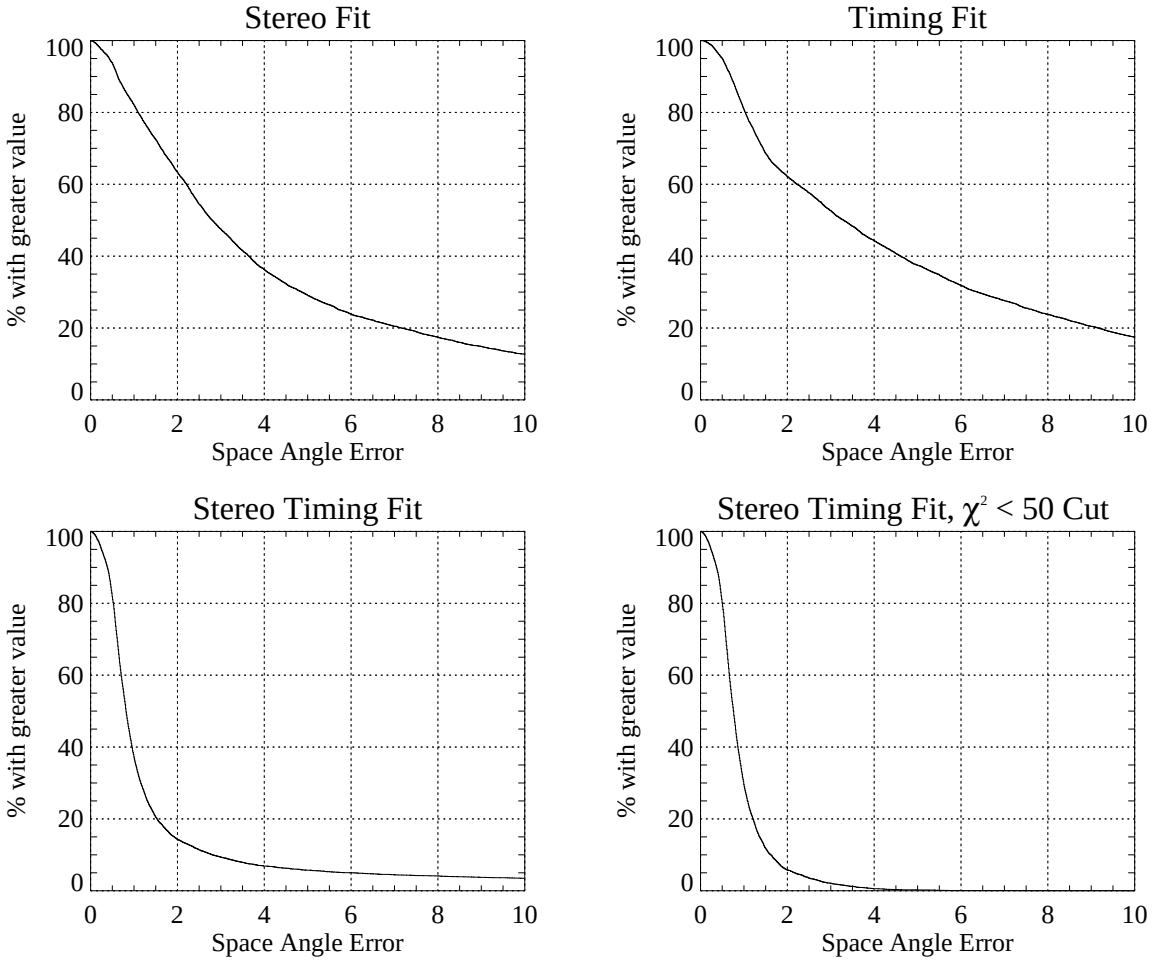

Figure 5.11: Space angle integral error distributions for different fitting techniques based on the nominal directions of the Laserscope for data taken on the 15th of October 1996 (predominantly small opening angles). Note how stereo-timing fitting once again improves on either stereo or timing fitting. Also note how application of a $\chi^2 < 50$ cut suppresses the tail of the distribution.

resulting in a larger space angle). The reasons for this effect were investigated but no other correlation (apart from that with small opening angle) were found (this effect was present over a wide range of tracklengths and amplitudes – see figures 5.5 and 5.6).

Timing fitting was also investigated, and found to be slightly worse than stereo in most cases. Whilst timing fitting was not subject to opening angle effects present in stereo fitting, uncertainty in the PMT triggering times meant that timing fitting generally did not perform significantly better than stereo in the case of small opening angles. It is interesting to note that the results from October 12th presented in table 5.3

Fit Type	Space Angle			χ^2	
	50%	90%	% > 2°	Max Bin	FWHM
Stereo	0.65°	2.5°	13%	6	7
Timing	0.8°	2.3°	12%	8	8
Stereo-Timing	0.4°	0.9°	1.7%	14	10
Stereo-Timing $\chi^2 < 50$	0.4°	0.85°	0.7%	14	10

Table 5.3: Reconstruction results for stereo viewed laser shots taken on the 12th of October 1997. The space angle error is the angle between the fitted and actual trajectory. Integral error distributions were obtained and the values containing 50% and 90% of the data are presented. Note how stereo and timing produce similar results, and that by combining the two in stereo-timing greatly increases the reconstruction accuracy. Placing a cut of $\chi^2 < 50$ enabled rejection of poorly reconstructed events (5% of the total number of events).

Fit Type	Space Angle			χ^2	
	50%	90%	% > 10°	Max Bin	FWHM
Stereo	2.75°	11.5°	13%	10	12
Timing	3.3°	14.7°	17%	8	7
Stereo-Timing	0.9°	2.9°	3%	19	12
Stereo-Timing $\chi^2 < 50$	0.8°	1.8°	0.05%	19	12

Table 5.4: Reconstruction results for stereo viewed laser shots taken on the 15th of October 1996. The space angle error is the angle between the fitted and actual trajectory. Integral error distributions were obtained and the values containing 50% and 90% of the data are presented. Note the poor resolution with stereo and timing reconstruction due to small opening angles, and how stereo-timing improves the reconstruction accuracy. Placing a cut of $\chi^2 < 50$ enabled rejection of poorly reconstructed events (16% of the total number of events).

(with opening angles generally greater than 10°) are comparable to those obtained with the Monte Carlo simulation presented in table 5.1. Thus one conclusion that we can draw is that the time slewing corrections being used are probably reasonable.

As was suggested by the preliminary Monte Carlo trials, stereo-timing fitting overcomes the systematic shifts present in stereo fitting to provide generally more accurate reconstruction. This improvement occurs because the fitter is restricted by the PMT triggering times – moving/twisting the trajectory away from the detector will have a detrimental effect on the timing χ^2 component thus preventing such behaviour. The

Fit Type	< Xcore > $\pm 1\sigma$ (km)	< Ycore > $\pm 1\sigma$ (km)	R Core Error	
			50%	% > 0.25
True Posn	1.459	6.708	(km)	(km)
Stereo	1.451 ± 0.06	6.659 ± 0.11	0.065	9%
Stereo-Timing	1.452 ± 0.04	6.682 ± 0.08	0.050	3%
Stereo-Timing $\chi^2 < 50$	1.452 ± 0.04	6.682 ± 0.08	0.050	2.5%

Table 5.5: Reconstruction results for stereo viewed laser shots taken on the 12th of October 1996. Fitted mean and 1σ X and Y core locations are shown compared to the true position. Integral error distributions were obtained for the radial error ($R = \sqrt{X^2 + Y^2}$) and the distances containing 50% and 90% of the data points are presented.

reconstruction accuracy as a function of opening angle for stereo-timing is presented in figure 5.12. These figures plot the median space angle and the 0-95% range as a function of opening angle (this range is effectively the 2σ error), before and after applying a $\chi^2 < 50$ cut. The $\chi^2 < 50$ cut was used to reject the occasional cases that failed the fitting process. After application of the $\chi^2 < 50$ cut it can be seen that the median error is almost always less than 1°, and is generally around 0.4° for opening angles greater than 10°. The 95% error is also generally less than 1°, increasing slightly as opening angle decreases (at small opening angles the poor performance of stereo does have a limiting effect on the performance of stereo-timing fitting). Encouragingly, these results are not much worse than those obtained with the Monte Carlo simulations (table 5.1) which were performed with a much more favourable opening angle range and assuming that time slewing effects were completely compensated for. These results thus give us confidence that we can accurately reconstruct the arrival directions of EAS to within one degree 95% of the time.

5.5 Reconstruction Accuracy for HiRes Stage 1.0

The configuration of the stage 1.0 HiRes detector is significantly different from that of the prototype. HiRes Stage 1.0 consists of a single ring of mirrors at HiRes 1 ($3° - 16.5°$ in elevation, 360° in azimuth) and two rings of mirrors at HiRes 2 ($3° - 30°$ in elevation, 360° in azimuth) designed to maximise the high energy aperture.

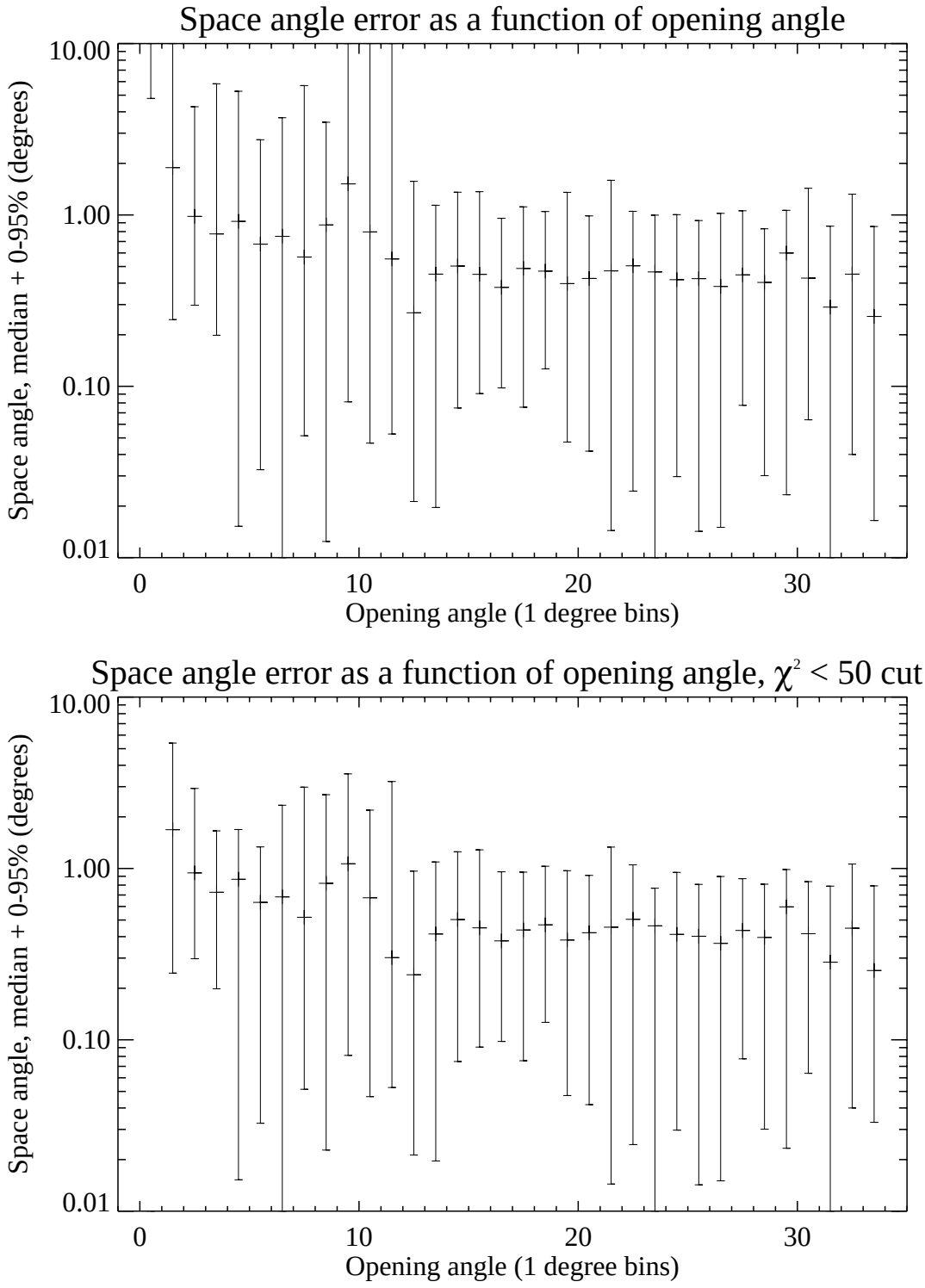

Figure 5.12: Space angle error as a function of opening angle for stereo-timing fit for combined Laserscope data from 12th and 15th of October 1996. Application of a $\chi^2 < 50$ cut reduces the 95% error level so that most events are reconstructed to better than 1°.

Whilst the reconstruction programs were written for reconstruction of prototype data, it is obviously of interest to examine how they perform on data from the stage 1.0 configuration. Such an analysis was performed, by rejecting all information from the top four elevation rings of HiRes 1. All information from HiRes 2 was retained. This restriction reduced the number of reconstructible events from 4343 to 2835 on the 12th, and from 6811 to 3819 on the 15th. The space angle error distributions for these events were calculated for both the stage 1.0 configuration and the prototype configuration The results from the 12th of October are summarised in table 5.6 and the results from the 15th of October are summarised in table 5.7. Space angle error distributions for Stage 1.0 results are presented in figure 5.13 (for both nights, before and after the $\chi^2 < 50$ cut).

Space Angle Error	50%	90%	% > 2°
Prototype configuration	0.45°	0.9°	2%
Stage 1.0 configuration	0.5°	1.3°	6%
After $\chi^2 < 50$ cut			
Prototype configuration	0.4°	0.8°	0.3%
Stage 1.0 configuration	0.5°	1.0°	1%

Table 5.6: Reconstruction results for Laserscope data from the 12th of October. Stage 1.0 configuration consisted of using ring 1 mirrors at HiRes 1 (mirrors 5 and 7) and all four HiRes 2 mirrors. The same set of 2835 events were used to produce all the statistics.

Space Angle Error	50%	90%	% > 2°	% > 10°
Prototype configuration	0.75°	3°	12%	3%
Stage 1.0 configuration	1.0°	57°	34%	22%
After $\chi^2 < 50$ cut				
Prototype configuration	0.75°	1.3°	2.5%	0
Stage 1.0 configuration	0.75°	2.0°	10%	0

Table 5.7: Reconstruction results for Laserscope data from the 15th of October. Stage 1.0 configuration consisted of using ring 1 mirrors at HiRes 1 (mirrors 5 and 7) and all four HiRes 2 mirrors. The same set of 3819 events were used to produce all the statistics.

The results are encouraging as they illustrate that fitting does very well despite the

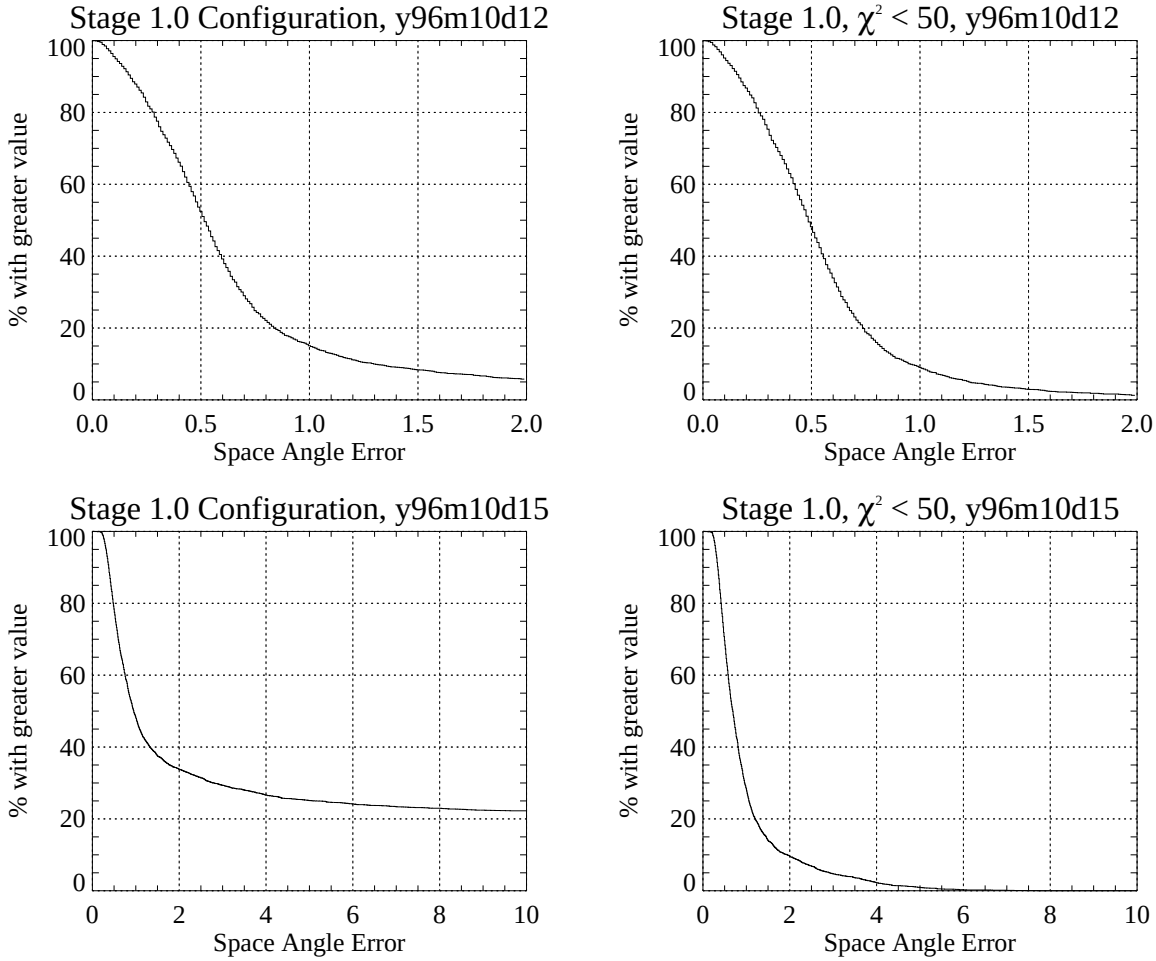

Figure 5.13: Space angle error distributions using the HiRes Stage 1.0 configuration (only ring1 mirrors at HiRes 1). Note how the tail of badly reconstructed events is eliminated by application of the $\chi^2 < 50$ cut.

loss of 54° of the zenith coverage. The majority of events were well reconstructed but there were a large number of events at small opening angles (data from the 15th of October) that were badly reconstructed. It was decided to look more closely at these events, as understanding why events fail the fitting process may allow us to develop ways to improve their reconstruction.

Events that had large space angles ($> 2°$ on the 12th and $> 10°$ on the 15th) were flagged for further analysis. These events were then broken down into those that only failed the stage 1.0 fit and those that failed both stage 1.0 and the prototype configuration (all mirrors). Following some initial investigations, analysis was concentrated on HiRes 1 mirror 7 data from the 12th and on HiRes 1 mirror 5 for data from the 15th, since the the majority of failed events passed through these mirrors as their field

of views were closest to the Laserscope on their respective nights.

Events that failed the stage 1.0 fit and events that failed both stage 1.0 and the prototype configuration fits were selected. The number of times each PMT in a mirror triggered was recorded and plotted for the two cases (using HiRes 1 mirror 7 for data from the 12th of October and HiRes 1 mirror 5 for data from the 15th of October). Figure 5.14 illustrates the number of times each PMT in the given mirror triggered for events that failed only the stage 1.0 configuration fit. Figure 5.15 illustrates the number of times each PMT in the given mirror triggered for events that failed both the stage 1.0 configuration fit and the normal prototype configuration fit.

To highlight observed trends, the individual PMT triggering rates for those that failed the stage 1.0 fit and those that failed both stage 1.0 and the prototype configuration fits were plotted. Figure 5.14 illustrates the PMT triggering rates for all PMTs in mirror 7 on the 12th and for all PMTs in mirror 5 on the 15th that failed only the stage 1.0 configuration fit. Figure 5.15 illustrates the PMT triggering rates for all PMTs in mirror 7 on the 12th and for all PMTs in mirror 5 on the 15th that failed both the stage 1.0 configuration fit and the normal prototype configuration fit.

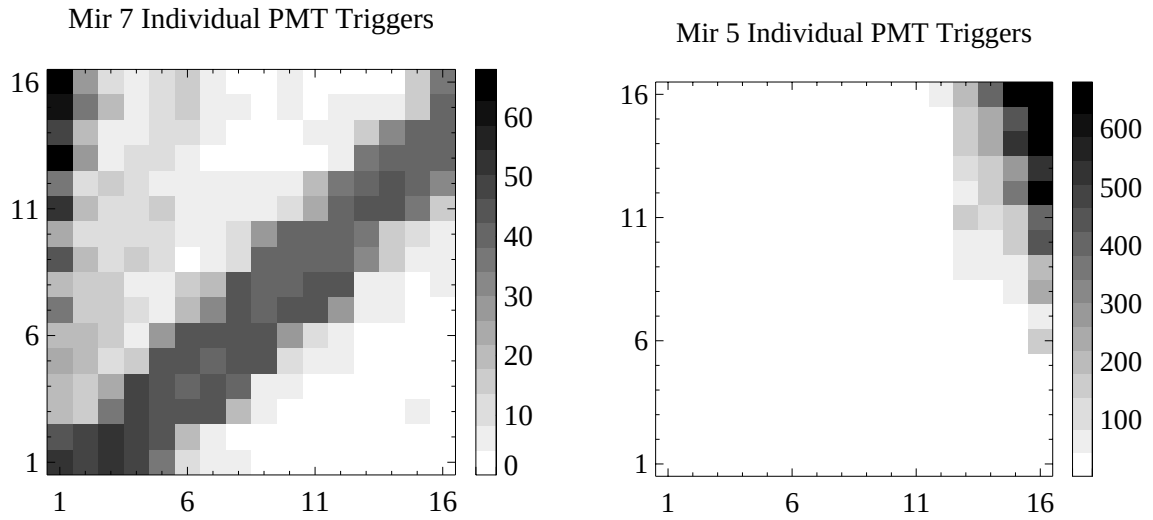

Figure 5.14: Plots of the number of times each PMT in HiRes 1 mirror 7 (for data from the 12th of October) and HiRes 1 mirror 5 (for data from the 15th of October) triggered for events that were badly reconstructed by stage 1.0 configuration fit, but not by the normal prototype configuration fit. Note the large number of events that are clipping the outside vertical edge of the mirrors (135 from 2835 events for mirror 7 and 771 from 3819 events for mirror 5).

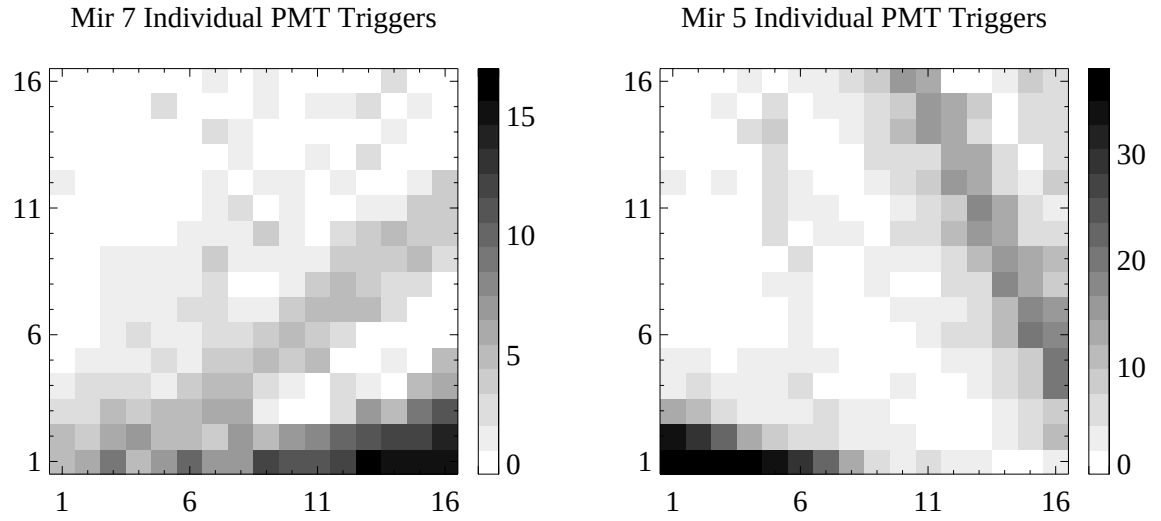

Figure 5.15: Plots of the number of times each PMT in HiRes 1 mirror 7 (for data from the 12th of October) and HiRes 1 mirror 5 (for data from the 15th of October) triggered for events that were badly reconstructed by both the stage 1.0 configuration fit and by the normal prototype configuration fit. Note how the majority of events that failed both fitters were close to horizontal in these mirrors (28 from 2835 events for mirror 7 and 79 from 3819 events for mirror 5).

Encouragingly, the majority of events that failed only stage 1.0 configuration occurred when the laser shots were clipping the outside vertical edge of the mirror. Given that stage 1.0 will consist of a full azimuth ring such gaps will not exist. This edge clipping prevents observing the full shower width, and as the fitting is geometrically based (it uses the offplane angle to estimate PMT amplitude) a significant loss of information, combined with noise and scattering, leads to the large fitting error. Such clipping also limits the number of PMTs in the event making reconstruction more difficult (as less information is available).

There were also some events which looked as though they should have been well reconstructed but were not. By examining individual events it was noticed that there was significant scattering occurring early in the tracks. This problem, along with the very short tracklength in mirror 5 and any noise PMTs, may have contributed to producing bad fits for these events.

Events that failed both fitting configurations were predominantly low elevation tracks. They generally appeared very short and near horizontal which probably limited the reconstruction. It is again interesting to note that many of these events were

clipped by the limited angular coverage of the prototype detector, and thus may be reconstructed with the true stage 1.0 detector as such tracks would trigger adjacent mirrors. Other events that failed both fitters often had a larger than normal number of noise PMTs present, which probably were not correctly flagged (noise rejection performs best when there are many more good PMTs than noise PMTs) and may have helped distort the fitting process. Based on these observations it would appear that with further work, many of these problems could be overcome by the time the detector begins operation in Stage 1.0.

5.6 Summary

In summary, a program to reconstruct stereo viewed EAS has been successfully developed for use on prototype data achieving a reconstruction accuracy of one degree 95% of the time for opening angles down to a few degrees. The results of reconstruction of Laserscope data support the results of Monte Carlo analysis, namely that stereo-timing reconstruction performs the best. This represents a significant achievement over the Fly's Eye, where stereo-timing reconstruction was not possible and only events with track lengths greater than 40° and opening angles of at least 20° were reconstructed. In the next chapter, the reconstruction programs developed will be applied to approximately two years of stereo data from HiRes prototype.

Chapter 6

Analysis of Stereo Observed EAS

The HiRes prototype collected almost two years of stereo observations with the GPS clocks. This chapter is concerned with the analysis of the stereo data obtained over this period. This covers the extraction of the cosmic ray candidates events from the dataset and their processing through the trajectory fitting program discussed in chapter 5. There follows a discussion of reconstruction of the shower light profile so as to estimate shower parameters such as depth of shower maximum and energy.

A profile fitting program previously developed for the analysis of coincident HiRes 1 and Michigan Muon Array (MIA) events[115] was modified for use on the stereo dataset. These modifications included updating the aerosol model, and thus a comparison of the effect on profile fitting and energy of different aerosol models is presented. Finally a brief summary of results of profile fitting the stereo dataset is presented together with a comparison of the reconstruction using the HiRes prototype and the Stage 1.0 configuration of HiRes.

6.1 Extracting Candidate Cosmic Ray Events

Approximately 880 hours of stereo data was obtained between January 1995 and November 1996 when the prototype detector was shut down in preparation for the stage 0.5 detector. The author was directly involved with collection of nearly $\sim 18\%$ of this data and was responsible for matching the data from the two detectors and then extracting any cosmic rays present.

6.1.1 Event Matching

The two HiRes detectors are operated independently, so events from the two detectors must be matched offline to obtain the stereo dataset. The matching program which was developed used a two pass timing filter (similar to that described in section 4.5.1) on the raw data to match events. The first pass checked that the Julian day event times at both sites were within one millisecond of each other. The second pass checked that the difference in holdoff times between the first mirror to trigger at each site, were within a specified time window.

The choice of the time window had to take into account the light travel time between the two sites (42μs), and that the different detectors may view different sections of an EAS. A process of trial and error led to a time window of -50μs and 150μs for the HiRes 2 – HiRes 1 first mirror holdoff time difference. This was found to be sufficiently wide to allow reliable matching of all stereo events. This process matched a total of 462,254 events from the 880 hours of stereo ontime (from over 42 million HiRes 1 and 84 million HiRes 2 events). These events were calibrated and then filtered to reject non-cosmic ray events.

6.1.2 Rejecting Non Cosmic Ray Events

The matched stereo data set comprised in excess of 400,000 events due to stereo triggers on random noise, aircraft, lightning, ground based atmospheric laser and Xenon flasher shots and cosmic rays. As very few of these events were cosmic rays, filtering was necessary to obtain the set of candidate cosmic ray events. Such filtering utilised the different characteristics (such as the pattern or order of triggered PMTs) possessed by the different event types. Examples of stereo triggers on non-cosmic ray events are presented in figures 6.1 and 6.2.

Most triggers due to random noise, aircraft, lighting and flares (the detector is located on a military base) could be removed using a filter based on the Rayleigh test which looked for a (non random) spatial and temporal progression in the PMT triggering. Triggers on ground based atmospheric shots from the fixed Yag laser, Xenon flashers and the Laserscope could be identified based on their upward going

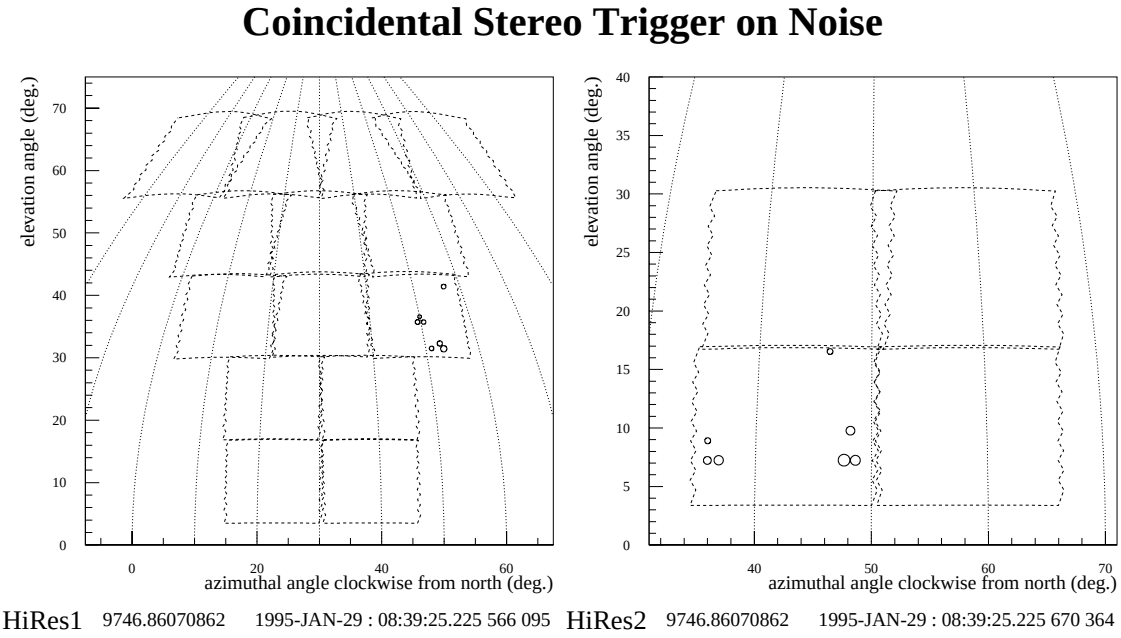

Figure 6.1: Examples of stereo triggers on noise and light from an aeroplane.

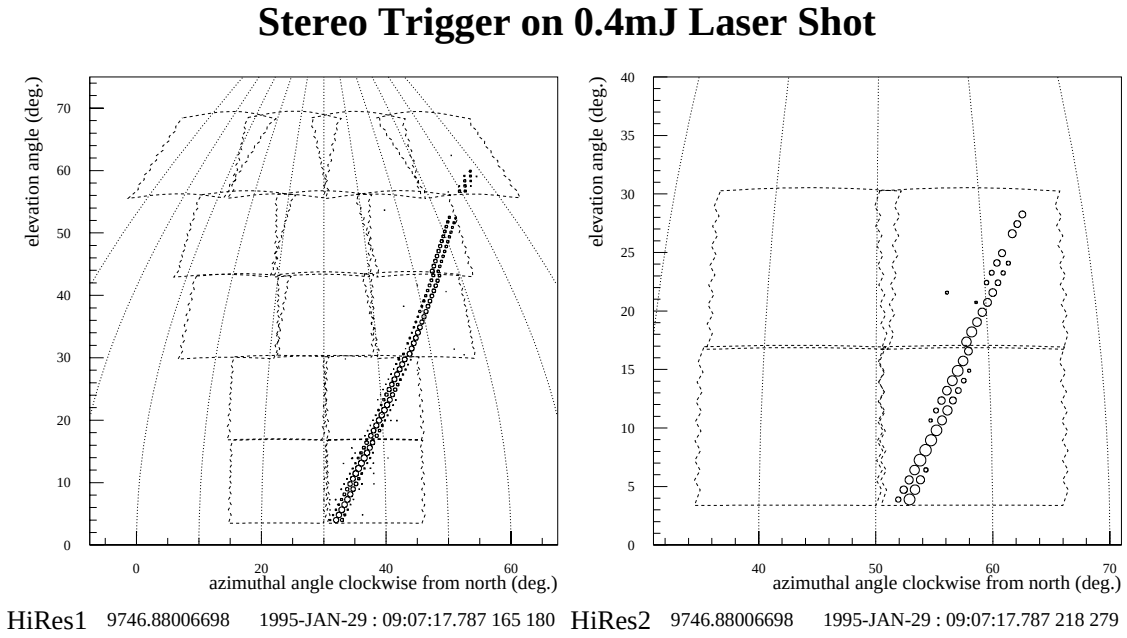

Figure 6.2: Examples of stereo triggers on atmospheric laser shots

nature, the standard PMT triggering patterns and the triggering frequency (they all fired at rates of $\sim$ 1Hz). These filters, and their effectiveness will now be described.

6.1.3 Rayleigh Filtering

The Rayleigh filter essentially compares the track length of the event with that expected from a two dimensional random walk for the same number of PMTs. The Rayleigh probability distribution function[147] describes the probability of obtaining a vector of total length between r and $r + dr$ when summing n random vectors in two dimensions. One can use this function to estimate the probability of obtaining a vector of length R, when adding n random vectors, through random chance alone.

In practise the program developed was a slight variant of the Rayleigh test. PMTs at each site were first time ordered. For each PMT, Rayleigh vectors (the vector difference between two PMTs pointing directions) were calculated between the current PMT and any PMTs that subsequently triggered and were within a space angle of 2.5°. This process is performed for all PMTs in the event (at each site) and the n vectors are added to obtain a vector of total length R. In noise events, the n individual vectors should be uncorrelated leading to a random walk based Rayleigh vector of length $\sim \sqrt{n}$. In real tracks, the individual vector directions should point in the approximate direction of the track, so that the sum of the n vectors approaches a length n. Hence events may be filtered by choosing a random chance probability and only accepting events which have a Rayleigh probability less than this value (ie they are unlikely to have a length R through random chance alone). It should be noted that the probability levels used are not the true probabilities since strictly the vector was not calculated in a two dimensional plane (in which the Rayleigh distribution was calculated). However, the surface of a sphere over a 2.5° solid angle is a reasonable approximation to a plane so that the probability levels used are close enough to be effective in selecting cosmic ray like events.

Cosmic ray like events were selected by requiring chance probabilities of less than 5% at both sites, and a downward pointing vector in at least one site. The Rayleigh filter was very effective in removing the vast majority of events due to triggers on

noise, aircraft and upward going atmospheric laser and Xenon flashers shots present in the data. The Rayleigh filter was only moderately effective on events in which very large numbers of PMTs triggered (at least half of PMTs at a site). Such events were usually due to lightning, bright aircraft or high intensity laser shots (20mJ). There were also occasional events comprising a downward going cosmic ray track in HiRes 1 and a upward going Xenon flasher in HiRes 2. Thus events passing the Rayleigh filter were scanned by eye to remove any obvious non-cosmic ray events.

6.1.4 Rejecting Ground Based Atmospheric Laser/Xenon Flasher Shots

A large percentage of the stereo dataset comprised triggers on atmospheric laser and Xenon flasher shots. The YAG laser (located at Fly's Eye II) was fired at the start of each hour in a regular set of geometries at intensities of 0.4mJ and 20mJ. The 0.4mJ intensity shots were used for atmospheric monitoring (see section 3.2.5) and such shots would generally trigger between 100 and 300 PMTs at HiRes 1 and form long upward going tracks in both sites. The intersite Xenon flasher (see section 3.2.5.1) fires every 7 minutes and produces upward going stereo tracks. Event times for intersite flashers events had been previously flagged in atmospheric studies and were thus easily removed from the dataset (these were also effectively filtered by the Rayleigh filter)

The high intensity 20mJ shots were taken from January to July 1995 whilst the YAG laser was being tested as a LIDAR system (see section 3.2.5.2). The high intensity nature of these shots, coupled with the closeness of HiRes 1 to the firing location (Fly's Eye II is $\sim$ 3km distant) meant that light scattered out of the beam was intense enough to trigger large numbers (sometimes all) of PMTs at HiRes 1. HiRes 2 was distant enough that it only triggered on the main beam (see figure 6.2).

The high intensity events events were somewhat problematic as they were not efficiently rejected by the Rayleigh filter and produced extremely large and somewhat unwieldy datasets (the stereo dataset from the first six months of 1995 is approximately 3.5 Gigabytes whilst the corresponding dataset from 1996 is only 0.5 Gigabytes). Thus it was decided to try to extract the laser shots from the dataset - both to produce a

more manageable dataset and as a check on the Rayleigh filter.

The task of selecting and removing laser shots from the data set took advantage of two basic properties of the laser shots – that the laser was firing at a constant rate of 1Hz and that the laser shots were upward going from a fixed location. Summary information was obtained for all events and the events were split split into two groups – those in which more than 100 PMTs triggered in HiRes 1 (lasers, intersite flasher, and cosmic rays) and those in which less than 100 PMTs triggered (noise, and cosmic rays). The events with less than 100 PMTs at HiRes 1 were filtered using the Rayleigh test on the assumption that they were mostly noise triggers. Laser identification concentrated on the dataset in which more than 100 PMTs triggered at HiRes 1.

Time differences between successive events for this dataset was then determined. All events with time differences between 0.95 and 1.05 seconds were flagged as laser shots. To ensure that these truly were laser shots and not cosmic rays that by chance slipped in, the events before and after each event were examined and 15 point running means of the number of PMTs that triggered in HiRes 1 calculated in both time directions from the current event (the current event was excluded from the mean calculations). Any events in which the number of triggered PMTs in HiRes 1 was more than 3 standard deviations from the mean in both directions were flagged and the events visually scanned. This cut worked on the assumption that sequential laser shots should have identical trajectories and any cosmic rays that slipped in would trigger a different number of PMTs to the local average. No cases were found in which cosmic rays were by chance within the 0.95 to 1.05 second time window (these events were generally laser shots in which a mirror did not trigger). Events with time differences outside 0.95-1.05 seconds were scanned by eye and consisted of triggers on the first laser shot of each geometry, aircraft, lightning and candidate cosmic rays which were flagged.

This process enabled identification of almost all laser shots as well as providing a check on the effectiveness of the Rayleigh filter. The cosmic rays found with this method were checked with those found by a Rayleigh filter for the 1995 dataset and the two methods were found to be equivalent. Occasionally the current method found a few more candidate events, but they were generally only track-like in one site, and

marginal in the other (possible triggers on cosmic rays at one site and an aircraft or Cerenkov blast at the other). Thus only the Rayleigh filter was used to produce a set of candidate events for the 1996 dataset.

6.2 Shower Profile Fitting

The stereo-timing fitting program discussed in chapter 5 was used to estimate trajectories for the candidate cosmic rays. Since the classification of candidate cosmic rays was fairly loose (see section 6.1) roughly one quarter of events failed the noise and time filtering tests (251 of 1020 events). A further 15% (107) events then failed the stereo-timing fitting process, where a fail was defined as a failure of one of the χ^2 components of equation 5.4. As some of these failures were due to timing alone it was decided to attempt to recover some of these events through the use of the stereo fitting technique. Thus events where the tracklength was greater than 15° in at least one site were chosen and the stereo fitting technique used. This resulted in the recovery of 20 (of the 107) events. Hence the trajectory fitting process reconstructed a total of 682 events from the 880 hours of stereo operation (~ 0.75 events per hour).

The next stage of the analysis was to use the fitted trajectory and the observed shower profile of light as a function of atmospheric depth to estimate the EAS parameters X_{max} (depth of shower maximum), N_{max} (number of particles at shower maximum) and primary particle energy.

The procedure consists of first binning the PMT signal data to calculate the light flux (in pe / (deg m^2)) from the shower arriving at the detector. The fitted trajectory is cut into 1 degree bins and each PMT is assigned a bin. When more than one PMT is assigned to a bin, their light signals are added statistically so that each bin contains a single estimate of the shower flux (and error) at the detector. A program to perform this binning operation was developed by Kidd[115] for work on analysis of events simultaneously detected by HiRes and the Michigan Muon Array (MIA)[115]. This program required only slight modifications (made by the author) to use trajectories from stereo-timing fitting, and to perform the binning operation on HiRes 2 data.

These observed fluxes are compared with those expected based on an EAS where

the particle number at each atmospheric depth is determined using the Gaisser-Hillas function (equation 2.12 in section 2.1.2) for some parameterisation of X_0, X_{max} and N_{max}. Estimating the expected flux at the detector also requires knowledge of the light production physics (how many photons due to fluorescence and Cerenkov processes will be produced by each shower particle), a model of atmospheric behaviour (to account for scattering of light towards the detector and absorption of light from the EAS to the detector) and a few other detector parameters (such as filter transmission and PMT quantum efficiency). A χ^2 fitting process is then used to determine the shower parameters X_{max} and N_{max} which minimise the difference between the observed and expected light fluxes. The shower profile may then be integrated to obtain the energy of the charged particle component which is then corrected for the undetected energy to give the total energy of the primary cosmic ray (see section 2.2.2 and Green[90] for a comparison of different theoretical corrections and experimental results).

6.2.1 Light Production Physics and the Effect of the Atmosphere

The light arriving at the detector from the EAS comes from four main sources. The first component is the isotropically emitted fluorescence photons from shower particles, the second is directly viewed Cerenkov photons, and the remaining two components are due to scattering of Cerenkov photons (from earlier sections of the shower) through the Rayleigh and Mie (aerosol) processes. The physics and equations to describe the production of light due to atmospheric fluorescence and Cerenkov radiation are well described in Fly's Eye literature[21][90], and thus will only briefly be described here.

6.2.1.1 Atmospheric Fluorescence light

As was briefly discussed in section 2.2.2, atmospheric fluorescence in our region of interest is dominated by the 2P and 1N bands of N_2 and N_2^+ respectively. The total yield of photons in the 300-400nm range is approximately 4 photons per metre per electron at sea level, with a slight temperature and pressure dependence. As fluorescence light is isotropic we obtain an expression for the number of photons emitted by

the EAS per unit length ($\mathrm{d}l$) per solid angle ($\mathrm{d}\Omega$) of:

$$\frac{\mathrm{d}^2 N_f}{\mathrm{d}l\mathrm{d}\Omega} = \frac{N_\gamma(T,h)N_e}{4\pi} \tag{6.1}$$

where $N_\gamma(T,h)$ is the number of fluorescence photons per electron and N_e is the number of electrons generating the light [21][90].

6.2.1.2 Direct Cerenkov Light

Relativistic electrons in the EAS will generate Cerenkov photons, primarily in the forward direction (see section 2.1.2.2). Calculation of the total number of Cerenkov photons per unit length and per solid angle can be considered separately:

$$\frac{\mathrm{d}^2 N_c}{\mathrm{d}l\mathrm{d}\Omega} = \frac{\mathrm{d}N_c}{\mathrm{d}l}\frac{\mathrm{d}N_c}{\mathrm{d}\Omega} \tag{6.2}$$

The number of Cerenkov photons per unit length is given by [21][90]

$$\frac{\mathrm{d}N_c}{\mathrm{d}l} = 2\pi\alpha N_e \int \mathrm{d}(1/\lambda) \int_{E_t}^{\infty} f(E)\left(2\delta - \frac{m^2c^4}{E^2}\right) dE \tag{6.3}$$

where α is the fine structure constant, λ is the wavelength of the photon, $f(E)$ is the fractional number of particles in the shower above an energy E and E_t is the threshold energy for Cerenkov photon production by a relativistic electron in air. The threshold energy depends upon the index of refraction in air, n, according to

$$E_t = \frac{m_e c^2}{\sqrt{2\delta}} \tag{6.4}$$

where δ is $1-n$ which exponentially decreases with altitude.

Of more importance to a detector such as HiRes is the angular distribution of Cerenkov light, which is given by[21]:

$$\frac{\mathrm{d}N_c}{\mathrm{d}\Omega} = \frac{\exp(-\theta/\theta_0)}{2\pi\theta_0 \sin\theta} \tag{6.5}$$

where θ is the angle with respect to the shower axis (generally we are only interested in angles that point towards the detector) and θ_0 depends on the threshold energy for Cerenkov production, parameterised by

$$\theta_0 = 0.83 E_t^{-0.67} \tag{6.6}$$

It is typically about 5°[90]. Hence for viewing angles of less than about 25° the Cerenkov component will dominate the weaker fluorescence signal making estimations of shower size less straightforward.

6.2.1.3 Rayleigh Scattering

Rayleigh, or molecular scattering of photons will have two effects on the light signal arriving at the detector. The first, which will be discussed later, is attenuation of the light signal from the shower due to scattering by atmospheric molecules. The second is scattering of Cerenkov photons from the shower towards the detector. Generally, these constitute a small fraction of the total signal observed by the detector (only the Cerenkov photons along the shower axis need to be considered as they constitute an intense beam and so dominate any other potential indirect light source).

The number of Cerenkov photons scattered out of the shower beam per unit length and solid angle by Rayleigh scattering is[21][130]

$$\frac{\mathrm{d}^2 N_\gamma}{\mathrm{d}l \mathrm{d}\Omega} = \frac{1}{4\pi}\frac{\mathrm{d}N_\gamma}{\mathrm{d}l} P_R(\theta) = \frac{1}{4\pi}\alpha_R(h) N_\gamma \left(\frac{400}{\lambda}\right)^4 P_R(\theta) \tag{6.7}$$

where $P_R(\theta)$ is the normalised phase function for Rayleigh scattering given by

$$P_R(\theta) = \frac{3}{4}(1 + \cos^2\theta) \tag{6.8}$$

for a scattering angle of θ, λ is the wavelength of light in nanometres and the Rayleigh scattering coefficient is

$$\alpha_R(h) = \frac{1}{L_R(h)} = \alpha_R(0) \exp\left(\frac{-h}{H_0}\right) \tag{6.9}$$

The Rayleigh scattering length $L_R(0)$ at sea level is 23km at 400nm and 7km at 300nm. It is stable with only a small seasonal variation caused by a change in the mean atmospheric density profile.

6.2.1.4 Aerosol (Mie) Scattering

Aerosol (Mie) scattering is the scattering of light by small particles and, like Rayleigh scattering, will both contribute to the attenuation of light signals from the shower as well as enhancing the signal through scattering of Cerenkov photons towards the detector.

Aerosol scattering is modeled using the Mie scattering approximation, in which the aerosol particles are assumed to be dielectric spheres. Mie theory is used to

develop equations for the scattering phase function $P_m(\theta)$ (which describes the angular distribution of scattering) and the extinction length L_M (or L_{aero}) which is the inverse of the extinction coefficient α_M. The number of Cerenkov photons scattered out of the shower beam per unit length and solid angle by Mie scattering is [21][130]:

$$\frac{\mathrm{d}^2 N_\gamma}{\mathrm{d}l \mathrm{d}\Omega} = \frac{1}{4\pi}\frac{\mathrm{d}N_\gamma}{\mathrm{d}l} P_m(\theta) = \frac{1}{4\pi} N_\gamma \alpha_M(h) P_m(\theta) \tag{6.10}$$

where $P_m(\theta)$ is the normalised phase function for Mie scattering and $\alpha_M(h)$ is the Mie scattering coefficient given by

$$\alpha_M(h) = \frac{1}{L_M(h)} = \alpha_M(0) \exp\left(\frac{-h}{H_M}\right) \tag{6.11}$$

where $H_M = 1.2$km is the Mie (aerosol) scale height and L_M is the aerosol extinction length (the Fly's Eye used a value of 11km at 400nm).

6.2.1.5 Attenuation

The previous equations describe the number of photons produced at the shower due to the different mechanisms. We now need to consider the effects of attenuation on these photons as they travel from the shower to the detector.

Atmospheric attenuation is generally divided into Rayleigh, Mie and Ozone attenuation, with Rayleigh and Mie being the most important factors for distant showers[90]. The total transmission factor (T_{ATM}) can be expressed as:

$$T_{ATM} = T_R T_M T_O \tag{6.12}$$

where T_R is the Rayleigh transmission factor, T_M is the Mie transmission factor and T_O is the ozone transmission factor.

The Rayleigh transmission factor has a λ^4 dependence and is given by

$$T_R = \exp\left[-\left(\frac{|X_1 - X_2|}{X_R}\right)\left(\frac{400nm}{\lambda}\right)^4\right] \tag{6.13}$$

where X_1 and X_2 are the source and receiver slant depth and X_R is the Rayleigh mean free path ($X_R = 2974 gcm^{-2}$ for light at $\lambda = 400nm$).

As the aerosol concentration falls off exponentially with height the transmission factor for Mie scattering is primarily a function of height. For light emitted at height

h_1 and detected at height h_2, the Mie transmission factor is[21]:

$$T_M = \exp\left[-\left(\exp\left(\frac{-h_1}{H_M}\right) - \exp\left(\frac{-h_2}{H_M}\right)\right)\left(\frac{H_M \sec\theta}{L_M}\right)\right] \tag{6.14}$$

6.2.1.6 Calculating the Expected Light Signal

Our aim is to now estimate the amount of light arriving in a 1° bin at the detector for a given trajectory and shower parameters X_0, X_{max}, and N_{max}. To calculate the expected signal from the EAS, we must first determine the individual light signals from fluorescence light, direct Cerenkov light, Rayleigh and Mie-scattered Cerenkov light. Each component is then multiplied by a transmission factor to account for attenuation losses in traveling from the shower to the detetector. Finally, we must include the effects of mirror area, filter transmission and PMT quantum efficiency to convert the number of photons arriving at the detector, to the number of photoelectrons measured. These processes are illustrated in figure 6.3.

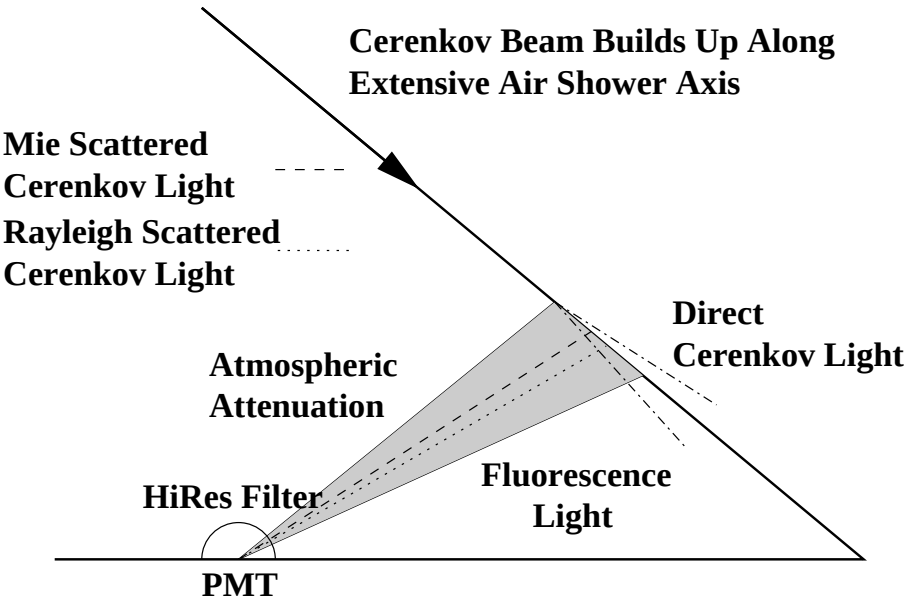

Figure 6.3: A summary of the factors that affect the light signal measured by the detector. Light is generated by the EAS and is attenuated as it travels to the detector. The actual signal measured will further depend upon detector parameters such as the transmission filter and PMT quantum efficiency. Note that most cases the light signal will be dominated by the fluorescence component.

It is also important to take into account the wavelength dependence of the different parameters (from production of the light to conversion to photoelectrons). Thus the

signal is calculated for each of sixteen 9nm wide wavelength ranges (covering 276nm to 419nm) so as to cover the full range of the HiRes transmission filter (see figure 3.15). These sixteen wavelength bins are then added to provide the total expected signal for a given track bin. The profile fitter compares these expected light fluxes with the observed light fluxes for a series of bins along the track, and a χ^2 fitting process is used to obtain the shower parameterisation that best fits the observed light fluxes. Figure 6.4 illustrates an example profile fit to an event seen by HiRes 1.

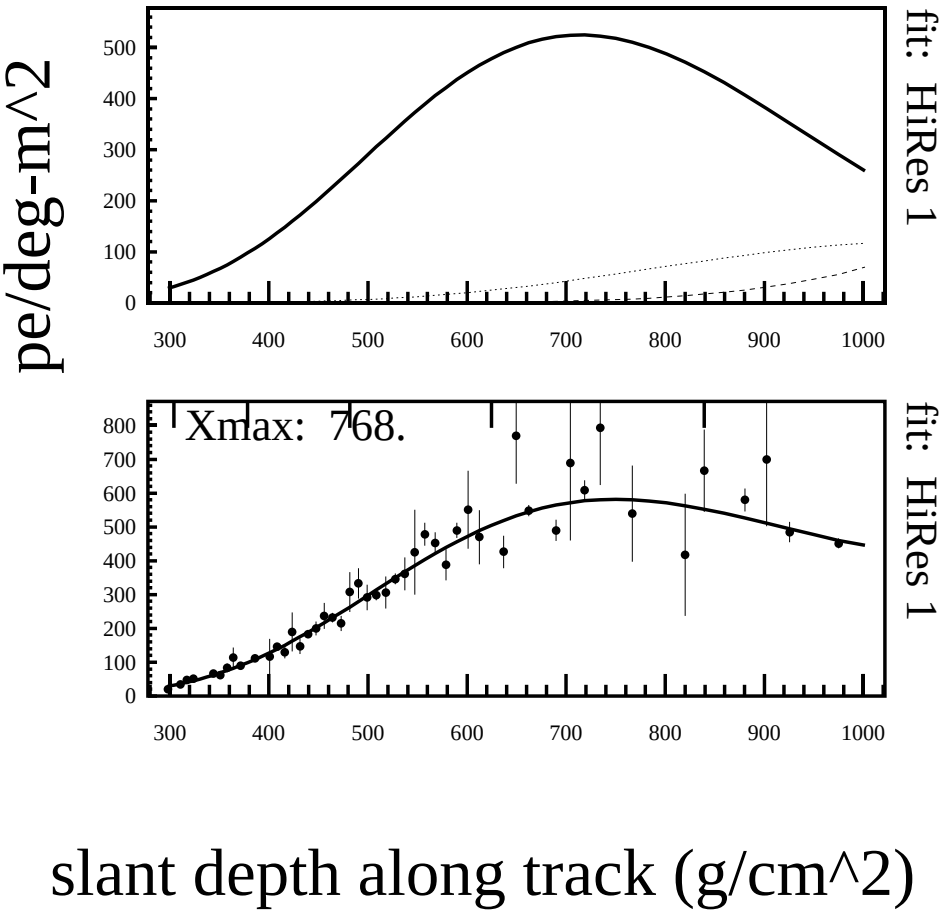

Figure 6.4: An example profile fit. The top plot illustrates the contribution to the expected light profile at the detector due to fluorescence light (thick solid line), direct Cerenkov light (thin solid line), Rayleigh scattered Cerenkov (dashed line) and Mie scattered Cerenkov (dotted line) light. The lower plot illustrates the total light signal and the the measured light signal in each bin (pe/(deg m^2) with 1σ errors as a function of the slant depth along the track. Also note that the fluorescence light profile does not necessarily maximise at X_{max} (shower maximum) due to geometrical effects and changes in the fluorescence yield with temperature and pressure.

6.2.1.7 Modifying the Profile Fitter

Much of the development work for the profile fitter was performed by Kidd[115] for analysis of coincident HiRes 1 – MIA events, and was based on programs developed for analysis of Fly's Eye data. The profile fitter used the Polak-Ribiere version of the Fletcher-Reeves conjugate gradient method discussed in Numerical Recipes[139] to fit for the shower parameters X_{max} and N_{max} from which shower energy was then calculated. Errors for X_{max} and N_{max} were determined through examination of the χ^2 space (see Numerical Recipes [139] for a discussion of this technique) and these errors were then propagated to obtain the error estimate in the energy. The atmospheric model used was based on the U.S standard atmosphere, and assumed[115][90][21]:

- a constant ground temperature of 10°C
- a isothermal decrease in temperature with height of 6°C per km.
- a exponential decrease in mass overburden with a scale height of 7.5km.
- an exponentially decreasing distribution of aerosols with a scale height of 1.2km an aerosol extinction length of $\sim$ 11km at 400nm (with a $1/\lambda$ dependence).

The profile fitter was tested by Kidd[115] on Monte Carlo data and the effect of modifying the different parameters (such as an temperature decreases or changes in the aerosol scale height) investigated. For the HiRes 1/MIA analysis this model was found to be quite appropriate, and fairly insensitive to changes in the different atmospheric parameters. This is not surprising, as MIA is located 3km from HiRes 1, so most coincident showers will be relatively close to HiRes 1 and not be significantly affected by atmospheric effects.

The author undertook the necessary modifications to enable use of the profile fitter on HiRes 2 data. These modifications allowed independent profile fitting utilising either HiRes 1 or HiRes 2 data, as well as a combined HiRes 1 / HiRes 2 fit which used data from both HiRes sites. Thus for each stereo event one could obtain three estimates of shower energy and parameters such as X_{max} and N_{max}.

All three versions of the profile fitter are executed in the same way – for a trial shower parameterisation (given by X_0, X_{max} and N_{max}), the expected fluorescence,

direct Cerenkov, Rayleigh and Mie scattered Cerenkov light signals are calculated at the shower. These light signals are then attenuated for the distance traveled from the shower to the detector and the total signal (from adding the four components) compared with the actual signal. The χ^2 components for each bin are then added to give the total χ^2, and a fitting process is used to determine the shower parameters that minimise the total χ^2 to give the best shower development profile. It is worth noting that for the combined HiRes 1/HiRes 2 fit one must keep track of which detector each bin is located at so that the correct amount of attenuation is applied. This also means that in many cases identical sections of the shower are being viewed at two different distances, which should make the combined fit more sensitive to atmospheric conditions. Finally, with the extra samples provided by combining data from the two detectors, the combined fit should be more likely to bracket the region around X_{max}, which is the basic requirement for a good profile fit (since the light profile should maximise in this region which is what the Gaisser-Hillas function is looking to fit).

The code was also rechecked and some modifications made. This included updating the calculation of the heights (and slant depths) to take into account the effects of the earth's curvature – previously heights were calculated with respect to the plane tangential to the surface of the earth at HiRes 1. This change ensured that for distant showers the correct heights were used in the calculations of effects such as attenuation (see equations 6.13 and 6.14). The most significant change made was in handling the effect of the atmosphere. The motivation for such changes, the changes made and their effects will now be discussed.

6.3 Aerosol Models

As can be seen from the equations in section 6.2.1, we must correctly account for scattering and attenuation of light to accurately determine the primary cosmic ray energy. This is reasonably trivial when dealing with Rayleigh scattering but is potentially more difficult when dealing with aerosol scattering due to its variability. The distribution of aerosols in the atmosphere may change by orders of magnitude over very short spaces of time (normally associated with a weather event), whilst at other times it can be

remarkably stable[27]. For HiRes, the most important effect of the aerosol variability is to change the aerosol extinction length which, as can be seen from equation 6.14 affects the amount of light attenuated in traveling from the EAS to the detector. Incorrect estimates of the extinction length, can potentially lead to large errors in the estimation of EAS energy for distant (and thus high energy) showers. For this reason, significant work has gone into understanding and attempting to characterise the aerosol content of the atmosphere in the vicinity of Dugway (see section 3.2.5). This section discusses the different aerosol models considered, and their effects on analysis of HiRes data.

Aerosol models are used to describe the distribution of aerosol particles in the atmosphere so as to derive (via Mie scattering theory) estimates for aerosol extinction lengths and the normalised scattering phase function. Luo[130] compared the standard Fly's Eye phase function with phase functions from the Longtin wind dependent desert aerosol model[129] and the D'Almeida desert aerosol model[63]. The major differences between the Fly's Eye model and the two other models is that the Fly's Eye model uses a power law size distribution of particles whilst the other two models use log normal size distributions. The Longtin model assumes there are three major components (each with their own log normal size distribution) and calculates atmospheric parameters under different wind speeds, with $0ms^{-1}$ corresponding to a constant background level of aerosols. The D'Almeida model was based upon measured size distributions of desert aerosols which were classified as either background, wind carrying dust or sandstorm distributions according to the horizontal visibility measurements taken at the same time. The different aerosol size distributions lead to different estimates of the phase function, aerosol extinction coefficient, and the wavelength dependence of the aerosol extinction coefficient.

Luo used laser shot measurements and Monte Carlo simulations to investigate the Mie scattering phase function most applicable to Dugway. He concluded that a log-normal distribution, and in particular the phase function for D'Almeida's background aerosol distribution, was most appropriate (this is reasonably similar to the Longtin $0ms^{-1}$ function). The different phase functions are presented in figure 6.5 for comparison.

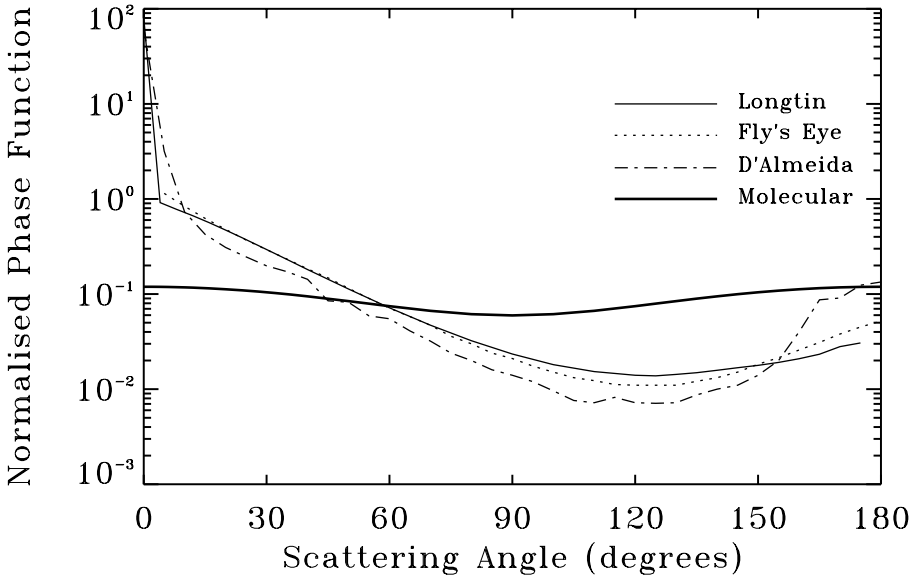

Figure 6.5: Normalised phase functions for the Longtin wind dependent aerosol model (0 ms^{-1} case), D'Almeida desert aerosol model (background case), Fly's Eye model and for molecular (Rayleigh) scattering[130][27]. Note how the Longtin and D'Almeida functions have strong forward peaks.

Luo also studied the variation of the aerosol extinction coefficient and made measurements very similar to the quality ratio measurements discussed in section 3.2.5. He also obtained estimates derived from visibility measurements made by the Army Meteorological Team at Dugway. These measurements were then compared with those expected using the Longtin model and found to be in reasonable agreement. Luo also studied the wavelength dependence (from $\sim$ 200-700nm) of the aerosol extinction coefficient obtained using the different aerosol models. He found that for the Fly's Eye power law size distribution of aerosols, the extinction coefficient has a $1/\lambda$ dependence whilst for a log normal size distribution there is almost no dependence[130].

Of most importance to HiRes, Luo found that by making quality ratio type measurements, it is possible to obtain a good estimate of the atmospheric conditions and specifically the atmospheric extinction length. This is the atmospheric parameter of most interest to HiRes as it affects the attenuation of *all* light signals traveling from the EAS to the detector (see equation 6.14).

Luo's work has been followed up by Bird *et al.*[27] who have studied the effects

of scattering and atmospheric attenuation. They used HiRes observations of light scattered from the intersite flasher (ISF) to produce quality ratio measurements at seven minute intervals for the stereo dataset (see section 3.2.5 or Bird *et al.*[27] for more details). These measurements were compared with the Longtin wind dependent aerosol model to obtain a relationship between quality ratio and atmospheric extinction length which is presented in table 6.1[28]. Note that the atmospheric extinction length L_{Atmos} is related to the aerosol extinction length (L_{aero}) and Rayleigh extinction length (L_R) according to $1/L_{Atmos} = 1/L_R + 1/L_{aero}$.

Longtin Model Wind Speed (ms^{-1})	Quality Ratio	Extinction Length (km)	
		Aerosol	Atmospheric
Rayleigh	1.5	∞	18
0	2.8	16	8
10	3.2	13	7.2
15	3.7	7	5
20	4.5	4	3

Table 6.1: Relationship between quality ratio, aerosol and atmospheric extinction lengths using the Longtin wind dependent aerosol model[28]. Values are also provided for a Rayleigh atmosphere which has no aerosol component. The Rayleigh extinction length is the value at 400nm, and aerosol extinction lengths are an average over the 300-400nm range. Note that $1/L_{Atmos} = 1/L_R + 1/L_{aero}$.

Given the high time resolution of the quality ratio (QR) measurements, it was decided to incorporate the measurements into the profile fitter. This however required deriving a relationship between quality ratio and aerosol extinction length, based on the results of Bird *et al.*[27][28]. Such a relationship was necessary, because the majority of the stereo data set was obtained when the atmosphere was somewhere between the Longtin aerosol background ($0ms^{-1}$ windspeed) and a pure Rayleigh, or Molecular atmosphere (81% of QR measurements were less than 2.8, and 90% were less than 3.5).

Several different functional forms relating L_{aero} and QR were considered and compared against the values in table 6.1, with the best results found using a form

$$\log\left(\frac{1}{L_{aero}}\right) = A + B(QR - 1.5) - \frac{C}{QR - 1.5} \tag{6.15}$$

Choice of the parameters A, B and C was performed by using a non-linear least squares fit. However, due to the lack of data points between QR values of 2.8 and 1.5, this

fitting method was not overly effective. Thus a heuristic fitting method was used by slightly varying each of the three parameters and plotting curves of atmospheric and aerosol extinction length as a function of QR. The "best" values (based on minimising the deviation of data points and producing a smooth curve that satisfies $\lim_{QR \to 1.5} = \infty$) for A, B and C were thus found to be –3.8, 0.85 and 1.25. Comparisons of the atmospheric and aerosol extinction length as a function of quality ratio are presented in figure 6.6 along with the values from table 6.1.

The profile fitter was modified to read in a file containing the quality ratio measurements, choose the value closest in time to the current event and convert this value to an aerosol extinction length L_M. Events with quality ratios greater than 5 were rejected on the basis of poor atmospheric conditions (such nights corresponded to high relative humidity and aerosol extinction lengths of less than 2.5km).

To allow further testing of the effect of aerosol scattering, the normalised phase function for the D'Almeida background aerosol distribution was also included. Thus events could be analysed using the standard Fly's Eye phase function and aerosol extinction length (fixed at 11km at 400nm with a $1/\lambda$ dependence), the Fly's Eye phase function with quality ratio (QR) based aerosol extinction length and finally using the D'Almeida phase function with quality ratio (QR) based aerosol extinction length.

Evaluation of the best atmospheric model to use is a difficult subject. Initially energy estimates from HiRes 1 and HiRes 2 profile fits were compared but neither aerosol model performed consistently well. Thus the combined HiRes 1/ HiRes 2 profile fit was developed to investigate if utilising all available information would improve the situation. This approach appeared to work well, as the combined fitter was able to produce good fits for events that were previously poorly fitted by one of the sites. Thus it was decided to use to the combined HiRes 1/ HiRes 2 profile fit to compare different atmospheric models for the larger dataset, together with a comparison of HiRes 1 and HiRes 2 energies for a small set of events that are well viewed in both detectors so as to interpret the effectiveness of the different models. However before we can perform a comparison some quality controlling of events is necessary, and this issue will now be discussed.

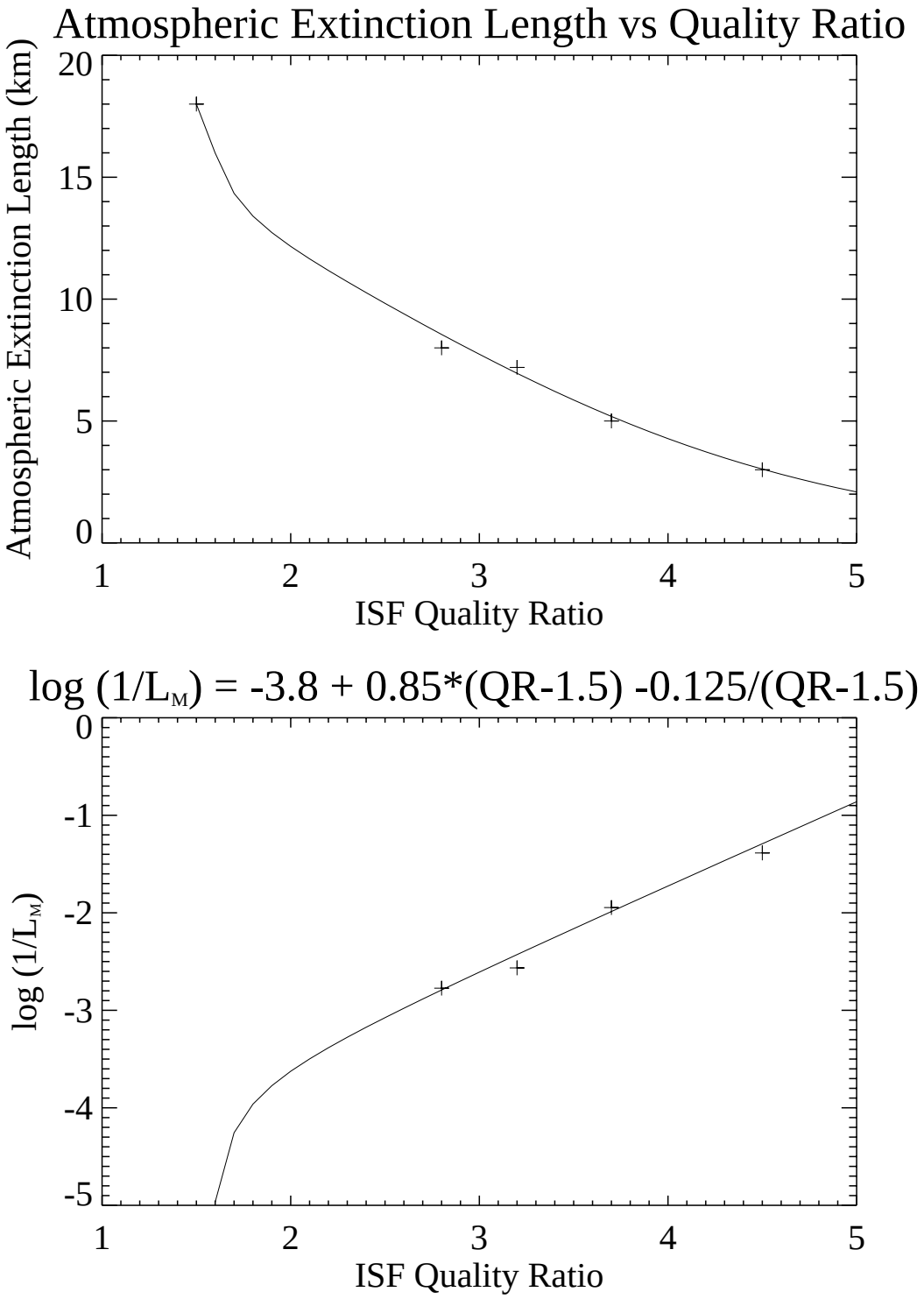

Figure 6.6: The relationship between extinction length and quality ratio based on data in table 6.1. Various functional forms for the aerosol extinction length (L_M or L_{aero}) were tried in an attempt to best fit the relationship between extinction length and quality ratio. Note that the Mie extinction length is assumed to be infinite at a quality ratio of 1.5. Using $\log(1/L_M) = -3.8 + 0.85(QR - 1.5) - 0.125/(QR - 1.5)$ was found to be a good parameterisation.

6.3.1 Quality Controlling

The events which successfully passed stereo-timing fitting were passed through the updated profile fitting program, with three different atmospheric cases being considered separately:

- Fly's Eye phase function and fixed aerosol extinction length ($\sim$ 11km at 400nm with a $1/\lambda$ wavelength dependence)

- Fly's Eye phase function and quality ratio (QR) based aerosol extinction length (using the parameterisation of equation 6.15 presented in figure 6.6), and

- D'Almeida phase function and quality ratio (QR) based aerosol extinction length.

In each case HiRes 1, HiRes 2 and the combined HiRes 1 / HiRes 2 profile fits were performed. In order to obtain a reasonable set of events for considering the effects of the atmosphere on reconstruction, events in which either the HiRes 1 or HiRes 2 profile fit failed were rejected. This ensured that there were three independent estimates of shower energy for each event. However, this did not guarantee that the estimates were reasonable, so the correlations between estimated energies were investigated. Of most interest was an examination of the correlation between the combined HiRes 1/2 fit which, given that it generally has more information should provide the best energy estimate, and the HiRes 1 fit, where atmospherics should have a relatively small effect on energy (as the majority of showers are quite close to HiRes 1 with R_p distances of less than 6km). The energy correlation for the fit using the Fly's Eye Phase function, and the QR based aerosol extinction lengths is presented in figure 6.7.

Figure 6.7 shows that in most cases there is good agreement between the combined HiRes 1/2 fit and the HiRes 1 fit (most point are close to the dotted line in the figure). However it was noted that there were quite a few events where the HiRes 1 energy was quite large but the combined estimate was much smaller, by up to a factor of $\sim$ 1000. Thus it was decided to closely examine all those events in which the HiRes 1 energy was estimated as more than 7.5EeV.

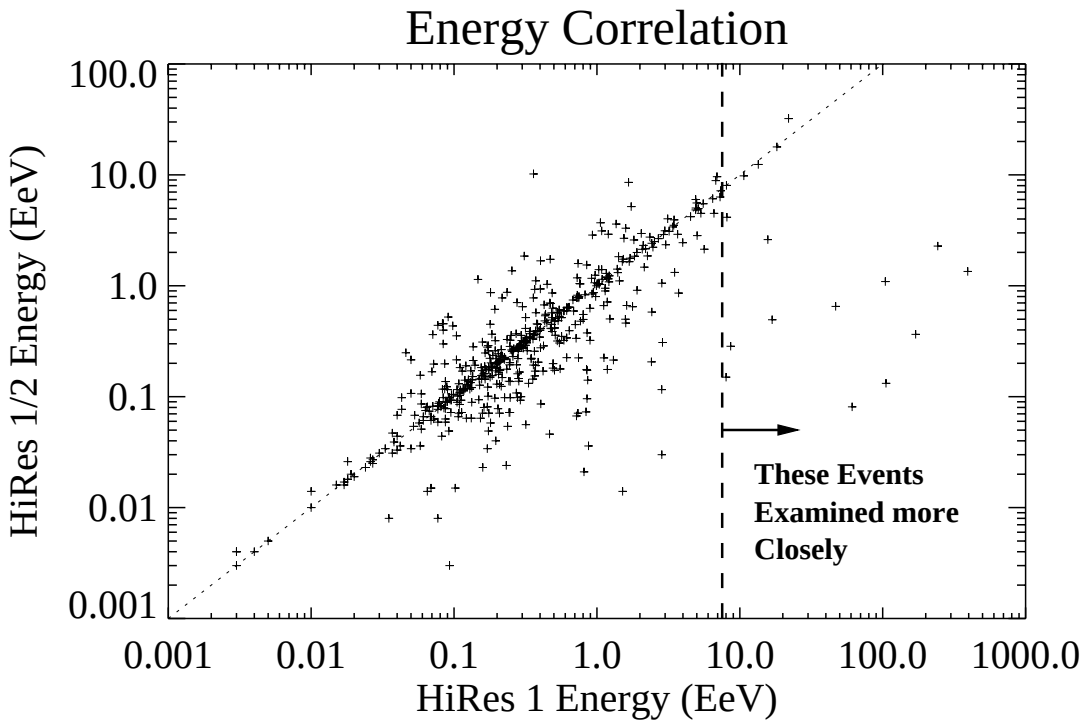

Figure 6.7: Energy correlation for events fitted using the combined HiRes 1/2 profile fit and HiRes 1 profile fit utilising the Fly's Eye Phase function, and the QR based aerosol extinction length. The dotted line represents a 1:1 agreement. All events with HiRes 1 energies greater than 7.5 EeV were flagged for closer examination. Note the number of cases where the combined HiRes 1/2 predicted a substantially smaller energy than the HiRes 1 fit (and that the opposite case occurred more rarely).

Table 6.2 presents more detailed information on each event examined. In general, the events in which the HiRes 1 energy was considerably larger than the HiRes 1/2 energy, had quite large errors. In many cases failures seem to be associated with poor bracketing of X_{max} which probably leads to the large error in the HiRes 1 energy (error estimates were based on the χ^2 surface). In most cases it appears that the inclusion of HiRes 2 information improves the profile fit, reducing the energy estimate and importantly, the relative error. This is illustrated in figure 6.8 which presents the same data as that in figure 6.7 but includes 1σ error bars.

It was decided to place a quality cut on the data by requiring that the relative error in energy from the combined HiRes 1/2 profile fit be less than 20%. An additional cut requiring that the $X_{max} - X_0$ difference was greater than $100 gcm^{-2}$ was also applied to ensure reasonable profiles. This cut was applied as it was noticed that the

Energy (in EeV, 1σ error)			Description
HiRes 1	HiRes 2	HiRes 1/2	(regarding event in HiRes 1)
8 ± 43	$.088 \pm .004$	$.150 \pm .004$	Top ring, observed prior to X_{max}
8 ± 22	12 ± 1	4.2 ± 0.4	4° Tracklength, observed prior to X_{max}
8.1 ± 0.2	7 ± 1	8.0 ± 0.2	Good, well observed EAS
9 ± 32	1.13 ± 0.04	0.29 ± 0.02	Cerenkov contamination, poor trajectory fit
11 ± 2	21 ± 70	10 ± 1	Good, well observed EAS
13.5 ± 0.4	10 ± 3	12.4 ± 0.4	Good, well observed EAS
16 ± 18	3 ± 2	2.6 ± 0.4	10° Tracklength, observed prior to X_{max}
17 ± 44	0.37 ± 0.05	0.49 ± 0.07	11° Tracklength, observed prior to X_{max}
18.2 ± 0.4	29 ± 6	17.9 ± 0.4	Good, well observed EAS
22 ± 1	28 ± 1	32 ± 2	Good, well observed EAS
47 ± 340	0.8 ± 0.2	0.7 ± 0.4	Noise Contamination / Poor noise filtering
61 ± 120	0.11 ± 0.01	$.081 \pm .008$	Top ring, observed prior to X_{max}
104 ± 280	0.4 ± 0.2	1 ± 2	Top ring, observed prior to X_{max}
105 ± 280	$.154 \pm .005$	$.132 \pm .004$	Top ring, observed prior to X_{max}
170 ± 520	0.29 ± 0.07	0.37 ± 0.07	6° Tracklength observed prior to X_{max}
243 ± 440	1.7 ± 0.2	2.3 ± 0.2	Top ring, observed prior to X_{max}
393 ± 380	0.24 ± 0.04	1.3 ± 0.8	Excessive Cerenkov contamination

Table 6.2: Case study of events in which HiRes 1 energy was estimated as more than 7.5EeV. The estimated energy (and 1σ error) for HiRes 1, HiRes 2, and the combined HiRes 1 / HiRes 2 profile fits are presented together with a description of the event. Note that those events seen only in the top ring of HiRes 1 had tracklengths ranging from 6° to 18°.

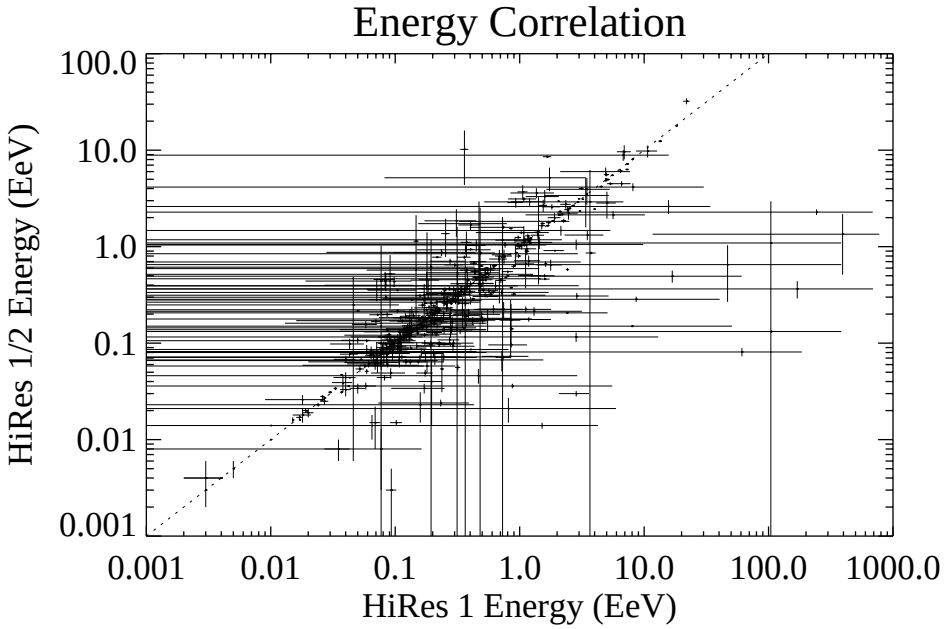

Figure 6.8: Energy correlation with 1σ error bars for events fitted using the combined HiRes 1/2 profile fit and HiRes 1 profile fit utilising the Fly's Eye Phase function, and the QR based aerosol extinction length.

fitter occasionally produced poor fits where the parameter X_0 wandered towards X_{max} (often, but not always, when there was a reasonable direct Cerenkov component). A total of 309 events passed these quality cut and were used in the following comparison of aerosol models. The HiRes 1 – HiRes 1 / HiRes 2 energy correlation for these events is presented in figure 6.9.

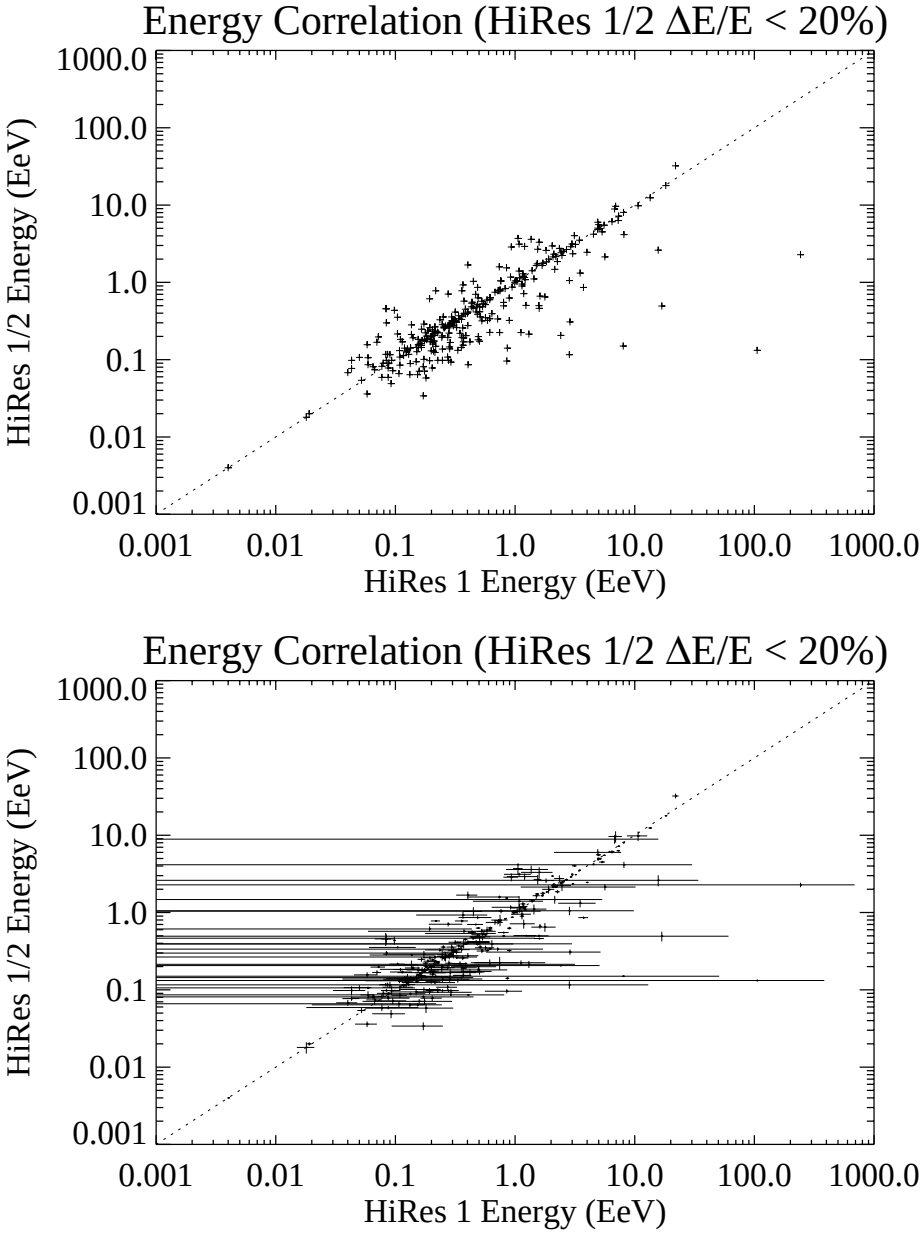

Figure 6.9: Energy correlation (with and without error bars) for events passing quality cuts that the relative error in the HiRes 1/2 energy estimate be less than 20% and the $X_{max} - X_0$ difference be greater than $100 gcm^{-2}$. Results are those from the profile fitter utilising the Fly's Eye Phase function and QR based aerosol extinction length. The dotted line represents a 1:1 agreement.

6.3.2 Comparing the Aerosol Models

Profile fits were performed on the 309 events that passed the quality cuts for the three different aerosol cases. To allow comparison between two aerosol models, the fractional energy difference, defined as,

$$\text{Fractional Energy difference} = \frac{\text{Model 1 Estimate} - \text{Model 2 Estimate}}{\text{Model 1 Estimate} + \text{Model 2 Estimate}} \tag{6.16}$$

was calculated for each event and the values histogramed. The range of the fractional energy difference is between -1 and 1, with a value of -0.5 implying that the model 2 estimate is a factor of three times the model 1 estimate, a value of -0.2 corresponds to a factor of 1.5 and a value of -0.1 corresponds to a factor of 1.2 (and vice versa for positive values).

Figure 6.10 plots histograms of the fractional energy difference for HiRes 1 profile fits for the three different aerosol cases. Similarly figure 6.11 are HiRes 2 profile fits and figure 6.12 are the results from the combined HiRes 1 / HiRes 2 profile fit.

The first point to note from the three figures is that in all cases the energy estimate using the Fly's Eye phase function and fixed extinction length is consistently larger than either of the two aerosol cases (the histograms are centered around a value of -0.1 – a factor of 1.2). Importantly, this effect is often quite large, as is indicated by the tail of the distributions towards a value of -1.0. This effect is quite severe for the HiRes 2 profile fit and is even worse for the combined HiRes 1 / HiRes 2 profile fit.

This behaviour is well understood due to variation in the aerosol extinction length. From the quality ratio measurements, we know that close to 90% of the nights had extinction lengths longer than the fixed value used in the Fly's Eye model (see table 6.1). Thus for a given light signal, the profile fitter would estimate a larger value for the energy of the shower as the fitter was overestimating the effects of attenuation. We expect this effect to be worse at HiRes 2 than HiRes 1 due to the extra $\sim$ 10km that light must travel to reach HiRes 2. It is also interesting to note that the tail is more populated for the combined HiRes 1 / HiRes 2 profile fit (figure 6.12) than even the HiRes 2 profile fit case (figure 6.11). This effect is presumably due to the increased sampling of the profile, leading to a, in principle, better estimate of the shower profile

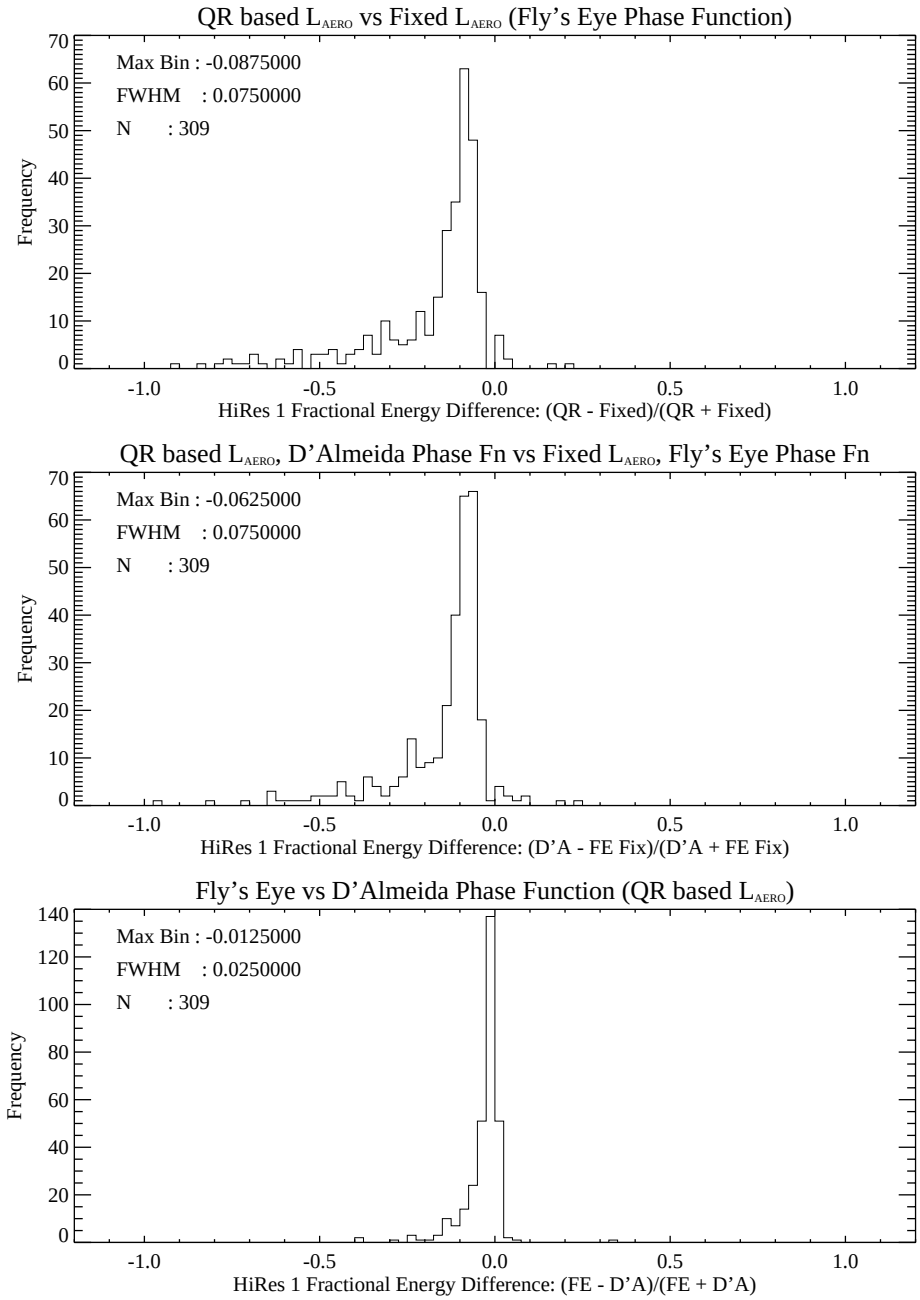

Figure 6.10: Comparison of different aerosol models for HiRes 1 profile fits. The top plot shows the effect of fixed versus variable aerosol extinction length with an identical phase function, the middle plots is a comparison of different phase functions and aerosol extinction lengths, and the bottom plot is the effect of different phase function for identical aerosol extinction lengths. Note how the original Fly's Eye model consistently produces larger estimates than the other two models. Values of -0.8 corresponds to an $9\times$ larger energy estimate for the second model with respect to the first model, -0.5 is a factor of 3, -0.2 is a factor of 1.5 and -0.1 is a factor of 1.2.

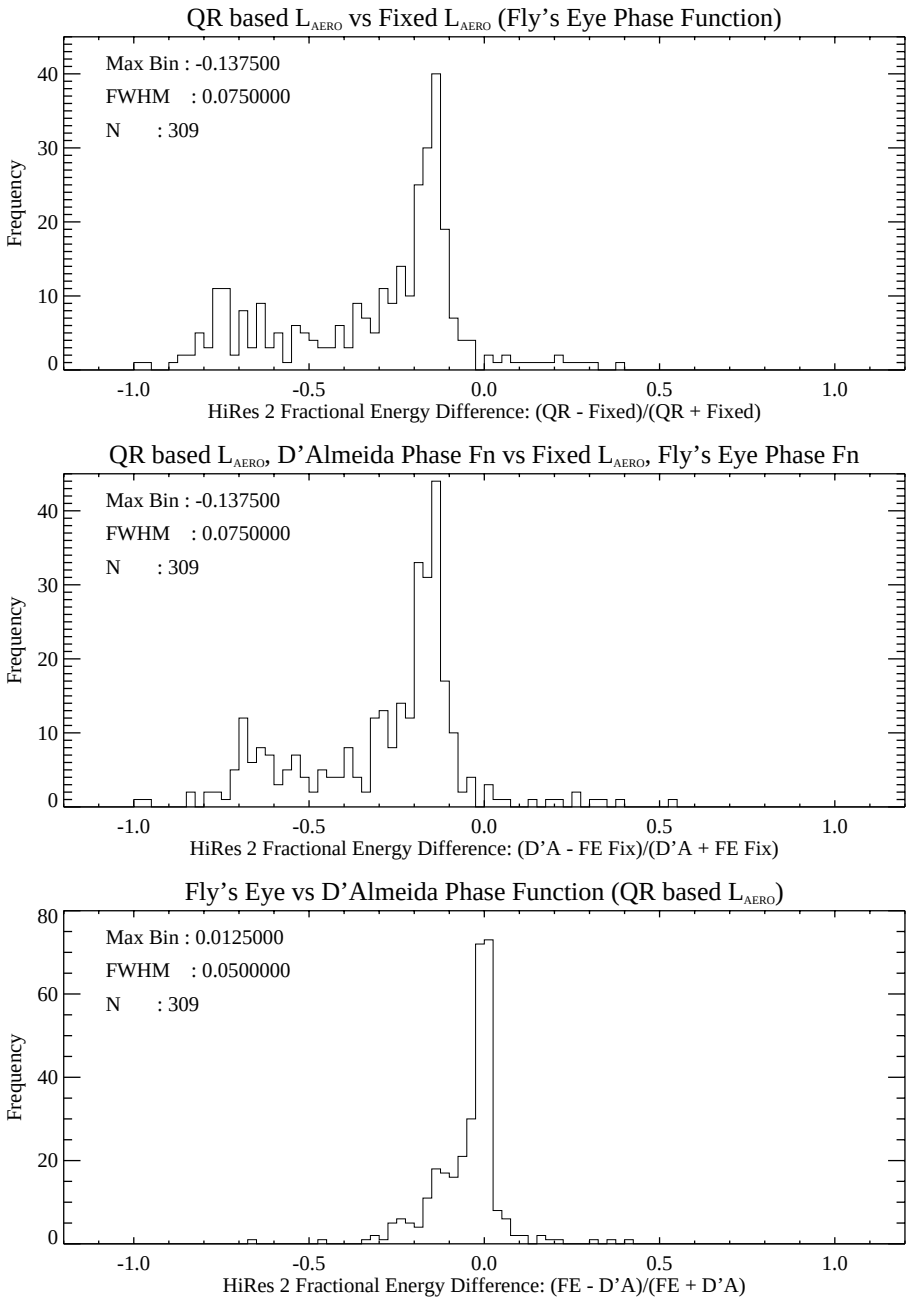

Figure 6.11: Comparison of different aerosol models for HiRes 2 profile fits. Note the large number of events at large fractional energy differences compared to the HiRes 1 case (figure 6.10, note the different scale on the y axis). This can be explained as due to the large number of nights in which the extinction length was significantly longer than the fixed Fly's Eye model estimate, leading to an overestimate of the attenuation by the Fly's Eye model (compared to the variable extinction length models).

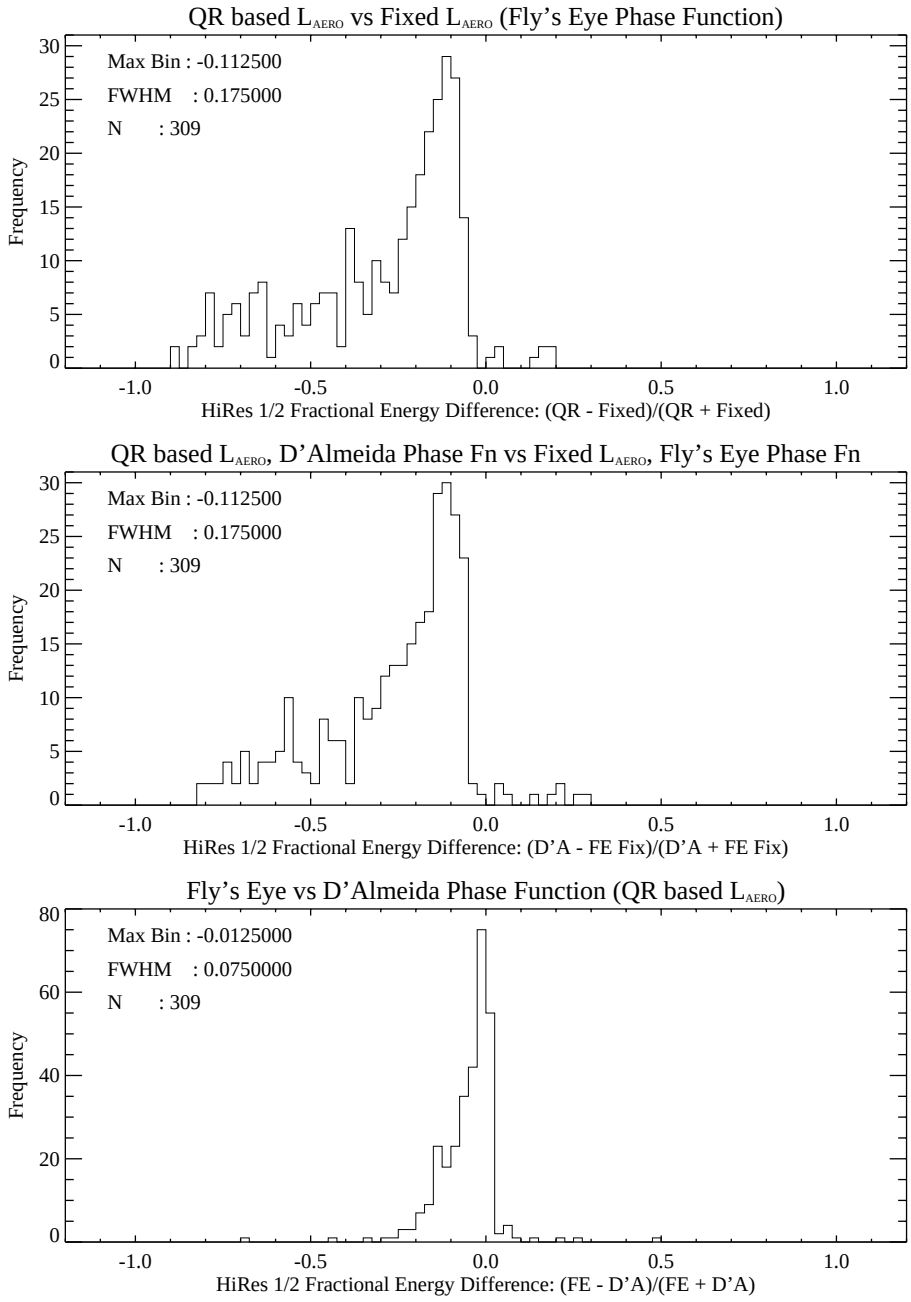

Figure 6.12: Comparison of different aerosol models for combined HiRes 1 / HiRes 2 profile fits. Note the larger population of events in the tail than for the HiRes 2 case (figure 6.11, note the different scale on the y axis). This is presumably due to the combination of better sampled profile with overestimate of the attenuation (compared to the variable extinction length models).

and energy. However the effects of over estimating the attenuation leads to significantly larger energy estimates compared to the other models. Finally we should note that our results do not prove that our variable extinction length values are correct. Rather, we have shown that the aerosol extinction length has a large effect on energy and that based on our understanding of the atmosphere, they should be more appropriate to use than a fixed value.

The second point to note is the relatively minor effect of using different phase functions (the lower plot in figures 6.10, 6.11 and 6.12). In the majority of the cases the use of a different phase function has no effect on the energy estimate (unlike the effect of a fixed extinction length). The distributions are slightly skewed towards higher energies for the D'Almeida phase function though, with this effect worse for the HiRes 2 profile fit and the combined HiRes 1 / HiRes 2 profile fit. This increase in the energy estimate is mostly less than a factor of 1.5 (again significantly less than the effect of a fixed extinction length). This increase in energy might be explained due to a decrease in the estimation of the amount of Mie scattered Cerenkov light. For most scattering angles, the D'Almeida phase function is smaller than the Fly's Eye phase function, only overtaking the this function for scattering angles of less than 10° (in which case direct Cerenkov light will dominate the signal).

6.3.2.1 Case Studies

To further answer the question of the best atmospheric model to use, a small subset of events was examined in detail. It was decided to examine the agreement between HiRes 1 and HiRes 2 energies using the different models to see if any particular model was favoured. This required the selection of a set of events well observed by both HiRes sites and cases when the measured quality ratios were small and large were considered separately.

For the cases when the quality ratios were small (QR < 2), three criterion were used to select events. The first two criteria required that each of the three profile fits had an energy resolution of 25% and a minimum X_0 and X_{max} separation of $100 gcm^{-2}$ (occasionally the profile fit performs poorly due to an incomplete view of the shower and X_0 approaches X_{max}). The final, and possibly most important criteria required

that both sites viewed the region around X_{max}. A further cut requiring that the HiRes 2 R_p distance was at least 15km was applied to ensure that light had to travel significant distances (and thus allow atmospheric effects to take effect).

After application of these tight quality cuts, we were left with a total of 3 events. The ratios of HiRes 2 to HiRes 1 energy for the 3 events with the different models are presented in table 6.3 in order of increasing (quality ratio estimated) aerosol extinction lengths (L_{aero}). From this table we can see that the models using the quality ratio (QR) based aerosol extinction lengths (L_{aero}) perform consistently better than the Fly's Eye model using a fixed value of L_{aero} (with a $1/\lambda$ dependence). There is also tentative evidence that the energy estimates using the D'Almeida phase function provide slightly better agreement than those with the Fly's Eye phase function (which is what we expected based on Luo's work). However as all ratios are larger than 1.0, it implies that, not surprisingly, there are still some problems in the profile fitting and energy estimation analysis. Some optimisation of the quality ratio – aerosol extinction length relationship was performed (notably varying C in equation 6.15) but this was found to have only a very minor effect (implying the problems are deeper within the fitting and/or the calibration processes).

However aerosols have only a very limited effect on these events, so to more fully investigate these effect of atmosphere it was decided to concentrate on a set of events when quality ratios indicated the presence of aerosols. Thus the set of events taken when quality ratios were larger than 2.8 (implying at least a background level of aerosols) were filtered to produce the best 10 events. The filtering process consisted of visually scanning all candidate events to obtain the set of best viewed events, with the basic requirement being that events were reasonably well viewed in both detectors (essentially that the region around X_{max} was viewed in both detectors and there was no large direct Cerenkov light contamination). The ten candidate events will now be discussed in the captions of table 6.4 to table 6.13, in order of increasing quality ratio (and thus decreasing L_{aero}) measurements. Profiles fits using the quality ratio based L_{aero} and Fly's Eye phase function are presented in figures 6.13,6.14 and 6.15 for each of the 10 cases. The different aerosol models produce different fits, and we should note that the fits presented are not always the best fit to the data.

HiRes 1 R_p = 10.8km, HiRes 2 R_p = 22.2km, L_{aero} = 43.0km				
Aerosol Model		Energy (EeV)		HiRes 2 / HiRes 1
L_{aero}	Phase Fn	HiRes 1	HiRes 2	Energy Ratio
QR based	Fly's Eye	3.1 ± 0.1	5.3 ± 0.3	1.3 ± 0.1
QR based	D'Almeida	3.4 ± 0.2	5.4 ± 0.3	1.3 ± 0.1
Fixed	Fly's Eye	4.3 ± 0.2	8.0 ± 0.5	1.7 ± 0.2

HiRes 1 R_p = 16.2km, HiRes 2 R_p = 28.4km, L_{aero} = 87.5km				
Aerosol Model		Energy (EeV)		HiRes 2 / HiRes 1
L_{aero}	Phase Fn	HiRes 1	HiRes 2	Energy Ratio
QR based	Fly's Eye	7.3 ± 0.2	8.6 ± 0.7	1.2 ± 0.1
QR based	D'Almeida	8.0 ± 0.2	9.2 ± 0.8	1.1 ± 0.1
Fixed	Fly's Eye	16.0 ± 0.5	25 ± 4	1.6 ± 0.3

HiRes 1 R_p = 7.0km, HiRes 2 R_p = 17.6km, L_{aero} = 465km				
Aerosol Model		Energy (EeV)		HiRes 2 / HiRes 1
L_{aero}	Phase Fn	HiRes 1	HiRes 2	Energy Ratio
QR based	Fly's Eye	5.0 ± 0.2	6.6 ± 0.4	1.7 ± 0.2
QR based	D'Almeida	5.0 ± 0.2	6.6 ± 0.4	1.6 ± 0.2
Fixed	Fly's Eye	5.7 ± 0.3	9.6 ± 0.6	1.9 ± 0.2

Table 6.3: Ratio of HiRes 2 to HiRes 1 energies assuming different atmospheric models for a set of distant, well viewed events. Note that the models using the quality ratio (QR) based aerosol extinction lengths (L_{aero}) perform consistently better than the fixed (L_{aero}) case, although not entirely without problems as the HiRes 2 estimate seems to be systematically larger than the HiRes 1 estimate. Energy estimates from the combined HiRes 1 / HiRes 2 fit tend to between the HiRes 1 and HiRes 2 estimates.

Case 1: Quality Ratio = 3.0				
HR 1 R_p	3.7km	HR 2 R_p	8.6km	L_{aero} = 13.6km
Aerosol Model		Energy (EeV)		HiRes 2 / HiRes 1
L_{aero}	Phase Fn	HiRes 1	HiRes 2	Energy Ratio
QR based	Fly's Eye	0.17 ± 0.02	0.37 ± 0.10	2.2 ± 0.8
QR based	D'Almeida	0.17 ± 0.02	0.40 ± 0.11	2.3 ± 0.9
Fixed	Fly's Eye	0.20 ± 0.02	0.62 ± 0.22	3.0 ± 1.4
No Aerosols		0.18 ± 0.02	0.43 ± 0.15	2.4 ± 1.1

Table 6.4: We can firstly note that there is poor agreement in all cases due to the large errors in the HiRes 2 energy estimate. The QR based cases seem to provide best agreement.

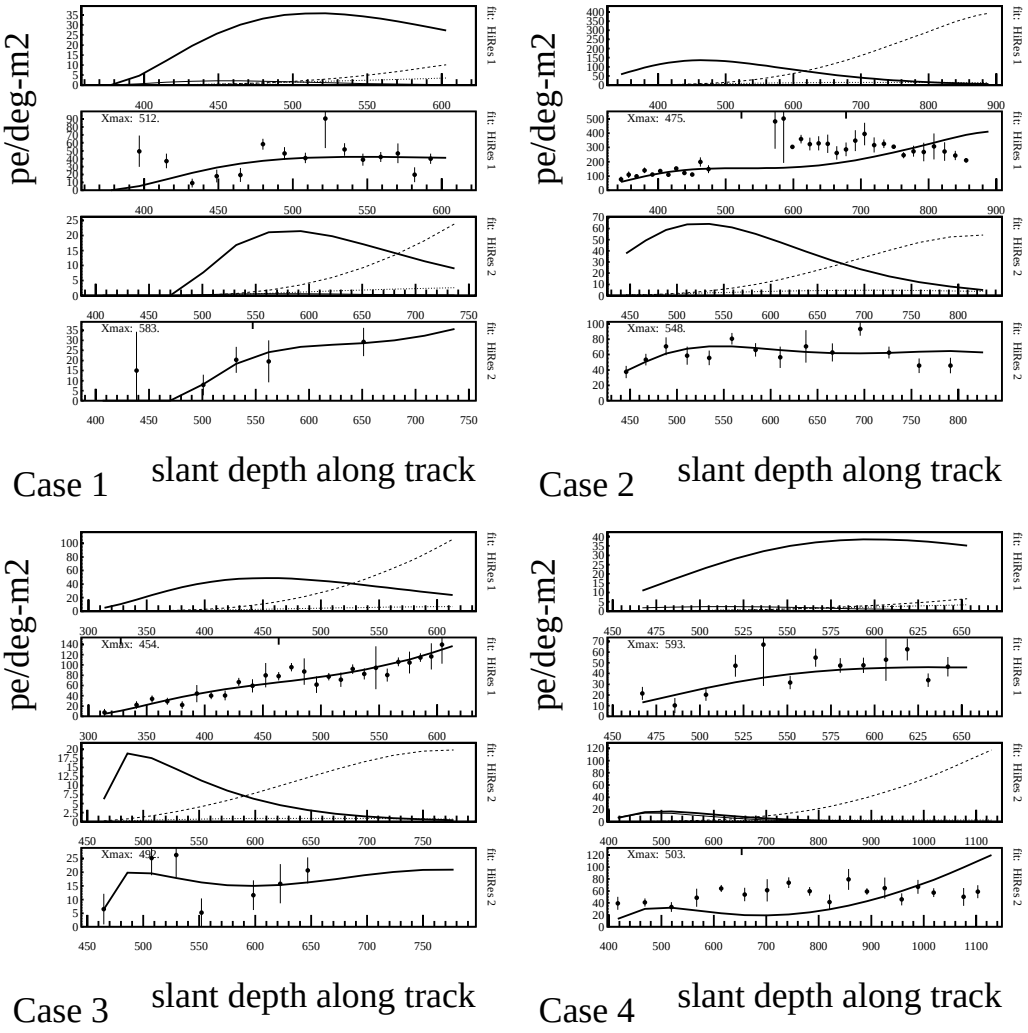

Figure 6.13: HiRes 1 and HiRes 2 profile fits using quality ratio based L_{aero} and Fly's Eye phase function the for the first four cases discussed in tables 6.4, 6.5, 6.6, and 6.7. For each site (and each case) the light due to each component is presented followed by a plot of the fitted light profile (the sum of the four components) to the measured light profile at the detector. In the plots of the four light components, the fluorescence component is the thick solid line, direct Cerenkov is the thin solid line, Rayleigh scattered Cerenkov is dotted line, and Mie (aerosol) scattered Cerenkov is the dashed line.

Case 2: Quality Ratio = 3.0				
HR 1 R_p	9.6km	HR 2 R_p	20.6km	L_{aero} = 13.5km
Aerosol Model		Energy (EeV)		HiRes 2 / HiRes 1
L_{aero}	Phase Fn	HiRes 1	HiRes 2	Energy Ratio
QR based	Fly's Eye	2.5 ± 0.1	4.9 ± 0.3	1.9 ± 0.2
QR based	D'Almeida	4.5 ± 0.1	8.2 ± 0.8	1.8 ± 0.2
Fixed	Fly's Eye	13.1 ± 0.6	19 ± 4	1.5 ± 0.4
No Aerosols		7.6 ± 0.2	5.9 ± 0.5	0.8 ± 0.1

Table 6.5: This event was taken not long after the operator noted that the weather had improved from being bad at the start of the night to being almost perfect. We note that the best agreement is obtained with the no aerosols case. A possible explanation is due to the presence of low ground fog (this had been explicitly observed two nights previously) which would bias the QR measurement and thus underestimate L_{aero}.

Case 3: Quality Ratio = 3.1				
HR 1 R_p	4.8km	HR 2 R_p	15.8km	L_{aero} = 13.0km
Aerosol Model		Energy (EeV)		HiRes 2 / HiRes 1
L_{aero}	Phase Fn	HiRes 1	HiRes 2	Energy Ratio
QR based	Fly's Eye	0.34 ± 0.02	0.42 ± 0.06	1.2 ± 0.2
QR based	D'Almeida	0.45 ± 0.03	0.7 ± 0.3	1.5 ± 0.8
Fixed	Fly's Eye	1.2 ± 0.2	4 ± 3	3 ± 3
No Aerosols		1.0 ± 0.2	1.5 ± 0.8	1.5 ± 1

Table 6.6: The best case appears to be using the QR based L_{aero} and the Fly's Eye phase function. The other models appear to be worse, but they do have larger errors due to the poor coverage at HiRes 2. It is also interesting to note large differences between the energy estimates of the different models (due to the different models predicting different amounts of aerosol scattered light).

Case 4: Quality Ratio = 3.1				
HR 1 R_p	3.7km	HR 2 R_p	5.5km	L_{aero} = 12.8km
Aerosol Model		Energy (EeV)		HiRes 2 / HiRes 1
L_{aero}	Phase Fn	HiRes 1	HiRes 2	Energy Ratio
QR based	Fly's Eye	0.21 ± 0.03	0.18 ± 0.01	0.9 ± 0.2
QR based	D'Almeida	0.21 ± 0.03	0.25 ± 0.01	1.1 ± 0.2
Fixed	Fly's Eye	0.24 ± 0.04	1.27 ± 0.05	5.2 ± 1.1
No Aerosols		0.21 ± 0.04	0.95 ± 0.04	4.4 ± 0.9

Table 6.7: The QR based L_{aero} profile fits appear to perform the best, although the HiRes 2 fit does seem to be overestimating the aerosol scattered Cerenkov component. This results in a lowered energy estimate as less of the total light is assigned to fluorescence. Even though the profile fit for this case in figure 6.13 appears to be quite poor, it does however perform substantially better than the no aerosols case.

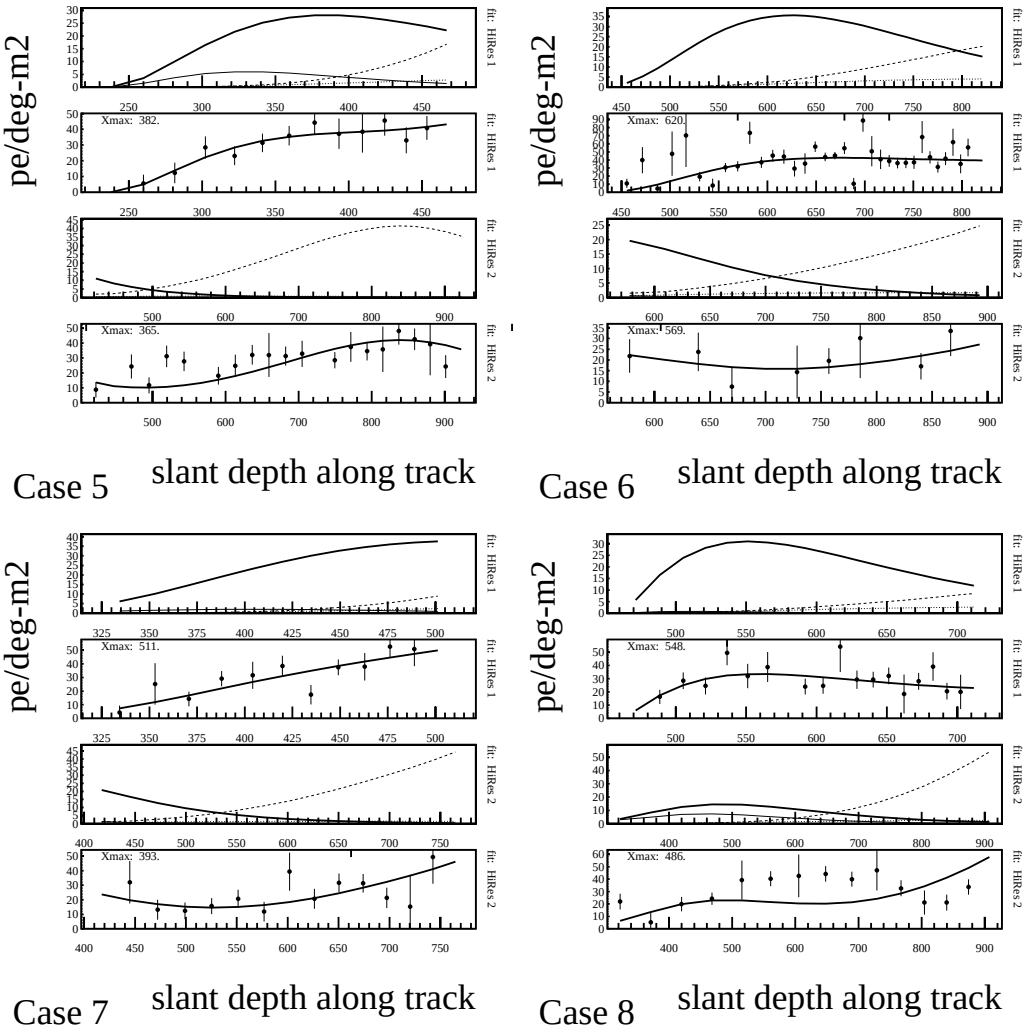

Figure 6.14: HiRes 1 and HiRes 2 profile fits using quality ratio based L_{aero} and Fly's Eye phase function the for the second four cases discussed in tables 6.8, 6.9, 6.10, and 6.11. For each site (and each case) the light due to each component is presented followed by a plot of the fitted light profile (the sum of the four components) to the measured light profile at the detector. In the plots of the four light components, the fluorescence component is the thick solid line, direct Cerenkov is the thin solid line, Rayleigh scattered Cerenkov is dotted line, and Mie (aerosol) scattered Cerenkov is the dashed line.

Case 5: Quality Ratio = 3.8				
HR 1 R_p	3.2km	HR 2 R_p	8.5km	L_{aero} = 6.9km
Aerosol Model		Energy (EeV)		HiRes 2 / HiRes 1
L_{aero}	Phase Fn	HiRes 1	HiRes 2	Energy Ratio
QR based	Fly's Eye	0.13 ± 0.02	0.17 ± 0.01	1.3 ± 0.2
QR based	D'Almeida	0.14 ± 0.02	0.20 ± 0.01	1.4 ± 0.3
Fixed	Fly's Eye	0.17 ± 0.03	1.7 ± 0.2	10 ± 3
No Aerosols		0.15 ± 0.03	0.99 ± 0.08	7 ± 2

Table 6.8: Best results are again obtained with QR based L_{aero} profile fits. However it does appear to attribute the majority of the observed light at HiRes 2 to the aerosol scattered Cerenkov component, thus reducing the fraction of the total light assigned to fluorescence (and thus probably underestimates the true energy).

Case 6: Quality Ratio = 3.8				
HR 1 R_p	5.3km	HR 2 R_p	9.5km	L_{aero} = 6.4km
Aerosol Model		Energy (EeV)		HiRes 2 / HiRes 1
L_{aero}	Phase Fn	HiRes 1	HiRes 2	Energy Ratio
QR based	Fly's Eye	0.32 ± 0.02	0.36 ± 0.05	1.1 ± 0.2
QR based	D'Almeida	0.36 ± 0.02	0.46 ± 0.12	1.3 ± 0.4
Fixed	Fly's Eye	0.42 ± 0.03	1.02 ± 0.16	2.4 ± 0.6
No Aerosols		0.37 ± 0.03	0.72 ± 0.11	2.0 ± 0.5

Table 6.9: This event was taken approximately two hours after the previous case. Best results are again obtained with QR based L_{aero} profile fits.

Case 7: Quality Ratio = 3.8				
HR 1 R_p	3.6km	HR 2 R_p	7.2km	L_{aero} = 6.4km
Aerosol Model		Energy (EeV)		HiRes 2 / HiRes 1
L_{aero}	Phase Fn	HiRes 1	HiRes 2	Energy Ratio
QR based	Fly's Eye	0.3 ± 0.2	0.21 ± 0.02	0.9 ± 0.7
QR based	D'Almeida	0.3 ± 0.2	0.24 ± 0.07	0.9 ± 0.9
Fixed	Fly's Eye	0.3 ± 0.3	1.1 ± 0.4	4 ± 4
No Aerosols		0.3 ± 0.2	0.8 ± 0.2	3 ± 3

Table 6.10: This night was noted as clear, but with high (64%) humidity. As would be expected due to the high humidity (water droplets will act as aerosols) the QR based L_{aero} profile fits appear to perform the best. However the poor X_{max} coverage at HiRes 1 leads to large errors in the energy estimate making the distinction between models less clear.

Case 8: Quality Ratio = 4.0				
HR 1 R_p	4.8km	HR 2 R_p	6.4km	$L_{aero} = 5.5$km
Aerosol Model		Energy (EeV)		HiRes 2 / HiRes 1
L_{aero}	Phase Fn	HiRes 1	HiRes 2	Energy Ratio
QR based	Fly's Eye	0.19 ± 0.01	0.37 ± 0.03	2.0 ± 0.3
QR based	D'Almeida	0.20 ± 0.02	0.46 ± 0.03	2.3 ± 0.4
Fixed	Fly's Eye	0.21 ± 0.04	0.84 ± 0.08	3.9 ± 1.0
No Aerosols		0.19 ± 0.03	0.62 ± 0.06	3.3 ± 0.9

Table 6.11: All models appear to perform poorly on this event. The operator noted the presence of fog and high humidity in the log. A possible explanation may be that ground fog is biasing the QR estimates of L_{aero} by making it too short. However due to the high humidity aerosols are still having an effect leading to the poor estimates with the no aerosol case.

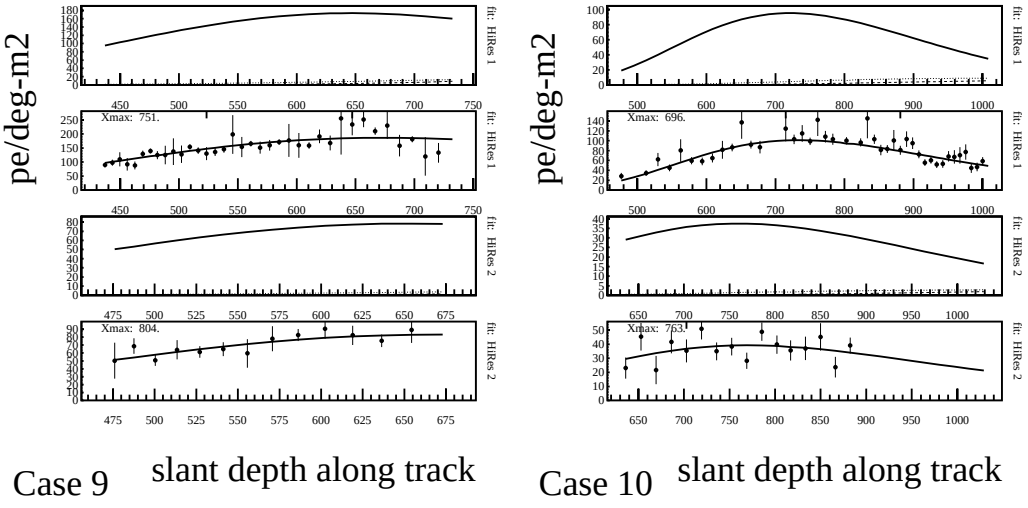

Figure 6.15: HiRes 1 and HiRes 2 profile fits using quality ratio based L_{aero} and Fly's Eye phase function the for the two cases discussed in tables 6.12 and 6.13. These two events were taken within 3 hours of each other. For each site (and each case) the light due to each component is presented followed by a plot of the fitted light profile (the sum of the four components) to the measured light profile at the detector. In the plots of the four light components, the fluorescence component is the thick solid line, direct Cerenkov is the thin solid line, Rayleigh scattered Cerenkov is dotted line, and Mie (aerosol) scattered Cerenkov is the dashed line.

Case 9: Quality Ratio = 4.6				
HR 1 R_p	10.6km	HR 2 R_p	18.5km	L_{aero} = 3.3km
Aerosol Model		Energy (EeV)		HiRes 2 / HiRes 1
L_{aero}	Phase Fn	HiRes 1	HiRes 2	Energy Ratio
QR based	Fly's Eye	11 ± 2	21 ± 70	2 ± 7
QR based	D'Almeida	11 ± 2	22 ± 100	2 ± 9
Fixed	Fly's Eye	7 ± 1	9 ± 15	1 ± 2
No Aerosols		6 ± 1	6 ± 5	1 ± 1

Table 6.12: This is a particularly interesting event due to the large distance the event was observed at, whilst the QR based L_{aero} was very small. The operator noted that the weather was good apart from the presence of ground fog. The presence of ground fog would seriously bias the value of the aerosol extinction length from the QR, pushing up the energy estimates due to the large distances involved. Not surprisingly, the best agreement is obtained with the no aerosols case, although error in HiRes 2 is still rather large (again due to poor X_{max} coverage).

Case 10: Quality Ratio = 4.7				
HR 1 R_p	9.7km	HR 2 R_p	19.5km	L_{aero} = 3.0km
Aerosol Model		Energy (EeV)		HiRes 2 / HiRes 1
L_{aero}	Phase Fn	HiRes 1	HiRes 2	Energy Ratio
QR based	Fly's Eye	3.45 ± 0.09	6 ± 2	1.8 ± 0.6
QR based	D'Almeida	3.50 ± 0.09	6 ± 2	1.8 ± 0.6
Fixed	Fly's Eye	2.44 ± 0.06	3 ± 1	1.3 ± 0.5
No Aerosols		2.06 ± 0.05	2.4 ± 0.8	1.2 ± 0.4

Table 6.13: This event was taken approximately 2.5 hours earlier than the previous night and thus suffers from the same problems due to ground fog. Not surprisingly, the best agreement is obtained with the no aerosols case. These last two cases indicate the need to account for ground fog.

A common failure is to attribute too much of the observed light to one source such as aerosol scattered Cerenkov light. In this case, less of the total observed light is attributed to fluorescence which then results in a reduced energy estimate. This also explains why the energy estimates using the D'Almeida phase function tend to be larger than those with the Fly's Eye phase function (assuming the same QR based L_{aero}). If we examine figure 6.5 we note that for scattering angles larger than about 10°, the Fly's Eye phase function is larger than D'Almeida phase function, and thus will scatter more Cerenkov light towards the detector. Hence we should expect the profile fit using the D'Almeida phase function to assign larger energies than the profile fit using the Fly's Eye phase function.

In conclusion, these case studies serve to reinforce our earlier conclusions – that the quality ratio based aerosol extinction lengths are more appropriate than the fixed values used by the Fly's Eye. No clear distinction between the two phase functions was possible. However based on the work by Luo[130] the preference should probably be the D'Almeida or a similar phase function based on a lognormal size distribution of aerosol particles. The case studies indicate the need for further work into the area of atmospheric models. It appears that quality ratio type measurements can provide useful information on the aerosol extinction length but they do have limitations that must be addressed. Namely, one must be aware of the presence of ground fog which will bias the value. We should also note that in this study we assumed a zero height mixing layer, an assumption that may not always be true and should thus be investigated (in fact one could view the presence of ground fog as a mixing layer). Further analysis of results from flasher arrays and cloud detectors[29] (which can be mounted on the actual flashers) should provide the necessary information to allow effective monitoring of the atmosphere.

Finally we should note that the results of these case studies indicate the need for further work on the profile fitter and possibly on the calibration so as to obtain closer agreement between the HiRes 1 and HiRes 2 profile fits. Further work is also needed to understand the performance and any biases within the combined HiRes 1/ HiRes 2 profile fits.

6.4 The HiRes Prototype Stereo Dataset

This section presents some preliminary results of the analysis of the HiRes prototype stereo dataset, and evaluates the likely performance of HiRes stage 1.0. Only those events that passed the quality cut discussed in section 6.3.1 were considered and based on the work done on aerosol models in section 6.3, it was decided to use the combined HiRes 1 / HiRes 2 profile fitter with the D'Almeida phase function and quality ratio based aerosol extinction length.

The distribution of energies in shown in figure 6.16 and the distribution of X_{max} values in figure 6.17. Zenith angle, tracklength and R_p distributions are presented in figure 6.18. A plot of the zenith angle distribution compensated for solid angle effects, $\mathrm{dN}(\theta)/\mathrm{d}\Omega$, is also plotted. The zenith angle distribution for a detector such as HiRes is vastly different from that of a ground array, which is of the form $\mathrm{dN}(\theta)/\mathrm{d}\Omega = \cos^{8.3}\theta$[91] and is plotted as the dotted line in the figure. This difference relates to the design of the detector – HiRes detects the isotropic fluorescence light from the EAS, and thus maximises its aperture by observing at low elevation angles. Ground arrays, must directly detect the passage of the EAS, so $\mathrm{dN}(\theta)/\mathrm{d}\Omega$ monotonically decreases as zenith angle increases due to atmospheric absorption of showers (which goes as $\sec\theta$). However a detector such as HiRes detects the isotropic fluorescence light from the EAS, and attempts to maximise its aperture by observing at low elevation angles. We thus have a selection effect towards inclined showers as we are more likely to view the development of these shower (needed to for accurate reconstruction) than for those with small zenith angles.

Ideally we would like to compare these results with those from Monte Carlo Simulations. However, no such simulations are available for this two site configuration of the HiRes detector (most simulations have been performed assuming HiRes stage 1 or 2 configurations). Such simulations have been left for further work. However we can still interpret these results to see if they are reasonable. The first point we can note is that the distributions of energies and X_{max} appears reasonable. Given the E^{-3} nature of the energy spectrum and our elevation coverage we not surprisingly see that the majority of events have energies between 10^{17} and 10^{18}eV. If we now examine the

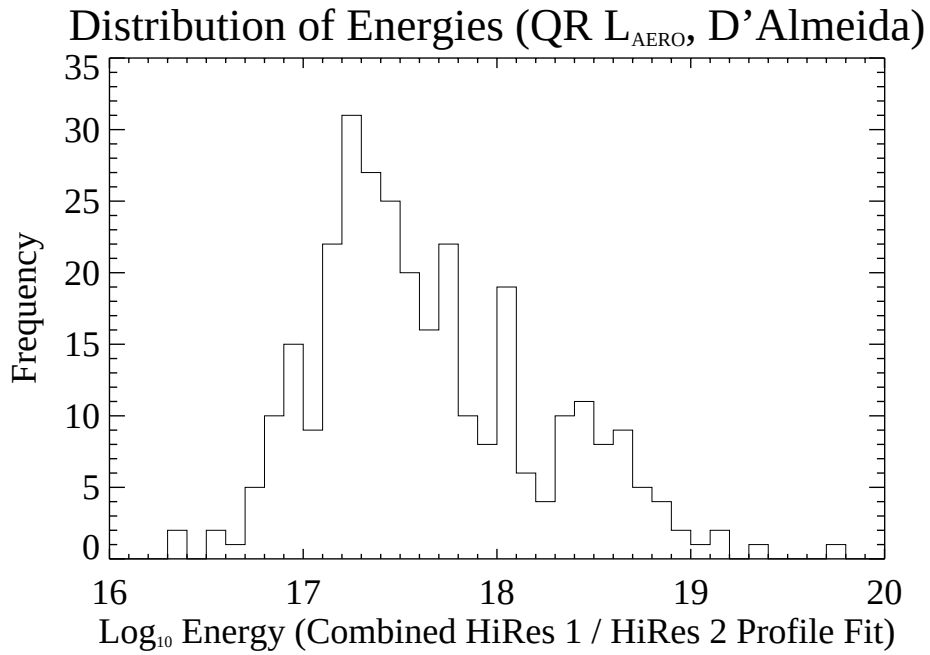

Figure 6.16: Distribution of energies of from combined HiRes 1 / HiRes 2 profile fit.

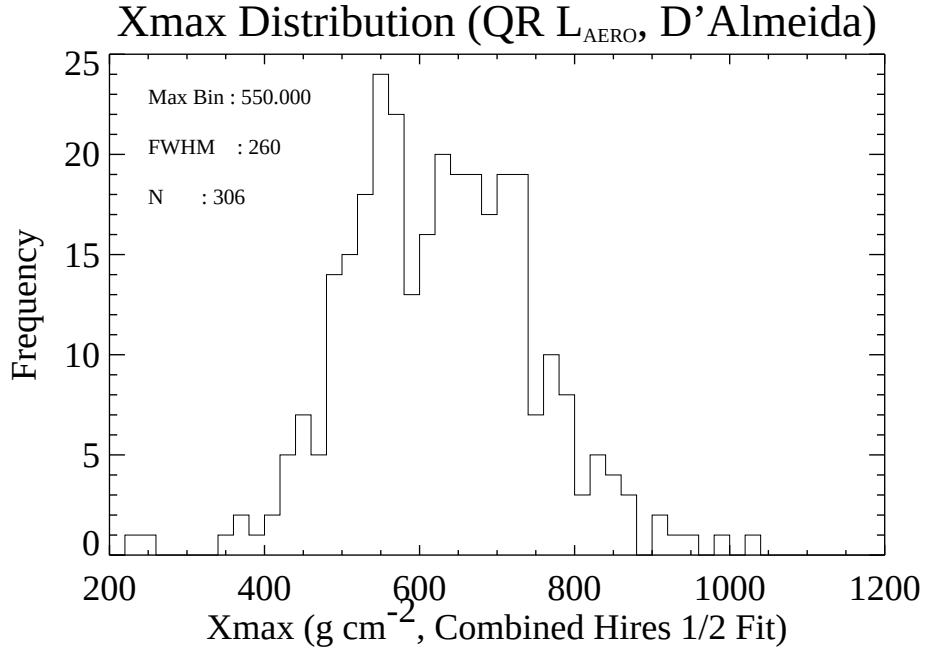

Figure 6.17: Distribution of X_{max} for the combined HiRes 1 / HiRes 2 profile fit. Errors in Xmax were less than $35 gcm^{-2}$ 90% of the time.

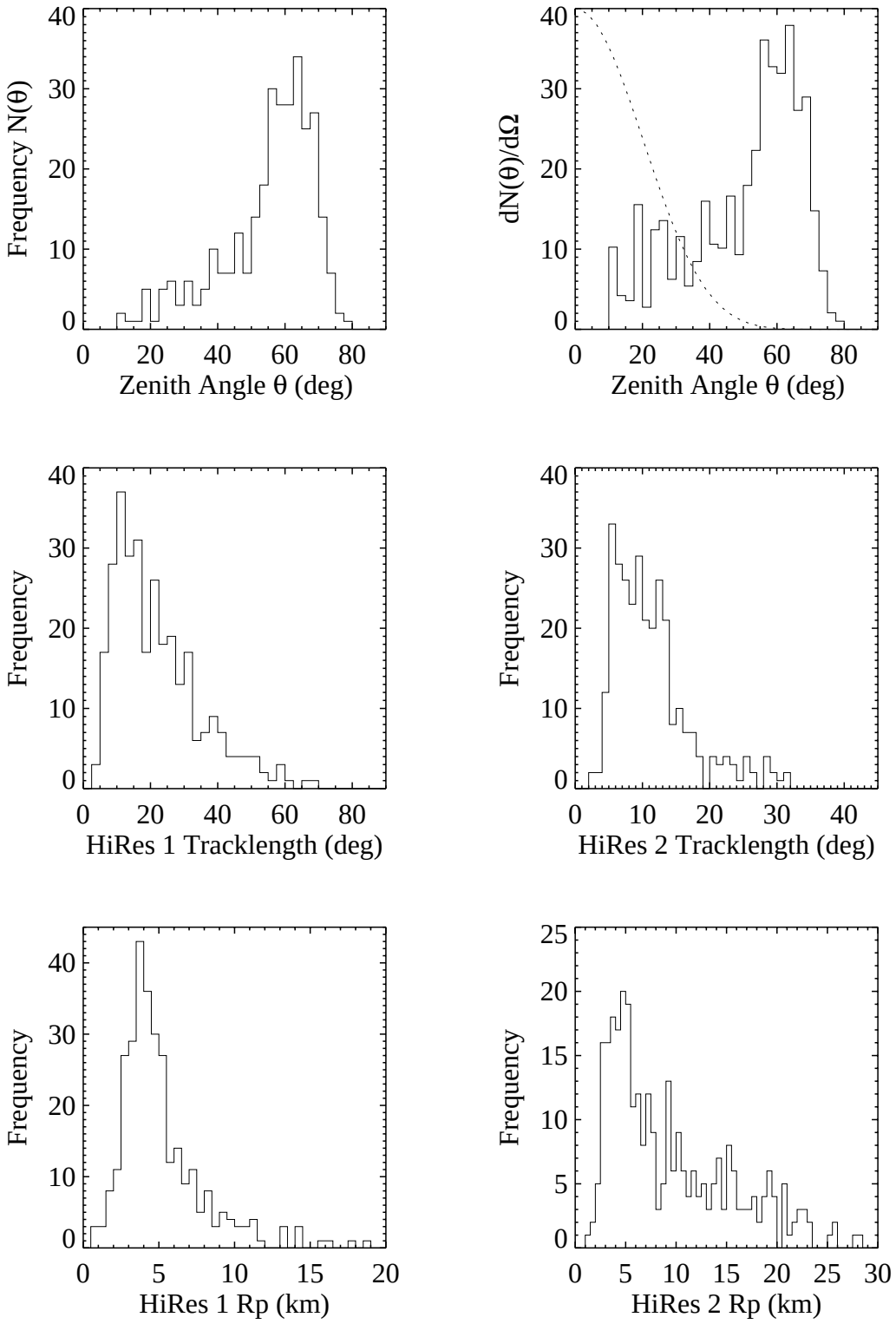

Figure 6.18: Zenith angle, zenith angle distribution compensated for solid angle, track-length and R_p distributions for the 309 cosmic rays in the HiRes prototype stereo dataset that passed the quality cuts discussed in section 6.3.1

tracklength and R_p distance distributions we see that the majority of events have small tracklengths and R_p values. Again, this is what we expect given the large number of showers around $10^{17} - 10^{18}$eV. These showers generate less light than the higher energy showers so we expect shorter tracklengths and smaller R_p distances.

If we examine the distribution of tracklengths in HiRes 2 we see a large bias towards tracklengths below about 20° indicating that most showers were detected in one or possibly two mirrors. This is approximately what we expect as low energy showers produce less light, so are likely to have small tracklengths, and higher energy showers are likely to be more distant which also contributes to the population of small tracklengths in HiRes 2.

One of the aims of the HiRes project is to detect significant numbers of high energy ($E > 10^{18}$eV) showers. Of the 309 well reconstructed showers considered, a total of 84 ($\sim 27\%$) events had energies above 10^{18}eV, and 5 events had energies above 10^{19}eV. The highest energy event observed had an estimated energy of $5.0 \pm 0.5 \times 10^{19}$eV and is displayed in figure 6.19. It is also worth noting that almost all the showers with HiRes 1 $R_p > 8$km and HiRes 2 $R_p > 17$km had energies above 10^{18}eV, quite clearly demonstrating an important property of fluorescence detectors – that their aperture increases with energy. A calculation of the actual aperture and energy spectrum has been left as further work.

A skymap (in right ascension and declination coordinates) of the arrival directions of the 309 cosmic rays are presented in figure 6.20. This plot shows the exposure bias of the northern hemisphere site ($\sim 40°$N). Further work to calculate the total exposure of the detector is needed before an anisotropy study may be performed.

6.4.1 Comparison of Prototype and Stage 1 Results

The HiRes prototype detector has been shut down and is currently operating in the stage 0.5 configuration, in preparation for stage 1.0 operation (see chapter 3 or Abu-Zayyad *et al.*[1] for details). It is obviously of interest to examine how profile fitting performs when the elevation angle coverage is reduced from that of the HiRes 1 prototype to the stage 1 configuration of a single elevation ring of mirrors at HiRes 1.

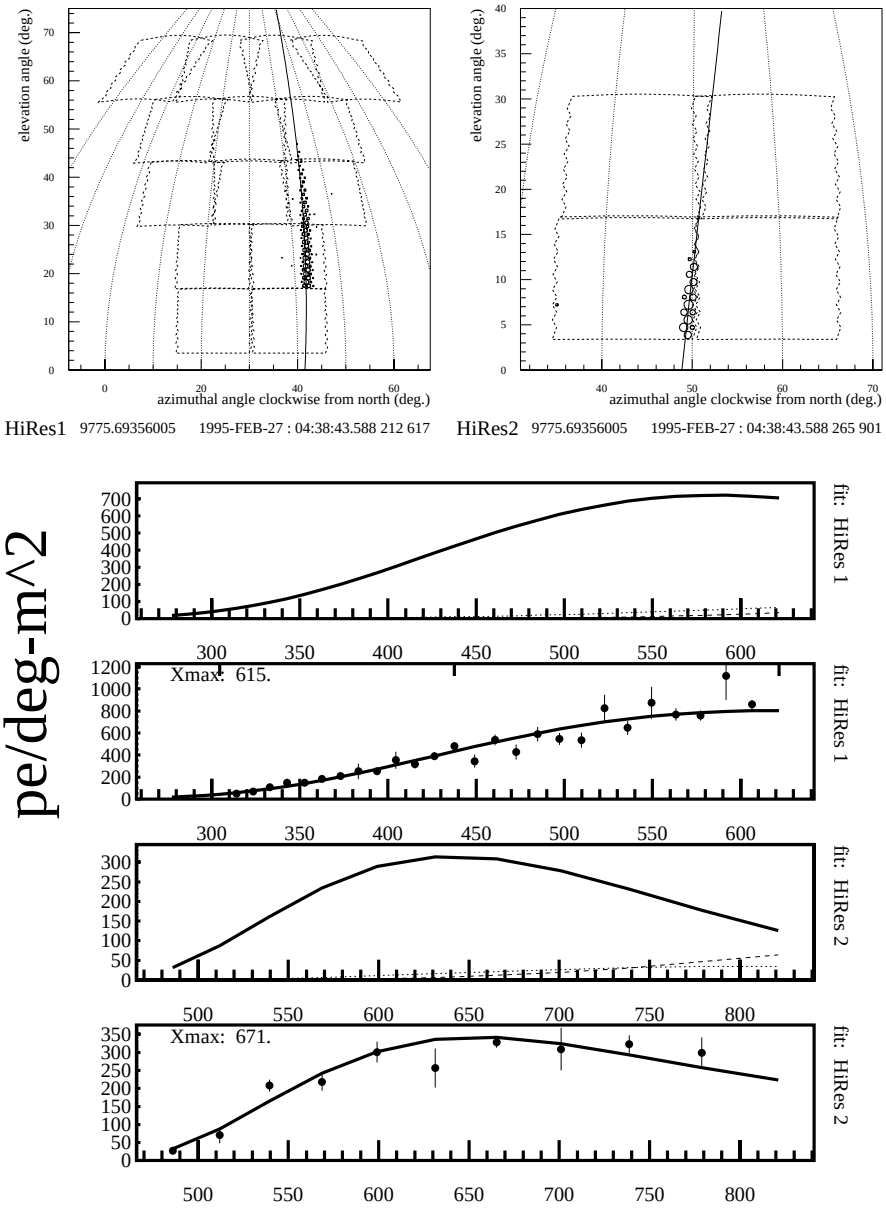

Figure 6.19: The highest energy event observed with HiRes prototype detector. The top two plots show the pattern of triggered PMTs and the fitted trajectory in both detectors followed by profile fits for HiRes 1 and HiRes 2. For each of the profile fits, the top plot illustrates the contribution due to fluorescence light (thick solid line), direct Cerenkov light (thin solid line), Rayleigh scattered Cerenkov (dashed line) and Mie scattered Cerenkov (dotted line). The lower plot illustrates the total light signal and the the measured light signal in each bin (pe/(deg m^2) with 1σ errors as a function of the slant depth along the track. The R_p distances were 11.5km and 23km for HiRes 1 and 2 respectively and the combined profile fit estimated an energy of $5.0\pm0.5\times10^{19}$eV.

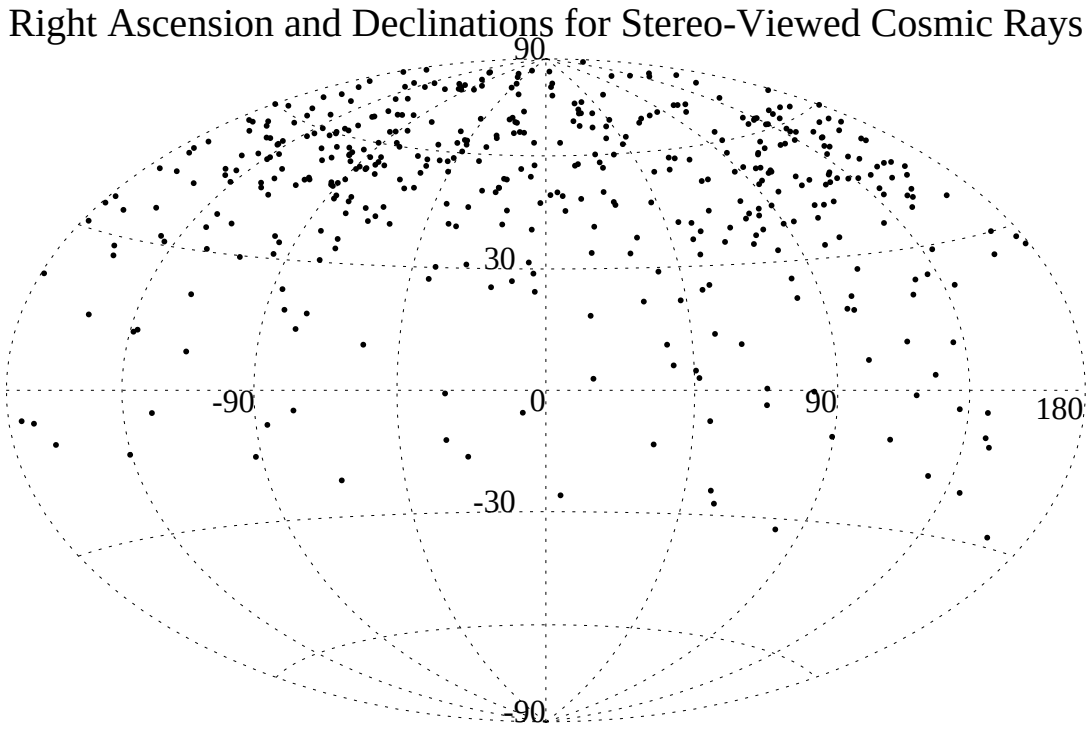

Figure 6.20: Skymap in right ascension and declination coordinates for the arrival directions of the 309 cosmic rays passing the quality cuts discussed in section 6.3.1. Note that before any anisotropy analysis is possible the exposure must be taken into account. This plot simply indicates the exposure bias due to the northern hemisphere site (a latitude of 40°N).

Thus the full stereo dataset (1020 events) were passed through the stereo-timing fitter, and reconstructed assuming a stage 1 configuration of mirrors. These events were then passed through the light binning program and finally the profile fitter (using the D'Almeida phase function and quality ratio based aerosol extinction length). A total of 40 events were reconstructed with 25 passing a quality cut that the relative error in the energy estimated by the combined HiRes 1 / HiRes 2 profile fit be less than 20%. These events were then compared with the corresponding events in which the full elevation angle coverage of the HiRes 1 detector was used.

Figure 6.21 shows the energy correlation between the HiRes prototype and HiRes stage 1.0 configuration for the HiRes 1 profile fit. Similarly, figure 6.22 presents the correlation for the HiRes 2 profile fit and figure 6.23 presents the correlation for the HiRes 1 / HiRes 2 profile fit.

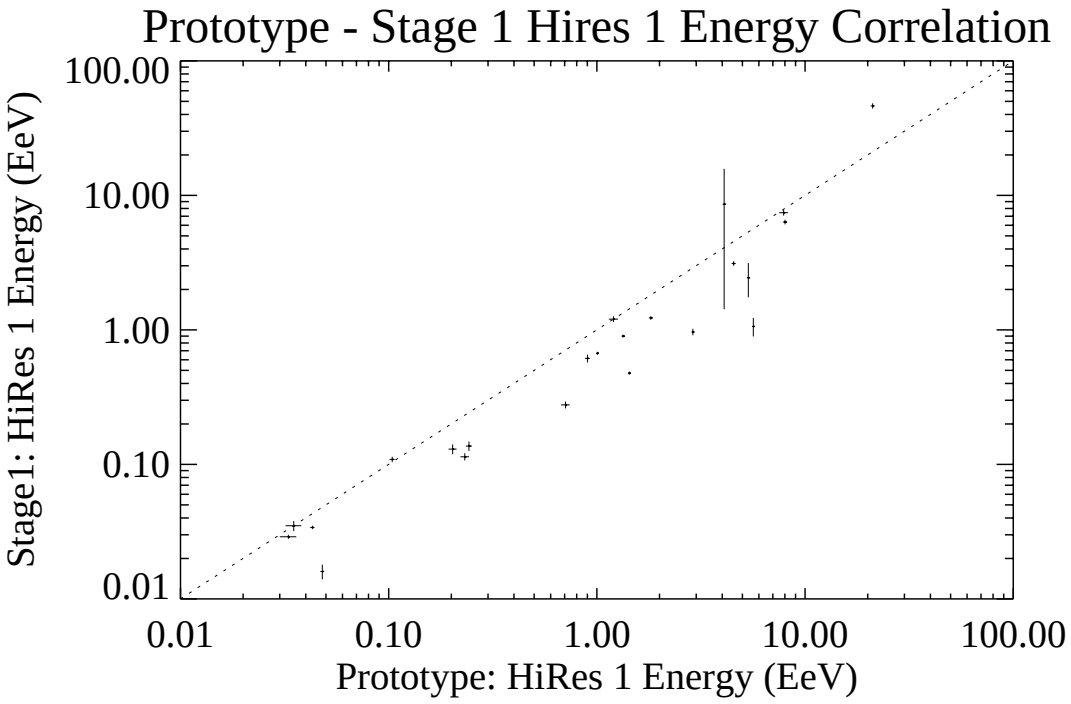

Figure 6.21: Energy correlation between the HiRes prototype and HiRes stage 1.0 (single elevation ring) configurations for the HiRes 1 profile fit.

For the case of the HiRes 1 profile fit (figure 6.21), we see the stage 1 configuration tends to underestimate the energy compared to the estimate using the full prototype detector configuration. In general a good profile fit requires viewing the shower around

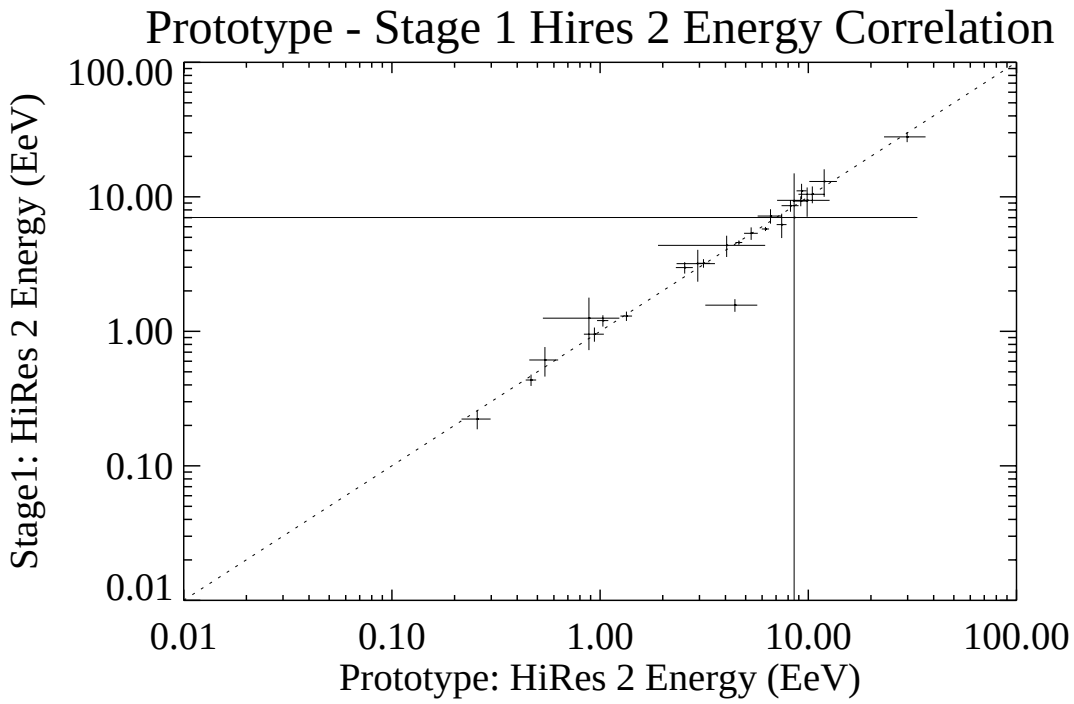

Figure 6.22: Energy correlation between the HiRes prototype and HiRes stage 1.0 (single elevation ring) configurations for the HiRes 2 profile fit. Energy differences are due to differences in fitting the EAS trajectory.

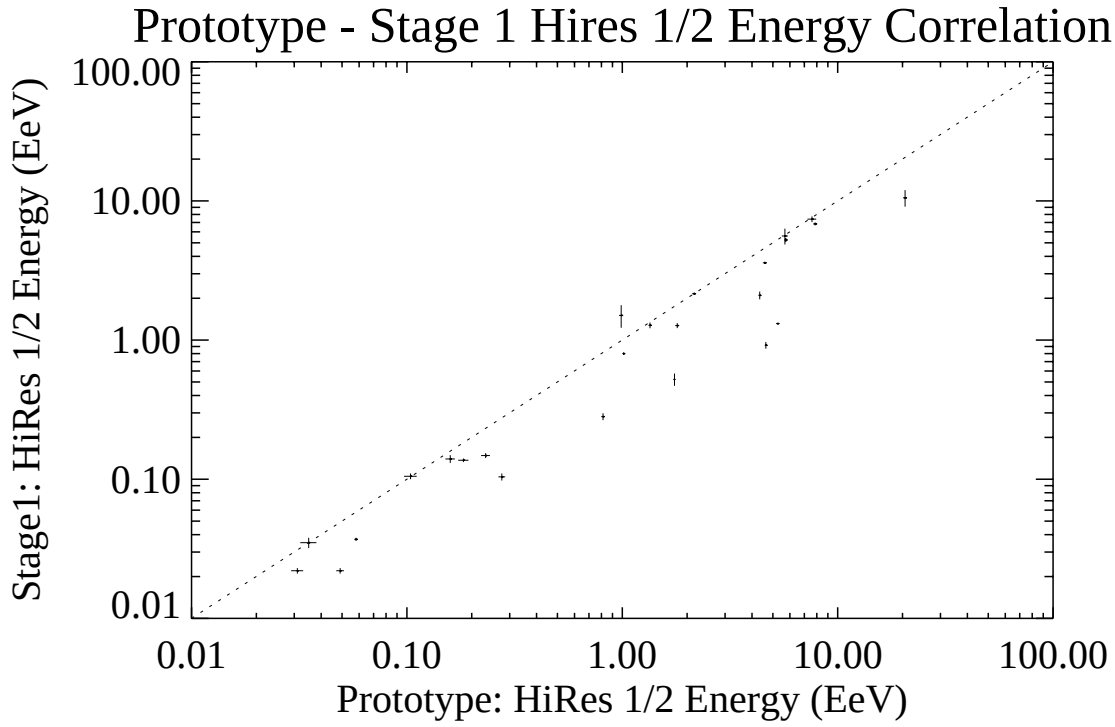

Figure 6.23: Energy correlation between the HiRes prototype and HiRes stage 1.0 (single elevation ring) configurations for the combined HiRes 1 / HiRes 2 profile fit.

X_{max}. However stage 1 will generally only view X_{max} for distant high energy showers. Hence for the majority of showers, which are nearby showers and/or lower energy showers, we should expect poorer profile fits and thus energy estimates

As would be expected, there is a good correlation in the HiRes 2 profile fit (figure 6.21). The only difference between the two profile fits arises dues to differences in the estimation of the shower trajectory. As the correlation is quite strong we can conclude that any such differences in the trajectory had a very minor effect on the profile fit. However we should note that this is probably just a selection effect of our energy resolution cut, from which we can infer that in events with poor trajectory fits, the profile fitter also failed.

Finally, for the combined HiRes 1 / HiRes 2 profile fit (figure 6.23) we see a reasonable correlation between energy estimates for the two configurations. We once again see that the stage 1 profile fit tends to predict lower energy than the prototype profile fit (as was the case in the HiRes 1 profile fit). A case study of the 25 events indicated that this reduction of energy by the stage 1 profile fit was generally due to viewing the tail of the shower after X_{max}. In general the more distant the shower the better the fit (which is why the inclusion of HiRes 2 information in this combined profile fit was able to improve the agreement between the two configurations over that of the HiRes 1 case.)

Thus to conclude we can infer that the loss of the elevation angular coverage between the Hires prototupe and the stage 1.0 detector should not adversely affect energy estimates of the more distant high energy showers. Provided the region around X_{max} is well viewed by either site, the energy estimate should be reasonable.

Chapter 7

Conclusions and Further Work

7.1 Summary and Conclusions

The HiRes detector represents a step forward in the use of the air fluorescence technique in the study of extremely high energy cosmic rays (discussed in chapter 1). It builds upon the success of the Fly's Eye detector and will detect larger numbers of high energy extensive air showers at greater distances and finer resolution. To achieve these aims has required the development and testing of new detector units, and has brought new problems and challenges.

This thesis presents work performed by the author on the prototype HiRes detector described in chapter 3. Whilst much of the development of HiRes was based on both past experience with the Fly's Eye detector and the use of Monte Carlo simulations, the author has sought to demonstrate that we have developed the necessary expertise to solve many of the expected problems on *experimental* data. However on such a large project, it becomes necessary to limit one's scope to a subset of all the problems and tasks associated with the development of a new detector. With this in mind the author has concentrated on the development and application of high precision timing information to allow the coherent use of information from both detector sites.

In chapter 4 the author details the development of Global Positioning System (GPS) based clocks to provide high precision relative timing accuracy between the two HiRes sites. As a result of this work, the relative timing accuracy of the two sites

is less than 50ns the majority of the time, with occasional degradations in the timing accuracy to around 100ns. Absolute timing accuracy is within 340ns of UTC 95% of the time. As part of this work the timing system was checked and calibrated giving us confidence in our ability to correctly assign triggering times of PMTs.

The implementation of high precision relative timing accuracy between the two HiRes sites allowed the development of a stereo-timing air shower reconstruction program which is discussed in chapter 5. The lack of high precision relative timing accuracy had previously prevented the use of this technique on the Fly's Eye detectors. However Monte Carlo simulations had indicated that if one had high precision relative timing between the two sites, and one could account for all timing systematics, then the technique should provide reconstruction accuracy better than any other method in use. Thus the author undertook the development and testing of a stereo-timing reconstruction program.

Testing and optimisation of the reconstruction program utilised the Laserscope, a portable telescope mounted UV laser which can be steered and fired to produce a beam of UV light in the atmosphere capable of triggering the HiRes detectors. The Laserscope thus provided a large dataset of cosmic ray like tracks with known positions and trajectories. The Laserscope data was also used in attempts to parameterise PMT trigger time slewing, a known source of systematic error in assigning PMT triggering times. The results of this work indicated that for EAS observed with opening angles greater than about 10° (where the opening angle is the angle between the two shower detector planes) the median reconstruction error was 0.4° with 95% of events being reconstructed with errors of less than 1°. For EAS viewed at small opening angles, the reconstruction accuracy is worse, with a median error of 0.8° and 95% limit of 1.8°. An evaluation of the performance of the stereo-timing reconstruction program on data from the stage 1.0 detector configuration was also performed by reconstructing showers using only the lowest elevation ring of mirrors at HiRes 1 (and the two elevation rings of mirrors at HiRes 2). Encouragingly results indicated only a small increase in the reconstruction error despite the loss of 54° of elevation angle coverage between the two configurations.

High precision relative timing accuracy between the two HiRes sites allowed the

development of an accurate stereo-timing reconstruction program. An accurately reconstructed trajectory is the important first step in determining EAS parameters such as depth of shower maximum and primary particle energy. These parameters are estimated through the use of a program to compare the measured light profile of the EAS with that expected assuming a Gaisser-Hillas shower development function. Chapter 6 thus describes the compilation of the stereo dataset and the development of a profile fitting program for use on this dataset.

Fitting the measured light profile to a Gaisser-Hillas function is a well understood problem. However application to the HiRes stereo dataset brings with it new problems. EAS are now being viewed at much larger distances than those detected by the Fly's Eye. The effect of the atmosphere, and in particular aerosol scattering and attenuation of light, is a much more significant problem than it was for the Fly's Eye. This has long been recognised, so that nightly monitoring of atmospheric conditions is performed.

These nightly measurements were incorporated into the profile fitting program, and a comparison made of the use of different aerosol models. The most significant atmospheric effect is attenuation due to aerosol scattering of light, which is partly characterised by an aerosol extinction length. The comparison indicated that the use of the Fly's Eye fixed aerosol extinction length tends to significantly overestimate the primary particle energy. This was due to measured extinction lengths being consistently longer than the Fly's Eye value, which, due to the significantly larger distances involved with the detection of light by HiRes 2, results in over estimation of primary particle energy. Care must be taken with the use of these nightly measurements to ensure that they are not biased by the presence of ground fog or an aerosol mixing layer. Evaluation of different aerosol scattering phase functions was more difficult, with the comparison being largely insensitive to the different phase functions considered. However it was noted that energy estimates using a phase function based on a log normal distribution of particles were systematically higher than those using the Fly's Eyes phase function which is based on a power law distribution of aerosol particles. Previous work indicates that a phase function based on a log normal distribution of particles should be more appropriate, so until further evidence is obtained preference should probably be given to a lognormal based phase function

From analysis of the stereo dataset, it appears that the HiRes detector is achieving the desired aims. We are able to well reconstruct EAS at very large distances from the detector. Energy and depth of shower maximum distributions appear reasonable, with the expected increase in aperture with energy being observed. The performance of event reconstruction assuming a stage 1.0 configuration was compared with results using the prototype configuration. This comparison indicated that, provided the region around shower maximum was observed, the energy estimates should be reasonable. Given the elevation angle coverage of the stage 1.0 detector this condition will only be met for the more distant (and in general more energetic) showers.

7.2 Further Work

Whilst the author has performed significant work to ensure the HiRes detector reaches its potential, there is always further work that may be performed. Thus in this section I will highlight any remaining problems or follow up work that should be performed.

It is obviously important that we maintain the high precision timing system currently in place. Thus it is important that we maintain checks, such as recording satellites being viewed by the GPS receivers at each site, and analysis of Laserscope shots (which has now been synchronised to fire on the GPS 1PPS output) to ensure we are maintaining our timing accuracy. One could also test the absolute timing accuracy by developing a stable clock (such as that based on the Rubidium oscillator used in this work) which could be synchronised to some time reference signal and then transported to the HiRes sites for comparison with the output of the GPS clocks. Such a device could also be used to ensure the two GPS clocks are synchronised to the sub-microsecond level. That is, assuming one clock is functioning and within 340ns of UTC, the other should also be within 340ns of UTC at the time of the measurement (which is of course different to the time of the first measurement and hence the reason we cannot test the relative timing accuracy of the system in this way).

It would also be interesting to use the GPS clocks 1PPS output to either drive or trigger a blue LED placed at the mirror surface so as to trigger an entire PMT cluster. The 1PPS is used to latch central timing (providing a reference trigger time), so that

provided one measures cable delays and the rise time of the LED's pulse, we can check directly check the accuracy of the PMT calibration process. Instead of a blue LED it might be possible to trigger the YAG or a Xenon flasher on the GPS 1PPS output instead.

Moving onto the stereo-timing fitter, there is also much scope for further development. When work on characterising PMT profile responses is completed, the new profile responses should be used to replace the older Monte Carlo responses. It is also desirable to more fully investigate the problem of trigger time slewing through the use of Laserscope shots. More Laserscope shots at a greater range of distances and intensities would allow us to further refine the time slewing parameterisation developed in this thesis. It would also be interesting to further investigate why certain geometries fail, and how to improve the initial guess used by the stereo-timing fitter. Finally, it will be worthwhile to test the reconstruction accuracy on Monte Carlo generated data, both as a comparison with the accuracy achieved using Laserscope data, and to allow further investigation of problematic events such as those at small opening angles or at the edges of the detector.

The HiRes prototype stereo dataset provides much scope for further work. Firstly the exposure of the detector should be calculated to enable spectrum and anisotropy work to be performed. It should also be possible to perform a cluster analysis through combining the high energy events in this dataset with those from other datasets such as the Fly's Eye and AGASA. Secondly there is more scope for work on atmospherics. This thesis investigated the use of an aerosol model with an exponential decrease in density with a fixed scale height. It would be interesting to examine how this changes with different conditions. The approach taken in this thesis was to vary the aerosol extinction length, but it might also be appropriate to consider variations in the scale height or even the presence of a mixing layer. Results from comparison of different aerosol models indicates there is still further work to be performed on the profile fitter, and possibly the absolute calibration. Further work on the newly developed combined HiRes 1/ HiRes 2 profile fitter is also needed to understand its the performance and any biases that may be present. Finally one could use the stereo dataset to follow up the comparison work between the prototype and stage 1 configuration of the detector.

One could further investigate why events were poorly reconstructed and possible ways to overcome this (such as fixing the depth of shower maximum and fitting for shower size).

In conclusion, the operation of the prototype HiRes detector has provided us with a wealth of information on the challenges facing the HiRes project. Significant advances have been made in allowing us to accurately reconstruct the trajectories and energies of large numbers of high energy cosmic rays. With further work we can improve and refine our understanding of the HiRes detector, and begin to solve some of the remaining questions on the nature of these extremely high energy particles.

Appendix A

The Global Positioning System

The Global Positioning System (GPS) was developed by the U.S.A's Department of Defense (DoD) to allow accurate determination of position, velocity and time anywhere in the world. It consists of a active constellation of 21 satellites (plus at least 3 spares) in 12 hour orbits distributed in 6 orbital planes (inclined at 55° to the equator) and at altitudes of approximately 18000 km. The distribution of satellites was designed so that 4 or more satellites are visible 24 hours a day, anywhere in the world, to allow an accurate determination of position. Excellent reviews of the global positioning system may be found in Hofmann-Wellenhof *et al.*[105] and Dana[64] and this appendix will cover some of the important aspects of the system.

A.1 Obtaining a position

To uniquely find the position of a unknown point in three dimensional space requires that we know the location of 3 other points in space as well as the distance from each of the known points to the unknown point. This can be mathematically expressed as solving the ranging equations for the unknown point $(x_{gps}, y_{gps}, z_{gps})$ when we know the distances ρ_i to each of three points (x_i, y_i, z_i):

$$\rho_{i=1,2,3} = \sqrt{(x_{gps} - x_i)^2 + (y_{gps} - y_i)^2 + (z_{gps} - z_i)^2} \tag{A.1}$$

This has direct application in GPS as the orbits of the GPS satellites are accurately known. Thus the satellites act as sources of known position by continuously

transmitting their locations to GPS receivers on the ground. Of course for this to be useful there must also be a way for the time and the satellite receiver distance to be accurately determined. To satisfy these requirements each satellite is fitted with an atomic clock (Cesium or Rubidium) that operates at a fundamental frequency of 10.23MHz. The satellite clocks are monitored by ground control stations and are daily synchronised to within 100ns of UTC by the master control station which has the primary reference for GPS.

The satellite receiver distance is determined by the receiver measuring the travel time of a radio signal sent by the satellite and converting this time to a distance by multiplying it by the speed of light. This distance is called a pseudorange, since it is a combination of the true distance along with errors due to relativistic and atmospheric effects.

To measure the pseudorange distance each satellite transmits a signal called the coarse/acquisition (C/A) code on the L1 carrier frequency of 1575.42MHz. The C/A code is a pseudorandom noise (PRN) code sequence (repeated every millisecond) with different sequences being generated by different initial conditions. This allows each satellite to have a unique identification code. There are 37 such codes used and satellites are referenced by which code sequence they use (e.g. satellite PRN 1). In addition to the C/A codes, the satellites also transmit another pseudorandom noise sequence known as the precise, or P code. The P code is encrypted and this sequence is then known as the Y code. The ability to decode the Y sequence is only available to military users of the system. The P code is a 267 day pseudorandom noise code and has been divide up into 37 seven day sections. The PRN number of the satellite (and the PRN of the C/A sequence) refers to which week of the P code the satellite is using. The P code sequence repeats weekly (starting at midnight on Saturday) and its use allows more accurate position determination. The generation of P and C/A codes will be discussed later.

GPS receivers are able to generate their own version of the C/A codes. Receivers will track satellites and compare the received code sequence with their locally generated versions to identify satellites. Satellites are either tracked on dedicated receiver channels (the Leica receivers used in our GPS clocks have 6 independent channels)

or track multiple satellites on one or two channels, rapidly switching between satellites (the GPS receiver used by the CASA expereiment tracks up to 6 satellites on 2 channels and switches satellites every 20ms).

The GPS receiver attempts to solve for receiver position by measuring satellite-receiver distances. The satellite-receiver distance is obtained by measuring the time offset between the received C/A code sequence and the locally generated C/A code. This offset is multiplied by the speed of light to give a pseudorange distance (ρ) which can be used to solve the ranging equations. However since the satellite and receiver clocks are not synchronised there is a clock bias that is introduced in the pseudorange estimate. The receiver clock bias is thus another variable in the ranging equations (A.1) so the full ranging equations that must be solved are:

$$(\rho_i - ClockBias \times c) = \sqrt{(x_{gps} - x_i)^2 + (y_{gps} - y_i)^2 + (z_{gps} - z_i)^2} \qquad (A.2)$$

where ρ_i is the pseudorange distance which still includes atmospheric, relativistic and selective availability effects and $i = 1, \ldots, 4$. The pseudorange distance will also be affected by satellite clock errors. The satellite clocks are monitored by the master control station which determines the bias in each satellite's clock. Correction parameters are uplinked to the satellite, and the satellite broadcasts them as part of the 50Hz navigation message discussed in section A.5. These correction terms are then used to adjust the measured pseudoranges. Selective availability (SA) only affects the C/A code and is a technique used to deny non authorised users (as determined by U.S.A. DoD) the full accuracy possible with GPS. Selective availability is discussed in more depth in section A.9. An important effect we should note, is that solving the ranging equations for the receiver positions has the byproduct of synchronising the receiver's clock with UTC. An important corollary is that if our position is well known, we need only track a single satellite to solve for the receiver bias to synchronise it with UTC.

In summary, to obtain a position we must solve the ranging equations for four unknowns - 3 spatial coordinates and the bias in the receiver's clock. This is achieved by tracking four satellites to obtain 4 pseudorange estimates which allows us to solve equation A.2 for all the 4 unknowns. Commercial GPS receivers are able to obtain accuracies of

- horizontal positioning to within 100 metres with a 95% probability, and to within 300 meters with a 99.99% probability.
- vertical positioning to within 140 metres with 95% probability, and
- timing accuracy to within 340 nanoseconds of UTC with a 95% probability.

A.2 Coordinate systems

GPS uses a coordinate system based on the World Geodectic System 1984 datum (WGS-84). This datum defines both a cartesian system (Earth Centered Earth Fixed or ECEF coordinates) and ellipsoidal (or geodectic) system having a common geocentric origin and is shown below in figure A.1. The cartesian ECEF coordinates are defined such that the Z axis is aligned along the mean position of the earth's rotational axis as defined by the Conventional International Origin[105]. The XY plane lies in the equatorial plane of the earth with the Y axis passing through the mean Greenwich Meridian and the X axis orthogonal to the other two axis with the origin at the centre of the earth. The ellipsoidal coordinates have the same origin and are defined in terms of latitude, longitude and height above a reference ellipsoidal surface defined by the WGS-84 datum[83][64]. GPS receivers use the WGS-84 ECEF rectangular coordinate system as the basis for position calculations and use on board software to transform coordinates into other desired geodectic datums. Thus care must be taken when using or comparing coordinates as the use of different datums can result in positional errors of up to a kilometre.

It is also useful to define a surface based on a gravitational equipotential, and such a surface is known as the geoid (note this is surface is different from the ellipsoid previously discussed). It is designed to closely approximate mean sea level, and is supposed to be the surface that would exist over the entire earth if the land and sea surface resulted from gravity alone (ie the surface if the sea was freely allowed to pass through land). This surface is usually approximated by spherical harmonics and is stored in the GPS receiver software so that heights can be expressed in terms of height above mean sea level (rather than height above the ellipsoid surface). Thus when

comparing or specifying positions, care must be taken to ensure are being referenced to the same surface. The simple relationship between heights using different reference systems is given by $h = d + A$ where

h is the ellipsoidal height (WGS-84 coordinates)

d is the geoidal height (difference between the WGS-84 ellipsoid and the geoid)

A is the altitude above mean sea level.

Strictly there may be some deflection between h and A (due to local gravitational anomalies) although this does not usually exceed 30 arcseconds.

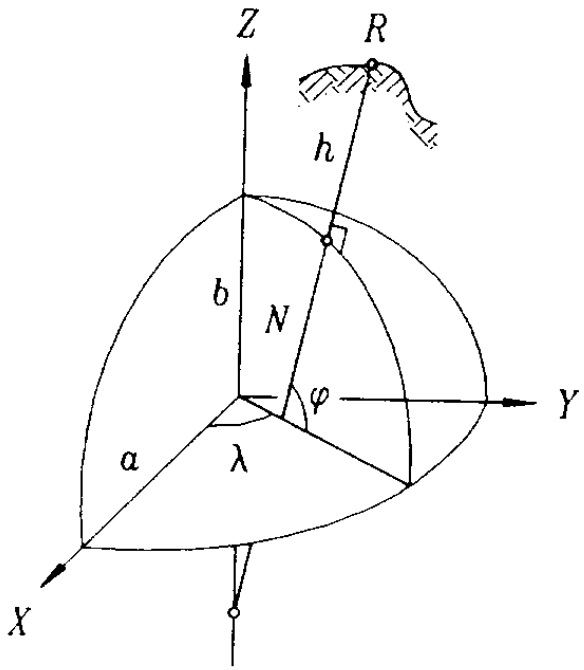

Figure A.1: Earth Centred Earth Fixed (ECEF) Cartesian (X,Y,Z) and Ellipsoidal Co-ordinates[105]. Ellipsoidal coordinates are based on a reference ellipsoidal defined by a semi-major axis a and a flattening factor from which the semi-minor axis b can be determined. Ellipsoidal coordinates are then specified in terms of latitude λ, longitude ϕ and geodectic height h. N is the normal to the ellipsoid.

The Leica receivers used in the HiRes detector provide measurements of latitude, longitude, altitude above mean sea level and geoidal height allowing a determination of position in terms of WGS-84 ellipsoidal coordinates. Details of the conversion formulas between ellipsoidal and rectangular coordinates can be found in Hofmann-Wellenhof *et al.*[105] or Dana[64].

A.3 Timing Systems.

The GPS system maintains its own time system known as GPS time. The primary reference clock is maintained by the GPS master control station located in Colorado Springs. GPS time and UTC time are very similar with the only difference being that GPS time does not count leap seconds whereas UTC does. This results in GPS time drifting away from UTC every time a leap second is added to UTC. The epoch for GPS time is January 6.0 1980 at which time GPS time and UTC were coincident. The difference between UTC and GPS time is broadcast by the GPS satellites as part of the 50Hz navigation message (see section A.5).

Each Satellite carries an atomic clock (plus three spares) that operate at a fundamental frequency of 10.23MHz. The stability of these clocks is at least one part in 10^{-13} or better over one day and their stability is monitored by ground stations. The master control station analyses this data and synchronises the satellites to within 100ns of GPS time each day. The timing accuracy obtainable with GPS is due primarily to selective availability effects which reduces the accuracy to within 340ns (2σ - 95%) of UTC[64].

A.4 Orbits, Ephemerides and the Almanac

The nominal orbits for the satellites are 12 hour orbits distributed in 6 orbital planes inclined at 55° to the equator and at altitudes of approximately 18000 km. However due to the rotation of the earth the satellite ground tracks have a period of a sidereal day (ie it takes 23 hours and 56 minutes for a satellite to return to the same point in the sky). The actual orbital positions are monitored by five control stations around the world, and data are analysed at the master control station (in Colorado, USA) to produce a reference orbit which is passed through a process known as Kalman filtering. This improves the accuracy of the initial orbit and allows deterministic extrapolation of the orbit so that it remains valid for up to four hours after it is uplinked to the satellite.

The orbit is described by a smooth keplerian orbit which is defined by six parameters

knows as the ephemerides, together with some secular and periodic correction terms. The satellites constantly transmit their ephemeris information to the receivers via the navigation message (taking 30 seconds for a full transmission; see section A.5) and provide each satellite's position needed to solve the ranging equation.

Almanac data, detailing general orbital parameters, satellite clock correction parameters and other information such as satellite health status, are uploaded to the satellites which continuously broadcast this information. The orbital information is less accurate than the ephemerides, but is provided for all satellites and is accurate for 180 days.This allows rapid satellite searching and acquisition by receivers as the receiver has information upon what satellites should be visible. The almanac is sent in parts via the navigation message taking 12.5 minutes to be fully sent.

A.5 Satellite Signals

The atomic clocks on board the satellites are used to provide a fundamental frequency f_0 of 10.23MHz. From this frequency, the two carrier frequencies L1 (1.57542 GHz $= 154f_0$) and L2 (1.2276 GHz $= 120f_0$) are produced. Information is transmitted through the use of binary code sequences where a high state causes a 180° phase shift in the carrier phase.

Three types of messages are sent on the carrier waves:

- the 10.23MHz Precise (P) pseudorandom noise (PRN) code,
- the 1.023MHz Coarse/Acquisition (C/A) PRN code and
- the 50Hz Navigation message.

The P code and the Navigation message are sent on both the L1 and L2 carrier frequencies whilst the C/A code is only sent on the L1 carrier wave. The C/A code is also phase shifted by 90° (quarter wavelength) with respect to the P code (ie if the L2 wave is described by a pure cosine term then the L1 comprises the L2 cosine term and a sin term due to the C/A component).

The P code and the C/A code are produced by a device called a tapped feedback shift register. The register contains a series of bits which are right shifted each clock

tick. Thus the register acts as a pipe - each clock tick a new value is pushed into the first bit, and the final bit from the previous clock tick is popped out. The new value of the first bit is determined by XOR'ing the bit values of two different bits known as the defining pair. In this way, the initial state of the register define the output bit sequence. By way of example, consider the following 5 bit register using bits 2 and 3 as the defining pair:

0	1	1	0	0

which after a clock tick right shifts everything and produces an output of 0 and a new bit 1 value of XOR(bit 2 & bit 3) = XOR(1&1)=0.

0	0	1	1	0

after another clock tick an output of 0 is produced and the new value of bit 1 is XOR(0&1)=1.

1	0	0	1	1

Thus the resultant output would be 0011001010.... The size of the register length, the initial values of the bits, and the choice of the defining pair allow many different codes to be generated.

The P code is generated by binary adding the bit sequences of from two registers. The first sequence repeats every 1.5 seconds leading to a length of 1.5345×10^7 bits. The second sequence has 37 more bits which when combined with the first sequence leads to a bit sequence that takes 266.4 days to repeat. This code sequence is divided up into 37 unique 1 week sequences and each satellite is assigned a specific week. The PRN ID of the satellite is determined by which week it is given thus leading to only 37 valid satellite PRN IDs. Thus every time a satellite is decommissioned its PRN ID becomes available for new satellites ensuring that there are always codes available to the system.

The P code is restarted at the beginning of every GPS week (which starts midnight Saturday). Currently this P code undergoes a technique called anti-spoofing in which

the public P code is encrypted to prevent someone transmitting false signals that could confuse a receiver. The encrypted P code is relabeled the Y code and the decryption algorithm is only supplied to authorised users (as defined by the US Department of Defense - normally this means friendly military forces only). Authorised users receive undegraded signals and can achieve the full positioning accuracy of the system known as the precise positioning service (PPS). The 2σ (95%) accuracy of the precise positioning service system is defined as

- 22 meter horizontal accuracy
- 27.7 meter vertical accuracy
- 100 nanoseconds time accuracy

The coarse/acquisition pseudorandom code is generated by using two 10 bit registers whose binary output is added to produce the PRN code. The PRN of the satellite determines which bits are used as the defining pair and what the initial register setup is. This information is public knowledge so that commercial receivers can use the C/A code to determine receiver position. The reception of just the C/A code which is affected by selective availability is known as the standard positioning service (SPS). The 2σ (95%) accuracy of this system is defined as

- 100 meter horizontal accuracy
- 156 meter vertical accuracy
- 340 nanoseconds time accuracy

The final type of message sent by the satellites is the 50Hz navigation message. This is used to send information about the satellite clock, orbit, health status and other correction data. The total message is 1500 bits long (taking 30 seconds to transmit) and is broken up into a series of 5 subframes used to transmit different pieces of information.

subframe(s) information

1^{st} parameters about the status of satellite clock.

2^{nd} **and** 3^{rd} satellite ephemeris information (valid for 4 hrs)

4^{th} Military, atmospheric, UTC and other general information. Almanac data of spare satellites.

5^{th} Almanac and health status of the primary 24 satellite constellation.

Note that the satellite ephemeris is for that satellite only and that subframes 4 and 5 are changed each message so that it takes 12.5 minutes for the complete transmission of all data.

A.6 Receivers and Antennas

Antennas used by GPS receivers are generally omnidirectional antennas and should be insensitive with respect to rotation and inclination. The antennas have gain patterns designed to reject satellites with low elevation and multipath signals. The signals are passed through a preamp and sent to the RF section of the receiver. An incoming signal is assigned to a channel and thus the more channels a receiver has the more satellites that can be simultaneously tracked. Older receivers tend to have few channels and cycle satellites through the channel (they track each satellite for short periods ($\sim$ 20ms) rather than continuously tracking a single satellite). Multichannel receivers are more accurate and less sensitive to loss of signal lock.

A.7 Atmospheric and Relativistic effects

In addition to satellite clock errors, errors arise due to atmospheric and relativistic effects which are compensated for by receivers. The atmospheric effects are due to ionospheric and tropospheric refraction. Ionospheric refraction arises due to the dispersive nature of this region (50-1000km) which arises from the presence of free electrons. The net effect is that the pseudorange overestimates the true range. This effect is dependent upon the number of free electrons so this effect ranges from 20-30m during the day down to 2-3m at night (due to recombination of electrons with ions in the ionosphere). Ionospheric refraction is wavelength dependent so dual frequency

receivers can eliminate it. Tropospheric refraction is due to the neutral atmosphere and is generally much smaller than ionspheric refractions. Receivers use atmospheric models to attempt to eliminate such delays and atmospheric parameters are sent by the satellites in the 50Hz navigation message to improve the accuracy of the models (The receivers used in our GPS clocks claim to be able to almost completely eliminate tropospheric delays provided the satellites are at elevations above 5 degrees).

Relativistic effects arise due to the satellites being in accelerated reference frames when compared with the earth based frame which is at rest. There are essentially four relativistic effects that affect pseudorange estimations. The first two effects are due to the earth's gravitational field. The field causes a relatively minor effect of inducing perturbations to the satellite orbit as well as space-time curvature of the satellite signal. The latter effect requires a small correction (always less than 20mm) to be applied to pseudorange estimates to obtain euclidean ranges. The third relativistic effect is a small shift in the frequency of the satellite clock due its motion and the difference in the gravitational field between satellite and receiver. These effects would cause a shift in 10.23MHz fundamental frequency of 4.55mHz. The satellite clocks take this into account by using a frequency offset from f_0 by this amount. The final effect is a frequency shift in the receiver clock due to its rotation with respect to the stationary geocentre reference frame. This gives rise to a frequency shift of one in 10^{-12} (about 10 ns over 3 hours) which is taken into account by receiver software. All such relativistic effects are well understood and their effects are taken into account when determining psuedoranges.

A.8 Dilution of Precision (DOPS)

The positioning accuracy achievable with GPS is dependent on the geometry of the satellites used to determine the receiver position. The quality of the satellite geometry is measured by a quantity known as a dilution of precision or DOP value. Positioning accuracy is given by $\sigma = \text{DOP} \times \sigma_0$ where σ_0 is the standard deviation in position. To obtain a DOP we must look at the satellite geometry. First consider a unit sphere centred on the receiver. Now work out what volume of the unit

sphere is contained by using the satellite positions as the vertices for this volume (rather similar to determining the solid angle defined by the satellites). The geometrical dilution of precision (GDOP) is then defined as the inverse of this volume. Thus the larger the volume then the smaller is the GDOP (a low GDOP thus implies the satellites used are well distributed in space). Several other DOP's can be defined. We have position and time DOPS (PDOP and TDOP respectively), which are related to the GDOP by $\text{GDOP} = \sqrt{\text{PDOP}^2 + \text{TDOP}^2}$. The position DOP can be further broken down into horizontal and vertical DOP's (HDOP and VDOP) where $\text{PDOP} = \sqrt{\text{HDOP}^2 + \text{VDOP}^2}$. HDOP can also then be broken down into a east and a north DOP where $\text{HDOP} = \sqrt{\text{EDOP}^2 + \text{NDOP}^2}$. DOP's can be worked out using the almanac or can be determined in real time by the receiver using its measured positions of the satellites.

A.9 Selective Availability

The global positioning system was designed and implemented by the US Department of Defense primarily to give its military forces a tactical battlefield advantage. It was realised that proposed system would have application in many civilian fields so it was decided that two levels of support to the system would be provided, namely, the Precise Positioning service and the Standard Positioning Service.

The Precise Positioning Service (PPS) is designated for military and military approved users only. The dual frequency receivers have the capability to decode the encrypted Y code (thus turning it back into the P code) and to use this for accurate navigation. The transmitted signals are also harder to interfere or jam than the signals used by the standard positioning system.

The Standard Positioning Service (SPS) is designated for civilian use and has its accuracy deliberately degraded from that obtainable with the PPS. Single frequency receivers are used to receive the C/A code for navigation (the C/A code is only transmitted on the L1 carrier frequency). The accuracy degradation is achieved by the use of a technique known as selective availability (SA).

Selective availability is a two fold attempt to degrade accuracy. Firstly, the empherides sent by the satellites in the 50Hz navigation message are truncated to reduce the accuracy of these empherides. The full, accurate version is released to the public two weeks after they are determined. The second effect is a dithering of the satellite clock frequency to introduce noise in determining the range to the satellite. The effect of these errors is that the satellite is not in the location it is transmitting, and thus the solution to the ranging equations will be incorrect. Selective availability is the dominant error source for commercial receivers, with positional spread about the true receiver position of 100m (2σ) and 300m 3σ horizontally, 140m 2σ vertically and a timing accuracy of 340ns (2σ) with respect to GPS or UTC time.

At present selective availability is applied by all block II satellites (the original block one satellites did not have the hardware to implement SA, but all have now been retired). On a presidential directive, selective availability may be used to further degrade the accuracy. However during the Gulf War (1991) and the invasion of Haiti (1994) selective availability was actually turned off to allow military users to use civilian receivers. Selective availability is due to be phased out within the next ten years[135].

A.9.1 Reducing the effects of Selective Availability

Selective availability is the dominant error source in civilian use of GPS. Thus techniques to circumvent its effects can greatly increase the usefulness of GPS receivers.

The effects of selective availability may be greatly reduced by the use of a differential GPS system. In such a system a receiver at a known, fixed position receives signals from the satellites and calculates individual satellite biases. These corrections are either stored for post-processing or maybe transmitted to all GPS receivers within range (typically 100km). Remote receivers receive the satellite corrections, which are then applied in real time to reduce position errors to $\sim$ 15m (3σ).

GPS receivers used for surveying are able to measure relative distances to mm accuracy over distances as large as 30km. These systems typically measure the carrier phase and use phase difference changes to determine three dimensional distances

between a reference station and a remote receiver.

Absolute timing errors due to selective availability are more difficult to overcome. However high relative timing accuracy ($\sim$ 10ns) between two receivers is possible if receiver locations are well known. This technique, known as common view time transfer, requires receivers to track a single common satellite. As receiver positions are known, the ranging equations need only be solved for receiver clock bias. Thus if two receivers are close (up to 30km), SA and atmospheric effects are common, and excellent relative timing accuracy is possible (a variation of this technique is used by the HiRes detector). If a reference site has a calibrated time source, it can calculate timing corrections which may be transmitted to remote receivers whose positions are well known. In this way, the remote receivers clock can be synchronised to within 10ns of the reference clock over distances as large as 2000km[64][51].

References

[1] T. Abu-Zayyad, M. Al-Seady,, K. Belov, D.J. Bird, J. Boyer *et al*, *Physics with HiRes Stage 0.5 and Stage 2.*, 25^{th} ICRC, Vol **5**, OG 10.6.1, 1997, pg 321-24.

[2] T. Abu-Zayyad, M. Al-Seady,, K. Belov, D.J. Bird, J. Boyer *et al*, *The capablities of the High Resolution Fly's Eye Detector*, 25^{th} ICRC, Vol **5**, OG 10.6.2, 1997, pg 325-28.

[3] T. Abu-Zayyad, M. Al-Seady,, K. Belov, D.J. Bird, J. Boyer *et al*, *Status of the High Resolution Fly's Eye Detector: Operation and Installation*, 25^{th} ICRC, Vol **5**, OG 10.6.3, 1997, pg 329-32.

[4] T. Abu-Zayyad, M. Al-Seady,, K. Belov, D.J. Bird, J. Boyer *et al*, *The Hires Detector: Absolute Calibration and Alignment*, 25^{th} ICRC, Vol **5**, OG 10.6.4, 1997, pg 333-36.

[5] T. Abu-Zayyad, M. Al-Seady,, K. Belov, D.J. Bird, J. Boyer *et al*, *Atmospheric monitoring at the High Resolution Fly's Eye: Atmospheric Scattering*, 25^{th} ICRC, Vol **5**, OG 10.6.7, 1997, pg 345-48.

[6] T. Abu-Zayyad, M. Al-Seady,, K. Belov, D.J. Bird, J. Boyer *et al*, *Testing the High Resolution Fly's Eye Using Laserscope*, 25^{th} ICRC, Vol **5**, OG 10.6.8, 1997, pg 349-52.

[7] T. Abu-Zayyad, M. Al-Seady,, K. Belov, D.J. Bird, J. Boyer *et al*, *Atmospheric monitoring at the High Resolution Fly's Eye: Data from the HiRes 2 Flasher Array*, 25^{th} ICRC, Vol **5**, OG 10.6.11, 1997, pg 361-64.

[8] T. Abu-Zayyad, M. Al-Seady,, K. Belov, D.J. Bird, J. Boyer *et al*, *Atmospheric monitoring at the High Resolution Fly's Eye: Monitoring Data via the HiRes Laser/LIDAR system*, 25^{th} ICRC, Vol **5**, OG 10.6.12, 1997, pg 365-68.

[9] B.N. Afanasiev, M.N. Dyakonov, T.A. Egorov, V.P. Egorova, N.N. Efremov *et al.*, *Recent Results From Yakutsk Experiment*,Tokyo Workshop on Techniques for the Study of Extremely High Energy Cosmic Rays, ed M. Nagano, ICRR, University of Tokyo, 1993, pg 35-51.

[10] B.N. Afanasiev, M.N. Dyakonov, V.P. Egorova, N.N. Efremov, A.V. Glushkov *et al.*, *Some Characteristics of EAS and Primary Cosmic Rays on Yakutsk Array Data*, Proceedings of the International Symposium on Extremely High Energy

Cosmic Rays: Astrophysics and Future Observatories. ed M. Nagano, ICRR, University of Tokyo, 1996, pg 32-49.

[11] H.R. Allan, *Radio Emission from Extensive Air Showers*, Progess in Elementary Particle and Cosmic Ray Physics, **10**, 1971, pg 169-302.

[12] M. Al-Seady, D.J. Bird, J. Boyer, G.F. Chen, R. Clay *et al*, *The High Resolution Fly's Eye (HiRes) Project* Proceedings of the International Symposium on Extremely High Energy Cosmic Rays: Astrophysics and Future Observatories. ed M. Nagano, ICRR, University of Tokyo, 1996, pg 191-204.

[13] N.A. Amos, C. Avila, W.F. Baker, M. Bertani, M.M. Block et al., *Measurement of the $\overline{p}p$ Total Cross Section as $\sqrt{s} = 1.8 TeV$*, Physical Review Letters, **63**, 1989, pg 2784-6.

[14] C.D. Anderson, *The Apparent Existence of Easily Deflectable Positives*, Science, **76**, 1932, pg 238.

[15] R. Armenteros *et al., The Properties of Charged V Particles*, Phil. Mag. **43**, 1952, pg 597.

[16] W. Au, J. Boyer, Y. Chi Y. Ho, W. Lee *et al.*, *Description and Status of the High Resolution (HiRes) Fly's Eye Experiment*, 22^{nd} ICRC, Dublin, Vol **2**, OG 10.4.9, 1991, pg 692-5.

[17] *The Pierre Auger Project Design Report*, The Auger collaboration, Fermilab, 1995.

[18] P. Auger, R. Maze, and J. Robley, Comptes Rendus de l'Académie des Sciences (Paris), **208**, 1938, pg 1641.

[19] W.I. Axford, *The Origin of Cosmic Rays*, Proc of the ICRR Int. Symp. - Astrophysical Aspects of the Most Energetic Cosmic Rays, ed M. Nagano and F. Takahara, World Scientific, Singapore, 1991, pg 406-20.

[20] R. M. Baltrusaitis, G.L. Cassiday, R. Cooper, J.W. Elbert, P.R. Gerhardy *et al.*, *Arrival Direction of Cosmic Rays of $E > 0.4$ EeV*, Ap. J., **303**, 1986, pg 333-35.

[21] R. M. Baltrusaitis, R. Cady, G.L. Cassiday, R. Cooper, J.W. Elbert *et al.*, *The Utah Fly's Eye Detector*, Nuclear Instruments and Methods in Physics Research A **240**, 1985, pg 410-28.

[22] P. Bassi, G. Clark and B. Rossi, *Distribution of Arrival Times of Air Shower Particles*, Physical Review **92**, 1953, pg 441.

[23] R. Beck, A. Brandeburg, D. Moss, A. Skukurov and D. Sokoloff, *Galactic Magnetism: Recent Developments and Perspectives* , Annual Reviews of Astronomy and Astrophysics, **34**, 1996, pg 155-206.

[24] H. Becquerel, *On the Invisible Radiation emitted by Phosphorescent Substances*, Comptes Rendus de l'Académie des Sciences (Paris), **122**, 1896, pg 501.

[25] J. Benecke, T.T. Chou, C.N. Yang and E. Yen, Hypothesis of Limiting Fragmentation in High Energy Collisions, Physical Review, **188**, 1969, pg 2159-69.

[26] P. Bhattacharjee, *Cosmic Topological Defects as Possible Sources of Extremely High Energy Cosmic Rays: The Current Status*, Proceedings of the International Symposium on Extremely High Energy Cosmic Rays: Astrophysics and Future Observatories. ed M. Nagano, ICRR, University of Tokyo, 1996, pg 125-36.

[27] D.J. Bird *et al.*, *Atmospheric Scattering Studies using the High Respolution Fly's Eye Cosmic Ray Detector*, In Preparation, Dec 1997.

[28] D.J. Bird, University of Adelaide, *Personal Communication*, 1998.

[29] D.J. Bird, R.W. Clay, B.R. Dawson, A.G. Gregory, A.G.K. Smith, M. Johnston and N.R. Wild, *Cloud Detection for Fluorescence and Cerenkov Detectors*, 25^{th} ICRC, Vol **5**, OG 10.6.9, 1997, pg 353-56.

[30] D.J. Bird, S.C. Corbato, H.Y. Dai, B.R. Dawson, J.W. Elbert *et al.*, *The Cosmic Ray Energy Spectrum Observed by the Fly's Eye*, Astrophysics Journal, **424**, 1994, pg 491-502.

[31] D.J. Bird, S. Corbató, H.Y. Dai, J.W. Elbert, M.J. Kidd *et al.*, *The calibration of the absolute sensitivity of photomultiplier tubes in the High Resolution Fly's Eye Detector*, Nuclear Instruments and Methods in Physics Research, **A349**, 1994, pg. 592-99.

[32] D.J. Bird S.C. Corbato, H.Y. Dai, B.R. Dawson, J.W. Elbert *et al.*, *Evidence for Correlated Changes in the Spectrum and Composition of Cosmic Rays at Extremely High Energies*, Physics Review Letters, **71**, 1993. pg 3401.

[33] D.J. Bird, S.C. Corbato, H.Y. Dai, J.W. Elbert, K.D. Green *et al.*, *Detection of a Cosmic Ray with Measured Energy Well Beyond the Expected Spectral Cutoff Due to Cosmic Microwave Background*, Ap. J., **441**, 1995, pg. 144-50.

[34] J.W. Elbert And P. Sommers, *In Search of a Source for the 320 EeV Fly's Eye Cosmic Ray*, Ap. J., **441**, 1995, pg. 151-61.

[35] D.J. Bird, J. Boyer, R.W. Clay, S.C. Corbato, H.Y. Dai *et al.*, *The HiRes Fly's Eye Prototype Detector – A Status Report*, 23^{rd} ICRC, OG 10.2.4, Calgary, **2**, 1993, pg. 462-65.

[36] D.J. Bird, J. Boyer, G.F. Chen, R.W. Clay, H.Y. Dai *et al.*, *The High Resolution Fly's Eye Project*, 24^{th} ICRC, Rome, **3**, 1995, pg. 504-7.

[37] D.J. Bird, J. Boyer, G.F. Chen, R.W. Clay, H.Y. Dai *et al.*, *The HiRes 2 Prototype and Coincident measurements with HiRes 1*, 24^{th} ICRC, Rome, **3**, 1995, pg. 548-51.

[38] D.J. Bird, R.W Clay, B.R. Dawson, K.M. Simpson, C.R. Wilkinson *et al.*, *Radio Controlled Xenon Flasers for Atmospheric Monitoring at the HiRes Cosmic Ray Observatory*, Nuclear Instruments and Methods in Physics Research A, *In Press*, 1997.

[39] P.M.S. Blackett and G.P.S. Occhialini, *Some Photographs of the Tracks of Penetrating Radiation*, Proceedings of the Royal Society, **A 139**, 1933, pg 699.

[40] A. Bonetti, R. Levi-Setti, M. Panetti, G. Tomasini, *Observation of the Deacy at Rest of a Heavy Particle*, Nuovo Cim, **10**, 1953, pg 345.

[41] Bothe and Kolhörster,*Nature of High-Altitude Radiation*, Z. Phys. **56**, 1929, pg 751.

[42] A. Brandenburg, K.J. Donner, D. Moss, A. Skukarov, D.D. Sokoloff and I. Tuominen, *Dynamos in Discs and Halos of Galaxies*, Astronomy and Astrophysics, **259**, 1992, pg 435-61.

[43] R.G. Brownlee, A.J. Fisher, L. Goorevich, P.C. Kohn, C.b.A. McCusker *et al.*, *Design of an Array to record air showers of energy up to* $10^{21}eV$, Canadian Journal of Physics, **46**, 1968, pg S259-62.

[44] A.N. Bunner, Ph.D. Thesis, Cornell University, 1964.

[45] A.N. Bunner, K. Greisen and P.B. Landecker, *An imaging system for EAS optical emission*, Canadian Journal of Physics, **46**, 1968, pg S266-9.

[46] G. L. Cassiday, *Observatory for Ultra High-Energy Processes: The Fly's Eye*, Ann. Rev. Nucl. Part. Sci., **35**, 1985, pg 321-49.

[47] G. L. Cassiday, R. Cooper, S.C. Corbato, B.R. Dawson, J.W. Elbert *et al.*, *Evidence for* $10^{18}eV$ *Neutral Particles from the Direction of Cygnus X-3*, Physical Review Letters, **62**, 1989, pg 383-6.

[48] G. L. Cassiday, R. Cooper, S.C. Corbato, B.R. Dawson, J.W. Elbert *et al.*, *A Coarse-Grain Search for Anisotropy in the Arrival Directions of Cosmic Rays Above* $10^{17}eV$, Astrophysical Journal, **351**, 1990, pg 454-8.

[49] G. L. Cassiday, R. Cooper, S.C. Corbato, B.R. Dawson, J.W. Elbert *et al.*, *Mapping the U.H.E. Sky in Search of Point Sources*, Nuclear Physics B (Proc Suppl) **14A**, 1990, 291-8.

[50] G. L. Cassiday, R. Cooper, S.C. Corbato, B.R. Dawson, J.W. Elbert *et al.*, *Measurements of Cosmic-Ray Air Shower Development at Energies Above* $10^{17}eV$, Astrophysical Journal, **356**, 1990, pg 669-74.

[51] M. Cervera, Defence Science Technology Organisation, *Personal Communication*, 1997.

[52] C.J. Cesarsky, *Cosmic Rays with* $E > 10^{19}eV$*: Origin and Transport*, Nuclear Physics B (Proc. Suppl.) **28B**, 1992., 51-60.

[53] G. Clark, J. Earl, W. Kraushaar, J. Linsley, B. Rossi and F. Scherb, *An Experiment on Air Showers Produced by High-Energy Cosmic Rays*, Nature, **180**, 1957, pg 353.

[54] G. Clark, J. Earl, W. Kraushaar, J. Linsley, B. Rossi, F. Scherb and D.W. Scott, *Cosmic-Ray Air Showers at Sea Level*, Physical Review, **122**, 1961, pg 637-654.

[55] J. Clay, Proceedings Academy of Amsterdam, **33**, 1930, pg 711.

[56] J. Clay, Physica, **1**, 1934, pg 363.

[57] G. Cocconi, L. Koerster, and D.H. Perkins, LRL Report No. UCID-1444, 1960 (unpublished).

[58] A.H. Compton, *A Geographic Study of Cosmic Rays*, Physical Review **43**, 1933, pg 387.

[59] R. Cooper, S.C. Corbato, H.Y. Dai, J.W. Elbert, B. Emerson *et al.*, *Fly's Eye Observations*, Proc of the ICRR Int. Symp. - Astrophysical Aspects of the Most Energetic Cosmic Rays, ed M. Nagano and F. Takahara, World Scientific, Singapore, 1991, pg 34-48.

[60] J.W. Cronin, *The highest Energy Cosmic Rays*, in *Unsolved Problems in Astrophysics*, ed J.N. Bahcall and J.P. Ostriker, Princeton University Press, New Jersey, 1997, pg 325-41.

[61] J.W. Cronin, *Science of Extremely High Energy Cosmic Rays*, Proceedings of the International Symposium on Extremely High Energy Cosmic Rays: Astrophysics and Future Observatories. ed M. Nagano, ICRR, University of Tokyo, 1996, pg 2-16.

[62] H.Y. Dai, K. Kasahara, Y. Matsubaru, M. Nagano and M. Teshima, J. Phys G: Nucl. Part. Phys., **14**, 1988, pg 793.

[63] G.A D'Almeida, *On the Variability of Desert Aerosol Radiative Characteristics*, Journal of Geophysical Research, **92**, 1987, pg 3017-26.

[64] P.H. Dana, *The Global Positioning System*, The Geographer's Craft Project, Department of Geography, The University of Texas, 1995.
`http://www.utexas.edu/depts/grg/gcraft/notes/gps/gps.html`

[65] B.R. Dawson, R.W. Clay, P.G. Edwards and J.R. Prescott, Nuovo Cim., **9C**, 1986, pg 1125.

[66] B.R. Dawson, *Some notes on the Hybrid Array Concept*, Tokyo Workshop on Techniques for the Study of Extremely High Energy Cosmic Rays, ed M. Nagano, ICRR, University of Tokyo, 1993, pg 125-132.

[67] B.R. Dawson, R. Meyhandan and K. Simpson, *A Comparison of Cosmic Ray Composition Measurements at the Highest Energies, Submitted to Astroparticle Physics, Jan 25 1998*, Available at
`http://xxx.lanl.gov/astro-ph/9801260`.

[68] B.R. Dawson, *Fluorescence Detector Techniques*, Proceedings of the Auger Meeting on Nitrogen Fluorescence Cosmic Ray Detectors (Salt Lake City)), Auger Technical Paper GAP-96-017, 1996.

[69] J.F. de Beer, B. Holyoak, J. Wdowczyk and A.W. Wolfendale, *A theoretical Analysis of Extensive Airshower. I. Near-vertical Showers at Sea Level*, Proceedings of the Physical Society London, **89**, 1966, pg 567-85.

[70] P.A.M. Dirac, *Quantised Singularities in the Electromagnetic Field*, Proc. Roy. Soc., **A133**, 1931, pg 60.

[71] L.O'C Drury, *A Survey of Diffusive Shock Acceleration*, Proc of the ICRR Int. Symp. - Astrophysical Aspects of the Most Energetic Cosmic Rays, ed M. Nagano and F. Takahara, World Scientific, Singapore, 1991, pg 252-60.

[72] N.N. Efimov, T.A. Egorov, A.V. Clushkov, M.I. Pravdin, I.Ye. Sleptsov, *The Energy Spectrum and Anisotropy of Primary Cosmic Rays at Energy* $E_0 > 10^{17} eV$ *Observed in Yakutsk*, Proc of the ICRR Int. Symp. – Astrophysical Aspects of the Most Energetic Cosmic Rays, ed M. Nagano and F. Takahara, World Scientific, Singapore, 1991, pg 20-34.

[73] J.W. Elbert, *Track reconstruction Techniques and Geometrical Resolution in HiRes*, Tokyo Workshop on Techniques for the Study of Extremely High Energy Cosmic Rays, ed M. Nagano, ICRR, University of Tokyo, 1993, pg 158-166.

[74] J.W. Elbert, *The HiRes Filter and Its effect on the Aperture*, Tokyo Workshop on Techniques for the Study of Extremely High Energy Cosmic Rays, ed M. Nagano, ICRR, University of Tokyo, 1993, pg 232-243.

[75] *GPS Antenna Type AU-6 Specfications*, Furuno Service Bulletin SB1816-1, International Marketing Division, 1993.

[76] J. Engel, T.K. Gaisser, P. Lipari and T. Stanev, *Nucleus-Nucleus Collisions and Interpretation of Cosmic-Ray Cascades*, Physical Review D, **46**, 1992, pg 5013-25.

[77] A.D. Erlykin *EAS Structure, Primary Cosmic Radiation, hA and AA Interactions and New Phenomenah*, Proc 21^{st} ICRC, Adelaide, **11**, 1990, pg 300-21.

[78] V.V. Ezhela, B.B. Filimonov, S.B. Lugovsky *et al.*, *Particle Physics. One hundred Years of Discoveries*, AIP Press, New York, 1996.

[79] E. Fermi, The Physical Review, **81**, 1951, pg 683.

[80] E. Fermi, *On the origin of the Cosmic Radiation*, The Physical Review, **75**, 1949, pg 1169.

[81] R.P. Feynman, *Very High-Energy Collisions of Hadrons*, Physical Review Letters, **23**, 1969, pg 1415-17.

[82] R.S. Fletcher, T.K. Gaisser, P. Lipari and T. Stanev, *SIBYLL: An Event Generator for Simulation of High Energy Cosmic Ray Cascades*, Physical Review D **50**, 1994, pg 5710-31.

[83] K.W. Foster and A. Boksenberg, *The Astronomical Almanac*, U.S Government Printing Office, Washington and HMSO London, 1997.

[84] T. K. Gaisser, *Cosmic Rays and Particle Physics*, Cambridge University Press, 1990.

[85] T. K. Gaisser and A. M. Hillas, *Reliability of the Method of Constant Intensity Cuts for Reconstructing the Average Development of Vertical Showers*, Proc 15*th* ICRC, Plovdiv, **8**, 1977, pg. 353-7.

[86] T.K. Gaisser, R.J. Protheroe, K.E. Turver and T.J.L. McComb, *Cosmic Ray Showers and Particle Physics at Energies* 10^{15} – $10^{18} eV$, Reviews of Modern Physics, **50**, 1978, pg 859-80.

[87] T. K. Gaisser, T.S. Stanev, S. Tilav, S.C. Corbato, H.Y. Dai, *et al.*, *Cosmic-ray composition around* 10^{18} *eV*, Phys Rev D, **47**, 1993, pg 1919-31.

[88] R.J. Glauber and G. Matthiae, Nuclear Physics B, **21**, 1970, pg 135.

[89] A.V. Glushkov, N.N. Efimov, N.N. Efremov, A.D. Krasilnikov, I.T. Makarov *et al.*, *The Analysis of the Flux of Primary Particles with* $E_0 > 10^{17} eV$ *from Cygnus X-3*, Proc 21^{st} ICRC (Adelaide), **2**, 1991, pg 64-6.

[90] K.D. Green, *The Cosmic Ray Spectrum Above 0.3 EeV*, Ph.D. Thesis, University of Utah, 1992.

[91] K. Greisen, *The Extensive Air Showers*, Progess in Elementary Particle and Cosmic Ray Physics, **3**, 1956, pg 1-141.

[92] K. Greisen, *Cosmic Ray Showers*, Annual Review Nuclear Science, **10**, 1960, pg 63-108.

[93] K. Greisen, *End to the Cosmic-Ray Spectrum?*, Physical Review Letters, **16**, 1966, pg 748-50.

[94] K. Greisen, *Highlights in Air-shower Studies, 1965*, Proceeding of the 9th ICRC, London: Institute of Physics, **2**, 1965, pg 609-15.

[95] N. Hayashida, K. Honda, M. Honda, S. Imaizumi, N. Inoue *et al.*, *Muons* $\geq$ *1 GeV in large extensive air showers of energies between* $10^{16.5}$ *eV and* $10^{19.5}$ *eV observed at Akeno*, J. Physics G: Nuclear Particle Physics, **21**, 1995, pg 1101-19.

[96] N. Hayashida, K. Honda, M. Honda, S. Imaizumi, K. Kadota *et al.*, *A possible clustering of most energetic cosmic rays observed by Akeno Giant Air Shower Array*, Phys. Rev. Lett., **77**(6), 1996, pg. 1000.

[97] N. Hayashida, K. Honda, M. Honda, N. Inoue, K. Kadota *et al.*, *Recent Results of AGASA Experiments*, Proceedings of the International Symposium on Extremely High Energy Cosmic Rays: Astrophysics and Future Observatories. ed M. Nagano, ICRR, University of Tokyo, 1996, pg 17-27.

[98] V.F. Hess, *Observation of Penetrating Radiation in Seven Balloon Flights*, Phys. Zeitschr. **13**, 1912, pg 1084.

[99] V.F. Hess, *On the Origin of Penetrating Radiation*, Phys. Zeitschr. **14**, 1913, pg 610.

[100] W. Heitler, *Quantum Theory of Radiation*, 2nd edition, Oxford University Press, 1944.

[101] A.M. Hillas, *Cosmic Rays*, Oxford, Pergamon Press, 1972.

[102] A. M. Hillas, J.D. Hollows, H.W. Hunter and D.J. Marsden, *Calculations on the Particle and Energy-Loss Densities in Extensive Air Showers at Large Axial Distances*, Acta. Physica Hung (Proc 11^{th} ICRC), 29 Suppl **3**, 1970, pg 533-8.

[103] A. M. Hillas, D.J. Marsden, J.D. Hollows and H.W. Hunter, *Measurement of Primary Energy of Air Showers in the Presence of Flucutations*, Proc 12*th* ICRC, Hobart, **3**, 1971, pg. 1001-6.

[104] A.M. Hillas, *The origin of Ultra-High-Energy Cosmic Rays*, Annual Reviews of Astronomy and Astrophysics, **22**, 1984, pg 425-44.

[105] B. Hofmann-Wellenhof, H. Lichtenegger, and J. Collins, *GPS: Theory and Practice*, Springer-Verlag, Wien, New York, 1993.

[106] L. Janossy, *Cosmic Rays*, Oxford University Press, London, 1948.

[107] T.H. Johnson and J.C. Street, *The Variation of Cosmic Ray Intensities with Azimuth on Mt Washington, N.H.*, Physical Review, **43**, 1933, pg 381.

[108] J.R. Jokipii and G. Morfill, *On the Origin of High-Energy Cosmic Rays*, The Astrophysical Journal, **290**, 1985, L1-4.

[109] J.R. Jokipii and G. Morfill, *Ultra-High-Energy Cosmic Rays in a Galactic Wind and its Termination Shock*, The Astrophysical Journal, **312**, 1987, pg 170-77.

[110] F. Kakimoto, E.C. Loh, M. Nagano, K. Okuno, M. Teshima, S. Ueno, *A Measurement of the Air Fluorescence Yield*, Nuclear Instruments and Methods in Physics Research A, **372**, 1996, pg 527-33.

[111] F. Kakimoto *et al.*, *Longitudinal development or air-shower muons studied from the arrival time distributions measured at 900 m above sea level*, J. Phys. G, **12**, 1986, pg. 151-60.

[112] N. Kalmykov *et al.*, Physics of Atomic Nuclei, **58**, 1995, pg 1728.

[113] K. Kamata and J. Nishimura, Progress in Theoretical Physics, Supplement **6**, (Kyoto), pg 93.

[114] L. Kewley, R.W. Clay, B.R. Dawson, *Arrival Directions of the Southern Highest Energy Cosmic Rays*, Astroparticle Physics, **5**, 1996, pg. 69-74.

[115] M.J. Kidd, *Properties of Extensive Air Showers around* $10^{17} eV$, Ph.D. Thesis, Univeristy of Illinois, 1997.

[116] F.X. Kneizys *et al.*, *Users Guide to Lowtran 7*, Air Force Geophysics Laboratory, AFGL-TR-880177, 1988.

[117] W. Kolhörster, Ber. Deutsch. Phys. Ges. **16**, 1914-19, pg 719.

[118] D.D. Krasilnikov, A.A. Ivanov, V.A. Kolosov, A.D. Krasilnikov, K.N. Makarov *et al.*, *Anisotropy of Intensity of Cosmic Rays with* $E_0 > 10^{17} eV$., Proc 18^{th} ICRC, Bangalore, **2**, 1983, pg145-48

[119] R. Lampard, R.W. Clay, B.R. Dawson, *Limits on the Source Distances for the Most Energetic Cosmic Rays*, Publications of the Astronomical Society of Australia, **14**, 1997, 258-64.

[120] L.D. Landau, Izv. Akad. Nauk S.S.S.R, **17**, 1953 pg 51. Translated in *Collected Papers of L.D. Landau*, Ed D. Ter Haar, Gordon and Breach, New York, 1965.

[121] M. A. Lawrence, R.J.O. Reid, and A. A. Watson, *The Cosmic Ray Energy Spectrum above* $4 \times 10^{17} eV$ *as measured by the Haverah Park Array*, J. Phys. G, **17**, 1991, pg 733-57.

[122] M. A. Lawrence, D.C. Prosser, and A. A. Watson, *Upper Limit to the Flux of Neutral Particles from Cygnus X-3 above* $5 \times 10^{17} eV$, Physical Review Letters, **63**, 1989, pg 1121-4.

[123] J. Linsley, *Standard Value for the Radiation Length in Air*, Proc. 19^{th} ICRC, La Jolla, **7**, 1985, pg. 163-6.

[124] J. Linsley, L. Scarsi and B. Rossi, *Energy Spectrum and Structure of Large Air showers*, Journal of Physical Society of Japan, **17**, Suplement A-III, 1962, pg 91-102.

[125] J. Linsley, *Primary Cosmic Rays of Energy* 10^{17} *to* $10^{20} eV$*; The Energy Spectrum and Arrival Directions*, Proc. 8^{th} ICRC Jaipur, **4**, 1964, pg 77-9.

[126] J. Linsley, *Evidence for a Primary Cosmic-Ray Particle with energy* $10^{20} eV$, Physical Review Letters, **10**, 1963, pg. 146-8.

[127] E.C. Loh, *Fabrication of HiRes Mirrors*, *Recent Results From Yakutsk Experiment*,Tokyo Workshop on Techniques for the Study of Extremely High Energy Cosmic Rays, ed M. Nagano, ICRR, University of Tokyo, 1993, pg 219-221.

[128] M.S. Longair, *High Energy Astrophysics*, Second Edition, Cambridge University Press, 1994.

[129] D.R. Longtin, *A Wind Dependent Desert Aerosol Model: Radiative Properties*, Air Force Geophysics Laboratory, AFGL-TR-88-0112, 1988.

[130] S.M. Luo, *Troposperhic Aerosol Study by Fly's Eye and LIDAR Technique*, Ph.D. Thesis, University of Utah, 1992.

[131] *Magnavox GPS Engine Integration guide and applications manual*, Prepared by Magnavox Electronic Systems Company, West Coast Division, Available through Leica, Navigation and Positining Division, Torrance, Calfornia, 1992.

[132] M. Miesowicz, *Fireball Model of Meson Production* , Progess in Elementary Particle and Cosmic Ray Physics, **10**, 1971, pg 101-168.

[133] L. Montanet et al., *Review of Particle Properties* Physical Review D **50**, (1994), pg 1173.

[134] M. Nagano, S. Kawaguchi, N. Inoue, T. Hara, N. Hayashida *et al.*, *A new 100km^2 Air Shower Array at Akeno (AGASA)*, Proc of the ICRR Int. Symp. - Astrophysical Aspects of the Most Energetic Cosmic Rays, ed M. Nagano and F. Takahara, World Scientific, Singapore, 1991, pg 335-44

[135] *Frequently Asked Questions on the Global Positioning System*, United States Coast Guard Navigation Center, 1997.
`http://www.navcen.uscg.mil/`

[136] S.H. Neddermeyer and C.D. Anderson, *Note on the Nature of Cosmic-Ray Particles*, Phys. Rev., **51**, 1937, pg 884.

[137] S. Ostapchenko, T. Thouw and K. Werner, *The New VENUS Model of Hadronic Interactions at Ultrarelativistic Energies*, Nuclear Physics B (Proc. Suppl.), **52B**, 1997, pg 3-8.

[138] D.H. Perkins, *Nuclear Disintegration by Meson Capture*, Nature, **159**, 1947, pg 126.

[139] W.H. Press, B.P. Flannery, S.A. Teukolsky, W. T. Vetterling, *Numerical Recipes*, Cambridge University Press, 1988.

[140] R.J. Protheroe, *Origin and propagation of the highest energy cosmic rays* in *Towards the Millennium in Astrophysics: Problems and Prospects*, Erice 1996, eds. M.M. Shapiro and J.P. Wefel (World Scientific, Singapore), in press. Available electronically at
`http://xxx.lanl.gov/astro-ph/9612212`.

[141] C.L. Pryke, J. Lloyd-Evans, *A high performance GPS based autonomous event time-tagging system with application in a next generation Extensive Air Shower array*, Nuclear Instruments and Methods in Physics Research A, **A354**, 1995, pg 560-6.

[142] C.L. Pryke, *Long baseline testing of a GPS based, autonomous event time-tagging system*, Nuclear Instruments and Methods in Physics Research A, **394**, Issue 3, 1997, pg 420-2.

[143] R.J. Rand and A.G. Lyne, *New Rotation Measures of Distance Pulsars in the Inner Galaxy and Magnetic Field Reversals*, Monthly Notices of the Royal Astronomical Society., **268**, 1994, 497-505.

[144] R.J. Rand and S.R. Kulkani, *The Local Galactic Magnetic Field*, The Astrophysical Journal, **343**, 1989, 760-72.

[145] J. Ranft, *Cosmic Ray Particle Production*, Presented at Int. Symp. on Multiparticle Dynamics, Frascati, Italy, 1997. Available electronically at `http://xxx.lanl.gov/hep-ph/9711334`.

[146] J. Ranft, *Dual Parton Model at Cosmic Ray Energies*, Physical Review D, **51**, 1995, pg 64-84.

[147] J.W. Strutt (Lord Rayleigh), *On the Problem of Random Vibrations, and of Random Flights in One, Two, and Three Dimensions*, Scientific Papers 1911-1919,**VI**, Cambridge University Press, 1920, pg 604-26.

[148] G.D. Rochester and C.C Butler, *Evidence for the existence of New Unstable Elementary Particles*, Nature, **160**, 1947, pg 855.

[149] In B. Rossi, *Cosmic Rays*, McGraw-Hill, New York, 1964, pg 8-12. It seems likely that the paper reference is (see pg 45 of [78]): Hoffman And Millikan, Nat. Acad. Sci. Pro., **12**, 1926, pg 48-55.

[150] B. Rossi and K. Greisen, Reviews of Modern Physics, **13**, 1941, pg 240.

[151] B. Rossi, *High Energy Particles*, Prentice Hall, 1952.

[152] B. Rossi, *Cosmic Rays*, McGraw-Hill, New York, 1964.

[153] B. Rossi, Z. Phys. **82**, 1933, pg 151.

[154] B. Rossi, Ric, Sci **5**, 1934, pg 583.

[155] Yu M. Shabelski, R.M. Weiner, G. Wilk and Z. Wlodarczyk, *Energy Dependance of Inelasticity from High-Energy Cosmic Rays*, J. Phys. G, **18**, 1992, 1281-90.

[156] K.M. Simpson, University of Adelaide, *Personal Communication*, 1997.

[157] D.V. Skobelzyn, *A New Type of Very Fast Beta Rays*, Z. Phys. **54**, 1929, pg 686.

[158] J. Smith *Electronics for the High Resolution EYE Detector*,Tokyo Workshop on Techniques for the Study of Extremely High Energy Cosmic Rays, ed M. Nagano, ICRR, University of Tokyo, 1993, pg 250-5.

[159] J. Smith *Data Acquisition for the High Resolution EYE Detector*,Tokyo Workshop on Techniques for the Study of Extremely High Energy Cosmic Rays, ed M. Nagano, ICRR, University of Tokyo, 1993, pg 265-268.

[160] P. Sokolsky, *Sky Noise and Atmospheric Transmission*,Tokyo Workshop on Techniques for the Study of Extremely High Energy Cosmic Rays, ed M. Nagano, ICRR, University of Tokyo, 1993, pg 280-97.

[161] P. Sokolsky, *Atmospheric Monitoring for Fluorescence Detector Experiments*, Proceedings of the International Symposium on Extremely High Energy Cosmic Rays: Astrophysics and Future Observatories. ed M. Nagano, ICRR, University of Tokyo, 1996, pg 253-70.

[162] P. Sokolsky, P. Sommers and B.R. Dawson, *Extremely High Energy Cosmic Rays*, Physics Reports, **217**, No 5, 1992.

[163] T. Stanev, P.L. Biermann, J. Lloyd-Evans, J.P. Rachen and A. Watson, Phys. Rev. Lett., **75**, 1995, pg. 3056-59.

[164] C. Störmer, Z. Astr. Phys. **1**, 1934, pg 237.

[165] F. Takahara, *Astronomical Source Candiates for Extremely High Energy Cosmic Rays*, Proceedings of the International Symposium on Extremely High Energy Cosmic Rays: Astrophysics and Future Observatories. ed M. Nagano, ICRR, University of Tokyo, 1996, pg 61-67.

[166] J.K.K. Tang, HiRes Internal Memo, April 9, 1992.

[167] M. Teshima, M. Nagano, T. Hara, N. Hayashida, M. Honda *et al.*, *Neutral Particles from Cygnus X-3 above* $5 \times 10^{17} eV$, Physical Review Letters, **64**, 1990, 1628-31.

[168] S. Thomas, University of Utah, Personal Communication, 1996.

[169] Y. Uchihori, N. Hayashida, K. Honda, *et al.*, *Cluster Analysis of Extremely High Energy Cosmic Rays in the Northern Sky*, Proceedings of the International Symposium on Extremely High Energy Cosmic Rays: Astrophysics and Future Observatories. ed M. Nagano, ICRR, University of Tokyo, 1996, pg 50-60.

[170] University of Utah, *Staged Construction Proposal for the High Resolution Fly's Eye (HiRes) Detector*, NSF Proposal, Sep. 10, 1993.

[171] A.A. Watson, *Studies made at Haverah Park of the Energy Spectrum, Mass Composition, and Anisotropy of Cosmic Rays Above* $4 \times 10^{17} eV$, Proc of the ICRR Int. Symp. - Astrophysical Aspects of the Most Energetic Cosmic Rays, ed M. Nagano and F. Takahara, World Scientific, Singapore, 1991, pg 1-19.

[172] A. Wolfendale, *Cosmic Rays*, George Newnes Limited, London, 1963.

[173] *Cosmic Rays at ground level*, ed A. Wolfendale, Institute of Physics, London, 1973.

[174] T. Wulf, Phys. Z. **11**, 1910 , pg 811.

[175] E. Yen, *New Scaling Variable and Early Scaling in Single-Particle Inclusive Distributions for Hadron-Hadron Collisions*, Physical Review D, **10**, 1974, pg 836-43.

[176] G.B. Yodh, Y. Pal and J.S. Trefil, *Evidence for Rapidly Rising $p-p$ Total Cross Section from Cosmic Ray Data*, Physical Review Letters, **28**, 1972, pg 1005-8.

[177] S. Yoshida, N. Hayashida, K. Honda, M. Honda, S. Imaizumi *et al.*, *The Cosmic Ray Energy Spectrum above $3\times10^{18}eV$ Measured by the Akeno Giant Air Shower Array*, Astroparticle Physics., **3**, 1995, pg 105.

[178] H. Yukawa, *On the Interaction of Elementary Particles*, Proc. Phys. Math. Soc. Japan. **17**, 1935, pg 48.

[179] G.T. Zatsepin and V.A. Kuzmin, *Upper Limit of the Spectrum of Cosmic Rays*, JETP Letters, **4**, 1966, pg 78-80.